Lecture Notes in Civil Engineering

Brahim Benmokrane
Khaled Mohamed
Ahmed Farghaly
Hamdy Mohamed *Editors*

# 8th International Conference on Advanced Composite Materials in Bridges and Structures

Volume 2

Springer

# Lecture Notes in Civil Engineering

## Volume 267

**Lecture Notes in Civil Engineering** (LNCE) publishes the latest developments in Civil Engineering—quickly, informally and in top quality. Though original research reported in proceedings and post-proceedings represents the core of LNCE, edited volumes of exceptionally high quality and interest may also be considered for publication. Volumes published in LNCE embrace all aspects and subfields of, as well as new challenges in, Civil Engineering. Topics in the series include:

- Construction and Structural Mechanics
- Building Materials
- Concrete, Steel and Timber Structures
- Geotechnical Engineering
- Earthquake Engineering
- Coastal Engineering
- Ocean and Offshore Engineering; Ships and Floating Structures
- Hydraulics, Hydrology and Water Resources Engineering
- Environmental Engineering and Sustainability
- Structural Health and Monitoring
- Surveying and Geographical Information Systems
- Indoor Environments
- Transportation and Traffic
- Risk Analysis
- Safety and Security

To submit a proposal or request further information, please contact the appropriate Springer Editor:

- Pierpaolo Riva at pierpaolo.riva@springer.com (Europe and Americas);
- Swati Meherishi at swati.meherishi@springer.com (Asia - except China, and Australia, New Zealand);
- Wayne Hu at wayne.hu@springer.com (China).

**All books in the series now indexed by Scopus and EI Compendex database!**

Brahim Benmokrane · Khaled Mohamed ·
Ahmed Farghaly · Hamdy Mohamed
Editors

# 8th International Conference on Advanced Composite Materials in Bridges and Structures

Volume 2

Springer

*Editors*
Brahim Benmokrane
Department of Civil & Building Engineering
Université de Sherbrooke
Quebec, QC, Canada

Ahmed Farghaly
Civil and Building Engineering
Université de Sherbrooke
Sherbrooke, QC, Canada

Khaled Mohamed
Civil and Building Engineering
Université de Sherbrooke
Sherbrooke, QC, Canada

Hamdy Mohamed
Civil and Building Engineering
Université de Sherbrooke
Sherbrooke, QC, Canada

ISSN 2366-2557 ISSN 2366-2565 (electronic)
Lecture Notes in Civil Engineering
ISBN 978-3-031-09408-8 ISBN 978-3-031-09409-5 (eBook)
https://doi.org/10.1007/978-3-031-09409-5

© Canadian Society for Civil Engineering 2023
This work is subject to copyright. All rights are solely and exclusively licensed by the Publisher, whether the whole or part of the material is concerned, specifically the rights of translation, reprinting, reuse of illustrations, recitation, broadcasting, reproduction on microfilms or in any other physical way, and transmission or information storage and retrieval, electronic adaptation, computer software, or by similar or dissimilar methodology now known or hereafter developed.
The use of general descriptive names, registered names, trademarks, service marks, etc. in this publication does not imply, even in the absence of a specific statement, that such names are exempt from the relevant protective laws and regulations and therefore free for general use.
The publisher, the authors, and the editors are safe to assume that the advice and information in this book are believed to be true and accurate at the date of publication. Neither the publisher nor the authors or the editors give a warranty, expressed or implied, with respect to the material contained herein or for any errors or omissions that may have been made. The publisher remains neutral with regard to jurisdictional claims in published maps and institutional affiliations.

This Springer imprint is published by the registered company Springer Nature Switzerland AG
The registered company address is: Gewerbestrasse 11, 6330 Cham, Switzerland

# Contents

# About the Editors

**Prof. Brahim Benmokrane** (Ph.D., P.Eng.) holds the prestigious Tier-1 Canada Research Chair in Advanced Composite Materials for Civil Structures and the Senior Industrial Research Chair in Innovative FRP Reinforcement for Sustainable Concrete Infrastructure at the Department of Civil & Building Engineering at University of Sherbrooke (Sherbrooke, QC, Canada). Professor Benmokrane is one of the world's leaders in the field of structural concrete internally reinforced with fiber-reinforced polymer (FRP) reinforcement. His research has significantly influenced the development of concrete structures reinforced with FRP bars, building codes, design specifications, and FRP reinforcement's practical use in North America and beyond. His research and professional services have been recognized with several awards. Some of his more note-worthy awards have come from ACI, CSCE, CSA, EIC, OIQ, IIFC, NSERC, and the Royal Society of Canada (Fellow of Academy of Science). He has published over 700 papers and books and has given over 250 lectures worldwide. He currently leads a research group of 36 and has trained 170 researchers. More than 30 of his former graduate students now hold faculty positions in Canada and abroad.

**Dr. Khaled Mohamed** is a Research Associate in the Department of Civil Engineering at the University of Sherbrooke, Canada, and an R&D engineer in Pultrall/V-ROD, Canada. He received his MSc from Assiut University, Egypt, and Ph.D. from the University of Sherbrooke, Canada. His research interest includes the structural behavior and durability of reinforced concrete structures reinforced with fiber-reinforced polymers.

**Dr. Ahmed Farghaly** is a Research Associate in the Department of Civil Engineering at the University of Sherbrooke, Canada. Professor in the Department of Civil Engineering at Assiut University. His research interests include nonlinear analysis of reinforced concrete structures, seismic analysis, performance-based analysis, and sustainability. He has an excellent grasp of structural engineering principles of being Lead Structure and Consultant Engineer with expertise in the field of Power, Oil & Gas industries.

**Dr. Hamdy Mohamed** is a civil engineer and holds a professional engineer license in Canada, with solid experience in research and teaching of reinforced concrete bridges and building structures. He holds a BSc with honors, MSc, Egypt, and Ph.D. in Civil Engineering, Canada. He has taken up several academic roles, including Research Associate, Lecturer, Assistant Professor, Associate Professor, and Course Director. He is a Senior Fellow of the Higher Education Academy (SFHEA) in the UK. Dr. Hamdy's research interest is the use of FRP reinforcement in concrete bridges, parking garages, continuous-reinforced concrete pavement (CRCP), water tanks, underground concrete chambers, and tunneling marine structures.

# Axial Capacity of Concrete Filled GFRP Tubes with Simulated Tube Damage

**Osvaldo Taveras, Abdeldayem Hadhood, Amir Fam, and Bhum Keun Song**

## 1 Introduction

Concrete-filled fiber-reinforced polymer (FRP) tubes (CFFTs) offer a number of advantages as an alternative to conventional reinforced concrete (RC) members and concrete-filled steel tubes due to their excellent corrosion resistance and the simplified and accelerated construction where the tube is also the formwork. CFFTs have been studied, and in several cases used, as poles, piles, overhead sign structures, girders, columns, and piers (Fam et al. 2003a, b). Many studies addressed the structural behavior of CFFTs in terms of strength and durability (Mirmiran and Shahawy 1997; Fam and Rizkalla 2001, 2002; Robert and Fam 2012), including CFFTs exposed to salty environment (Robert and Fam 2012), the residual strength of CFFTs after fire exposure (Echevarria et al. 2015) and the effect of blast and impact loading on CFFTs (Qasrawi et al. 2014).

Given that the FRP tube is exposed, it may be vulnerable to accidental or deliberate damage and vandalism. Accidental damage may be caused by sharp blades of snow plowers tractors, vehicle collisions, or ship impact in marine applications, while vandalism may be caused by sharp tools such as axes, saws, or knives. Lu et al. (2019) addressed this problem for CFFTs subjected to flexural loads. Various configurations

---

O. Taveras · A. Hadhood · A. Fam (✉)
Department of Civil Engineering, Queen's University, 58 University Ave, Kingston, ON, Canada
e-mail: Amir.Fam@queensu.ca

O. Taveras
e-mail: 18odt@queensu.ca

A. Hadhood
e-mail: Ahmed.Abdeldayem@queensu.ca

B. K. Song
Korea Institute of Carbon Convergence Technology (KCTECH), Jeonju 54853, Korea
e-mail: bksong@kctech.re.kr

B. Benmokrane et al. (eds.), *8th International Conference on Advanced Composite Materials in Bridges and Structures*, Lecture Notes in Civil Engineering 267,
https://doi.org/10.1007/978-3-031-09409-5_1

of cuts were induced in the GFRP tube, including cuts in the circumferential and longitudinal directions and cuts on the tension and compression sides, separately. The circumferential cut at the extreme tension side was the most critical type of damage in flexure. The CFFT lost up to 75% of its original moment capacity at a cut equal to 20% of the perimeter. Flexural tension failure governed the failure of most specimens of different types of cuts.

CFFT axial compression members take more advantage of the GFRP tube than flexural members in terms of concrete confinement. The confinement increases both the axial strength and ductility of concrete significantly. This increase is function of tube thickness, tube laminate structure, and the angle of fibers, among other parameters. This study is the first to address the effect of damage of the GFRP tubes on the axial strength of CFFTs.

## 2 Experimental Program

### 2.1 Materials: FRP Tubes and Concrete

Two different types of FRP tubes, designated as G1 and G2, were used in this study. Both were made of E-glass fibers and Epoxy resin using the filament winding method. The G1 and G2 tubes had an outer diameter of 144 mm and 168 mm, respectively, and total wall thickness of 5.5 mm and 4.3 mm, respectively, as shown in Table 1. A burn-off test was used to determine the laminate structure of G1. This involved burning off the epoxy resin from the FRP tube samples in a muffle furnace at 600 °C and exposing the fiber structure. The layers of the FRP were not perfectly uniform along the tube, and the average angles relative to the longitudinal axis were [+61°/−62°]. Tension and compression coupon tests were carried out on G1 tube following a modified version of ASTM D3039 (ASTM 2017) and ASTM D3410 (ASTM 2016). The ultimate longitudinal tensile strength of G1 were 54 MPa and 6.9 GPa, respectively, whereas the ultimate longitudinal compressive strength and Young's modulus of G1 were 122 MPa and 6.4 GPa, respectively. The laminate structure and mechanical properties of G2 were provided by the manufacturer. The average fiber angles relative to longitudinal axis were [+85°/−6°] and the ultimate longitudinal tensile strength and Young's modulus were 110 MPa and 20.7 GPa, respectively.

All CFFT specimens using G1 and G2 tubes were cast on the same day with normal-weight, ready-mixed concrete with 9 mm maximum aggregate size and 120 mm slump. The unconfined compressive strength of concrete was determined by testing plain concrete specimens as reported in Table 1 and was 51.9 MPa and 49.1 GPa for G1 and G2 specimens, respectively.

**Table 1** Test matrix

| No | Specimen ID | Tube Group | Concrete strength (MPa) | H (mm) | D (mm) | Tube | | | | Peak load (kN) |
|---|---|---|---|---|---|---|---|---|---|---|
| | | | | | | t (mm) | Fiber angle | x (mm) | x/H | |
| 1 | G1-P | – | 51.9 | 410 | 133 | – | – | – | – | 721 |
| 2 | G1-C | G1 | | 434 | 144 | 5.5 ± 0.1 | [61°/-62°] | – | – | 1406 |
| 3 | G1-D1 | | | 430 | | | | 46 | 0.11 | 1064 |
| 4 | G1-D2 | | | 421 | | | | 124 | 0.29 | 795 |
| 5 | G2-P | – | 49.1 | 458 | 164 | – | – | – | – | 1036 |
| 6 | G2-C | G2 | | 460 | 168 | 4.3 ± 0.2 | [85/-6] | – | – | 2065 |
| 7 | G2-D1 | | | 456 | | | | 50 | 0.11 | 1515 |
| 8 | G2-D2 | | | 456 | | | | 100 | 0.22 | 1237 |

"H" stands for Height; "t" stands for tube thickness; "x" stands for the longitudinal cut length.

### 2.2 Test Specimens

A total of eight specimens were fabricated and tested in axial compression, in two groups, G1 and G2. Each group includes four specimens. The target nominal height-to-diameter ratio was 3, which was achieved for group G2 but because of the maximum clearance within the testing machine, a nominal ratio of 2.7 was used for group G1. The small differences in heights among specimens resulted from grinding the ends to achieve smooth and flat surfaces. The contribution of unconfined concrete was examined by specimens G1-P and G2-P as plain concrete specimens with the same diameter and height as the core of the CFFTs. The axial capacity and behavior of control CFFT specimens without damage were examined by G1-C and G2-C. The damage effect was simulated by inducing a longitudinal cut throughout the full tube thickness at mid-height, with two different lengths-to-height (x/H) ratios of 11% and 29% in the two remaining specimens of each group, as shown in Table 1. These cuts also represent 10% and 27% of the perimeter (πD) of G1 and 9.5% and 19% for G2 perimeter.

### 2.3 Simulated Damage, Instrumentations, and Testing Procedure

A concrete grinder was used to prepare the ends of the CFFTs to ensure flat and square ends. The damage was then simulated by cutting a longitudinal slit in the GFRP tube using a hand-held rotary tool with a diamond burr nail bit of 1.1 mm diameter. All cuts were made within the middle third of the height of specimens. The specimens were instrumented by electric resistance biaxial strain gauges that were installed in the vicinity of the induced cuts to capture strains in these regions. Other gauges were also mounted around the perimeter to capture the axial and circumferential strains of the undamaged parts. All CFFTs were tested under concentric axial compression using a 2000 kN Forney machine, as shown in Fig. 1, at a rate of 0.25 MPa/s. Load was applied on the full surface of either end including both the concrete and tube.

## 3 Experimental Results

### 3.1 General Behavior

The behavior of CFFTs under consideration is discussed in terms of the load-axial strain profiles. Bilinear responses were observed for the CFFTs as shown in Figs. 2 and 3 where different peak loads were attained. The tested CFFTs exhibited the same initial stiffness until an axial strain level of approximately −0.0008 for G1 and −0.0004 for G2, after which the slope of the curve is reduced to a strain hardening response, with

Fig. 1 Testing of CFFTs under compression loading

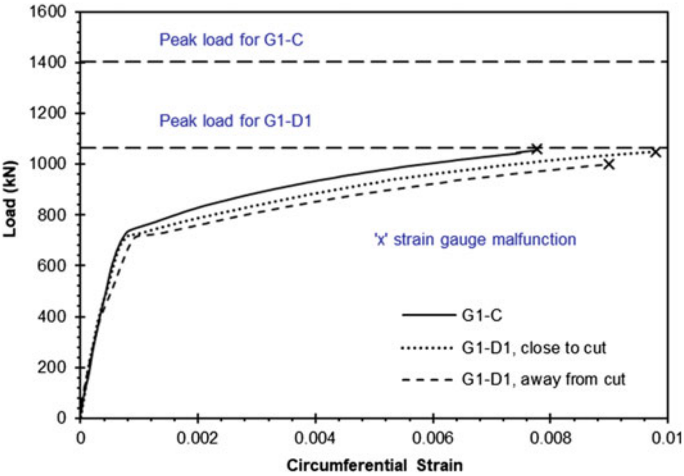

Fig. 2 Load–axial strain relationship for G1

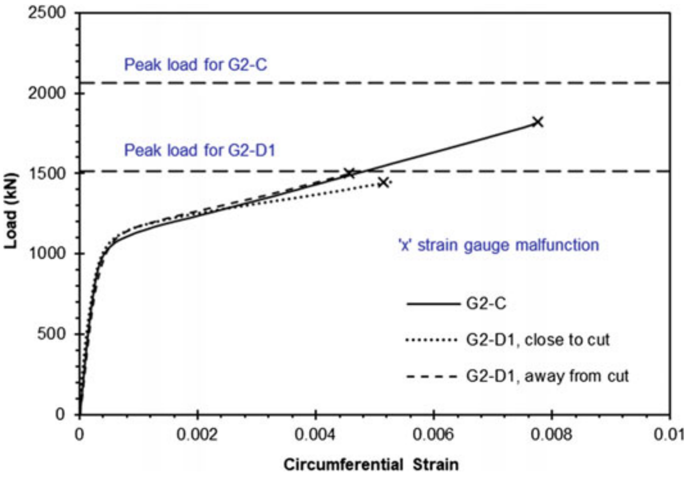

**Fig. 3** Load–axial strain relationship for G2

a nonlinear transition zone. The strain gauges malfunctioned at strain levels ranging between −0.0045 and −0.01.

The strain profile on the circumferential revealed that the induced cut undermined the confinement provided by the tubes on both groups. The control specimens developed the highest level of confinement and achieved the largest peak loads. The tested CFFTs G1-C and G2-C achieved 95% and 99% higher load over plain concrete G1-P and G2-P, respectively, showing the effect of the intact confinement. Cut lengths-to-height of 11% reduced the gain of strength resulting from the tube to 48% and 46% for G1-D1 and G2-D1, compared to G1-P and G2-P, respectively. The induced cut caused discontinuity in the fibers and weakened the confinement effect at mid-height. Increasing the cut length-to-height to 29% and 22% for the G1-D2 and G2-D2, respectively, severely influenced the effectiveness of confinement. Only 10% and 19% gain in strength were achieved for these specimens over G1-P and G2-P, respectively. A comparison of the maximum loads attained by all specimens above the unconfined load is presented in Fig. 4. Figure 5 shows the axial strength retention as function of cut length (as percentage of perimeter).

### 3.2 Failure Mode

The CFFTs generally failed in tension due to the rupture of the tube fibers. The induced cuts accelerated the failure of the damaged CFFTs in this study. The tube fracture initiated at the ends of the longitudinal cuts. Figure 6 shows a sample of a failed specimen from group G1.

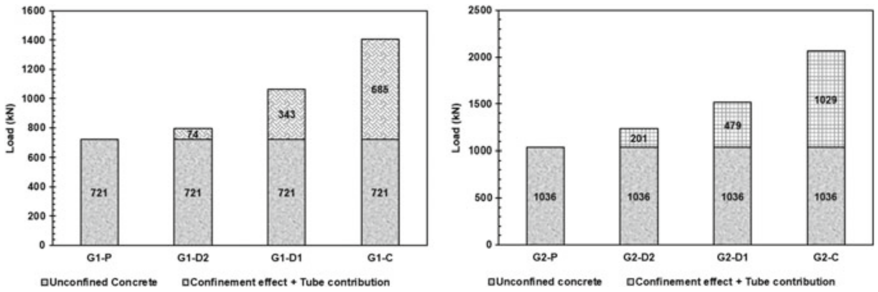

**Fig. 4** Effect of damaged tubes on the axial capacity of G1 (left) and G2 (right)

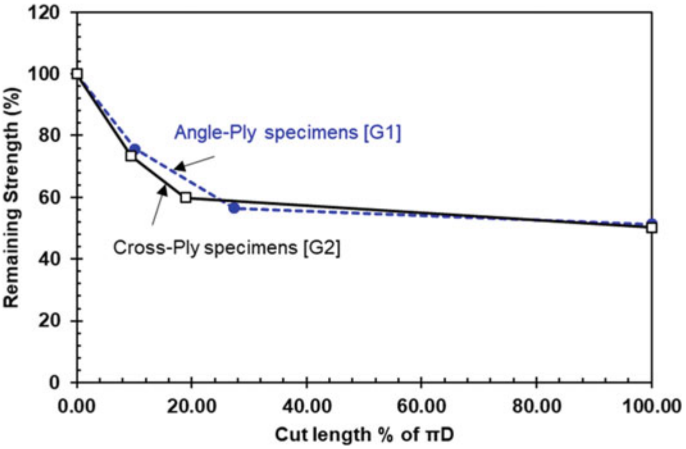

**Fig. 5** Effect of cut length on axial strength retention

# 4 Conclusions

This study is the first to investigate the effect of tube damage on the axial capacity of concrete-filled FRP tubes. The investigation considered two types of tubes including group G1, with angle-ply laminates, and group G2 with near-cross-ply laminate with fibers oriented close to the longitudinal and circumferential directions. The cuts were induced vertically at mid-height with two cut length-to-height ratios of 11% and 27%, which are equivalent to 9.5–10.2% and 19–27.4% of the perimeter. The following conclusions are drawn:

- The confinement provided by the FRP tubes increased the ultimate capacity of the plain concrete specimens by 95% and 99% for the angle-ply and near-cross-ply control CFFTs without cuts, respectively.
- The induced vertical cuts reduced the axial strength of CFFTs. The tube's contribution to the increased axial strength of CFFT reduced from 95 to 48% for

**Fig. 6** Sample of failure of G1

angle-ply CFFT and from 99 to 46% for near-cross-ply CFFT, respectively, at cut length-to-height ratio of 11%

- At cut length-to-height ratios of 29% (in angle-ply) and 22% (in near cross-ply); tubes contribution to axial strength reduced further to 10% and 19%, respectively.
- All CFFTs failed by fracture of the tube in tension. Fracture initiated at the two ends of the longitudinal cuts.

## References

Echevarria A, Zaghi A, Christenson R, Plank R (2015) Residual axial capacity comparison of CFFT and RC bridge columns after fire. Polymers 7(5):876–895

Fam AZ, Rizkalla SH (2001) Behavior of axially loaded concrete- filled circular fiber-reinforced polymer tubes. ACI Struct J 98(3):280–289

Fam AZ, Rizkalla SH (2002) Flexural behavior of concrete-filled fiber-reinforced polymer circular tubes. J Compos Constr 6(2):123–132

Fam A, Greene R, Rizkalla S (2003a) Field applications of concrete-filled FRP tubes for marine piles. Spec Publ 215:161–180

Fam A, Pando M, Filz G, Rizkalla S (2003b) Precast piles for Route 40 bridge in Virginia using concrete filled FRP tubes. PCI J 48(3):32–45

Lu C, St. Onge J, Fam A (2019) Damage threshold of near-cross-ply tubes used in concrete-filled FRP tubes loaded in flexure. J Compos Constr 24(2):04019063

Mirmiran A, Shahawy M (1997) Behavior of concrete columns confined by fiber composites. J Struct Eng 123(5):583–590

Qasrawi Y, Heffernan PJ, Fam A (2014) Performance of concrete-filled FRP tubes under field close-in blast loading. J Compos Constr 19(4):04014067

Robert M, Fam AZ (2012) Long-term performance of GFRP tubes filled with concrete and subjected to salt solution. J Compos Constr 16(2):217–224

# Durability Performance of Various Corrosion Resistant Reinforcing Materials Under Severe Environmental Exposure

**Raafat El-Hacha, Mouhammad Amiri, Martin Hudecek, and Kip Skabar**

## 1 Introduction

Durability of reinforced concrete structures affects mainly the long-term performance and overall life span of a structure, and as such, it significantly influences maintenance and retrofit-related costs. Bridges, parking garages, and port and marine facilities are great representatives of structures that require the application of durable materials the most. These structures face harsh weather conditions, which are oftentimes intensified by chloride-rich solutions resulting from de-icing salts and or the presence of seawater. In response to a need for corrosion-resistant reinforcement replacing conventional corrosion-prone uncoated steel, aka black steel, several types of advanced materials have been developed and used in several industrial applications. Specific materials have been studied and tested independently or in small groups. However, broader comparisons are rare. Therefore, this research focused on durability testing of concrete beams reinforced with various bars exposed to identical conditions simultaneously and tested in the same environment. In this assignment, Stantec Consulting Ltd. (Stantec) initiated the research idea and engaged the University of Calgary (University) to collaborate on the testing that utilized the state-of-the-art climate chamber at the facility of the University.

---

R. El-Hacha · M. Amiri
Department of Civil Engineering, University of Calgary, 2500 University Dr NW, Calgary, AB T2N 1N4, Canada
e-mail: relhacha@ucalgary.ca

M. Hudecek (✉) · K. Skabar
Stantec Consulting Ltd, 1100-111 Dunsmuir St, Vancouver, BC V6B 6A3, Canada
e-mail: martin.hudecek@stantec.com

K. Skabar
e-mail: kip.skabar@stantec.com

B. Benmokrane et al. (eds.), *8th International Conference on Advanced Composite Materials in Bridges and Structures*, Lecture Notes in Civil Engineering 267,
https://doi.org/10.1007/978-3-031-09409-5_2

## 2 Research Goal

The goal of the research was to evaluate the performance of concrete beams reinforced with various types of durable corrosion-resistant bars exposed to a harsh environment accelerated in a climate chamber. The novel approach of this research is to capture and compare with others the behaviour of beams reinforced with newly emerging bars with basalt fibres. The objectives of the research were to evaluate the performance of the beams in the following categories: (1) cracking behaviour at service and ultimate loads, (2) Flexural capacity at ultimate, (3) load–deflection behaviour and (4) ductility. It should be noted that while the aim was to encounter as many parameters as possible, the focus of the experiment was to test beams designed to achieve solely similar ultimate bending resistance. The other parameters mainly required to satisfy serviceability requirements—such as crack width and/or deflection—were not set to govern the design of the beams.

## 3 Background

The durability performance of reinforced concrete members resulting from the application of advanced corrosion-resistant materials has been studied by many researchers. At a general level in the industry, there are two groups of these materials: metal-based and non-metal-based bars. Fibre Reinforced Polymers (FRP) represent the non-metal-based rebars. The loss of bond strength between the FRP rebar and concrete, when exposed to severe environmental conditions, was studied by Chen (2007). Micelli (2004) investigated the effect of severe environmental conditions at an accelerated rate, including cycles of freezing and thawing, exposure to high humidity and temperature, and exposure to ultraviolet (UV) rays, long-term durability of Glass FRP and Carbon FRP bars. The durability of GFRP rebar embedded in the concrete was studied by Chen (2007). Bond strength of GFRP and CFRP rebar, influenced by exposure to water and elevated temperatures, was tested by Dalavos and Chen (2008). The durability of the newly emerging Basalt FRP was investigated by Quagliarini (2016) and Lu (2015). While several research initiatives focusing on specific materials have been carried out, performance comparisons of a broader group of materials are rare.

## 4 Experimental Program

### 4.1 Methodology

The durability investigation, including preparation of the specimens, accelerated exposure, flexural testing and results extraction, was carried out at the facility of

Fig. 1 Arrangement of the testing apparatus and climate chamber

the University. The beams were designed in accordance with CAN/CSA-S6-14 to have similar flexural capacity at ultimate. The reinforcement ratio was selected to assure flexural failure; the beams were "under-reinforced". Prior placement in the climate chamber imposing simulated harsh environmental conditions, all beams were pre-cracked by load reaching 40% of beams' ultimate capacity to generate service life-like cracks allowing chloride-rich solution access to the bars. A set up of the four-point testing apparatus used for pre-cracking and ultimate capacity testing and beams loaded in the climate chamber is shown in Fig. 1.

To accommodate the types four of rebar, sixteen beams (W-150 mm × H-300 mm × L-2,000 mm, supports spaced 1,800 mm apart) were cast. Three beams of each kind were placed into the climate chamber, and one was kept outside as a control beam. Each beam contained four bars placed in two layers. All bars in one beam were of the same diameter.

## *4.2 Materials*

The four types of internal reinforcing bars were (1) basalt-fibre-reinforced polymers by Shanghai Shen Xiang CO, Ltd. (BF), (2) glass-fibre-reinforced polymers by Owens Corning (formerly Hughes Brothers Inc.) (GF-H), (3) glass-fibre-reinforced polymers by Pultral (GF-P) and (4) carbon-fibre-reinforced polymers by Pultral (CF-P). Properties and total area of the bars in one beam, $Ab_{(TOT)}$, are summarized in Table 1.

**Table 1** Properties of the reinforcing bars

| Rebar | Grade | E [GPa] | Diam. [mm] | $Ab_{(TOT)}$ [mm$^2$] | $f_u$ [MPa] | Strain (%) |
|---|---|---|---|---|---|---|
| BF | Grade 52 | 52 | 19.0 | 1136 | 1050 | 2.0 |
| GF-H | Aslan 100 | 46 | 22.0 | 1548 | 655 | 1.4 |
| GF-P | V-Rod Grade 60 | 60 | 19.1 | 1136 | 1100 | 2.1 |
| CF-P | V-Rod Carbon | 144 | 13.0 | 507 | 1765 | 1.3 |

The concrete mix was designed and prepared at the University to meet minimum requirements for Precast reinforced concrete barriers as per section 941.02 of the Standard Specifications for Highway Construction in British Columbia. The minimum requirements were compressive strength 30 MPa, minimum cement content 320 kg/m$^3$, maximum water/cement ratio 0.45, coarse aggregate maximum size 28 mm, slump 50 mm ± 20 mm and entrained air 5–8%. It should be noted that while the minimum requirements were met, the variability in specific concrete strength, $f_c$’, was greater than expected since the concrete batches were prepared in small volumes individually reflecting the size limitation of the laboratory. Variation of the $f_c$’ was also affected by the exposure regimes. Due to the high temperatures of the thawing cycle, $f_c$’ of the exposed beams was greater than $f_c$’ of the control beams; the difference in $f_c$’ ranged between 2 and 14 MPa. Such variation was considered, and collected results were normalized to allow accurate evaluation.

## 4.3 Exposure Regimes

A schematic representation of one cycle of the exposure regime is shown in Fig. 2. The environmental exposure was simulated in a climate chamber allowing for cycles of freezing and thawing in a temperature range between −34 °C and +34 °C, combined with spraying saltwater with 3.5% NaCl concentration. With the frequency of 3 freeze/thaw cycles per day, 195 cycles were completed in 65 days (9.3 weeks ~ 2.3 months). Such accelerated exposure represented an equivalent of 5 years in real conditions. The regimes were selected based on CAN/CSA-S6-14 Figures A3.1.1 and A3.1.2 and the work of Omran and El-Hacha (2014) and Rojob and El-Hacha (2017).

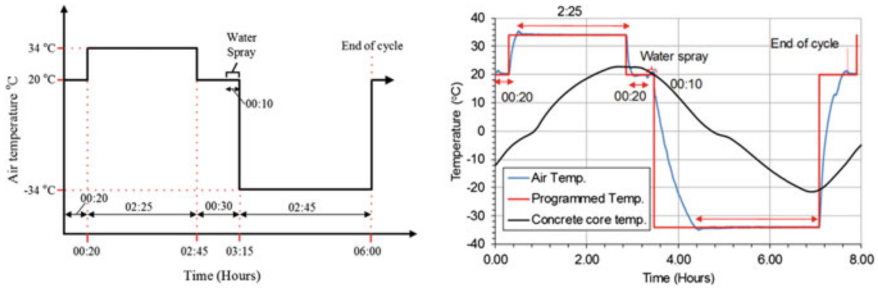

**Fig. 2** Freeze/thaw cycle of the exposure regime in the climate chamber

# 5 Results

## 5.1 *Cracking Behaviour at Service and Ultimate Loads*

A comparison of the number of cracks and crack width is shown in Fig. 3. Figure 3a indicates that the average number of cracks at the pre-cracking stage (40% of flexural capacity) in the beams with conventional FRPs, i.e. GF-H, GF-P and CF-P is smaller than in beams with novel BF. As expected, the modulus of elasticity of the reinforcement ($E_{frp}$) plays a significant role, the beams with CF-P ($E_{frp} = 144$ GPa) experience 30% less cracks than beams with BF. However, the comparison shows that it is not only $E_{frp}$ but the strain at ultimate that governs the number of cracks. Beams with GF-H of lowest $E_{frp}$ (46 GPa) had smaller strain than BF bars (1.4% vs 2.0%, respectively), and therefore, 16% fewer cracks than beams with BF of higher $E_{frp}$ (52 GPa). At ultimate loads (100% of flexural capacity) after the exposure to severe environmental conditions, the trend is similar as shown in Fig. 3b. Crack width measured at midspan is the largest and smallest in beams with BF (large strain) and CF-P (highest $E_{frp}$), respectively. Crack width in both types of conventional GF-H and GF-P is 26% and 49% smaller, respectively, than in beams with BF.

## 5.2 *Flexural Capacity at Ultimate*

The effect of exposure on flexural capacity, interpreted via flexural stiffness of the beams at ultimate, is shown in Fig. 4. From the figure is apparent that difference is the smallest in beams with BF (3%) and greatest in beams with GH-P (23%). Response of the beams to the exposure is function of several parameters, such as properties of the concrete, number and size of cracks and properties of the bars. Analysis and data postprocessing confirmed that compressive strength of the concrete of the exposed

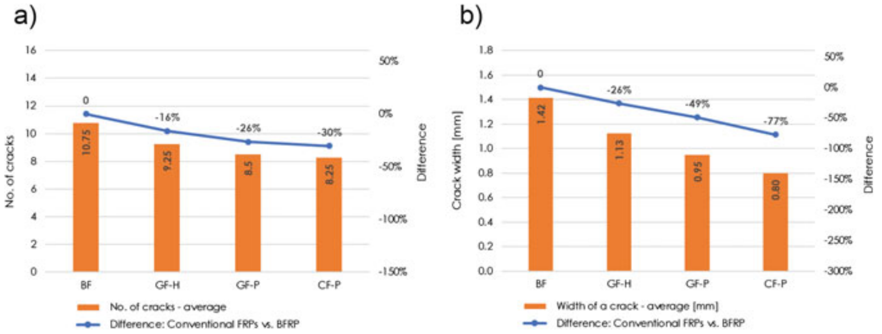

**Fig. 3** **a** Number of cracks in pre-loaded beams (40% capacity), **b** Crack width in the exposed beams at ultimate load (100% capacity)

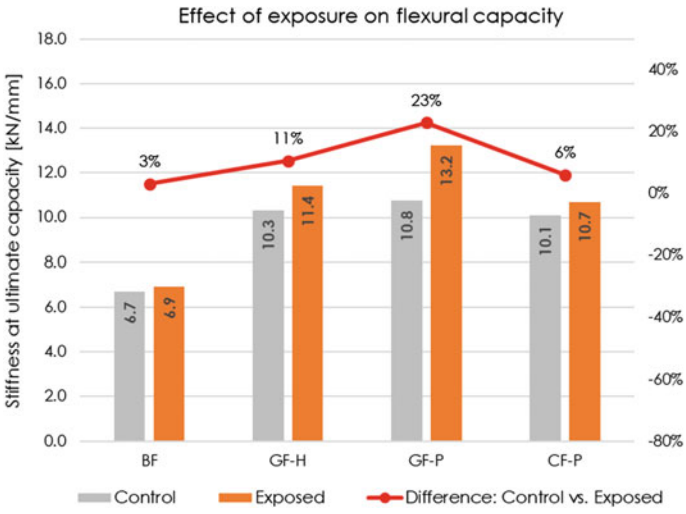

**Fig. 4** Flexural stiffness of the control and exposed beams

beams was enhanced due to elevated temperature of the thawing cycle. As expected, properties of the bars played a significant role. Bars with low E or large strain at ultimate developed frequent and deep cracks, and therefore, despite the concrete properties were enhanced due to the exposure, the concrete deteriorated at greater level and resulted in smaller increase in flexural stiffness. Therefore, when evaluating data shown in Fig. 4, one can conclude that the greater the difference between control and exposed beams is, the smaller impact the environmental exposure has on the beam's response. In other words, the beams with overall low durability (experiencing a lot of concrete spalling, cracks, etc.) will result in low improvement of flexural stiffness. These observations indicate that, when considering solely ultimate flexural capacity, the beams with GF-H and GF-P experience the smallest impact of the exposure, and therefore, have the greatest durability from the considered materials.

## *5.3 Load–Deflection Behaviour*

The load–deflection curves of the control and exposed beams with the emerging BF bars and convectional FRP bars showing high performance, i.e. the GF-P, are depicted in Fig. 5. It should be noted that the main intention was to compare the trends in load–deflection response affected by the exposure and not the maxima of deflections, as those were influenced by enhanced $f_c$'. From the figure is apparent that all test specimens acted similarly at the portion of initial stiffness. However, the load–deflection distribution changes at the onset of crack formation, after which it

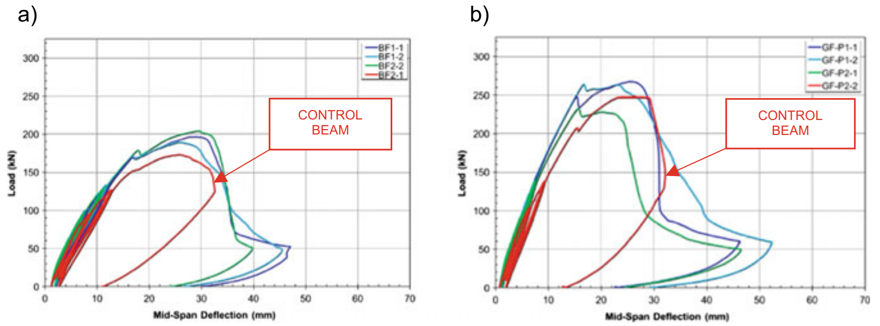

**Fig. 5** Load deflection curves of control and exposed beams with **a** BF bars, **b** GF-P bars

**Table 2** Deformability index of beams reinforced with corrosion-resistant bars

| BF | GF-H | GF-P | CF-P |
|---|---|---|---|
| 17.2 | 18.5 | 19.8 | 18.4 |

is the modulus of elasticity that controls the magnitude of displacement. Overall, the effect of exposure on load–deflection distribution is minimal up to the maximum load.

### 5.4 Ductility

The ductility was evaluated via deformability index, which was calculated as a ratio of energy dissipated at ultimate loads over energy dissipated at service. The dissipated energy was calculated as the area under the load–deflection curve. The outcomes of the analysis are summarized in Table 2.

From the table is apparent that beams reinforced with GF-P experience the greatest ductility (19.8) as expected due to its high $E_{frp}$ (60 GPa). The effect of strain at ultimate and low $E_{frp}$ was confirmed in beams with BF bars. The ductility is 13% smaller in beams with BF than in beams with GF-P. Nevertheless, similarly to the effect of exposure on flexural stiffness, the level of concrete deterioration played a significant role. Beams with CF-P experienced ductility only 7% greater than beams with BF. Therefore, properties and composition of concrete mix need to be selected in accordance with properties of the bars.

**Table 3** Comparison of improved level of durability in beams reinforced with conventional FRP bars

| Objective (Parameter considered) | Material | | |
|---|---|---|---|
| | GF-H | GF-P | CF-P |
| Cracking up to 40% | ☑☑ | ☑☑☑ | ☑☑☑ |
| Cracking up to 100% | ☑☑ | ☑☑☑ | ☑☑☑☑ |
| Flexural capacity (exposed) | ☑☑☑ | ☑☑☑☑ | ☑☑ |
| Load-deflection response | ☑☑ | ☑☑☑☑ | ☑☑☑ |
| Ductility | ☑☑ | ☑☑☑ | ☑☑ |

Improvement: High: ☑☑☑☑☑ Medium-High: ☑☑☑☑ Medium ☑☑☑ Low-Medium: ☑☑ Low: ☑

## 6 Conclusions

The research examined the durability of four types of bars internally reinforcing concrete beams representing a bridge parapet located in a splash zone. Considering the main objective was to have all the beams with similar flexural capacity, it can be concluded that the effect of harsh environmental exposure simulated in accelerated conditions of the climate chamber was influenced by the modulus of elasticity of the bars and quality of concrete. The overall performance of beams correlated with the formation of cracks at service and ultimate loads, affecting not only load-defection distribution but also deterioration of the concrete. The level of improved durability while using conventional FRP bars over novel bars with basalt fibres, summarizing the research outcomes, is compared in Table 3. This table can serve as a guideline in applications where flexural capacity at ultimate of the members exposed to harsh environment plays a key role.

**Acknowledgements** For the generous donation of the rebars, we would like to thank V-rod Canada, Owens Corning (formerly Hughes Brothers Inc.) and Shanghai Shen Xiang CO, Ltd. We thank the University of Calgary, Mitacs and the Natural Sciences and Engineering Research Council of Canada (NSERC) for their financial support of this research project. We appreciate the work of Mouhammad Amiri, a Master of Science student who carried out the laboratory work at the University of Calgary. We also like to thank the technical staff at the University of Calgary for their expertise and help on this project.

## References

Chen Y, Davalos JF (2007) Accelerated aging tests for evaluations of durability performance of FRP reinf. bars for concrete structures. Compos Struct 78(1):101–111

Dalavos JF, Chen Y (2008) Effect of FRP bar degradation on interface bond with high strength concrete. Cement Concrete Compos 30(8):722–730

Lu Z, Xian G (2015) Effects of elevated temperatures on the mechanical properties of basalt fibers and BFRP plates. Constr Build Mater 127:1029–1036

Micelli F, Nanni A 2004 Durability of FRP rods for concrete structures. Constr Build Mater 18(7):491–503

Omran HY, El-Hacha R (2014) Effects of sustained load and freeze-thaw exposure on RC beams strengthened with Prestressed NSM-CFRP strips. Adv Struct Eng, 1801–1816

Quagliarini E, Monni F (2016) Basalt fiber ropes and rods: Durability tests for their use in building engineering. J Build Eng 5:142–150

Rojob H, El-Hacha R (2017) Self-prestressing using iron-based shape memory alloy for flexural strengthening of reinforced concrete beams. Amer Concrete Inst (ACI) 114(2):523–532

# Dynamic Response Calibration of Hybrid Floating Bridge System Using Rayleigh Damping

**Ahmed S. Elareshy, M. M. Abdel Wahab, Sherif A. Mazek, and Ashraf Osman**

## 1 Introduction

The floating bridges provide an economic and efficient solution for crossing water obstacles where the situation is unstable for traditional bridges (Viecili et al. 2014). Recently, the use of floating bridges has gained more attention due to the fact of conventional bridges are about four times costlier than floating bridges (Watanabe et al. 2004). However, different structural systems of floating bridges can be used based on the site condition (i.e., separated or continuous, moored or cable anchored, etc.). There are no defined rules to analyze and design floating bridges. There is no code to find out the dynamic behavior due to the large variation in many factors such as water current, wave forces, depth of water, and the width of the water channel (El-Desouky 2011). Every floating bridge response has to be designed and studied case by case. Therefore, the aim of this study is to investigate the dynamic response of three different connected ribbon floating bridge units, seeking more rapid mobility and maneuverability. Due to the structural system variance in masses, stiffnesses, and damping behavior, an effort in the current study is exerted to calibrate the dynamic response using Rayleigh proportional damping.

## 2 Floating Bridge Description

The full floating bridge system is an integration between the Heavy Communication Bridge (HCB) and the assault bridge PMM71 by using the interconnecting pontoon (NCP). The HCB and the PMM71 depths are 1.5 m (4.92 ft) and 0.75 m (2.46 ft),

---

A. S. Elareshy · M. M. Abdel Wahab · S. A. Mazek · A. Osman (✉)
Department of Civil Engineering, Military Technical College, Kobry Al-Kobba, Egypt
e-mail: Ashraf.osman@mtc.edu.eg

B. Benmokrane et al. (eds.), *8th International Conference on Advanced Composite Materials in Bridges and Structures*, Lecture Notes in Civil Engineering 267,
https://doi.org/10.1007/978-3-031-09409-5_3

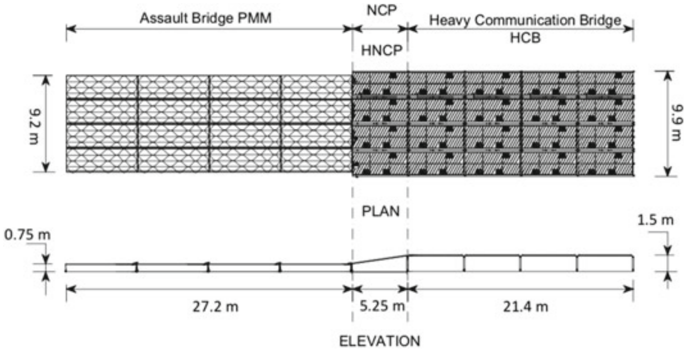

**Fig. 1** An illustration of floating bridge system

respectively, with a double difference in height. Therefore, the genuine steel NCP, hence the HNCP has a trapezoidal shape in the longitudinal traffic direction in order to connect the traffic line and provides a suitable transition slope through its length for the passing vehicles. The buoyancy stability of the individual floating steel NCP was studied by Elareshy et al. (2020), such that a single NCP unit can be easily connected to both HCB and PMM71 systems with a slight difference in connection height. The floating bridge system clear span is 53.85 m (176.67 ft) without the shoring ramp units divided as follows: the assault floating units PMM71 has a 27.2 m span, a length of 21.4 m (70.21 ft) is covered by the HCB, and the interconnecting NCP is of 5.25 m (17.22 ft) length. The assembled full floating bridge module is of 9.55 m (31.33 ft) average width that provides one traffic lane. The HCB, NCP width is 9.9 m (32.48 ft) and the assault PMM71 is 9.2 m (30.18 ft). The HCB traffic width is assembled using four separate pontoon units by connecting them together laterally in the transverse direction of traffic, similarly, the steel and HNCP are placed, whereas the assault PMM71 system is launched in the water from the carrying trucks already assembled of four pontoons in a W shape. Four assault floating PMM71 units of length 6.7 m (21.98 ft) each including four spaces of 0.1 m (0.33 ft) in between form the 27.2 m (89.24 ft) covered by this system. A schematic drawing of the whole floating bridge assembly is presented in Fig. 1.

## 3 Numerical Modeling

### *3.1 Geometry Description*

A 3D finite element model of the whole floating bridge system is built using the ANSYS workbench. The floating bridge model of the HCB, the PMM71, and the steel NCP presented and validated with the experimental results by Elareshy et al. (2020) is used in the current study to calibrate the dynamic response of the bridge system, such that, the same material property, connection types and element types used for metallic steel sheets and sections are kept the same in the current model, whereas the HNCP is redesigned and modeled to replace the genuine steel NCP. The prediction of the dynamic response for this model is a more complex model due to the different connection types used to integrate the system, such that, three connection types are used in assembling the bridge floating system: rigid connections, hinged connections along with steel wire connections. All HCB pontoons are connected using rigid connections in which structural moments are transferred between the units, such that deflections and vibrations are minimized, whereas the PMM71 are assembled using hinged and steel wire connections that lead to higher deflections and vibrations. As a result, the NCP has the three types of connections to be equipped with the ability to connect both floating bridge systems (i.e., HCB, and PMM71). The wire connections are modeled as nonlinear connections where a nonlinear behavior in the internal force–displacement relationship is provided. Steel type (St.44) is used in manufacturing the different steel floating pontoons. According to ECP 205/2012, St.44 has a nominal yield strength of 2.8 t/cm$^2$ (39.83 kips) and ultimate strength of 4.4 t/cm$^2$ (62.6 kips). The element type used to simulate the steel internal structure and diaphragms of pontoons is the 3D beam element (beam188), the steel and CFRP laminated sheets are modeled using the 3D element (shell181) which has an isotropic and orthotropic layered material model capability, the nonlinear connections are modeled using the link element type (link180), such that tension only for wire cables and compression only for contact of steel pads between pontoons can be precisely simulated. Figure 2 shows the three different types of connections in NCP pontoons.

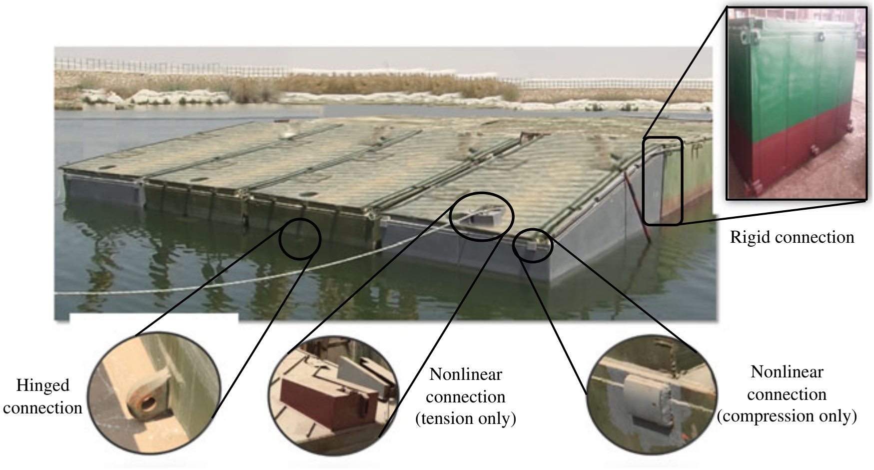

**Fig. 2** A photo represents the three connection types used for the integration of floating bridge system Elareshy (2020)

### 3.2 Hybrid NCP

The steel NCP is designed of sheet plates of 4 mm thickness for side skins and 6 mm thickness for upper and lower skins, as well as different steel IPE, UPN, and equal angle sections for the internal structure, given this, a weight of 16.8 tons is obtained for four NCP units to assemble the traffic line. Figure 3a, b show the steel NCP internal structure skeleton and used sections; and the geometry dimensions, respectively. Seeking more improvement in rapid mobility, the NCP is redesigned as a hybrid combination between CFRP laminated sheets and internal steel skeleton, such that CFRP composite laminated sheets are used for sides and lower skin cladding and sandwich composite laminated structure is applied for decking the surface of transverse vehicles, the deck is supported by internal transverse CFRP diaphragms and bulkheads, whereas the internal steel sections are forming a marginal skeleton to enable the welding of connection joints. Figure 4a. illustrates the HNCP steel internal structure, and Fig. 4b. shows the sandwich composite deck and laminated sheet surfaces. All composite CFRP sheets for the HNCP hull, internal longitudinal and transverse diaphragms, and bulkheads are modeled of 14 carbon/epoxy UD layers of $[0, \pm 45, 90, \pm 45, 0]_s$ fiber architect. The resulting total composite sheet thickness is 10.5 mm (0.41 in), considering a VARTM technique is used to manufacture the composite sheets that would result in an average thickness of 0.75 mm (0.03 in) mm/layer. The composite CFRP sandwich structure for the deck is composed of an aluminum alloy honeycomb core of depth 60 mm (2.36 in), and of 23.76 kg/m$^2$ (4.87 psf) areal weight, as well as upper and lower skins of 11 carbon/epoxy UD layers of

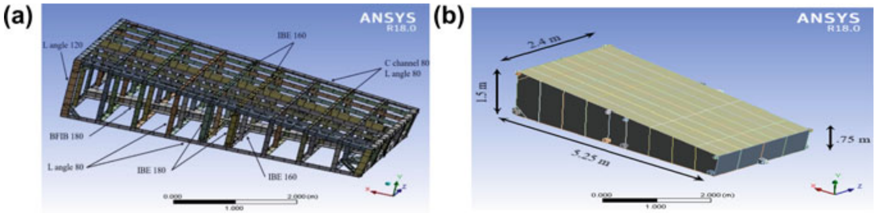

**Fig. 3** **a** Steel NCP internal structure, **b** NCP geometric dimensions

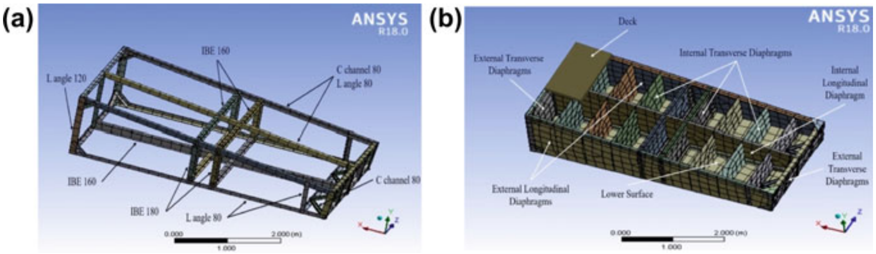

**Fig. 4** **a** HNCP internal steel structure, **b** HNCP deck and CFRP sheets

$[0_3, \pm 45, 90, \pm 45, 0_3]$ fiber arrangement. The carbon martial and resin formulation used are the same applied for the Composite Assault Bridge (CAB) system. This carbon/epoxy material is characterized by an excellent performance in the wet/hot conditions based on Kosmatka et al. (2000) experimental testing.

### 3.3 Boundary Conditions and Failure Criteria

The applied load is a hypothetical vehicle tank load of Military Loading Class 70 tons (MLC70) as per stated in the Trilateral Design and Testing Code of Military Bridging and Gap Crossing Operations (TDTC 2005). TDTC is a code that states provisions for the analysis and design of composite, metallic, deployable, or floating bridges to be internationally accepted for service under extreme conditions. The tank footprint of MLC70 vehicle is 4.57 m (14.99 ft) in length and 0.6 m (1.97 ft) in width. A transient dynamic analysis is performed using the applied load and considering a geometrical nonlinearity. The load is applied as a centric load traveling over the whole bridge span. In the current bridge case study, the wind loads are negligible due to the low profile of the whole bridge system. On the other hand, despite the great effect of water current forces affecting the flooded part of this type of ribbon bridge, the lateral supports performed by using small boats along the bridge span are balancing the water current actions. Due to the relatively medium span of the studied bridge, wave tidal loads are not considered in the current study. In general, the floating bridge is modeled as a simply supported beam rested on elastic supports, the elastic support stiffness is equivalent to the buoyancy stiffness.

In the present case study, analysis of load combinations on a single composite laminated sheet may be difficult to predict, therefore, the Tsai-Wu failure criterion as well as the maximum strain and maximum stress are considered as the design failure criteria. The minimum factor of safety of the three-failure criterion analysis output is the one considered. On the other hand, the face sheet failure criterion, core failure criterion, and shear crimping criterion are considered for the CFRP sandwich composite design and analysis.

## 4 Equation of Motion and Rayleigh Damping

The ribbon floating bridge system can be considered as a multi-degree of freedom system under externally applied time-dependent load, Fig. 5 shows a representation of the floating bridge system free body diagram subjected to a traveling vehicle load, and can be expressed as

$$m \cdot \ddot{\chi} + c \cdot \dot{\chi} + \kappa \cdot \chi = P(t) \tag{1}$$

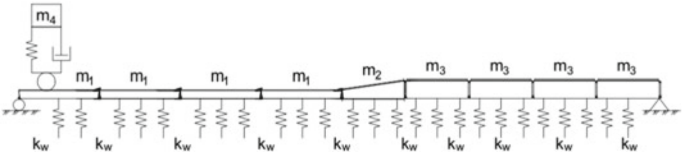

**Fig. 5** Multi-degree of freedom representation of the ribbon floating bridge system

where $m$ is the structural mass and added mass (i.e., the hydrodynamic forces and moments caused by the displaced surrounding fluid), $c$ is the damping factor, $\kappa$ is the pontoon stiffness, and the stiffness of the underlying water simulated as elastic springs, considering a six degree of freedom at each node, the system is represented in the matrix formulation as

$$\sum_{k=1}^{6}\left[M_{jk}^{G}\cdot\ddot{\chi}_{k}+C_{jk}^{G}\cdot\dot{\chi}_{k}+K_{jk}^{G}\cdot\chi_{k}\right]=P_{j}\cdot e^{-i\omega_{e}t},\ j=1,2,3,\ldots,6 \tag{2}$$

where $M^G$, $C^G$, and $K^G$ are $6 \times 6$ global matrix of mass and added mass matrix, global damping matrix, and global stiffness matrix of the floating bridge, respectively. $\ddot{\chi}_k$, $\dot{\chi}_k$, and $\chi_k$ are $6 \times 1$ vectors of acceleration, velocity, and displacements of the floating bridge in three translations and three rotations, respectively, and $P_j$ is $6 \times 1$ global load vector acting of the bridge (Faltinsen 1993), the above equation in matrix form can be solved by integration in the time domain if all the coefficients are constants. For the numerical analysis in this study, the global mass $M^G$ and global stiffness $K^G$ matrices are found by the FE calculations, whereas the global damping matrix $C^G$ has to be input by the engineer.

The damping of the floating bridge system is playing an instrumental role in predicting a precise dynamic response of bridge structure. In the current study, system damping is occurred by the bridge structure itself as well as the water structure interaction, in other words, the floating structure damping is caused by the pontoons material (i.e., hysteretic damping), the friction between the pontoon connections (i.e., frictional damping), in addition to a larger effect by the water damping (i.e., hydrodynamic damping), thus the physical engineering problem can be considered highly nonlinear. In the present case, different damping values have to be assigned for the three connection types used in assembling the floating pontoons. Material and water damping also have to be quantified, all these values must be obtained from the extensive experimental evaluation. Another way to predict the global floating bridge damping response is to derive the damping matrix $C^G$ from proportional or Rayleigh damping. The Rayleigh method in the matrix form can be expressed as follows (Chobra 1995):

$$C_{jk}^{G}=\alpha\cdot M_{jk}^{G}+\beta\cdot K_{jk}^{G} \tag{3}$$

where $\alpha$ and $\beta$ are the mass and stiffness Rayleigh constants, respectively, such that, by knowing the damping ratios $\zeta_i$ and $\zeta_j$ of the $i^{th}$ and the $j^{th}$ modes by using Eq. (4), $\alpha$ and $\beta$ can be calculated from Eq. (5)

$$\zeta_i = \frac{c}{c_{cr}} = \frac{c}{2m\omega_i} \tag{4}$$

$$\begin{Bmatrix} \zeta_i \\ \zeta_j \end{Bmatrix} = \begin{Bmatrix} \alpha \\ \beta \end{Bmatrix} \cdot \frac{1}{2}\begin{bmatrix} 1/\omega_i & \omega_i \\ 1/\omega_j & \omega_j \end{bmatrix}$$

and

$$\alpha = \zeta_i \cdot \frac{2\omega_i \cdot \omega_j}{\omega_i + \omega_j}, \beta = \zeta_j \cdot \frac{2}{\omega_i + \omega_j} \tag{5}$$

## 5 Damping Calibration of NCP and HNCP

A transit dynamic analysis is performed on the steel NCP without taking the global damping of the ribbon floating bridge into consideration, the preliminary results showed a significant oscillation in displacement time history response. Therefore, the proportional Rayleigh damping is used to calibrate the dynamic response of the bridge. Firstly, modal analysis is carried out to quantify natural frequency, natural period, and cumulative mass participation in all transitional degrees of freedom, with a remarkable consideration for the cumulative mass in the heaving, uncoupled direction of bridge motion as well as the direction of torsional stiffness of the bridge. It is reasonably noted that more than 75% of the cumulative mass has participated in the first mode shape in the upward-downward direction of motion. Due to the large number of model degrees of freedom, the modal analysis is performed up to reaching 90% of cumulative mass participation in the uncoupled direction of the bridge, which resulted in the 16th modal shape. It is concluded that the first 16 modal shapes are the governing modes of the floating bridge because 90% cumulative mass is reached in both heave and water current directions, as well as 75% in the longitudinal direction of motion. Table 1 illustrates the natural frequency values and the mass participation percent in the first and the sixteenth modal shapes. Secondly, the natural frequencies of the first and the sixteenth modal shapes are applied to compute the Rayleigh constants $\alpha$ and $\beta$ in Eq. (5) while assuming both modes having the same damping ratio $\zeta$ of 0.2. As a result, $\alpha$ and $\beta$ values are found to be 0.89878 and 0.00254, respectively. Similarly, $\alpha$ and $\beta$ factors are obtained to calibrate the bridge dynamic response while using the HNCP instead of NCP for assembling the bridge. $\alpha$ and $\beta$ are computed as 0.78274 and 0.0034, respectively.

**Table 1** Natural frequency values and mass participation of the 1st and 16th modal shapes

| Mode | Natural cyclic frequency ($f$) | Natural circular frequency ($\omega$) | Natural period ($T$) | X Direction of vehicle motion | | Y heaving direction | | Z direction of water current | |
|---|---|---|---|---|---|---|---|---|---|
| | | | | Effective Mass | Cumulative ratio | Effective mass | Cumulative ratio | Effective Mass | Cumulative ratio |
| | (Hz) | (rad/sec) | (sec) | Kg | % | kg | % | kg | % |
| 1 | 0.3631 | 2.28 | 2.754 | 72.216 | 0.05 | 111,656 | 77.31 | 0.0735 | 0.00 |
| 16 | 24.675 | 154.96 | 0.041 | 30.767 | 78.44 | 1.0101 | 91.04 | 0.0003 | 93.81 |

Figure 6 shows the maximum draft time history response due to the oscillated and calibrated heaving motion using Rayleigh damping of the floating bridge integrated using the NCP.

Figure 7 the first and sixteenth modal shapes of the full floating bridge system of the HNCP. Figure 8 shows the maximum calibrated draft time history response of the floating bridge at the two tank vehicle speeds of 8 km/h and 16 km/h assembled once using NCP and another using HNCP. The results showed an improvement of the draft values by a difference of 3.8% and 3.69% for the 8 km/h and 16 km/h

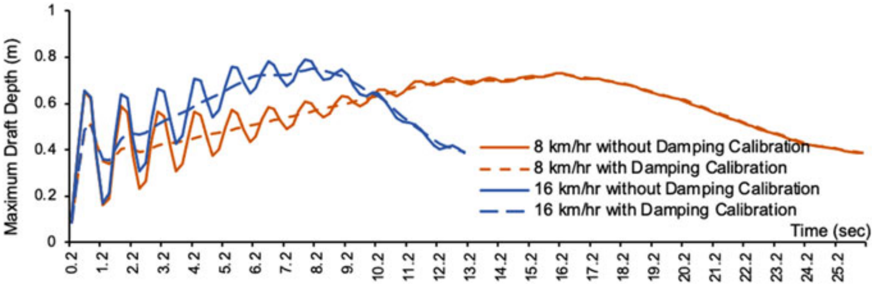

**Fig. 6** Maximum draft time history response of bridge oscillated and calibrated heaving motion

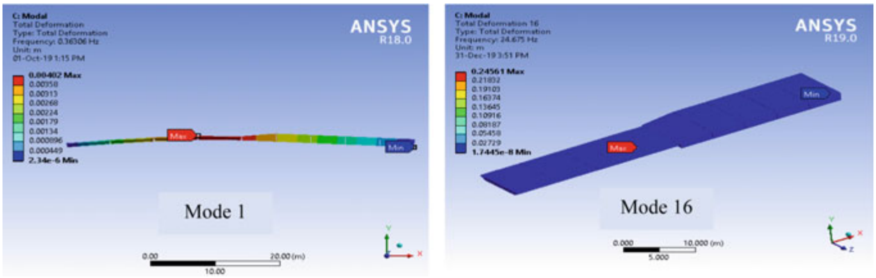

**Fig. 7** Representation of the 1st and 16th modal shapes of the ribbon floating bridge system

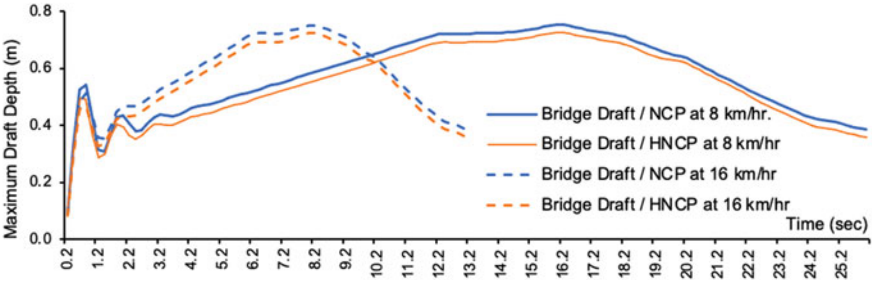

**Fig. 8** Comparison between maximum draft time history response of bridge calibrated heaving motion

vehicle speeds, respectively. Considering the small mass of HNCP compared to the full metallic floating system, the floating bridge draft values are expected to enhance to a considerable limit when manufacturing pontoons using FRP composite sheets.

Table 2 illustrates the obtained maximum equivalent steel stress values in the ribbon floating bridge during a vehicular load motion at the two speeds of 8 and 16 km/h, in addition to the minimum safety factors obtained from all failure criteria of CFRP composite sheets and CFRP sandwich deck.

## 6 Conclusions

This study aims to investigate the dynamic response of hybrid structure of ribbon floating bridge using the proportional damping of the Rayleigh method. The study was based on a validated numerical FE model with experimental results for a maximum draft of a ribbon floating steel bridge. The dynamic response of the validated model is calibrated using Rayleigh damping. The ongoing research is aiming to implement hybrid CFRP and steel floating pontoons seeking more rapid mobility. An assembled unit of hybrid NCP is used to connect the HCB and assault floating bridge PMM71 for rapid maneuverability. The dynamic response of the integrated full floating bridge is investigated and calibrated similarly using proportional damping. The obtained results showed an acceptable improvement in the difference between maximum draft time history values of experimental and numerical FE models. Therefore, the process is applied to study the dynamic response of HNCP connecting HCB and the assault bridge PMM71. The results showed a similar dynamic response with better draft values. Despite the relative enhancement obtained in maximum draft time history values, the calculated proportional stiffness damping factor is too small, that would result in minimizing the effect of water damping. It is more realistic to numerically simulate the ribbon floating bridge as the beam rested on an elastic foundation with viscous damping capability, subsequently, perform a parametric study on the viscous damper to enhance the draft difference between experimental and numerical values. This is expected to have an effect on the natural frequency values to maximize the proportional stiffness damping term. On the other hand, the sandwich composite deck of aluminum honeycomb core provides two-way bending capability which is not mandatory for the case of ribbon floating military bridges. Moreover, it provides a typical deck areal weight of 28.56 kg/m$^2$ (5.85 psf). Other CFRP sandwich cores for extreme loading applications have better areal weight such as the one developed by Robinson and Kosmatka (2008) and Osman (2016) up to 48% and 62% lighter, respectively. However, they need an accurate evaluation of the core orthotropic properties due to their one-way bending capability. Utilizing these cores has a significant reduction in composite pontoons' weight hence, enhance their rapid mobility.

**Table 2** Summary of steel maximum equivalent stresses and minimum CFRP safety factors

| Maximum equivalent stresses (t/cm$^2$) | | | | Minimum obtained safety factor | | | | | |
|---|---|---|---|---|---|---|---|---|---|
| NCP | | HNCP | | CFRP composite sheets | | | CFRP sandwich deck | | |
| Full bridge | NCP | Full bridge | HNCP | Max. stress failure | Max. strain failure | Tasi-Wu criterion | Face sheet failure | Core failure | Shear crimping failure |
| 1.36 | 0.913 | 1.4 | 0.89 | 2.36 | | | | | |

## References

Chobra AK (1995) Dynamics of structures, theory and applications to earthquake engineering. Prentice Hall Ch 11:416–419

Elareshy A (2020) Study the behavior of different laminated sections under the effect of static and dynamic loads. MSc Thesis, Military Technical College, Egypt

El-Desouky O (2011) Dynamic behaviour of short-term floating bridges, PhD thesis, Department of Civil and Environmental Engineering, Carleton University, Ottawa, Ontario

Elareshy A et al (2020) Numerical modelling of new connection pontoon under static and dynamic loads. The 13th international conference on civil and architectural engineering, ICCAE-13

Faltinsen O (1993) Sea loads on ships and offshore structures. Cambridge University Press

Kosmatka J et al (2000) Advanced composites for bridge infra-structure renewal- phase II. DARPA: University of California San Diego p 326

Osman A (2016) Design optimization of composite deployable bridge systems using hybrid meta-heuristic methods for rapid post-disaster mobility. PhD Thesis, Concordia University, Canada

Robinson M, Kosmatka J (2008) Light-weight fibre-reinforced polymer composite deck panels for extreme applications. J Compos Constr 12(3):344–354

Trilateral Design and Test Code for Military Bridging and Gap Crossing Equipment (2005) Trilateral design and analysis group of the united states, federal republic of germany and the United Kingdom of Great Britain

Viecili G et al (2014) Transportation optimization of ribbon floating bridges: analytical and experimental investigation. Open Civ Eng J 8(1):42–56

Watanabe E et al (2004) Very large floating structures: applications, analysis and design. National University of Singapore, Singapore

# Numerical Modeling of Hybrid Steel/GFRP Reinforced Concrete Bridges Piers

**Ahmed Arafa and Brahim Benmokrane**

## 1 Introduction

The well-known corrosion of steel in reinforced concrete (RC) structures has been an annoying problem for the structural engineering community for a long time. Extensive research has been conducted looking for a suitable solution. The use of non-corroded fiber-reinforced polymer (FRP) composites has been proposed as one of the most viable alternatives. Many standards and guides have already been published for the design and construction of concrete structures reinforced with FRP bars such as the CSA S806 (2012) and the ACI 440.1R (2015). Recently, concern has been triggered on the feasibility of using FRP-reinforced elements in seismic regions. This was due to the limited ultimate strain and the elastic nature of FRP bars. To fill the gap of knowledge and give an answer to these concerns, Fukuyama et al. (1995) conducted a pioneer experimental study on the lateral response of a half-scale three-story moment-resisting frame (MRF) reinforced completely with aramid FRP rebars and stirrups. This was followed by a number of studies (Hasaballa and El-Salakawy 2016; Ghomi and El-Salakawy 2016; Elshamandy et al. 2018) that included testing of different structural elements under reversed cyclic loading. The results showed that FRP-reinforced elements exhibited stable linear behavior up to failure with a low energy-dissipation capacity and minimal damage. Recent application extended to the behavior of GFRP-reinforced bridge piers. Arafa et al. (2018) implemented an experimental study that included testing nine large-scale bridge piers. The results indicated that using GFRP bars could be viable in region exposed to low-to-moderate

---

A. Arafa
Civil Engineering, Sohag University, Sohag, Egypt
e-mail: ahmed_arafa@eng.sohag.edu.eg

B. Benmokrane (✉)
Department of Civil Engineering, University of Sherbrooke, Sherbrooke, Quebec, Canada
e-mail: Brahim.Benmokrane@USherbrooke.ca

B. Benmokrane et al. (eds.), *8th International Conference on Advanced Composite Materials in Bridges and Structures*, Lecture Notes in Civil Engineering 267,
https://doi.org/10.1007/978-3-031-09409-5_4

earthquakes. The study also suggested that using hybrid reinforcement (steel/FRP) would be more effective in buildings located in strong earthquake regions. The present paper verifies the validity of this expectation through a finite element modeling of steel/FRP-reinforced bridge piers.

## 2 Finite Element Model and Validation

In this section, the behavior of full-scale GFRP and steel-reinforced bridge piers subjected to a reversed cyclic lateral loading has been investigated. Specialized FE software "Vector 2" was adopted in building the model (Wong and Vecchio 2002). A 2D finite element model was developed considering both the material and geometric nonlinearity in addition to modeling the bond behavior between the longitudinal reinforcement and the surrounded concrete. Figure 1 shows the modeled specimen's geometry, reinforcement details, and test setup. Table 1 provides the mechanical properties of the reinforcement. For ease reference, the GFRP and steel-reinforced specimens were designated as G4-80, and S4-80, respectively. More details can be found elsewhere (Arafa et al. 2018).

In the analysis model, the vertical and horizontal bars are modeled as truss elements, while four-node quadrilateral elements are used to model the concrete. Figure 2 shows a Typical FE meshing. A modified Bertero-Eligehausen-Popov model for bond between sand-coated GFRP bars and concrete is used. GFRP is modeled as

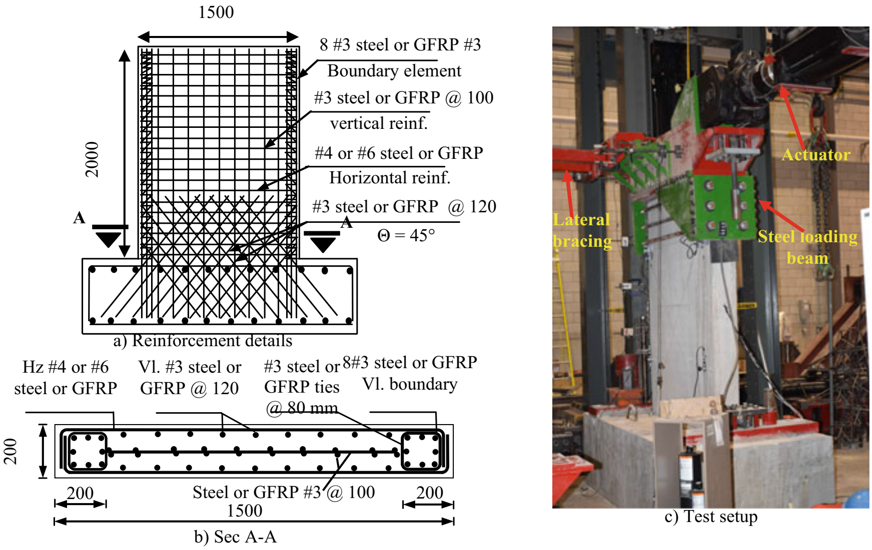

a) Reinforcement details

b) Sec A-A

c) Test setup

**Fig. 1** Concrete dimensions, reinforcement details, and test setup for the test specimens (S4-80, and G4-80)

**Table 1** Tensile properties of the reinforcement

| Bar | Designated bar diameter (mm) | Nominal area[a] ($mm^2$) | Tensile modulus of elasticity (GPa) | Tensile strength[b, c] (MPa) | Average strain at ultimate (%) |
|---|---|---|---|---|---|
| *Straight bars* | | | | | |
| #3 GFRP | 9.5 | 71 | 65 | 1372 | 2.1 |
| #3 steel | 9.5 | 71 | 200 | $f_y = 420$ | $\varepsilon_y = 0.2$ |
| #4 steel | 12.7 | 129 | 200 | $f_y = 420$ | $\varepsilon_y = 0.2$ |
| *Bent #3 GFRP—rectilinear spiral* | | | | | |
| Straight | 9.5 | 71 | 50 | 1065 | 2.1 |
| Bent | | | – | 460 | – |
| *Bent #4 GFRP—horizontal bar* | | | | | |
| Straight | 12.7 | 129 | 50 | 1020 | 2.0 |
| Bent | | | – | 459 | – |
| *Bent #6 GFRP—horizontal bar* | | | | | |
| Straight | 19.1 | 285 | 50 | 1028 | 2.0 |
| Bent | | | – | 463 | – |

$f_y$: steel yielding strength, $\varepsilon_y$: steel yielding strain

[a] According to CSA S807 (CSA 2010)

[b] Tensile properties were calculated using nominal cross-sectional areas

[c] Guaranteed tensile strength: Average value – 3 × standard deviation (ACI 440.1R-15)

*Note* 1 mm = 0.0394 in; 1 MPa = 145 φ

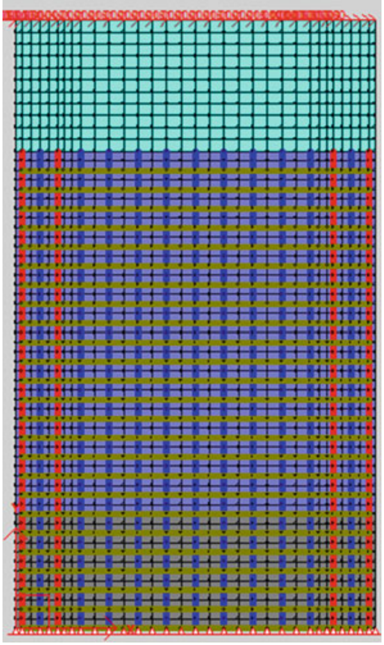

**Fig. 2** Typical FE meshing

a brittle perfectly elastic material. The pre-peak and post-peak response of concrete are modeled with a Hognestad parabola and a modified Kent-Park formulation, respectively. Concrete confinement provided by the closed stirrups at the bridge pier boundaries is considered.

Figure 3 shows a comparison between the predicted and the experimental results. Obviously, the model is capable of predicting crack pattern and failure mode. As

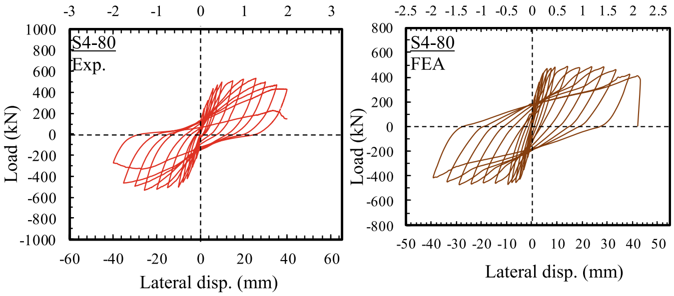

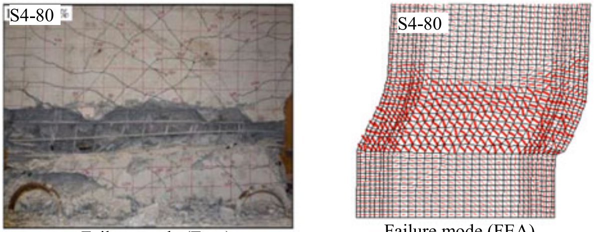

Failure mode (Exp.) Failure mode (FEA)

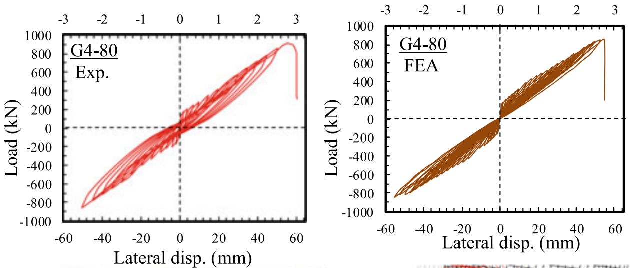

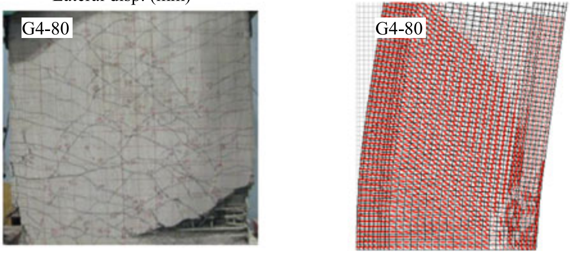

Failure mode (Exp.) Failure mode (FEA)

**Fig. 3** FEA versus experimental results

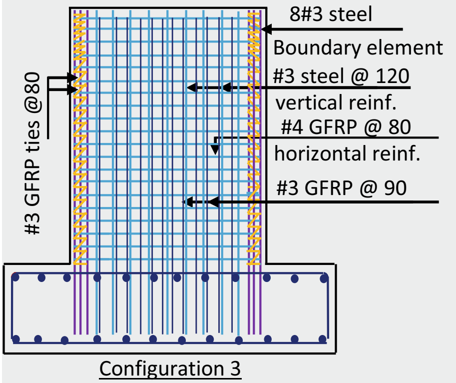

**Fig. 4** The examined hybrid reinforced specimen (GS3)

evidenced experimentally, the FEA revealed that the failure of steel-reinforced specimen was premature sliding while the GFRP-reinforced specimen was flexural crushing of concrete. Figure 3 also compares the predicted load–displacement hysteretic response to the companion experimentally obtained. Clearly, the model could predict the specimen's strength, stiffness, and deformation capacity with good accuracy; the difference within 10%. Based on the validation results, it can be concluded that the developed FEM can be extended to assess the effect of using hybrid reinforcement.

## 3 Proposed Hybrid Reinforcement Configuration

Many hybrid reinforcement configurations were investigated. One configuration, however, is introduced in the present study. Figure 4 shows reinforcement details. The specimen is identical to the previously tested steel-reinforced specimen (S4-80), but the diagonal sliding reinforcement was replaced with identical ratio of vertical GFRP bars along the bridge pier's height. The specimen was designated as GS3.

## 4 Analysis Results and Discussion

Figure 5 shows the crack patterns and failure modes of GS3. Failure occurred due to sequential rupture of the GFRP bars and was associated with abrupt loss of lateral strength. The ruptures of bars were recorded from the measured strain at tension zone which exceeded rupture strain. Further, it is clear from Fig. 5 that meshes at tension zone have noticeable vertical deformation that implies bars rupture. Apparently, the behavior has completely changed compared to S4-80. In spite of excessive yielding of the longitudinal reinforcement, the horizontal crack that was responsible for sliding was prevented. Hence, the specimen continued to carry load without

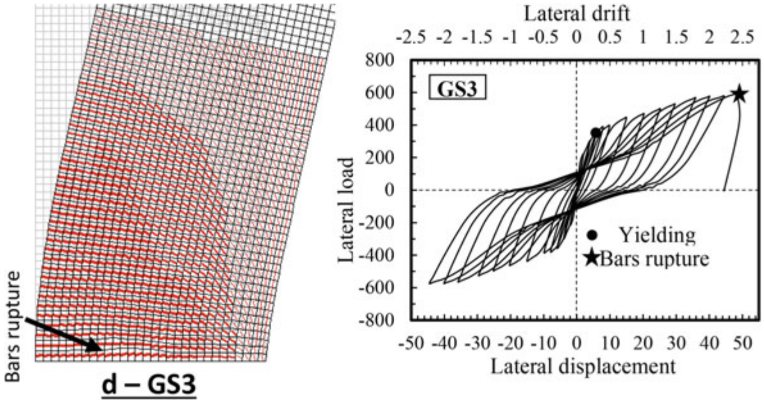

**Fig. 5** Failure mode and load–displacement hysteretic response (GS3)

strength degradation. Furthermore, specimen GS3 safely achieved an acceptable level of deformation according to NBCC (2015) and ASCE/SEI 41 (2013) (maximum drift ratio 2%), as well as a stable hysteretic response with no sign of premature failure.

To facilitate comparison between the proposed GS reinforcement configurations in term of their efficiency in controlling damage, the residual displacement (displacement at zero loading) was determined at each drift level and normalized to that of the reference specimen (S4-80) at the same drift level. Figure 6a shows the obtained normalized residual deformations (*r*) versus drift ratio. The results indicate that including both steel and FRP resulted in substantial control of residual deformations; 40% reduction in residual deformation can be observed in specimen GS3 compared to S4-80.

Given its importance, the capability of the GS-RC bridge piers to dissipate energy should be investigated. In this context, the cumulative energy dissipation of the

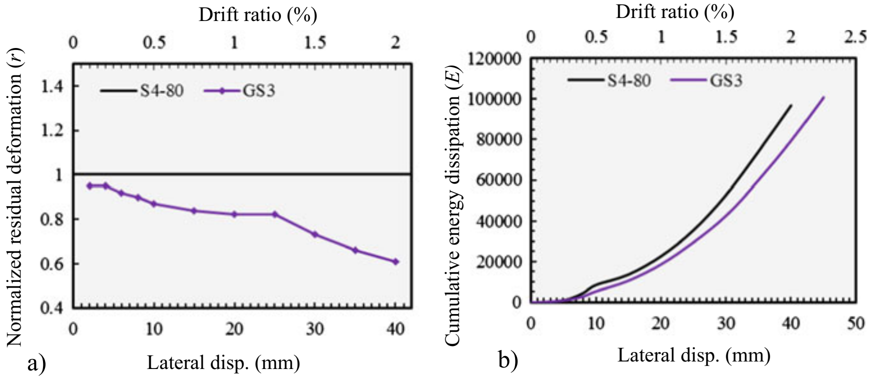

**Fig. 6** Normalized residual deformations, cumulative energy dissipation versus drift ratio

simulated specimens, which is a common index to describe the ability of a structure to dissipate imposed seismic energy, was determined and plotted against drift ratio, as shown in Fig. 6b. Clearly, the higher strength of GS3 compared to S4-80 contributed to increasing their energy-dissipation capacity, leading to a comparable ability to dissipate energy. For instance, at the onset of sliding deformation, the difference was almost 6%; then this difference increased slightly to reach 8% at a lateral drift of 2.1% (failure of S4-80). Overall, it can be concluded that controlling damage in GS3 did not significantly impair its ability to dissipate energy.

## 5 Conclusions

This paper examines the behavior of hybrid (steel/GFRP) reinforced concrete bridge piers. The study is based on modeling analysis using 2D analysis program (Vector 2). Based on the results and the presented discussion, the following conclusions can be drawn:

1. The proposed model accurately predicted the behavior of both the steel and GFRP-reinforced bridge piers available in the literature.
2. The lateral response of hybrid steel/GFRP-reinforced bridge pier supports the feasibility of using the hybrid reinforcement concept as a simple/ direct damage-controllable tool to achieve the required seismic performance.
3. More studies are needed to provide design guidelines that can be incorporated into the next seismic design codes editions.

**Acknowledgements** This research was conducted with funding from the Tier-1 Canada Research Chair in Advanced Composite Materials for Civil Structures, the Natural Sciences and Engineering Research Council of Canada (NSERC), and the NSERC Industrial Research Chair in FRP Reinforcement for Concrete Infrastructure.

## References

American Concrete Institute (ACI) (2015) Guide for the design and construction of structural concrete reinforced with fiber-reinforced polymer (FRP) Bars. ACI 440.1R-15, Farmington Hills, MI

Arafa A, Farghaly AS, Benmokrane B (2018) Experimental behavior of GFRP-reinforced concrete squat walls subjected to simulated earthquake load. J Comp Constr 22(2):1943–5614, 0000836

Canadian Standards Association (CAN/CSA) (2012) Design and construction of building components with fiber-reinforced polymers (S806-12).CSA, Mississauga, (ON, Canada), 208 pp

Elshamandy MG, Farghaly AF, Benmokrane B (2018) Experimental behavior of glass fiber-reinforced polymer- reinforced concrete columns under lateral cyclic load. ACI Struct J 115(2):337–349

Fukuyama H, Masuda Y, Sonobe Y, Tanigaki M (1995) Structural performances of concrete frame reinforced with FRP reinforcement. In: 2nd international RILEM symposium, non-metallic (FRP) reinforcement for concrete structures. Chapman & Hall, Ghent, Belgium, pp 275–86

Ghomi SK, El-Salakawy E (2016) Seismic performance of GFRP-RC exterior beam-column joints with lateral beams. J Compos Constr 20:04015019

Hasaballa M, El-Salakawy E (2016) Shear capacity of exterior beam-column joints reinforced with GFRP bars and stirrups. J Compos Constr 20:04015047

Wong PS, Vecchio FJ (2002) VecTor 2 & formworks user's manuals. Department of Civil Engineering, University of Toronto, Toronto, ON, Canada, p 213

# Field Investigation of CFRP Bond on RC Bridges

**Kenneth C. Crawford**

## 1 Introduction

Transportation infrastructure is an integral part of a nation's economy consisting of a complex network of roads, bridges, railroads, airports and seaports. Maintaining large infrastructure systems requires dedicated maintenance programs, long-term investment, and the use of new and evolving technologies. One of these technologies is the use of carbon fiber-reinforced polymer (CFRP) structural systems to strengthen RC (reinforced concrete) highway bridges. Over the past four decades these systems have provided an efficient means of improving the performance and life cycle of bridges. One of the challenges using CFRP systems is defining and quantifying its long-term durability and bond performance on concrete structures. Specifically, how does the CFRP-concrete bond perform over time, e.g., 15, 30, 50 years? Do CFRP systems remain fully bonded over long periods of time under cyclic loading, moisture, and freeze–thaw cycles? To answer this question a field investigation was undertaken in the Republic of Macedonia to test CFRP systems applied to twelve highway bridges, and to determine if the CFRP material remains bonded to the concrete structural members 18 years after installation (Alkhrdaji et al. 2014).

While a large number of RC highway bridges were strengthened with CFRP systems over the past four decades in the USA, Canada, Europe, and the Far East, there is currently no effective field-testing method to quantify, evaluate, and verify long-term bonding performance of CFRP systems. This paper presents the test method used on the M2 bridges, results of the impact testing, signal analysis of the data obtained, and discussion on the condition of the CFRP systems on the bridges today. Quantifying long-term durability of CFRP structural systems applied to concrete highway bridges is a focus of interest.

---

K. C. Crawford (✉)
Institute for Bridge Reinforcement and Rehabilitation (IBRR), Bloomington, IN 47401, USA
e-mail: ken.crawford@ibrr.org

B. Benmokrane et al. (eds.), *8th International Conference on Advanced Composite Materials in Bridges and Structures*, Lecture Notes in Civil Engineering 267,
https://doi.org/10.1007/978-3-031-09409-5_5

## 2 Background

A NATO operation in 2000 required the movement of heavy US military transports from a railhead in Bulgaria through Macedonia to Kosovo. Following a highway bridge survey by the US Army Corps of Engineers in Bulgaria and Macedonia in Nov 1999, the Macedonian Ministry of Transport with the Faculty of Civil Engineering, University of Sts Cyril and Methodius, performed structural analysis of highway bridges from Deve Bair on the Bulgarian border on the M2 and M1 to Skopje. The analysis required strengthening 17 highway bridges on the M2(EC-8) and two bridges on the M1 to NATO Military Load Class (MLC) 100. Nineteen RC highway bridges over 80 km in northeastern Macedonia on European Corridor 8 (EC-8) were strengthened using CFRP structural systems (Crawford and Nikolovski 2007). The 19 bridges were constructed between 1962 and 1971 in accordance with 1949 YU Regulations PTP-5 for an M-25 vehicle load. To meet Eurocode 2-Part 2 (EN 1992-2:2005) 19 slab and girder bridges were designed and strengthened with 10,847 m of CFRP plate, increasing the average bending moment from 400 to 600 kN·m to achieve the NATO MLC 100.

## 3 Research Significance

The purpose of this research was to investigate changes in the condition of transportation infrastructure. For the M2 retrofitted highway bridges the objective was to apply an innovative non-destructive testing method to evaluate the performance and bond of CFRP-strengthening systems applied in 2001. Field testing and evaluation of CFRP structural systems applied to RC highway bridges is of interest to users of these systems (Banthia et al. 2010) but remains a challenge to quantify and to collect relevant system performance data. The NDT method presented is a means to scan and evaluate CFRP laminate bond condition on concrete structures. This paper expands the research and field-testing presented in CICE-2018, paper P193 (Crawford 2018) with analysis of CFRP plate impact frequencies and waveforms.

## 4 Method of Investigation

This investigation uses the impulse-excitation principle with the impact-echo technique to produce resonant responses from the CFRP-concrete bond (CCB) structure (Sansalone and Street 1998). For impact modal testing the ideal impact to a structure is a perfect impulse, with an infinitely small duration, producing an output with a sinusoidal waveform with constant amplitude in the frequency domain (Swarnakar et al. 2007). In this investigation the impact hammer is applied with a constant force and impact time (duration) across the CFRP plates producing a consistent frequency

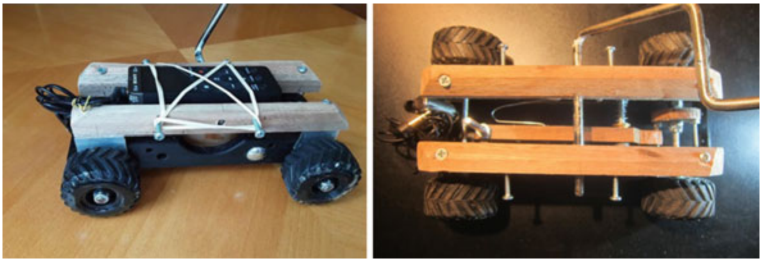

**Fig. 1** Impact machine with data recorder

and waveform for bonded CFRP plates. When the CCB condition changes to a de-bonded state the impact output frequency and waveform changes. Detecting changes in frequency and waveform indicates de-bonded CFRP plates. Impact tests conducted on CFRP test plates in the laboratory show a direct correlation between impact frequency and waveform and plate bond condition.

### *4.1 Machine Operation*

The machine is designed to produce a series of uniform hammer impacts on bonded CFRP plates to generate low-frequency acoustic emissions. Each impact is a data point with a specific frequency and waveform. The impact machine, Fig. 1, is a low-profile 6 cm × 20 cm rigid frame with four wheel bearing blocks with an impact lever fulcrum. A 2-pin actuator wheel is mounted on the rear drive axle to drive the impact lever hammer. A single-wire spring drives the impact lever with a force of 0.4 pounds. With 5 cm diameter wheels one impact on the CFRP plate occurs every 7.8 cm, or 13 impacts per meter.

### *4.2 Signal Analysis*

Rolling across a CFRP plate the impact machine produces low (<2 kHz) frequency emissions recorded on an audio recorder. The frequency and waveform produced are a function of the CCB condition. The frequency is determined by the impact force and duration and the condition of the material impacted (Crawford et al. 2017). The waveform is an exponentially decaying sinusoid with specific damping ratios, phase times, and amplitudes, dependent on the CCB condition. Signal analysis of recorded impact data shows consistent frequencies and decaying sinusoidal waveforms and damping ratios for bonded CFRP plates. De-bonded CFRP material had lower frequencies with faster decaying waveforms. To analyze impact sinusoidal

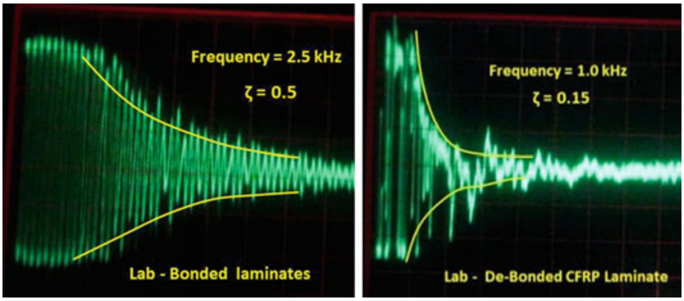

**Fig. 2** Frequency and damping ratio for bonded/de-bonded lab CFRP laminate

waveforms it is useful to consider the characteristics of a decaying harmonic oscillation. The general solution of the function $f(t)$ for a dampened harmonic waveform is given by Eq. 1.

$$f(t) = \mathrm{A}e^{-\zeta\omega \mathrm{n}t}(\cos(\omega_{\mathrm{d}} - \phi)) \tag{1}$$

where A is initial amplitude, $\omega_n$ is the natural frequency in rad/sec, $\phi$ is phase angle, $\zeta$ is the damping ratio on $\omega_n$. The dampened frequency $\omega_d$ is the natural frequency $\omega_n$ modified by the dampening ratio.

The rate of exponential decay in a harmonic oscillation is expressed by the damping ratio, a system parameter denoted by zeta ($\zeta$) that characterizes the frequency response of the harmonic oscillation.

Figure 2 displays the frequencies and damping ratios of the decaying sinusoidal waveforms for laboratory bonded and de-bonded a CFRP laminate plate. These frequencies and damping ratios are used as the reference for the impact data obtained for the investigation of the twelve M2 highway bridges.

## 5 Field Investigation

The purpose of this NDT field investigation was to determine the condition and performance of the CFRP structural systems applied to RC highway bridges on the M2 in North Macedonia in 2001. The procedure involved testing the condition of the CFRP laminate bond on 12 of the 17 bridges with the impact machine in Fig. 1. Each slab and girder bridge had different CFRP plate configurations depending on the degree of strengthening required to bring the bridge up to the MLC 100 loading. Slab bridges have basically two configurations: straight CFRP plates, or a cross-hatch of smaller laminates. Girder bridges normally had the main girders, cross girders, and deck slab strengthened. Two girder bridges had only the cross girders and deck slab strengthened. The impact machine on an extended pole provided the ability to reach and scan across individual CFRP plates on the twelve bridges. The goal was to test as many CFRP plates as possible on each of the 12 bridges and to record the impact data for signal analysis.

## *5.1 Investigation Procedure*

The testing procedure required direct application of the impact machine to the surface of the bonded CFRP laminates. The testing process involved rolling the machine across the CFRP plates with the data recorder logging each impact (Crawford 2016). The impact machine was rolled at a constant speed on the plate producing 13 impacts per meter. The machine has the capability to scan approximately 30–40 m per minute, depending on the CFRP laminate configuration and extension pole reach. Pictures and recording logs were made for each bridge tested. Areas of visible de-bonding were tested.

Over two days 12 of the 17 M2 retrofitted bridges, over 55 km, were tested with the impact machine. All twelve bridges were tested in five hours, seven bridges the first day, five bridges the second day. The primary finding for the twelve bridges confirmed the CFRP plates are still 100% bonded on all bridge structural members, with the exception of several small areas of de-bonding on four bridges.

Table 1 lists the 12 bridges tested in this investigation with location, dimensions, CFRP laminate configuration, test results, and test data time recorded. Bonded* indicates small areas of de-bonding were found. The de-bonding was caused by water damage in the bridge concrete, most often occurring near the bridge joints where water and chlorides have come through over time. Overall the condition of the CFRP laminates on the bridge concrete on all 12 bridges appeared to be in excellent condition.

The impact tests confirmed the CFRP laminates remain fully bonded and are performing as originally designed. Of the total 4,780 m on the twelve bridges, approximately 2,800 m (60%) were impact tested. With laminates in the same physical condition every second or third laminate was tested.

### 5.1.1 Bridge B36 Test

Bridge B36, Fig. 3a, on the M2 is a two-tier slab bridge constructed in 1971 in accordance with YU Regulation PTP-5, and strengthened in March 2001 with 1,031 m of Sika S1512. A post-strengthening load test was performed May 2001, confirming the CFRP application as designed increased the bridge load capacity to MLC 100. No other tests have been performed on the bridge since 2001. The B36 impact test conducted on 7 Oct 2019, confirmed 99.9% of the 1,031 m of the S1512 CFRP plates remain fully bonded to the bridge concrete. Less than 10 m, <1%, have become de-bonded in areas where the concrete has sustained water damage. These areas are at the ends of the CFRP laminates near the bridge end joints, Fig. 3c (where water has

**Table 1** Twelve M2 highway bridges investigated

| Bridge | Location (km)* | Type | Length (m) | Tier lengths (m) | No. CFRP | CFRP plate | Bond status | Data |
|---|---|---|---|---|---|---|---|---|
| | | | | | Plates | Length (m)–Area (m2) | | Record time |
| B7 | 14 + 027 | Girder | 120 | 6 × 20 | 72 | 1478–116 | Bonded | *4:41* |
| B11 | 21 + 876 | Slab | 10 | 10 | 26 | 198–30 | Bonded | *4:06* |
| B18 | 38 + 444 | Slab | 36 | 11 13 11 | 54 | 218–33 | Bonded* | *9:15* |
| B19 | 38 + 675 | Slab | 36 | 11 13 11 | 54 | 218–33 | Bonded* | *7:04* |
| B22 | 41 + 786 | Slab | 30 | 9 11 9 | 54 | 218–33 | Bonded | *5:51* |
| B27 | 47 + 626 | Girder | 80 | 4 × 20,4 × 18 | 153 | 592–40 | Bonded | *5:45* |
| B28 | 49 + 631 | Girder | 50 | 16 18 16 | 197 | 674–72 | Bonded | *7:37* |
| B29 | 49 + 883 | Slab | 10.5 | 10.5 | 16 | 128–19 | Bonded | *2.27* |
| B30 | 53 + 893 | Girder | 12.5 | 12 12 | 19 | 74–9 | Bonded | *4.53* |
| B35 | 66 + 058 | Girder | 46 | 16 20 16 | 20 | 346–41 | Bonded | *10:53* |
| B36 | 67 + 409 | Slab | 21 | 10.4 10.4 | 80 | 1031–83 | Bonded* | *15:12* |
| B37 | 68 + 452 | Girder | 17 | 17.2 | 36 | 415–34 | Bonded* | *17:32* |
| | | | | Totals | 574 pcs | 4780 m—470m2 | | *1:35:16* |

**Fig. 3** **a** Bridge B36. **b** Impact testing. **c** XX de-bonded areas

seeped through), are outside the maximum bending moments of the two tiers and thus do not lower the MLC 100 load rating.

The B36 impact waveforms, Fig. 4, show a bonded frequency of 2 kHz and a damping ratio ζ of 0.4, and a de-bonded frequency of 1.2 kHz and a damping ration $\zeta = 0.2$. These values remained consistent for bonded and de-bonded laminate conditions across all twelve bridges.

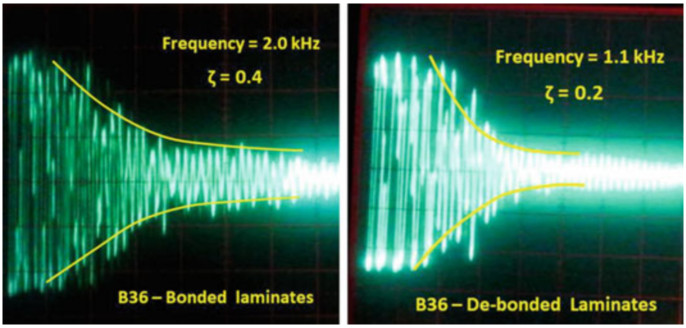

**Fig. 4** B36 impact waveforms for bonded and de-bonded plates

### 5.1.2 Other Bridges Tested

### 5.1.3 Bridge Harfa on E57 Over Ljubljancia River in Slovenia

The bridge Harfa (Most Harfa) on the E57 east of Ljubljana over the River Ljubljancia is a 120 m cable-stay four-lane European corridor bridge constructed in the 1970s. The bridge was strengthened in 1998 to facilitate the movement of a 750-ton nuclear vessel, Fig. 5a., from the Port of Koper to the Krsko 696 MWe nuclear power plant in eastern Slovenia. The Harfa bridge was strengthened with 3,800 m of CFRP laminates, Fig. 5b. for the 750-ton load. Impact testing, Fig. 5c, was performed 12 Oct 19, on a number of laminates on the south end of the bridge, above a walkway. All laminates tested are still fully bonded, 21 years after installation. The entire configuration of CFRP material appeared to be in excellent condition with no signs of water damage in the concrete or any de-bonding.

**Fig. 5** **a** 750-ton vessel on bridge. **b** CFRP configuration. **c** Impact testing

The Harfa bridge is one of three bridges on E61, E57, and A2 in Slovenia to be strengthened with CFRP systems to facilitate the movement of the 740-ton vessel to Krsko, in 1999, from Koper.

## 6 Conclusion

The purpose of this investigation was to determine the condition and status of the CFRP structural systems applied to RC highway bridges on the M2 in the Republic of Macedonia North Macedonia after 18 years of service. A light impact machine was used to test and scan 12 of the 17 retrofitted bridges over a 55 km distance, with testing completed in five hours over two days. The significant finding in this NDT investigation is the fact all CFRP laminates on the 12 bridges remain fully bonded after 18 years. Four bridges have small areas of de-bonding from concrete water damage. The CFRP laminates on the Harfa bridge in Slovenia are still fully bonded, 21 years after application. The impact machine, scanning up to 40 m per minute, was affective in identifying bonded and de-bonded laminates. The data recording on the machine logged over 36,000 data points in the 1 h and 35 min of recording time. Signal analysis of the data successfully differentiated between bonded and de-bonded laminates. The NDT investigation in Macedonia and Slovenia has validated the concept of using a light impact machine and data recorder to determine the condition of CFRP-concrete bond and system performance on RC highway bridges. Further testing will confirm CFRP systems applied to RC highway bridges (in the absence of water in the concrete) will endure and provide full-service performance for many years.

**Acknowledgements** The author thanks Wabash College for their support, in particular Prof. Lon Porter and the 3D Printing and Fabrication Center, for the fabrication of the impact machine frame.

Special thanks is given to the Sintek Company, Skopje, Republic of Macedonia, contractor for the M2 project in 2001, for their support in the impact testing of the twelve M2 bridges in Oct 2019.

## References

Alkhrdaji T, Thomas T, Nanni A, Huck M (2014) Strengthening of off-system bridges using FRP composites. CiteSeerX, OAI. Psu: 10.1.1506.4417

Banthia N, Abdolrahimzadeh A, Demers M, Mufti AA, Sheikh SA (2010) Durability of FRP-concrete bond in FRP-strengthened bridges. ACI Concrete Int'l 32(8):45–51

Crawford K, Nikolovski T (2007) The application of ACI 440 for FRP system design to strengthen 19 concrete highway bridges on European corridor 8. In: 8th international conference on fiber reinforced polymer for reinforcement of concrete structures, Paper 15-4, pp 570–571

Crawford K (2016) NDT evaluation of long-term bond durability on CFRP-structural systems applied to RC highway bridges. Int J Adv Struct Eng 8(2):161–168

Crawford K, Chapman C, Porter L (2017) Low frequency analysis of CFRP-laminate bond on RC bridges. In: Proceedings of 7th international conference on advanced composite materials in bridges and structures (ACMBS-VII), August 2017, Vancouver, BC, CA, paper 065

Crawford K (2018) NDT signal analysis of FRP-laminate bond on RC bridges. In: 9th international conference on fibre-reinforced polymer (FRP) composites in civil engineering (CICE 2018), Paris, 17–19 July 2018. Paper A193

Eurocode 2-Part 2 (EN 1992-2:2005)

Sansalone M, Street W (1998) The impact-echo method. Ndtnet 3(2):3–5

Swarnakar AK, Gimenez S, Salehi S, Vieugels J, Van der Biest O (2007) Recent advances in material characteristics using the impulse excitation technique (IET). Key Eng Mater 333:235–238

# Examining the Effect of Load Type and History Using Reliability on Optimizing the Design of FRP-Strengthened RC Members in Flexure

**Connor Petrie and Fadi Oudah**

## 1 Introduction

Aging existing infrastructure in North America is becoming an increasing issue for civil engineers. Limited funds allocated towards repair budgets are allowing existing infrastructure to reach, or exceed, its service life. It has become essential to find economical ways to extend the service-life of these structures. The use of fiber-reinforced polymer (FRP), externally bonded (EB) for strengthening RC flexural members, can be an effective way to accomplish this task. This is achieved in beams by increasing the capacity of members within the structure through rehabilitation. Several reliability studies have been conducted on the application of FRP strengthening in flexure (Plevris et al. 1995; Wang et al. 2010; Wieghaus and Atadero 2011; and Huang et al. 2019), but none considers load type or history into the analysis, that can be incorporated through measuring certain parameters of an existing structure. Measuring the type and maximum loads experienced by the structure allow the removal of some of the uncertainty that was present before construction. The structure has been service proven; thus, the failure surface can be truncated, and the structure will usually see an improvement in reliability (Hong 1998). With cost still being a major factor in choosing FRP in Canada, further research into the optimization of design for strengthening members using reliability is key to furthering the competitiveness of EB-FRP with conventional repair techniques in today's market.

In this paper, an innovative approach is proposed to develop reliability-based framework to generate user-friendly design aids, in the form of charts, to be used

---

C. Petrie (✉) · F. Oudah
Department of Civil and Resource Engineering, Dalhousie University, 1360 Barrington Street, Halifax, NS, Canada
e-mail: connor.petrie@dal.ca

F. Oudah
e-mail: fadi.oudah@dal.ca

B. Benmokrane et al. (eds.), *8th International Conference on Advanced Composite Materials in Bridges and Structures*, Lecture Notes in Civil Engineering 267,
https://doi.org/10.1007/978-3-031-09409-5_6

by engineers to evaluate the safety of existing concrete beams and optimize the repair scheme. The charts allow the user to find a strength multiplier, $M_S/M_R$, which represents the minimum amount of FRP needed to meet a target reliability, should the member be deficient. The reliability framework uses the principles of updated reliability, by taking into account the load type and history of the structure, using the principles of conditional probability.

A database of experimental tests based on current studies in literature is formulated to obtain descriptive statistics for strengthened RC beams. The statistics of unstrengthened beam and load are taken as the values used to calibrate the ACI 318 and NBCC codes, respectively.

## 2 Experimental Database

Review of experimental studies, from literature, that examines the use of EB-FRP for strengthening RC beams in flexure, was conducted. A database was obtained of rectangular RC beams, strengthened with EB-FRP, that fail in either crushing of concrete or rupture of FRP (flexure). The strain limit imposed by the CSA S806-17 standard limits the allowable stress on the FRP, so that debonding is avoided. For this reason, beams that fail due to debonding were excluded from the present study.

The database consists of 41 experimentally tested beams, taken from studies done from 1998 to 2015. It consists of two sets of RC beam data: EB-FRP strengthened beams and unstrengthened (control) beams. The following parameters are reported for every point in the database: beam geometry, concrete strength, steel yield strength, steel modulus of elasticity, area and location of internal reinforcement, nominal predicted strength based on the design provisions of CSA S806-17 and CSA A23.3-19 (strengthened and unstrengthened, respectively), actual resistance based on experimental tests (strengthened and unstrengthened), FRP ultimate strength, FRP modulus of elasticity, and area of FRP used for strengthening.

Descriptive statistics (bias, COV, distribution type) are found for every point of the database. The mean bias and COV for the strengthened beams were found to be 1.22 and 0.19, respectively, while the unstrengthened beams reported values of 1.19 and 0.089, respectively. The latter values used for unstrengthened beams were taken as the value used in calibration of ACI 318 code.

## 3 Reliability Analysis

First-order reliability method (FORM) is employed based on conditional reliability to yield updated reliability index. The following subsection describes the framework utilized to execute the reliability analysis.

## 3.1 Updated Reliability

The factors for load and resistance included in Canadian codes (NBCC 2015; CSA A23.3-14; CSA S806-17) were calibrated using reliability methods to meet predefined target safety limits for new construction. As stated by the NBCC 2015 in the Notes to Part 1 of Division A, practicing engineers should be careful in applying the code provisions when evaluating existing structures since these provisions may not necessarily reflect consistent safety levels when used in evaluating existing structures. Consequently, the use of reliability methods to optimize the evaluation and repair of existing structures taking into account load history is recommended. The principles of conditional probability will be used to accomplish this, using Eq. (1) for finding the updated probability of failure based on the Bayes theorem:

$$P(B|A) = \frac{P(A)P(A|B)}{P(B)} \tag{1}$$

The current study utilizes the work by Hong (1998) to calculate reliability based on service-proven dead loads and measured maximum loads experienced, based on satisfactory field inspection over a given period of time. All random variables in the limit state are lumped into two variables load, $L$, and resistance above the dead load, $R$. Both are assumed to be independent and lognormally distributed. This method allows FORM to be utilized to find the updated reliability by Eq. (2):

$$\beta_{up} = -\Phi^{-1}(P_{fup}) \tag{2}$$

$$P_{fup} = \Phi(\beta_o) + \frac{\int_0^{\rho} \Phi(-\beta_o, -\beta_s, r)dr}{\Phi(-\beta_s)} \tag{3}$$

$$\Phi(-\beta_o, -\beta_s, r)dr = \frac{1}{2\pi\sqrt{1-r^2}}\exp\left(\frac{-(\beta_o^2 + \beta_s^2 - 2\beta_o\beta_s r)}{2(1-r^2)}\right) \tag{4}$$

$$\beta_o = \frac{m_{lnR} - m_{lnL}}{\sqrt{\sigma_{lnR}^2 + \sigma_{lnL}^2}} \tag{5}$$

$$\beta_s = \frac{m_{lnS_T} - m_{lnR}}{\sigma_{lnR}} \tag{6}$$

$$\rho = \frac{-\zeta}{\sqrt{\zeta^2 + 1}} \tag{7}$$

$$\zeta = \frac{V_R}{V_L} \tag{8}$$

where term $S_T$ denotes the maximum live load experienced by the member during the service life to date.

The descriptive statistics for resistance (strengthened and unstrengthened) used in the reliability analysis are those found in Sect. 2. The bias and COV for the loads used are 1.05 and 0.1, respectively, for dead load, and 0.9 and 0.17, respectively, for live load (Bartlett et al. 2003a, b).

## 3.2 Equivalent Phi Factor

Canadian codes use the concept of material resistance factors ($\phi_c$, $\phi_s$, $\phi_{frp}$) applied to each component that makes up the member. Conversely, American codes use member strength reduction factors, applied to the action rather than each material to achieve the same reduction ($\phi M_u$). Both approaches can be calibrated to meet a pre-defined reliability index although the level of safety will be slightly different. To be able to use FORM to find the updated reliability, an equivalent phi factor, $\phi_e$, must be introduced as an overall resistance reduction factor.

This factor will be equivalent to using the partial phi factors ($\phi_c$, $\phi_s$, $\phi_{frp}$) from CSA S806-17 and is found by calculating the factored resistance, as per the code, and dividing this value by the nominal (unfactored) resistance as shown in Eq. (9):

$$\phi_e = \frac{Factored\,moment\,resistance}{Nominal\,moment\,resistance} = \frac{M_r}{M_u} \tag{9}$$

A parametric analysis was completed in MATLAB using the database described in Sect. 2 consisting of rectangular RC beam samples. The results of applying Eq. 9 for every point in the database yielded a mean equivalent phi factor of 0.8368 with a coefficient of variation equal to 0.016. A value of $\phi_e = 0.84$ is selected to be used in this study.

## 3.3 Solution Scheme

The framework presented in the following section can be applied to flexural members (slabs and beams). The charts are based on the well-known parameter of utilization ratio. The steps in the following procedure were used to generate the user-friendly charts presented in Sect. 4:

- Step 1: Select the following input parameters: target reliability index, $\beta_t$, utilization ratio, *U.R.* (ratio of factored loads over factored resistance), ratio of maximum live load experienced over design live load, $\psi_L$, ratio of maximum dead load experienced over design dead load, $\psi_D$, ratio of dead-to-live load, *D*/*L*, and the governing load combination (*1.25D* + *1.5L*).

- Step 2: Calculate the members predicted flexural resistance, $M_u$, above and beyond the dead load based on parameters selected in step 1. Multiply $M_u$ by the equivalent phi factor, $\phi_e$, to obtain the factored resistance above dead load, $M_R$.
- Step 3: Calculate the updated reliability, $\beta_{up}$, for the unstrengthened member using Eq. (2), based on the statistics for unstrengthened beams presented in Sect. 2.
- Step 4: Compare the updated reliability index found in step 3 with the selected target reliability. If $\beta_{up} > \beta_t$, then the member is not deficient (terminate algorithm). If $\beta_{up} < \beta_t$, the member is deficient and repair is required, proceed to the next step.
- Step 5: A strength multiplier, $M_S/M_R$, is calculated to achieve the target reliability index selected. A new updated reliability based on the strengthened section, $\beta_{up,new}$, is calculated and iterated until $\beta_{up,new} = \beta_t$. This multiplier is optimized, based on the statistics presented earlier in this paper (Sect. 2) for strengthened beams, to be the minimum value needed to achieve a suitable level of safety.
- Step 6: For a given set of $D/L$ and $\beta_t$ values, user-friendly charts can be made to show how $M_S/M_R$ changes with increasing utilization ratio.

## 4 Reliability Analysis

The solution scheme of Sect. 3.3 was programmed into MATLAB, to conduct a parametric study examining the sensitivity of the abovementioned variables, on the needed amount of flexural strengthening. The parametric study included varying the following parameters for the given ranges: $D/L = [1, 2, 3, 4]$; $\beta_t = [3.0, 3.5, 4.0]$; $\Psi_D = [0.9, 1.0, 1.1]$; and $\Psi_L = [0.5, 0.7, 0.9]$. The lines for the deterministic code and FORM are presented in the same plot. Strict application of NBCC (2015) and CSA S806-17 (referred herein as the "code" or "codes") in determining the strength multiplier yields a linear relationship as shown, whereas reliability analysis from this study yield a non-linear curve that varies with inputs; sample analysis results are described herein.

The following figures show the effect of the load history and type on the amount of strengthening (strength multiplier, $M_S/M_R$) needed as utilization ratio increases. Results of FORM for a range of $D/L = 1.0, 3.0$, $\psi_D = 0.9, 1.0, 1.1$ and $\psi_L = 0.5, 0.9$ are plotted. The figures show a practical range of utilization ratio and the corresponding strength multiplier, $M_S/M_R$. Figure 1 shows the values of $M_S/M_R$ needed for a reliability index of $\beta_t = 4.0$ and Fig. 2 shows a lower target reliability, $\beta_t = 3.5$, for the various inputs.

The figures show that for higher $D/L$ ratios, the FORM curves become more non-linear. This causes the x-intercept to shift right, meaning the beam does not require any strengthening for utilization above unity, with some curves starting as high as $U.R. = 1.38$. These times when the curve given by the FORM is below the deterministic code line for the same $U.R.$ indicate times when the code's approach finds the member deficient, but the reliability analysis does not. The code is not sensitive to taking into account the load type and history of an existing building

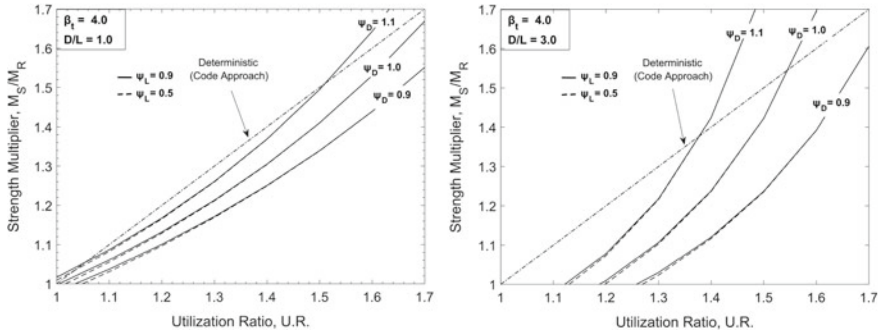

**Fig. 1** Generated sample plots of $M_S/M_R$ versus *U.R.* for $\beta_t = 4.0$ for *D*/*L* = [1.0 3.0]

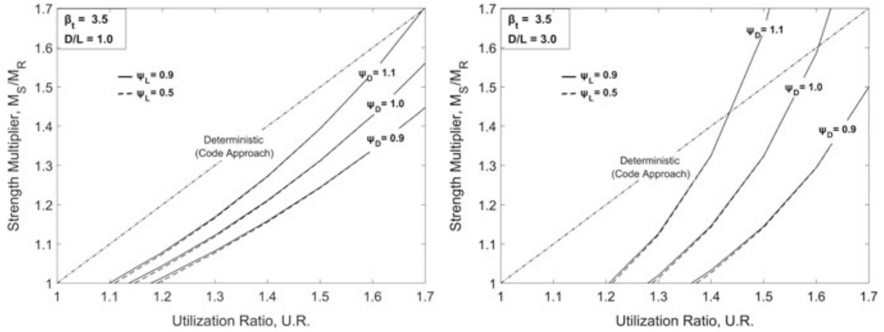

**Fig. 2** Generated sample plots of $M_S/M_R$ versus *U.R.* for $\beta_t = 3.5$ for *D*/*L* = [1.0 3.0]

during assessment, and may give costly, over-conservative designs due to this. It was found that as the selected target reliability index, $\beta_t$, increases, the value of the x-intercept decreases (i.e., the value of *U.R.* at which repair is first needed decreases with increasing $\beta_t$).

It should be noted that as the *U.R.* increases there is a point at which the deterministic and reliability lines intersect, with the FORM line now above the deterministic code line. This means for higher *U.R.*, it is possible for the code to under-prescribe the amount of FRP needed to strengthen the section and does not meet the selected target reliability index. This intersection point, where the switch happens, varies for each set of input parameters, as shown.

The effect of ratio of measured-to-design live load, $\psi_L$, experienced does not affect the results significantly for any set of input parameters as shown, and thus, can be neglected.

## Case Study—Flexural Strengthening of an RC Beam

To show how this framework can be applied, a simply supported rectangular beam will be examined. The beam is a typical interior beam, of a multistory RC building, in Canada. The beam is cast-in-place and supports pre-cast double tees that sit on top to make up the floor system, having a span of 8.0 m and a tributary width of 3.5 m. The beam itself has dimensions of 300 mm × 400 mm, with the area of internal steel, $A_s = 1095$ mm$^2$, and a depth to neutral axis, $d = 365$ mm. The material strength of the concrete and steel is 35 MPa and 400 MPa, respectively. The building is part of an ongoing structural health monitoring program, in which measurements have been taken so that the load type and history of the structure can be known. It is reported that the live load used in design is $LL = 2.4$ kPa, the ratio of dead-to-live load is $D/L = 1.0$, the ratio of measured-to-design live load is $\Psi_L = 1.0$, the ratio of measured-to-design dead load is $\Psi_D = 0.9$. A target reliability index of $\beta_t = 3.5$ is selected for repair.

Using the provisions of the CSA S806-17 standard and the governing load combinations from the NBCC (2015) ($1.25D + 1.5L$), it was found that the factored moment resistance of the section is $M_r = 122$ kNm, and the factored demand on the beam is $M_f = 175$ kNm. This means that the beam is deficient, with a utilization ratio of $U.R. = 1.43$. Using the right-side graph of Fig. 2 (presented in Sect. 4 of this paper), the optimized strength multiplier, $M_S/M_R$, is found for the given input parameters. It was found using the reliability method, the strength multiplier needed is $M_S/M_R = 1.24$. Conversely, applying the deterministic CSA S806-17 approach yields a strength multiplier of $M_S/M_R = 1.43$. The calibration of the resistance and load factors in current codes is conducted to ensure that a design meets a pre-determined target safety level (Allen 1975). Code calibration is conducted for new construction and does not consider that the structure is service proven. The resulting design becomes over-conservative for the amount of FRP needed for repair, as shown by the difference in strength multiplier found.

The use of carbon fiber-reinforced polymer (CFRP) is used for repair. A common, industry found type of CFRP composite will be used, having properties of one-layer thickness, $t_{frp}$, equal to 0.33 mm, a modulus of elasticity, $E_{frp}$, equal to 227 GPa and an ultimate strength, $f_{\mathrm{frp}}$, equal to 3800 MPa. The number of FRP layers needed to meet the selected reliability is calculated by multiplying the value of $M_S/M_R$ found, by the unstrengthened moment resistance, $M_R$, to get the required strengthened moment resistance, $M_S$. Results show that the code approach requires 50% more material than required by FORM to achieve the code target safety limit; with the code requiring two layers of CFRP, while the reliability analysis conducted in this research requires only one-layer of CFRP.

## 5 Conclusion

The present study introduces a framework to optimize the repair of existing RC beams deficient in flexure, with EB-FRP, using load type and history to reduce the uncertainty. Review of available literature was completed to establish a database of experimental tests of beams failing in flexure. Bias and COV values are obtained for the strengthened beams. These values are used in combination with the load statistics used to calibrate the NBCC (2015) to perform reliability analysis. As part of the solution scheme, unstrengthened beams are evaluated based on input parameters of load history and type, to determine if they meet a predetermined target reliability index, using FORM. Should the beam be deficient, an optimized strength multiplier, $M_S/M_R$, is calculated. This multiplier is the minimum amount of additional material needed to meet the selected target reliability index. It was found that $M_S/M_R$ is most sensitive to input parameters $\beta_t$, $\Psi_D$, $D/L$, while the effect of $\Psi_L$ can be neglected. It should be noted for lower *U.R.* closer to unity, the code tends to give over-conservative amounts of FRP needed to strengthen, whereas, at higher *U.R.,* the opposite effect is found. Both trends show the poor sensitivity of the CSA S806-17 standard to parameters of load type and history.

The inclusion of load type and history into a basic reliability framework for assessing existing beams will further aid in reducing the over-conservative designs given by the CSA S806-17 design standard, in some cases, when choosing FRP as a means for external strengthening. The charts generated are derived to be compatible with the Canadian building codes (NBCC 2015; CSA S806-17) and show the framework can produce safe, economical designs. Further work is needed to include the partial resistance factors in analysis by the use of more robust reliability techniques, such as Monte Carlo simulation. Furthermore, a recommendation for a larger database of experimentally tested beams, so more accurate updated reliability can be found.

**Acknowledgements** The authors would like to acknowledge MITACS, Norlander Oudah Engineering Limited (NOEL), and the Natural Sciences and Engineering Research Council (NSERC) for the financial support of the present research.

## References

Bartlett M, Hong HP, Zhou W (2003a) Load factor calibration for the proposed 2005 edition of the National Building Code of Canada: statistics of loads and load effects. Can J Civ Eng 30(2):429–439

Bartlett M, Hong HP, Zhou W (2003b) Load factor calibration for the proposed 2005 edition of the National Building Code of Canada: companion-action load combinations. Can J Civ Eng 30(2):440–448

CSA A23.1-14/A23.2-14, Concrete materials and methods of concrete construction/Test methods and standard practices for concrete. Canadian Standards Association, Mississauga (Ontario)

CSA S806-17, Design, and construction of building structures with fibre-reinforced polymers. Canadian Standards Association, Mississauga (Ontario)

Hong HP (1998) Reliability of existing structures. Civ Eng Environ Syst 15(1):187–206

Huang X, Sui L, Xing F, Zhou Y, Wu Y (2019) Reliability assessment for flexural FRP-strengthened reinforced concrete beams based on importance sampling. Compos Part B Eng 156:378–398

NBCC (2015) National building code of Canada. National Research Council, Ottawa (Ontario)

Plevris N, Triantafillou TC, Veneziano D (1995) Reliability of RC members strengthened with CFRP laminates. J Struct Eng 121(7):1037–1044

Wang N, Ellingwood BR, Zureick A-H (2010) Reliability-based evaluation of flexural members strengthened with externally bonded fiber-reinforced polymer composites. J Struct Eng 136(9):1151–1160

Wieghaus KT, Atadero RA (2011) Effect of existing structure and FRP uncertainties on the reliability of FRP-based repair. J Compos Constr 15(4):635–643

# Design and Performance of GFRP Reinforced Bridge Decks in NOVA SCOTIA—Preliminary Analysis

**David Idemudia, John Newhook, and Fadi Oudah**

## 1 Introduction

The durability of bridge decks largely influences the lifespan of bridge structures. Environmental factors such as high pH, salt water, high temperature, freeze–thaw cycles and wet/dry cycles cause long-term durability issues in concrete bridge decks leading to a reduced lifespan (Kim et al. 2012). Advanced composite materials such as fibre-reinforced polymers (FRP) have been used as reinforcing material for bridge decks to tackle the effects of adverse environmental conditions (Benmokrane et al. 2020). Glass fibre-reinforced polymers (GFRP) bars are the most frequently used type of FRP bars in bridge engineering mostly because they are high strength, lightweight, non-corrosive and economical, making it ideal for use in bridge environments (ISIS 2007).

The Canadian Highway Bridge Design Code, CSA S6-19, permits the use of FRP bars, and practicing engineers have been designing with FRP as the primary concrete deck reinforcing material for the last two decades. Despite the significant benefits of FRP bars, there is some uncertainty concerning the long-term performance of the material which resulted in having most codes include an 'environmental factor' in the calculation of the capacity of FRP-reinforced members. The durability of FRP bars used in concrete decks still needs to rely heavily on lab testing and statistical

---

D. Idemudia (✉) · J. Newhook · F. Oudah
Department of Civil and Resource Engineering, Dalhousie University, 1360 Barrington Street, Halifax, NS, Canada
e-mail: david.idemudia@dal.ca

J. Newhook
e-mail: john.newhook@dal.ca

F. Oudah
e-mail: fadi.oudah@dal.ca

B. Benmokrane et al. (eds.), *8th International Conference on Advanced Composite Materials in Bridges and Structures*, Lecture Notes in Civil Engineering 267,
https://doi.org/10.1007/978-3-031-09409-5_7

analysis for any quantitative data on performance, but this can be supplemented by continual inspection and assessment of existing structures.

The Center for Innovation in Infrastructure (CII) at Dalhousie University is currently conducting a research programme in collaboration with Nova Scotia Department of Transportation and Infrastructure Renewal (NSTIR) to propose guidelines for designing durable bridge decks in Nova Scotia (NS). The research consists of two interrelated phases. Phase I consists of categorizing and evaluating FRP-reinforced bridge deck design practice in NS over the past 20 years, while Phase II consists of developing a framework to assess the structural reliability of FRP-reinforced bridge deck design options subjected to the province's specific environmental exposure. In this paper, parts of Phase I and Phase II are presented.

## 2 Phase I: Analysis of GFRP-Reinforced Bridge Decks in Nova Scotia (NS)

A database comprising of the design details of select bridges in NS was developed, summarizing the bridges into categories such as date of construction, abutment type, girder type, concrete compressive strength, deck thickness, span length and other relevant categories. Information for these bridges was obtained, such as stamped engineering design drawings, inspection reports and strength testing reports. This database currently consists of 20 bridges with parameters summarized in Table 1.

Five (5) bridges with FRP-reinforced bridge decks were selected and analysed for the purpose of this paper based on geographical location to capture different regions in NS. The five bridges were selected from the Northern, Central, Cape Breton and South Shore regions of the province. Table 1 also shows a summary of the parameters of the five bridges selected for analysis.

### *2.1 Analysis Basis*

The data collected from the five bridges selected were analysed to determine the demand, capacity and utilization ratios (U.R.) for various parts of the bridge deck. The analysis basis used for the bridges is described as follows:

- All analyses and design checks were performed in accordance with the Canadian Highway Bridge Design Code (CSA S6-19).
- Project details and designs were extracted from approved and stamped engineering design drawings.
- Design loads were taken from methods specified in Sect. 3 (Loads) of CSA S6-19.
- The Flexural Method of evaluating bridge decks as described in Sect. 5 (Methods of analysis) of CSA S6-19 was used to evaluate the flexural capacity of the bridge decks.

**Table 1** Summary of bridges in database

| Parameter | Value/range | Number of bridges | |
|---|---|---|---|
| | | Database (20) | Analysed for this paper (5) |
| Date of construction | 2011–2015 | 12 | 2 |
| | 2016–2020 | 8 | 3 |
| Abutment type | Integral abutment | 18 | 5 |
| | Semi-integral abutment | 2 | 0 |
| Girder type | New England Bulb Tee (NEBT) | 15 | 5 |
| | Box girder | 3 | 0 |
| | Next beam type B | 1 | 0 |
| | 28F Next beam | 1 | 0 |
| Concrete compressive strength | 45 MPa | 19 | 5 |
| | 50 MPa | 1 | 0 |
| Deck thickness | 175 mm | 1 | 0 |
| | 200 mm | 1 | 0 |
| | 225 mm | 14 | 4 |
| | 250 mm | 4 | 1 |
| Span length | 15–24 m | 3 | 0 |
| | 25–34 m | 5 | 2 |
| | 35–44 m | 9 | 3 |
| | 45–54 m | 0 | 0 |
| | 55–65 m | 3 | 0 |

- Methods pertaining to the design of FRP-reinforced bridge decks were used in accordance with Sect. 16 (Fibre-reinforced structures) of CSA S6-19.

## 2.2 *Analysis Results and Discussion*

The summarized results of the analyses are presented in Table 2, showing the utilization ratios (U.R.) for both positive and negative moments in the bridge deck's interior and exterior spans. The concept of a utilization ratio was also adopted in evaluating crack width calculations. The utilization ratios were calculated by dividing the load effect (factored bending moment load or crack width) by the applicable resistance (factored bending moment resistance or acceptable crack width limit).

**Table 2** Utilization Ratios (U.R.) for the five bridges analysed

| Span | Loading direction | Utilization ratio for bridges | | | | | Mean | Standard deviation |
|---|---|---|---|---|---|---|---|---|
| | | 1 | 2 | 3 | 4 | 5 | | |
| Interior spans | Negative transverse bending | 0.80 | 0.51 | 0.42 | 0.78 | 0.63 | 0.63 | 0.17 |
| | Positive transverse bending | 0.51 | 0.31 | 0.38 | 0.56 | 0.51 | 0.45 | 0.10 |
| | Positive longitudinal bending | 0.53 | 0.35 | 0.29 | 0.60 | 0.56 | 0.47 | 0.14 |
| Exterior spans | Negative transverse bending | 0.79 | 0.66 | 0.46 | 0.53 | 0.59 | 0.61 | 0.13 |
| | Negative transverse bending—barrier load | 0.77 | 0.70 | 0.55 | 0.67 | 0.63 | 0.66 | 0.08 |
| Interior spans | Crack width: negative transverse | 1.54 | 0.99 | 0.88 | 1.34 | 0.88 | 1.13 | 0.30 |
| | Crack width: positive transverse | 0.50 | 0.22 | 0.68 | 0.60 | 0.55 | 0.51 | 0.18 |
| | Crack width: positive longitudinal | 1.01 | 0.71 | 0.63 | 1.20 | 1.09 | 0.93 | 0.25 |
| Exterior spans | Crack width: negative transverse | 0.81 | 0.70 | 0.51 | 0.45 | 0.46 | 0.59 | 0.16 |

As seen in Table 2, the critical zone for bending in the interior spans of the bridge deck on average is the negative transverse direction, with a mean U.R. of 0.63. This corresponds to the location of the largest bending moment in the interior spans in the negative transverse direction. For exterior or cantilever spans, the negative transverse moment caused by barrier loads has the highest mean U.R. of 0.66. The U.R. for crack widths in parts of the deck undergoing negative bending in the interior spans have a mean value of 1.13 which is above 1.0, signifying that on average, the theoretical crack widths are greater than the specified limit, 0.7 mm, as specified in the CSA S6-19 flexural design method. It should be noted that the actual crack widths in these zones have not been verified in the existing structures due to the presence of asphalt wearing surfaces.

These findings indicate that the portions of bridge deck over the interior girders subjected to negative bending are the critical region for the designer to ensure that the transverse crack width criteria in the code is satisfied in the flexural design approach. The designer's choice of the flexural design method versus the empirical design method will result in significant differences in the amount of reinforcement selected at the identified critical region. Also, in the empirical method, the need for a crack width check is waived. The choice of the design method is not available on the drawings so it could not be verified for this study. However, Khanna et al. (2000) and Mufti et al. (1999) have demonstrated, both experimentally and theoretically, that the top layer of reinforcement is not critical to the strength and safety of the bridge deck under wheel loads.

## 3 Phase II: Reliability-Based Model

A framework was established to develop a reliability-based model that will be used to propose a set of durable bridge deck design criteria for NS. This framework involves performing Monte-Carlo simulations based on identifying and categorizing the factors that contribute to the factored moment demand, $M_f$, and the factored moment of resistance of the concrete bridge deck, $M_r$, at ultimate limit state, and identifying the corresponding statistical parameters (mean, bias, standard deviation). The reliability-based model is currently in the early stages of development. Preliminary discussion about the live loads used in the model is provided in this paper.

The maximum wheel load from the live load, $P$, shall be compared to the maximum wheel load as specified in CSA S6-19 to establish a bias ratio (i.e. actual maximum wheel load divided by the code specified maximum wheel load), determine the distribution type and quantify the variance of the live load. Real-life live load data was needed to conduct a live load analysis of trucks in NS.

A year's worth of weigh-in-motion (WIM) data was received from the NSTIR at a truck scale site in Nova Scotia. This data consists of Class 13 (7 or more axles), Class 12 (6-axle) and Class 11 (5-axle) vehicles, separated into the number of axles, axle weights and distance between axles. With Class 13 vehicles being the highest weight class, more emphasis was made on its categorization and analysis. With approximately 33,300 Class 13 vehicles received, a histogram was created to capture the distribution of the data. This distribution will be used to predict the maximum wheel load for 1-in-75 and 1-in-2 return period.

Figure 1 shows the histogram of the total weights, in kilonewtons (kN), of Class 13 vehicles. It can be seen in this figure that three peaks are present, with two being more visibly prominent. It was recognized that the three peaks show the weight distribution of unloaded trucks, partially loaded trucks and fully loaded trucks (Schmidt et al. 2016). The peaks for unloaded and fully loaded trucks are very distinct and can easily be distinguished, whereas the peak for partially loaded trucks is short and has a wider variance. This is because a significant number of trucks on the road are neither completely empty nor completely full, and a lot of trucks fall somewhere in-between as the data suggests.

After further investigation, the axle loads were categorized into histograms and the same three-peak trend was found for most of the axles. Axle 1 showed a single peak which meant that the load in the back of the Class 13 trucks does not affect the loads in the first axle. A normal distribution probability density function (PDF) was fitted to the data from Axle 1.

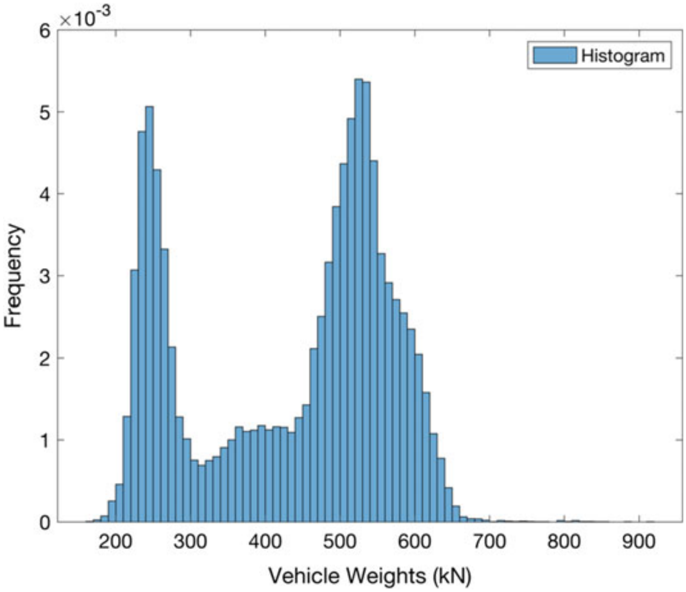

**Fig. 1** Histogram of total weights of Class 13 vehicles

The other axles (2–9) showed the three-peak behaviour as well and three normal distributions were fitted to each peak to get a mean value and standard deviation for each. Axle 3 was found to have the largest mean value for the fully loaded trucks (third peak), with a mean of 89 kN and a standard deviation of 5.69 kN. The third peak of Axle 3 is of interest because it shows the maximum axle load of fully loaded trucks and therefore will be used to establish the bias with the maximum value specified in CSA S6-19 once the values have been extrapolated for larger return periods. The probability density function (PDF) and histogram for Axle 3 are shown in Fig. 2.

## 4 Conclusion

Bridge structures are often under adverse environmental conditions that could reduce their lifespan, and the use of GFRP-reinforced bars helps tackle some of the durability issues that exist. The long-term objectives of this research programme are to provide a critical review of the design methods for GFRP-reinforced bridge decks in Nova Scotia and recommend reliability-based regional specific durability-based design criteria for GFRP-reinforced bridge decks. This paper presents parts of the two-phase approach taken by the research group.

In Phase I, a database was created to summarize the properties and characteristics bridges in NS, where five bridge decks were analysed to obtain the utilization ratios (ratio of demand-to-capacity) at critical locations within the bridge deck. The

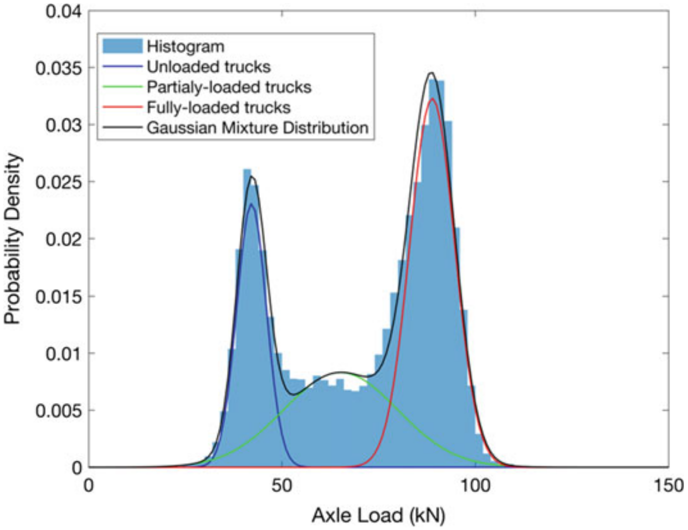

**Fig. 2** PDFs and histogram of Axle 3 loads of Class 13 vehicles

utilization ratios for bending moments were below 1.0, ranging from 0.29 to 0.80. The max average U.R. for bending moments was found in the negative transverse loading direction caused by barrier loads, having a value of 0.66. While for crack widths, the max average U.R. was found in the negative transverse bending direction, with a value of 1.13, which is greater than 1.0 signifying that this zone could be the area of the deck most susceptible to cracking.

In Phase II, the live load data used in developing the reliability-based model was briefly discussed. The live load data from a truck scale in NS was obtained and normal distributions were fitted to the axle loads. Most of the axles displayed a three-peak trend which signified that some of the trucks were either unloaded, partially loaded, or fully loaded. Axle 3 of Class 13 vehicles were found to have the highest average weight of all the fully loaded trucks and will be extrapolated for larger return periods when used in the reliability model.

## 5 Future Work

The statistical parameters for other variables identified in the reliability-based framework will be obtained either from research literature, lab testing, or analytical analyses to perform the Monte-Carlo simulations required for the model. More research will be done on the live load data to extrapolate the maximum axle load for longer return periods: 2-years for evaluating existing bridges and 75-years for designing new bridges. The research team plans to perform lab testing on concrete beams reinforced with GFRP bars that have been subjected to the local Nova Scotia environment and weather conditions for the last 12 years to account for any deterioration or degradation in the GFRP bars and concrete. This combined with previous research literature will help tackle the durability issues faced by concrete bridge decks in Nova Scotia.

**Acknowledgements** The research team would like to thank the Nova Scotia Department of Transportation and Infrastructure Renewal for approving and sponsoring this project, alongside Dalhousie University.

## References

Benmokrane B, Brown VL, Ali AH, Mohamed K, Shield C (2020) Reconsideration of the environmental reduction factor CE for GFRP reinforcing bars in concrete structures. J Compos Constr 24(4):06020001

CSA S6-19, The Canadian highway bridge design code. Canadian Standards Association, Toronto (Ontario)

ISIS, Design Manual No. 3 (2007) Reinforcing concrete structures with fibre reinforced polymers. Intell Sens Innov Struct Can 449–458

Khanna OS, Mufti AA, Bakht B (2000) Experimental investigation of the role of reinforcement in the strength of concrete deck slabs. Can J Civ Eng 27(3):475–480

Kim YH, Trejo D, Gardoni P (2012) Time-variant reliability analysis and flexural design of GFRP-reinforced bridge decks. J Compos Constr 16(4):359–370

Mufti AA, Newhook JP, Khanna OS (1999) Predicting the punching behaviour of reinforced concrete bridge decks. In: Proceedings of the Canadian society for civil engineering annual conference, Regina, vol I, pp 325–334

Schmidt F, Jacob B, Domprobst F (2016).Investigation of truck weights and dimensions using WIM data. Transp Res Procedia 14:811–819

# Three-Dimensional CT Imaging Analysis of Concrete: Effects of Water and Sand Contents on Pore Characteristics

**Mustafa Alhusain and Adil Al-Mayah**

## 1 Introduction

The composition of concrete has a significant impact on its pore properties, and consequently, on mechanical strength. The low strength of concrete makes it more susceptible to surrounding environmental conditions that result in the deterioration of the concrete structure and necessitate concrete repair and strengthening. As estimated by the American Society of Civil Engineering (ASCE), the repair of concrete infrastructure is expected to cost the United States alone about $2 trillion by 2025 (ASCE Infrastructure Report Card 2017). Thus, determining the appropriate water-to-cement (W/C) and sand-to-cement (S/C) ratios for different structural applications is critical for improving the durability of concrete structures. This, however, requires a better understanding of the effects of W/C and S/C ratios on the internal microstructure of concrete including the pore properties and the overall quality of concrete.

Through destructive experimental testing, it was reported that increasing the W/C ratio can degrade the compressive, tensile, and flexural strengths of concrete (Lotfi-Omran et al. 2019; Nikbin et al. 2014; Wanasinghe et al. 2020). Albeit, applying a higher W/C ratio can decrease the permeability of concrete resulting in improved

---

M. Alhusain (✉) · A. Al-Mayah
Mechanical and Mechatronics Engineering, University of Waterloo, 200 University Ave W, Waterloo, ON, Canada
e-mail: malhusain@uwaterloo.ca

A. Al-Mayah
e-mail: aalmayah@uwaterloo.ca

A. Al-Mayah
Civil and Environmental Engineering, University of Waterloo, 200 University Ave W, Waterloo, ON, Canada

M. Alhusain
Mechanical Engineering, King Faisal University, Hofuf, Saudi Arabia

B. Benmokrane et al. (eds.), *8th International Conference on Advanced Composite Materials in Bridges and Structures*, Lecture Notes in Civil Engineering 267,
https://doi.org/10.1007/978-3-031-09409-5_8

resistance to reinforcement corrosion and freeze–thaw damage (Pereira da Costa et al. 2020). On the contrary, increasing the S/C ratio can enhance the compressive, tensile, and flexural strengths of concrete (Bu et al. 2017), but it deteriorates the freeze–thaw resistance of concrete (Grubesa et al. 2019). These opposite effects of W/C and S/C ratios on the mechanical strength and freeze–thaw resistance of concrete can be better explained by investigating how changing the concrete composition alters its pore structure.

A unique micro-computed tomography (μCT) imaging technique was applied here to investigate the internal structure of concrete without cutting the specimen to preserve the specimen's original structure. Three-dimensional high-resolution images of the concrete specimens were captured and analyzed to study the effects of W/C and S/C ratios on the pore structure of concrete in a non-destructive manner. The pore properties of concrete were represented and evaluated using the porosity and the volume ratio of small and large voids.

## 2 Materials and Methodologies

### *2.1 Specimens*

Small concrete specimens with a diameter of 15 mm were cast, cured for 28 days, and dried at room temperature for several days before μCT imaging. A total of 9 specimens were examined to study the effects of the W/C and S/C ratios on the pore structure of concrete. While the first 6 specimens were prepared using W/C ratios of 0.4–0.9 with a fixed S/C of 1.0, the other 3 specimens were cast using S/C ratios of 0.5, 2, and 3 with a fixed W/C of 0.5. The mixing proportions of the concrete specimens were listed in Table 1.

**Table 1** Composition of concrete specimens

| Specimen | Mix ratio (C:W:S:A) |
|---|---|
| W/C = 0.4 ǁ S/C = 1 | 1:0.4:1:1.5 |
| W/C = 0.5 ǁ S/C = 1 | 1:0.5:1:1.5 |
| W/C = 0.6 ǁ S/C = 1 | 1:0.6:1:1.5 |
| W/C = 0.7 ǁ S/C = 1 | 1:0.7:1:1.5 |
| W/C = 0.8 ǁ S/C = 1 | 1:0.8:1:1.5 |
| W/C = 0.9 ǁ S/C = 1 | 1:0.9:1:1.5 |
| S/C = 0.5 ǁ W/C = 0.5 | 1:0.5:0.5:1.5 |
| S/C = 2 ǁ W/C = 0.5 | 1:0.5:2:1.5 |
| S/C = 3 ǁ W/C = 0.5 | 1:0.5:3:1.5 |

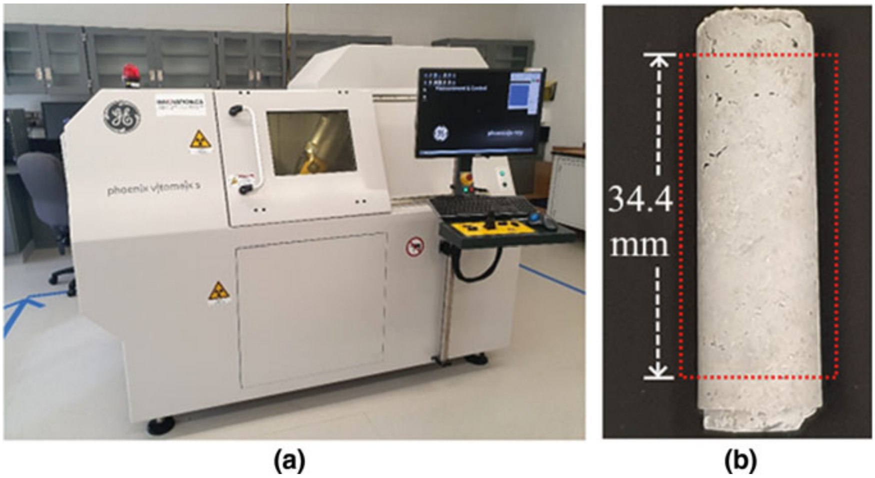

**Fig. 1** **a** μCT imaging system and **b** Region of interest of specimens

### 2.2 CT Imaging

An advanced micro-focus CT imaging system was employed to detect and analyze the concrete voids, as shown in Fig. 1a. The CT scans were performed using tube voltage and current of 110 kV and 80 μA, respectively. An X-ray exposure time of 0.33 s was utilized for capturing a total of 1,000 images with a voxel size of 49.1 μm. These imaging parameters were suitable for capturing high-resolution CT images efficiently. Identical post-imaging processes were applied to the collected images to minimize scanning artifacts and analyze the internal pores of the concrete specimens. Pore analysis was conducted on the 34.4 mm long midsection of the specimens, illustrated in Fig. 1b, to avoid the error caused by the rough top and bottom surfaces.

## 3 Results and Discussion

### 3.1 General

Three-dimensional (3D) reconstructions of the detected pores were generated, post-processed, and analyzed as shown in Fig. 2. As illustrated in the image, changing the mixing proportion of concrete can substantially alter the nature of its pore structure, and consequently, its mechanical performance. After conducting pore analysis, it was revealed that increasing the W/C ratio beyond the appropriate level resulted in higher porosity and volume of large voids, which explained the concrete weakening

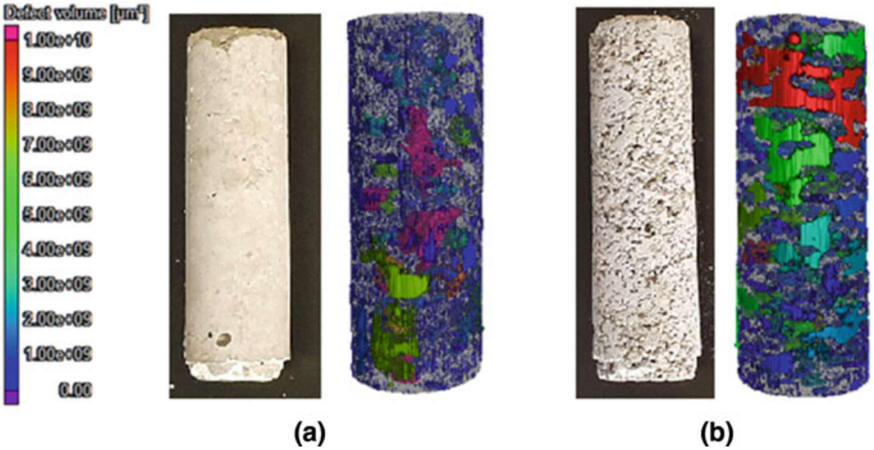

**Fig. 2** 3D representation of air voids of **a** S/C = 0.5 and **b** S/C = 3 concrete specimens

effect reported in the literature (Lotfi-Omran et al. 2019; Nikbin et al. 2014). Similarly, applying a high S/C ratio was observed to degrade the workability of concrete producing a higher void density. Nevertheless, increasing the S/C ratio seemed to decrease the volume ratio of large pores, and therefore, improve the strength of concrete, which matched the published findings (Bu et al. 2017). Notably, applying the appropriate W/C and S/C ratios of 0.6 and 1, respectively, prevented extreme cases of underhydration and overhydration of the concrete mix resulting in the least porosity of 3.26%.

### *3.2 Effect of W/C Ratio*

Six concrete specimens with W/C ratios of 0.4–0.9 were imaged. It was observed that using a low W/C ratio of 0.4 reduced the workability of the concrete mix producing a porosity of 4.62%. Increasing the W/C ratio up to 0.6 improved the workability, and subsequently, decreased the porosity to 3.26%. However, the addition of more water increased the produced porosity to 4.44%. Notably, increasing the W/C ratio from 0.7 to 0.9 did not considerably change the resulted porosity. This can be attributed to excessive bleeding of the high-water content concrete mix, which pushed the excess water to the top surface of the specimens. The porosity of concrete under different W/C ratios was plotted in Fig. 3a. As illustrated, using a W/C ratio of 0.6 can yield the least porosity.

The effect of the W/C ratio on the quality of the pore structure was represented by the volume ratio of small (<200 voxels) and large (>200 voxels) voids as shown in Fig. 3b. It was clearly shown that increasing the W/C ratio generally reduced the volume of small voids and increased the volume of the larger and more detrimental

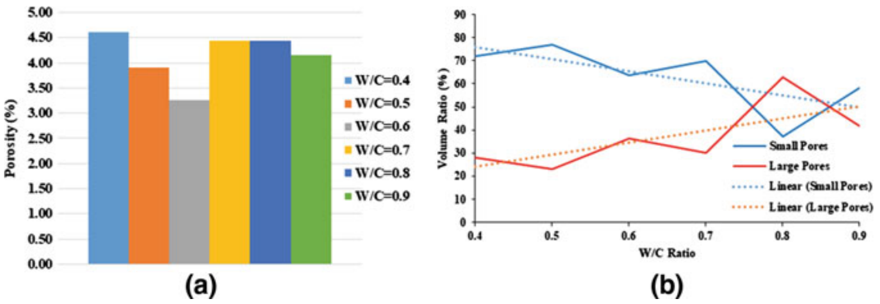

**Fig. 3** **a** Porosity, and **b** Volume ratio of small (<200 voxels) and large (>200 voxels) pores of specimens with different W/C ratios

voids. This shows that although increasing the W/C ratio from 0.4 to 0.9 did not significantly affect the porosity of concrete, it most likely degraded the concrete strength by considerably increasing the volume ratio of the large damaging voids. It was also worth noting that even though the excessive concrete bleeding prevented further growth of the porosity as the W/C ratio was increased from 0.7 to 0.9, it did not control the volume ratio of large pores as demonstrated in Fig. 3b. Based on these results, it can be deduced that applying a W/C ratio beyond 0.6 can deteriorate the performance of concrete by increasing both the porosity as well as the volume ratio of large voids. However, while decreasing the W/C ratio below 0.6 increased the porosity, it also improved the quality of the pore structure by maximizing the volume ratio of small voids. Thus, further research is needed to determine the optimal W/C ratios for specific concrete applications.

## 3.3 Effect of S/C Ratio

Micro-computed tomography was utilized to investigate the effect of the sand-to-cement (S/C) ratio on the pore properties of concrete specimens prepared using S/C ratios of 0.5, 1, 2, and 3. It was found that using an insufficient amount of sand (S/C = 0.5) produced more porous specimens. Increasing the S/C ratio from 0.5 to 1 improved the workability of concrete and decreased its porosity from 4.99% to 3.9%. Applying higher S/C ratios (e.g. S/C = 3) degraded the workability of concrete resulting in higher void content. The concrete porosity produced under different S/C ratios was shown in Fig. 4 a. Notably, the S/C and W/C ratios have a contrary effect on the porosity of concrete.

The effect of the S/C ratio on the quality of the pore structure represented by the volume ratio of small and large voids was not obvious possibly due to the small number and size of the specimens, as illustrated in Fig. 4b. However, based on the plotted trendlines, it seemed that applying an S/C ratio of 0.5 increased the volume ratio of large voids. On the other hand, applying an S/C ratio of 3 reduced the

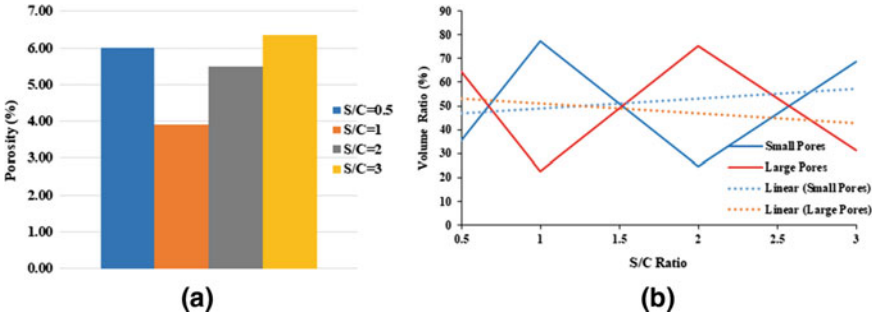

**Fig. 4** **a** Porosity and **b** Volume ratio of small (<200 voxels) and large (>200 voxels) pores of specimens with different S/C ratios

workability of concrete as well as the volume ratio of large pores. In other words, while the volume ratio of large pores was increased by overhydration of the concrete mix, it was decreased by insufficient hydration. These results matched the previous observations reported in the last section. The aforementioned results indicated that applying an S/C ratio of 1 can considerably improve the performance of concrete by minimizing both the concrete porosity as well as the volume ratio of large voids.

## 4 Summary and Conclusions

This paper presents a pilot study that utilized a high-resolution micro-computed tomography (μCT) imaging system to examine the effect of water-to-cement (W/C) and sand-to-cement (S/C) ratios on the pore properties of small concrete specimens. After examining several concrete specimens prepared using a W/C ratio of 0.4–0.9 and an S/C ratio of 0.5–3, the following points were concluded:

- The W/C and S/C ratios can considerably affect not only the porosity of concrete, but also the quality of its pore structure, thus affecting its mechanical strength and durability under different environmental conditions.
- The W/C and S/C ratios seem to have opposite effects on the porosity and volume fraction of small and large voids.
- Overhydration of the concrete mix reached by applying a high W/C ratio or a low S/C ratio can increase both the porosity and the volume fraction of large pores; hence, it can weaken the strength and freeze–thaw resistance of concrete.
- Insufficient hydration of the concrete mix attained by decreasing the W/C ratio or increasing the S/C ratio can increase the porosity but reduce the volume fraction of large voids, which can enhance the concrete strength.
- Applying the appropriate W/C and S/C ratios of 0.6 and 1, respectively, produced a high-quality concrete specimen with the least porosity and an improved pore structure.

## References

ASCE Infrastructure Report Card (2017) American Society of Civil Engineers (ASCE)

Bu J, Tian Z, Zheng S, Tang Z (2017) Effect of sand content on strength and pore structure of cement mortar. J Wuhan Univ Technol Mater Sci Ed 32:382–390. https://doi.org/10.1007/s11595-017-1607-9

Grubesa IN, Markovic B, Vracevic M, Tunkiewicz M, Szenti I, Kukovecz A (2019) Pore structure as a response to the freeze/thaw resistance of mortars. Materials 12. https://doi.org/10.3390/ma12193196

Lotfi-Omran O, Sadrmomtazi A, Nikbin IM (2019) A comprehensive study on the effect of water to cement ratio on the mechanical and radiation shielding properties of heavyweight concrete. Constr Build Mater 229:116905. https://doi.org/10.1016/j.conbuildmat.2019.116905

Nikbin IM, Beygi MHA, Kazemi MT, Vaseghi Amiri J, Rabbanifar S, Rahmani E, Rahimi S (2014) A comprehensive investigation into the effect of water to cement ratio and powder content on mechanical properties of self-compacting concrete. Constr Build Mater 57, 69–80. https://doi.org/10.1016/j.conbuildmat.2014.01.098

Pereira da Costa FB, Haselbach LM, da Silva Filho LCP (2020) Pervious concrete for desired porosity: influence of w/c ratio and a rheology-modifying admixture. Constr Build Mater 121084. https://doi.org/10.1016/j.conbuildmat.2020.121084

Wanasinghe D, Aslani F, Ma G (2020) Effect of water to cement ratio, fly ash, and slag on the electromagnetic shielding effectiveness of mortar. Constr Build Mater 256:119409. https://doi.org/10.1016/j.conbuildmat.2020.119409

# An Innovative Wedge Anchorage for CFRP Plates: Finite Element Modeling and Experimental Verification

**Mustafa Alhusain and Adil Al-Mayah**

## 1 Introduction

Based on the American Society of Civil Engineering (ASCE) report (2017), the rehabilitation of concrete structures is projected to cost the United States about $2 trillion by 2025 (ASCE Infrastructure Report Card 2017). Thus, extensive research has examined the potential of strengthening concrete structures using the corrosion-resistant carbon fiber reinforced polymer (CFRP) accredited to its high tensile strength and lightweight (Al-Mahaidi and Kalfat 2011; Van Den Einde et al. 2003). The effectiveness of CFRP reinforcement can be increased through the application of post-tensioning. However, prestressing CFRP is challenging due to its susceptibility to lateral loading imposed by the required gripping system (Sun et al. 2019). Thus, utilizing suitable anchorage systems is essential for efficient CFRP applications. One of the proposed efficient gripping systems is the friction-based wedge anchorage, which is compact in size, reusable, and easy to install. The mechanical wedge anchorage consists of an external cylindrical barrel and multiple internal wedges in addition to soft sleeves, which are used to minimize stress concentration within the CFRP plate (Al-Mayah et al. 2013). The wedges are marginally larger than the

---

M. Alhusain (✉) · A. Al-Mayah
Mechanical and Mechatronics Engineering, University of Waterloo, 200 University Ave W, Waterloo, ON, Canada
e-mail: malhusain@uwaterloo.ca

A. Al-Mayah
e-mail: aalmayah@uwaterloo.ca

A. Al-Mayah
Civil and Environmental Engineering, University of Waterloo, 200 University Ave W, Waterloo, ON, Canada

M. Alhusain
Mechanical Engineering, King Faisal University, Hofuf, Saudi Arabia

B. Benmokrane et al. (eds.), *8th International Conference on Advanced Composite Materials in Bridges and Structures*, Lecture Notes in Civil Engineering 267,
https://doi.org/10.1007/978-3-031-09409-5_9

passage of the housing hollow barrel; therefore, applying press-fitting causes an interference between the wedges and the barrel resulting in lateral compression of the CFRP plate (CFRP contact pressure).

The performance of the wedge anchorage and its ultimate load-carrying capacity are crucially dependent on the intensity and distribution of the contact pressure on the CFRP plate. While applying insufficient CFRP contact pressure produces inadequate gripping strength leading to considerable CFRP slippage, applying excessively high CFRP contact pressure can lead to its premature failure. Therefore, a thorough examination of the wedge anchorage performance using different sets of dimensions is critical for identifying the appropriate dimensions. This task can be achieved in a cost-effective and timely manner using finite element (FE) modeling. Little research has been conducted on the development of a three-dimensional (3D) FE model of a wedge anchorage for CFRP plates. Hence, the main objective of this paper was the development of a realistic FE model of the wedge anchorage using the appropriate boundary and contact conditions. The post-loading stress distribution within the anchorage was analyzed, and the accuracy of the FE model was investigated by comparing its results to experimental data.

## 2 Finite Element (FE) Model

### *2.1 General*

The wedge anchorage was made of four components, which were a CFRP plate, two copper sleeves, two steel wedges, and a steel barrel. Only a quarter section of the symmetric anchorage was simulated using ABAQUS software to reduce the required processing power and time, as shown in Fig. 1. The compact size of the anchorage was represented by the barrel length and outer diameter of 70 mm and 76.2 mm, respectively. The actual CFRP specimen was 1.2 mm thick, 50 mm wide, and 1,000 mm long. Likewise, the copper sleeves were 0.81 mm thick, 50 mm wide, and 75 mm long. However, the thickness and width of the CFRP plate and the width of the copper sleeves were halved in the FE model since only a quarter section was modeled. The contacting surfaces of the wedges and barrel were made of a combination of circular and linear segments. The circular segment was introduced to allow a gradual increase of interference between the wedges and barrel along

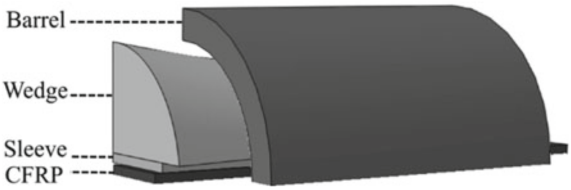

**Fig. 1** Quarter model of wedge anchorage (Alhusain and Al-Mayah 2020b)

the length of the anchorage to prevent stress concentration at the loading tip of the CFRP plate while the linear segment was used to maintain the interference within a suitable range near the freeloading end. The dimensions of the wedges and barrel were discussed in detail in a preceding publication (Alhusain and Al-Mayah 2020a). In accordance with a prior parametric study (Alhusain 2018), neither CFRP premature failure nor anchorage plastic deformation was observed after applying the full CFRP tensile load. The soft copper sleeves were expected to experience plastic deformation upon loading; hence, a new set of sleeves were employed per test. Therefore, the FE elements were treated as elastic materials.

### *2.2 Boundary, Contact, and Loading Conditions*

The appropriate boundary, contact, and loading conditions were employed to simulate the post-tensioning process applied in the field. The first two roller boundary conditions were applied on the mirroring surfaces of the CFRP plate, the sleeve, the wedge, and the barrel to accurately mimic the behavior of the wedge anchorage using only a quarter section. Throughout the press-fitting (presetting) and CFRP tensile loading processes, the loading end (Edge 1) of the barrel, shown in Fig. 2, was supported by a fixed frame; thus a roller boundary condition was introduced at the loading face of the barrel to constrain its displacement along the loading direction. Another boundary condition was applied on the pressing end (Edge 2) of the wedge to simulate the displacement-controlled presetting process of the anchorage. The total presetting displacement utilized in this study was 6 mm. After press-fitting the wedge anchorage, a tensile loading of 2,800 MPa, which was equivalent to the CFRP tensile strength, was applied on the loading end (Edge 1) of the CFRP plate as demonstrated in Fig. 2. More details of the FE models can be found in (Alhusain and Al-Mayah 2020b).

Three surface contact conditions were applied on the CFRP-sleeve, sleeve-wedge, and wedge-barrel interfaces, as shown in Fig. 3, to simulate the mechanical interaction between the elements. In order to improve the accuracy of the FE model, a hard-surface contact condition was applied on the interacting surfaces to minimize node penetration. Also, since no relative slippage was detected between the wedges and the sleeves (Al-Mayah et al. 2001), a rough (no-slip) contact condition was used in the sleeve-wedge interface. On the other hand, friction-based sliding contact conditions

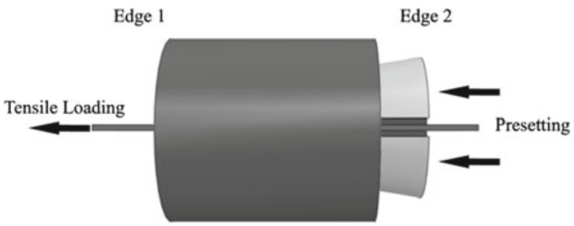

**Fig. 2** Press-fitting (presetting) and CFRP tensile loading conditions

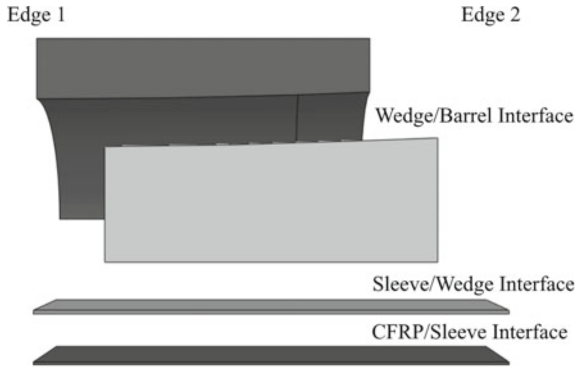

**Fig. 3** Surface contact conditions

with friction coefficients of 0.39 and 0.05 were applied, respectively, on the CFRP-sleeve and wedge-barrel interfaces (Mohee et al. 2016).

# 3 Results and Discussion

## *3.1 General*

The finite element model was utilized to assess the performance of the wedge anchorage and analyze the post-loading stress distribution within the CFRP plate, the wedges, and the barrel. The stress distribution within the wedges and the barrel was represented using von Mises stress. On the other hand, the stress distribution within the CFRP plate was analyzed using the longitudinal and lateral (contact) stresses. The maximum recorded von Mises stress within the wedges and the barrel was 707 MPa and 1,153 MPa, respectively, which were less than the yield strength of 1,896 MPa. Thus, the wedges and the barrel were not anticipated to experience plastic deformation. Likewise, the maximum longitudinal stress within the CFRP plate reached its full tensile load of 2,800 MPa. In other words, based on the FE model, neither CFRP premature failure nor anchorage plastic deformation was projected, which matched the observations made in a prior publication (Alhusain and Al-Mayah 2020a).

## *3.2 Stress Distribution*

The stress distribution within the wedge anchorage and the CFRP plate was analyzed after applying the full tensile load of 2,800 MPa. In general, the von Mises stress within the wedges and barrel as well as the lateral contact pressure within the CFRP plate were minimum at the loading end (Edge 1) of the anchorage, as demonstrated in Fig. 4a, b, and c. The stresses increase along the length up to the transition point

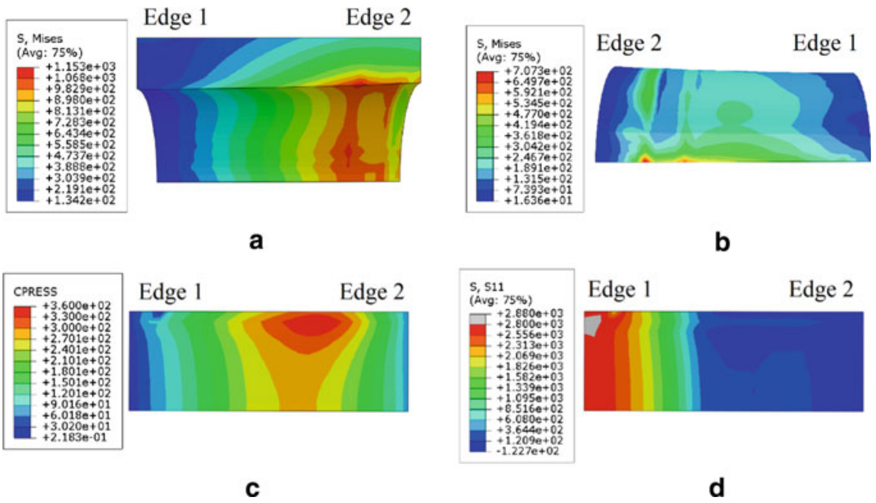

**Fig. 4** Von Mises stress distribution within the **a** Barrel and **b** Wedge, and the **c** Lateral and **d** Longitudinal stresses within the CFRP plate

between the circular and linear segments of the wedge anchorage, after which the stresses drop to lower levels. This stress distribution was desired because it minimizes the lateral stress within the loading end of the CFRP plate to prevent its premature failure, and it also controls the stress nearby the pressing end (Edge 2) of the wedge anchorage to minimize its plastic deformation. The longitudinal stress within the CFRP plate was analyzed as shown in Fig. 4d. As illustrated, only a small part of the CFRP plate (gray area) seems to fail when the full tensile load was applied. Based on the aforementioned results, it was clear that the utilized dimensional configuration of the wedge anchorage distributed the internal such that both anchorage plastic deformation and CFRP premature failure were prevented.

### *3.3 Verification of FE Model*

The accuracy of the finite element (FE) model was examined by comparing its results to experimental data. The tensile load–displacement relationship was used in the comparison to capture the full performance of the anchorage. Three experiments were conducted and simulated under identical press-fitting and tensile loading conditions. To better assess the accuracy of the FE model, three distinct levels of presetting were applied. Tests 1–3 were conducted under presetting levels of 3.4 mm, 4.2 mm, and 4.9 mm, respectively. It was worth mentioning that presetting the anchorage by pushing wedges within the passage of the barrel can be performed by a simple hammer or hydraulic jack without affecting the ultimate load-carrying capacity of the system. The tensile load was applied using a servo-hydraulic Material Testing System (MTS),

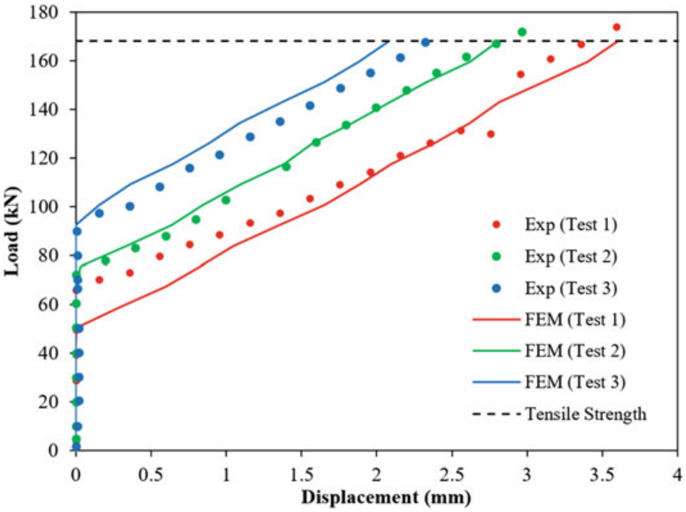

**Fig. 5** Tensile load (kN) versus Wedge displacement (mm) for experimental tests and FE simulations (Alhusain and Al-Mayah 2020b)

and a linear variable differential transformer (LVDT) was employed to measure the displacement of the wedges throughout the loading process. Upon completion of experimental testing, it was determined that the wedge anchorage successfully gripped the CFRP plate until its full reported tensile strength of 2,800 MPa (168 kN) was reached, which confirms the successful elimination of CFRP premature failure as indicated by the FE model. Likewise, the load–displacement data attained through the experimental tests and the FE model were compared as demonstrated in Fig. 5, and a notable agreement was observed. Based on the aforementioned results, it was possible to conclude that the FE model has a reasonable degree of accuracy.

## 4 Conclusions

A three-dimensional finite element (FE) model with a good degree of accuracy was developed and experimentally verified. As revealed by the FE model, the dimensional configuration of the wedge anchorage minimized the post-loading internal stress nearby the loading end (Edge 1) and the pressing end (Edge 2), which allowed effective gripping of the CFRP plate besides preventing plastic deformation within the anchorage. These results were verified by experimental testing, through which neither CFRP premature failure nor anchorage plastic deformation was observed. The accuracy of the FE model was examined by comparing its load–displacement data with experimental readings, from which a notable accuracy was illustrated.

## References

Alhusain M, Al-Mayah A (2020a) Innovative wedge anchorage for CFRP plates: development and testing

Alhusain M, Al-Mayah A (2020b) Wedge anchorage for CFRP plates: finite element modelling and experimental verification

Alhusain M (2018) Development, optimization and testing of an innovative wedge anchorage for CFRP plates (Master's thesis). University of Waterloo

Al-Mahaidi R, Kalfat R (2011) Investigation into CFRP plate end anchorage utilising uni-directional fabric wrap. Compos Struct 93:821–830. https://doi.org/10.1016/j.compstruct.2010.07.012

Al-Mayah A, Soudki K, Plumtree A (2001) Experimental and analytical investigation of a stainless steel anchorage for CFRP prestressing tendons. PCI J 46:88–99

Al-Mayah A, Soudki K, Plumtree A (2013) Simplified anchor system for CFRP rods. J Compos Constr 17:584–590. https://doi.org/10.1061/(ASCE)CC.1943-5614.0000367

ASCE Infrastructure Report Card (2017) American Society of Civil Engineers (ASCE)

Mohee F, Al-Mayah A, Plumtree A (2016) Friction characteristics of CFRP plates in contact with copper plates under high contact pressure. J Compos Constr 20. https://doi.org/10.1061/(ASCE)CC.1943-5614.0000673

Sun W, He T, Liu S (2019) Developing an anchored CFRP reinforcement for efficiently and readily strengthening reinforced concrete structures. Compos Part B Eng 176:107199. https://doi.org/10.1016/j.compositesb.2019.107199

Van Den Einde L, Zhao L, Seible F (2003) Use of FRP composites in civil structural applications. Constr Build Mater Fibre-Reinf Polym Compos Constr 17:389–403. https://doi.org/10.1016/S0950-0618(03)00040-0

# Effects of Load Level on the Structural Fire Behaviour of GFRP-Reinforced Concrete Beams with Straight-End bar Lap Splices

**Sobita Gurung and Osama Salem**

## 1 Introduction

Glass fibre-reinforced polymer (GFRP) is a composite material that is made of glass fibres embedded in a polymer matrix. For a few decades, GFRP bars have been gaining acceptance as an economical alternative to steel rebar for concrete structures to enhance their durability, especially those structures which are susceptible to corrosion. Properties such as high chemical and corrosion resistance and high strength-to-weight ratio make GFRP a desirable engineering material. However, the application of GFRP-reinforced concrete is still mostly limited to only certain components in bridges and marine structures where the fire is not a primary consideration. This is mainly because the structural behaviour of GFRP-reinforced concrete elements at elevated temperatures is yet to be understood well since only limited research has been done in this regard. GFRP bars have very good bond strength with concrete at ambient temperature. However, they are known for their poor thermal resistance and consequent loss of bond with concrete at elevated temperatures above the glass transition temperature of the polymer matrix used in their composition. The glass transition temperature of GFRPs is relatively low as it lies between 93 °C and 120 °C. Thus, the bond strength of GFRP bars with concrete is the most vulnerable characteristic in fire conditions and could be the main reason for the failure of GFRP-reinforced concrete structural elements when subjected to elevated temperatures. For instance, in a study conducted by Katz et al. (1999) to investigate the effects of high temperatures on the behaviour of GFRP bars, it was observed that the loss of bond strength of GFRP bars

---

S. Gurung · O. Salem (✉)
Department of Civil Engineering, Lakehead University, 955 Oliver Road, Thunder Bay, ON P7B 5E1, Canada
e-mail: sam.salem@lakeheadu.ca

S. Gurung
e-mail: sgurung@lakeheadu.ca

B. Benmokrane et al. (eds.), *8th International Conference on Advanced Composite Materials in Bridges and Structures*, Lecture Notes in Civil Engineering 267,
https://doi.org/10.1007/978-3-031-09409-5_10

with concrete decreased by 80% to 90% when the temperature was raised from 20 °C to 250 °C.

One of the important factors that affect the structural fire behaviour of a concrete beam is the magnitude of applied load during fire tests. The higher the level of the applied load is, the greater the deflections and more subsequent cracks that can be developed in a concrete beam are. With more cracks developed on the exposed surfaces of a concrete beam, more heat can penetrate the beam cross-section, which leads to an increase in the temperatures of the reinforcing bars. In a study conducted by Rafi and Nadjai (2014) to investigate the fire behaviour of CFRP-reinforced concrete beams subjected to varying load ratios, i.e., 20, 30, 40, 50, and 60%, of the beam moment capacity, the fire resistance time of the beams were 221, 197, 179, 161 and 144 min, respectively. In that study, all beams had cross-sectional dimensions of 120 mm wide × 200 mm deep and a length of 2000 mm. The applied load ratio also has a significant effect on the post-fire residual flexure strength of concrete beams. As per the results of a numerical study conducted by Yu and Kodur (2013), doubling the load ratio from 30% to 60% resulted in a reduction of the post-fire residual flexure strength of steel-reinforced concrete beams from 15% to 26%. Another parameter that could affect the fire resistance of concrete beams is the provision of the lap splices for tensile reinforcement, as the length of the bar lap splice directly affects the bond strength and crack pattern in GFRP-reinforced concrete beams.

The applications of GFRP-reinforced concrete structures can be an economical alternative to steel-reinforced concrete structures in extreme conditions where steel reinforcement is susceptible to corrosion. Although some studies have been conducted to investigate the fire performance of GFRP-reinforced concrete beams, most of them are of small size and/or utilize continuous reinforcement. Thus, the lack of sufficient research on the fire behaviour of GFRP-reinforced concrete beams with bar lap splices is noticeable. Also, the gap in the available literature with respect to the effects of load ratio on the fire behaviour of GFRP-reinforced concrete beams is evident. Accordingly, this study aimed to investigate the effects of applied load ratio on the fire behaviour of GFRP-reinforced concrete beams having straight-end bar lap splices at their midspan.

## 2 Experimental Programme

This paper presents the experimental study of two GFRP-reinforced concrete beams at elevated temperatures (labelled BG85-I and BG85-II). The experimental findings were compared to those of two other identical beams (labelled BG40-I and BG40-II) subjected to lower load ratio, which were tested in a prior related study conducted by Nour et al. (2021), to examine the effects of increasing the load ratio on the structural fire performance of GFRP-reinforced concrete beams with straight-end bar lap splices.

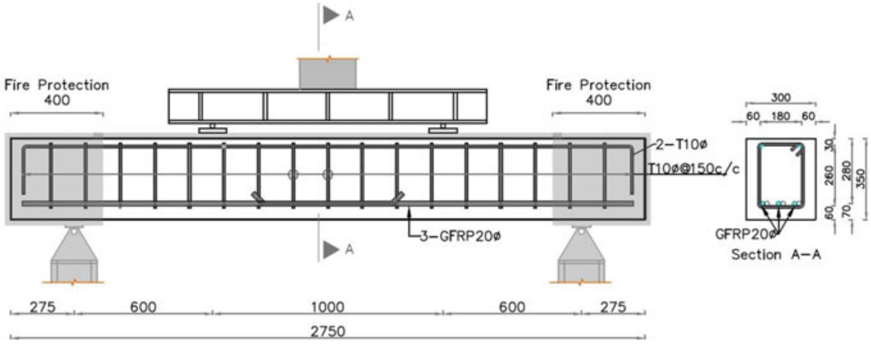

**Fig. 1** Dimensions and reinforcement details of a typical concrete beam

**Table 1** Summary of beam design bending moment values according to CSA-S806-12

| Beam ID | Lap splice length (mm) | Load ratio (%) | Applied load (kN.m) | Cracking moment (kN.m) | Service moment (kN.m) | Ultimate design moment (kN.m) | Resisting moment (kN.m) |
|---|---|---|---|---|---|---|---|
| BG85-I | 550 | 85 | 27.0 | 23.5 | 23.6 | 31.6 | 101.98 |
| BG85-II | | | | | | | |

## 2.1 Details of Test Specimens

The experimental programme included two beams reinforced with GFRP bars. The beams were 2750 mm long with cross-sectional dimensions of 300 mm × 350 mm high. Three 20-mm diameter GFRP bars were provided as tensile longitudinal reinforcement. Also, 10-mm diameter steel stirrups were provided at a spacing of 150 mm along the beam length with two 10-mm diameter stirrup hanger bars. The beams had bar lap splices of 550 mm overall length at the beam midspan where the maximum bending moment existed. A concrete cover of 60 mm thick was provided on all sides of the beam cross-section except on the top, where only a 30 mm thick concrete cover was provided. The dimensions and details of the reinforcement of the two test specimens are provided in Fig. 1. Also, Table 1 summarizes the values of the calculated bending moments according to CSA-S806-12 design standard.

## 2.2 Fire Test Setup

All fire tests of this study as well as those in (Nour et al. 2021) were conducted at Lakehead University Fire Testing and Research Laboratory (LUFTRL). The beams were simply supported with a clear span of 2200 mm and tested under four-point flexure bending. The beams were exposed to fire on three sides only, where the top side along a 400 mm distance from each end of the beam were thermally insulated using two layers of 25 mm thick ceramic fibre blankets. This is to simulate the existence of a concrete slab on top of the beam as well as a concrete column at each end as it would be in a real construction configuration. During fire tests, the two beams of this study were exposed to elevated temperatures that followed the CAN/ULC S101 standard fire time–temperature curve while being subjected to 85% of the beam ultimate design moment (27 kN.m). The beams were deliberately subjected to this moment magnitude, which is above the beam cracking moment (23.5 kN.m), so cracks could develop before commencing the fire tests to investigate how direct heat penetration through those cracks can affect the fire performance of the beams. The transverse load was applied using a hydraulic cylinder connected to a manual pump through a vertical steel loading post, which was then transferred to the test specimen at two points, 1000 mm apart through a spreader steel beam. The load was applied in four increments, each of 25% of the total load magnitude, until the target load (27 kN.m) was reached at least 30 min before the commencing of the fire test and then maintained throughout the test duration.

## 3 Results and Discussion

### *3.1 Furnace Temperature*

The temperature inside the large-size furnace accommodated at LUFTRL was consistently monitored using four metal-shielded Type-K thermocouples extended out of the furnace back wall to precisely follow the standard fire time–temperature curve via the furnace's advanced computer programmable control panel with an accuracy of ± 2%. The fire tests of beams BG85-I and BG85-II lasted for 51 min and 62 min with the furnace average temperature reaching 908 °C and 933 °C, respectively. Figure 2 illustrates the actual time–temperature curves for the two fire tests.

### *3.2 Beam Deflections*

The load-carrying capacity of beams BG85-I and BG85-II dropped markedly at 51 min and 62 min, respectively, indicating the beam failure as shown in Fig. 3. Thus, the fire resistance time of the two beams tested in this study is very close to that of beams BG40-I and BG40-II (53 min and 60 min, respectively) reported by Nour et al. (2021) and were subjected to slightly less than half the load applied on the beams presented in this paper. As reported by Nour et al. (2021), due to the lower load

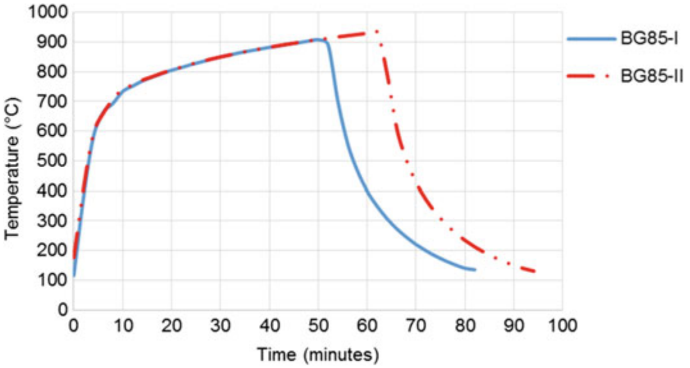

**Fig. 2** Time–temperature curves for fire tests

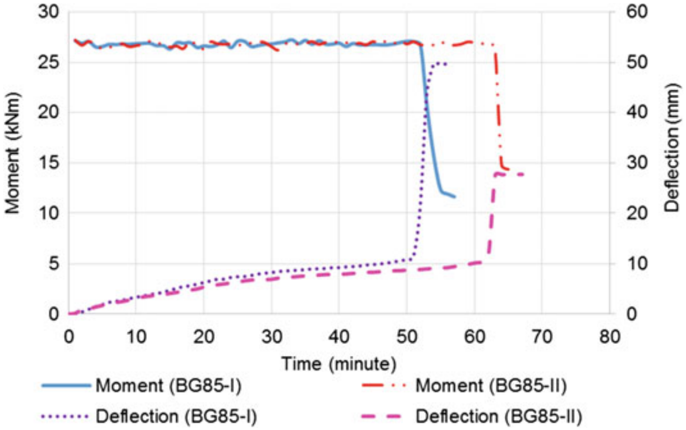

**Fig. 3** Relationships of load versus time and mid-span deflection versus time

ratio applied on their GFRP-reinforced beams no cracks were developed in the beams during the pre-loading stage before the commencing of the fire tests. However, cracks were observed in beams BG40-I and BG40-II after 35 min and 50 min, respectively, from the start of the fire tests, which then propagated with time. Although the beams subjected to a higher load ratio (BG85-I and BG85-II) had cracks formed during the pre-loading stage before the commencement of the fire tests, which started to widen only just a few minutes before the failure of the beams, the exposure time of the GFRP bars to direct heat through the developed cracks was not long enough to affect the beam fire resistance time. It can, therefore, be inferred that the fire resistance of the GFRP-reinforced concrete beams with straight-end bar lap splices is mainly affected by the length of the exposure to fire as the failure of the beams was mainly due to the loss of the bond strength of the bars with concrete because of elevated temperatures rather than the inability of the beam to maintain the increased applied load (i.e., 85% load ratio).

The relationship between the beam mid-span deflection and fire exposure time is relatively linear until failure as shown in Fig. 3. The mid-span deflections exhibited by the two beams subjected to a higher load ratio right before failure (12.5 mm and 12.7 mm for beams BG85-I and BG85-II, respectively) were almost the same as those exhibited by the similar beams but subjected to a lower load ratio (11.0 mm and 13.5 mm for beams BG40-I and BG40-II, respectively). However, as the beam was subjected to a higher load ratio, its mid-span deflection started to run away as it increased very rapidly from 12.5 mm to 20.5 mm within only 30 s in beam BG85-I, and then reached 49.0 mm in the next minute. Whereas in beam BG85-II, the deflection increased from 12.7 mm to 27.5 mm within only 60 s.

## 3.3 Beam Failure Modes

All beams including those tested by Nour et al. (2021) failed in flexure within the maximum moment zone in the middle of the beam accompanied by vertical and longitudinal cracks, as shown in Fig. 4. Beams BG85-I and BG85-II failed due to the splitting of the concrete because of slippage of the spliced bars within the fire-exposed zone in the middle of the beam. It was also noticed that slippage of the bars in beam BG85-I was greater than that in BG85-II, which may have contributed

**(a) (adapted from Nour et al., 2021)**

**(b)**

**Fig. 4** Fire damaged beams: **a** subjected to 40% load ratio (Nour et al. 2021), **b** subjected to 85% load ratio to the early failure of the former beam at just 51 min, compared to 62 min for the later beam (BG85-II). The thermal measurments (not included in this paper) of the thermocouples installed inside the beam at different locations indicate that the temperatures experienced by the bars within the lap splice zone were near or slightly above the glass transition temperature of the utilized GFRP bars. At temperatures above the glass transition temperature of the GFRP bars, the degradation of the mechanical properties of the polymer matrix is significant and can result in loss of the bond strength between the bars and the surrounding concrete. Hence, the mode of failure of the fire-tested beams was concrete splitting followed by debonding of the bars due to elevated temperatures.

The crack patterns in the examined beams were also observed closely as it was noticed that the cracks developed in the beams subjected to higher load ratio (BG85-I and BG85-II) were more than those developed in the beams subjected to lower load ratio (BG40-I and BG40-II), as shown in Fig. 4. Moreover, it was observed that the span of crack development in the beams subjected to lower load ratio (BG40-I and BG40-II) as reported by Nour et al. (2021) was contained within the lap splice zone, as shown in Fig. 4a. Whereas in the beams subjected to higher load ratio (BG85-I and BG85-II) presented in this paper, some cracks were observed beyond the bar splice zone, as shown in Fig. 4b.

## 4 Conclusions

This paper presents the findings of a unique experimental study that investigated the effects of the applied load ratio on the structural fire performance of GFRP-reinforced concrete beams having straight-end bar lap splices at their mid-span. The main findings of this study are listed below:

- The effect of the applied load level (load ratio) on the fire resistance time of the GFRP-reinforced concrete beams having straight-end bar lap splices is insignificant.
- The increase rate of the mid-span deflections at failure was higher for the beams subjected to higher load ratio compaired to that for the beams subjected to lower load ratio.
- The failure of all beams occurred due to splitting of the concrete followed by slippage of the bars in the lap splice zone when the bar temperature approached or slightly exceeded the glass transition temperature of the utilized GFRP bars.

**Acknowledgements** The authors would like to thank the FRP bars manufacturer (former TemCorp Industries Ltd.) for providing all GFRP bars as well as the technical information required for the design of the test specimens for this project. Thanks are also extended to Mr. C. Hubbard and Mr. R. Timoon, the technical staff at Lakehead University's Structures Laboratory, for their assistance. Lastly, special thanks go to K.M. Barber who assisted during the experimental phase of this research project.

## References

CAN/ULC S101 (2014) Standard methods of fire endurance tests of building construction and materials Underwriters laboratories of Canada

CSA-S806 (2012) Design and construction of building structures with fibre-reinforced polymers. Canadian standards association

Katz A, Berma N, Bank L (1999) Effect of high temperature on bond strength of frp reinforcing bar. J Compos Constr 3(2): 73–81

Nour O, Salem OS, Mostafa A (2021) Experimental fire testing of large-scale gfrp-reinforced concrete beams with mid-span straight-end bar lap splices. Fire Mater 46(2):360–375

Rafi M, Nadjai A (2014) Parametric finite element analysis of FRP reinforced beams in fire and design guidelines. Fire Mater 38:293–311

Yu B, Kodur VKR (2013) Factors governing the fire response of concrete beams reinforced with FRP rebars. Compos Struct 100:257–269

# Durability Assessment of Fiber-Reinforced Polymer Composites Externally Bonded to a Concrete Bridge After 26-Year Exposure

**Sandra Milev and Jovan Tatar**

## 1 Introduction

Foulk Road bridge #26, located in Wilmington, Delaware, is a concrete bridge originally built in 1965. The bridge superstructure consists of 23 prestressed adjacent box-beam girders. Each girder is 0.9 m wide, 0.7 m deep, and 16.4 m long. The bridge was retrofitted in 1994 due to severe longitudinal cracking on the bottom face of the girders. It is believed that cracking was caused by tensile stresses induced by freezing of the water trapped in the hollow voids and reinforcement corrosion. An investigation of this problem conducted at the University of Delaware (Chajes et al. 1993) showed a lack of transverse reinforcement in the bottom of the box section (Fig. 1) in bridges constructed before 1973. To address this issue, unidirectional CFRP sheets were externally bonded to the bottom face of the girders, with fibers oriented in the transverse direction to the beam length to act as a replacement for the transverse reinforcement (Fig. 1).

Adjacent box girders are widely used in the US for short and medium spans up to 100 ft (Federal Highway Administration 2018). Despite the fact that adjacent box girder bridges have many advantages (ease of construction, shallow superstructure depth, and high torsional stiffness) issues with durability performance resulted in premature deterioration in many bridges in the US. After 25–30 years in service, several box-beam bridges in Delaware, built in mid-1960s, developed longitudinal cracking on the beam soffit. Investigation of this problem showed that cracking in the grout keys and overlay above the keys is the leading cause of major issues.

---

S. Milev (✉) · J. Tatar
Department of Civil and Environmental Engineering, University of Delaware, Newark, Delaware, USA
e-mail: milev@udel.edu

J. Tatar
e-mail: jtatar@udel.edu

B. Benmokrane et al. (eds.), *8th International Conference on Advanced Composite Materials in Bridges and Structures*, Lecture Notes in Civil Engineering 267,
https://doi.org/10.1007/978-3-031-09409-5_11

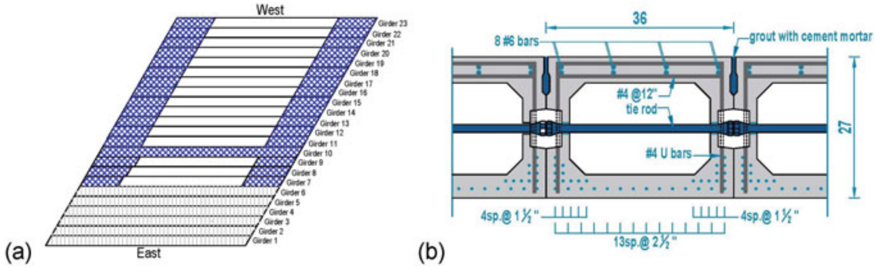

**Fig. 1** Foulk Road bridge: **a** plan of repaired girders (hatch pattern indicates fiber direction), **b** typical cross-section

Cracks in the overlay allow water and Deicing chemicals to penetrate into the empty voids and between the shear keys along the full length of the beams. Permeability of concrete allows chlorides and other aggressive agents present in the water to diffuse into concrete and initiate corrosion of reinforcement and prestressing strands, which subsequently cause cracking, spalling, and breaking of prestressing tendons (Attanayake and Aktan 2017).

Repairs were carried out using Tonen Corporation's Forca Tow Sheets, FTS-C1-20 and FTS-C5-30. Five of the six beams were strengthened with one ply of FTS-C1-20 (tensile strength: 3790 MPa, tensile modulus 250 GPa), which was designed as an equivalent to #4 bar. Two of these beams—G3 and G4—had a longitudinal crack at the time of repair. Girder G6 was retrofitted with 2 plies of FTS-C5-30 (tensile strength: 3200 MPa, tensile modulus 400 GPa) to result in a similar stiffness as the missing transverse reinforcement. The commercial name of the epoxy used is not documented, but it was most probably Tonen's corporation FP-E3P epoxy resin. The intention of the installed repairs was to extend the service life of the bridge by 5–10 years. This system consists of unidirectional carbon fibers, a two-part epoxy primer, and a two-part epoxy resin. Primer was applied to enhance adhesion, and the epoxy resin is used as an adhesive and saturate. There is no information if UV protective paint was applied to the surface of the CFRP. As a part of quality control testing, only a tapping test with a small hammer was conducted. However, tensile testing to determine the tensile strength of the Tow sheet and quality of the bond to the concrete were not performed. The detailed procedure can be found in the published literature (Finch 1997).

## 2 Field Evaluation

### 2.1 *Visual Inspection*

A visual inspection of the bridge was conducted in September 2020. The focus was on the CFRP repairs. However, the overall condition of the bridge girders was

**Fig. 2** Foulk Road bridge in Wilmington, DE

visually evaluated. Each girder was photographed to record the presence of discoloration, debonding, composite degradation, concrete cracking, corrosion, spalling, etc. Design plans for the FRP strengthening of girders G7-G23 were not found. Based on the visual inspection, they were repaired with externally bonded bidirectional CFRP. Unlike the girders repaired in 1994, girders G7-G23 were strengthened only near the supports—approximately 4 m on each side of the girder length was wrapped with CFRP (Fig. 1).

Signs of deterioration were observed on CFRP repairs installed in 1994, especially on G1 and G2: insufficient saturation, discoloration, debonding and damage of CFRP, and water staining (Fig. 3a, b). In general, the CFRP strengthening of the girders G7-G23 seemed to be in a good condition, but the damage of the repairs of several girders was noticed—G10, G11, G15 (Fig. 3c). Debonding and damage of CFRP occurred at the locations of severe girder damage. Severe cracking in the middle of the span (approximately 6 m from the south support) of G8 was observed (Fig. 3d). According to available documentation, 4 m long crack in this girder already existed in 1994 (Finch 1997). In most of the girders, the presence of spalling, corrosion, and efflorescence of concrete was observed. Inspection of joints revealed the presence of debris, motor oil, and efflorescence.

## 2.2 *Bond Pull-Off Tests*

Girders G1 and G23 were selected as locations for pull-off tests because they had more exposure to moisture from the rain and water draining from the deck than other girders. Pull-off tests were conducted on the locations where CFRP was bonded and away from the edges of the girders. A 57 mm diamond-coated core saw was used to drill approximately 4 mm into the concrete through the CFRP. The test surface was sanded to remove the paint and cleaned with alcohol before attaching the pucks. Tests were conducted on the following week according to ASTM D7522 (2015) using a Proceed adhesion tester. The load was applied at the rate of 13 kPa/s until failure. Maximum failure load, failure mode, and photographs of all the pucks after the tests

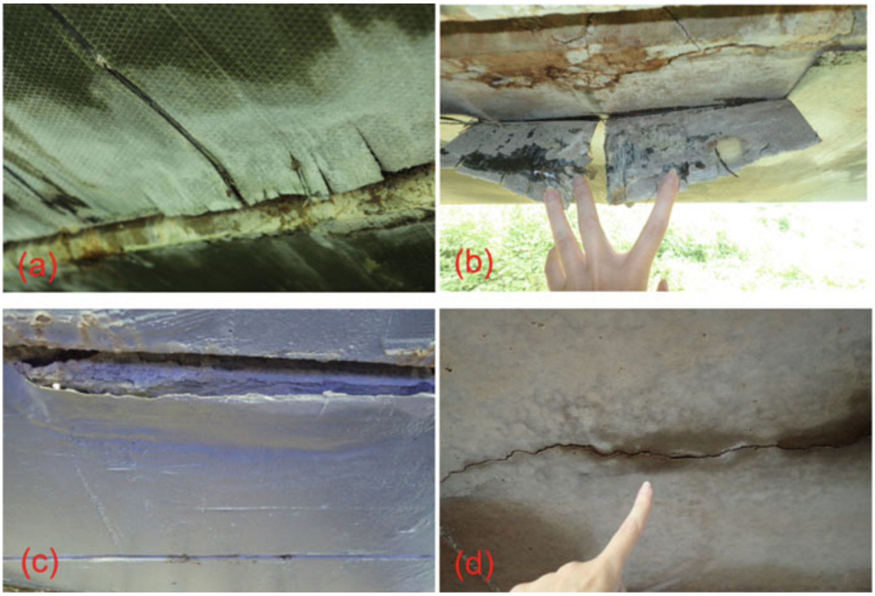

**Fig.3** **a** Debonding, discoloration, and damage to the CFRP, **b** Debonding and damage to CFRP and concrete, and **d** Cracking of concrete girder G8

were recorded. Failure modes were evaluated according to ASTM D7522 (2015), where five types of failures are defined: (1) bonding adhesive failure—Mode A, (2) cohesive failure in FRP laminate—Mode B, (3) adhesive failure at FRP/adhesive interface—mode C, (4) cohesive failure in adhesive—mode D, and (5) adhesive failure at FRP concrete interface—mode E.

Failure loads on G1 varied from 2.2 to 2.86 MPa. All the tests conducted on this girder resulted in Mode B failure—failure of the composite (Fig. 4a). Significant variation in pull-off bond strength values of G23 was observed. Failure load varied from 0.95 to 4.4 MPa. All failure modes on this girder were Mode E—failure at FRP/concrete interface (Fig. 4b). Since initial pull-off test results at the time of installation of the original FRO were not available, quantitative analaysis of bond

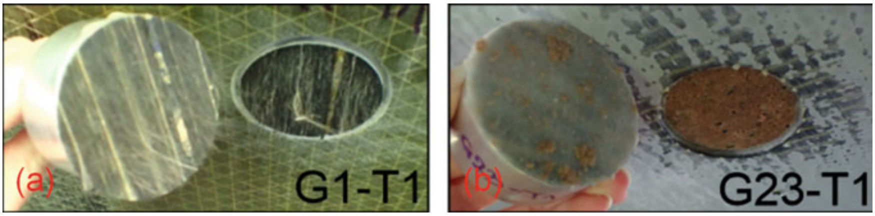

**Fig. 4** Two failure modes were observed: **a** Mode B on girder 1, **b** Mode E on girder 23

**Table 1** Pull-off test results-Foulk Road bridge

| Label | Bond strength (MPa) | Failure mode | Failure mode | Interpretation of failure mode |
|---|---|---|---|---|
| G23-T1 | 0.95 | E | Epoxy failure at FRP/concrete interface | Indicates poor adhesion between epoxy and concrete which could be due to inadequate surface preparation, improper installation, and environmental degradation |
| G23-T2 | 1.33 | | | |
| G23-T3 | 4.39 | | | |
| G1-T1 | 2.44 | B | Cohesive failure in FRP laminate | Indicates that the out-of-plane strength of the composite is lower than the strength of concrete, epoxy adhesive, and epoxy/concrete interface. This failure mode is rarely observed and points out to possible degradation of the composite |
| G1-T2 | 2.82 | | | |
| G1-T3 | 2.15 | | | |

strength was not possible. Therefore, pull-off test results are analyzed only from the standpoint of bond quality requirements recommended in the ACI 440.2R (2017).

The pull-off bond strength of CFRP repairs on G1 (Table 1) was considerably above the minimum value of 1.37 MPa specified by ACI 440.2R (2017) Cohesive failure of the composite (mode B) that occurred on G1 is rarely observed and it indicates incomplete saturation or environmental degradation. Pull-off bond strength at two of three tested locations on girder G23 was lower than recommended in the design guide—1.37 MPa. Additionally, failure Mode E indicates that bond strength is lower than the strength of the composite or concrete. This type of failure is identified as an undesirable failure. Possible causes of epoxy failure at FRP/concrete interface are inadequate surface preparation, use of an unsuitable type of epoxy, incomplete epoxy curing, or environmental degradation.

# 3 Laboratory Testing

## 3.1 *Differential Scanning Calorimetry*

Differential scanning calorimetry (DSC) was conducted to detect a potential effect of the environment on the glass transition temperature ($T_g$) of the CFRP after 26-year service life and to examine if any difference exists between new and old repairs. The glass transition is the temperature range over which polymers change from a hard and rigid state to a more flexible, rubbery state, which results in decreased strength and stiffness. This is the reason why design specifications define the maximum service temperature for CFRP strengthened structures. According to ACI 440.2R, the $T_g$ of the composite system should be at least 15 °C higher than the service temperature to ensure that the load capacity of the strengthened structural member is not reduced during their service life. American Association of State Highway and Transportation Officials guide specifications (AASHTO-FRPS-1 2010) are more conservative recommending that $T_g$ is at least 22 °C higher than the maximum design temperature. The presence of moisture and chemical degradation can reduce the $T_g$ and their effects on $T_g$ should be evaluated and taken into account for the safe application of CFRP.

Three replicate samples, weighing between 5 and 20 mg from girders 1, 2, and 23 were tested on TA instruments Netzsch DSC (Selb, Germany). The tests were performed under nitrogen atmosphere, using a 10 °C/min ramp rate from –20 to 250 °C. The $T_g$ was evaluated by NETZSCH Proteus TA software and according to ASTM E1356 (2008). Reported $T_g$ is the midpoint temperature as defined in ASTM E1356.

Measured $T_g$ for three girders is presented in Fig. 5. The highest $T_g$ measured on the older repairs was only 51.4 °C, and it was significantly lower compared to G23 where $T_g$ of 65 °C was observed. To evaluate if 26-year environmental exposure had any effect on the $T_g$, its initial values are required. There is little information about

**Fig. 5** Glass transition temperature measured on samples from girders G1, G2, and G23

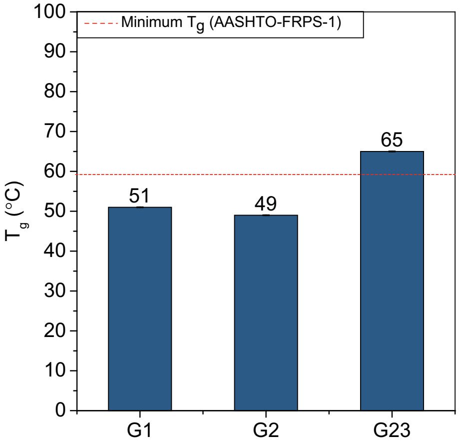

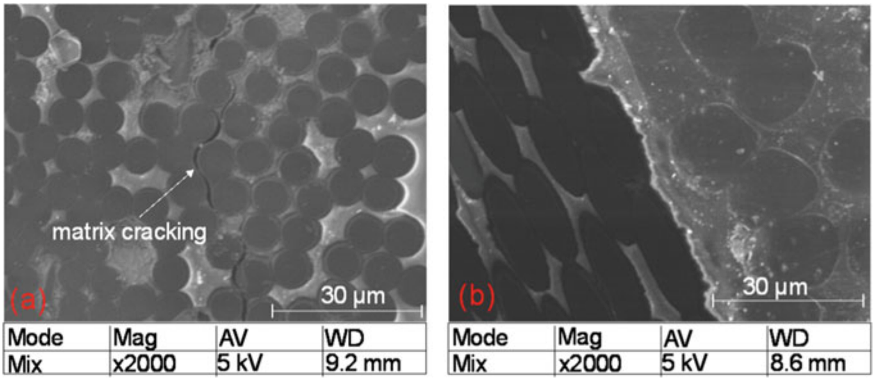

**Fig. 6** SEM images of CFRP collected from **a** Girder G1, **b** Girder G2

the used resin, most likely it was Tonen-manufactured FR-E3P (Naaman et al. 1997). Some reports indicate that the $T_g$ of this resin cured at room temperature is 51 °C (Naaman et al. 1997; Saito 1998). If it is assumed that this was the initial $T_g$ value of the CFRP, environmental exposure had minimal effect. However, a low value like this is considered to be unsatisfactory, considering that the maximum design temperature for concrete bridges in Delaware is 37 °C (AASHTO 2017).

## *3.2 Scanning Electron Microscopy (SEM)*

CFRP material microstructure was analyzed using a Hitachi TM-3000 scanning electron tabletop microscope. The cross-sectional area of the CFRP samples was sanded using silicon carbide grinding paper and afterward polished with alumina suspension. The observation has been done in secondary electron mode, backscattering mode, and mixed-mode, at an accelerating voltage of 5 kV. Samples were examined at low and high magnification. Typical SEM images showing a cross-section of the samples extracted from G1 and G23 are shown in Fig. 6.

Significant matrix cracking can be seen at the fiber/matrix interface in the CFRP sample from girder G1 (Fig. 6). Previous research has shown that the interface between the fiber and matrix is the most probable location for crack initiation due to its relative weakness. This type of failure is considered to be one of the most significant damage mechanisms in composites exposed to static and/or cyclic loading. It results in stiffness reduction and eventually failure of the composite through merging of multiple cracks. No evidence of damage was observed in the sample from girder G23 (Fig. 6b).

## 4 Summary and Conclusions

Evaluation of CFRP repairs installed on Foulk Road Bridge (Wilmington, DE) was conducted to provide information on the durability performance of CFRP after being in service for approximately 26 years. The condition of the repairs was assessed through visual inspection, pull-off bond tests, and laboratory testing of material samples collected from the bridge. Laboratory testing included thermal analysis, spectroscopy, and microscopic observations to determine potential physical and chemical degradation due to long-term environmental exposure. Based on the field and laboratory evaluation of Foulk Road bridge CFRP composite repairs, the following conclusions may be made:

- The presence of FRP damage, debonding, discoloration, insufficient matrix saturation, and water stains were observed on repairs installed in 1994 on girders 1 to 6. CFRP repairs of girders G7 through G23 appear to be in visually good condition. Based on the condition of some girders (Fig. 3 b, c), it can be inferred that installing CFRP as a replacement for transverse reinforcement did not prevent the cracking of the girders.
- Pull-off tests on girder 1, repaired in 1994, indicate good bond strength according to ACI 440.2R recommendations—bond strength significantly higher than 1.37 MPa. However, the inadequate failure mode of the composite indicates that the adhesive, adhesive/concrete bond, and concrete have greater strength than the composite itself. Undesirable failure mode at the CFRP/concrete interface and low bond strength was observed on girder G23, repaired with newer bidirectional CFRP.
- $T_g$ of 50 °C, measured on CFRP installed in 1994 was lower than the minimum value recommended by ACI 440.2R (2017) Higher $T_g$ values of 65 °C measured on newer bidirectional CFRP satisfy the minimum recommended temperature.
- SEM images display matrix cracking at the fiber/matrix interface in CFRP installed in 1994. No signs of degradation were noticed in the bidirectional CFRP sample.

## 5 Future Work

Demonstration projects that included CFRP installation on two steel bridges conducted by the University of Delaware in the early 2000s (Chajes et al. 2003; Miller et al. 2001) will be the focus of future research. This will include visual inspection, materials, and bond characterization. Planned tensile tests of the CFRP composite collected from Foulk Road Bridge, after being in service for 26 years, will help to refine existing environmental reduction factors. In design practice, environmental effects on the composite are considered through environmental knock-down factors on FRP design tensile strength. Collected data will be compared to a database consisting of laboratory durability data and data from other field studies to develop design recommendations.

**Acknowledgements** This work was supported by the sub-award no. 5903-UD-DOT-7103 to the University of Delaware by the United States Department of Transportation—Center for Integrated Asset Management for Multimodal Transportation Infrastructure Systems at the Pennsylvania State University (Federal Grant No. 69A3551847103). The authors thank the Delaware Department of Transportation for providing access to the bridge. Any opinions, findings, conclusions, or recommendations expressed in this paper are those of the authors and do not necessarily reflect the views of the United States Department of Transportation or the Delaware Department of Transportation.

## References

AASHTO-FRPS-1 (2010) Guide specifications for design of bonded FRP systems for repair and strengthening of concrete bridge elements. American Association of State Highway and Transportation Officials, Washington, DC

AASHTO (2017) AASHTO LRFD bridge design specifications. American Association of State Highway and Transportation Officials, Washington, DC

ACI 440.2R (2017) Guide for the design and construction of externally bonded frp systems for strengthening concrete structures. American Concrete Institute, Farmington Hills

ASTM D7522 (2015) Standard test method for pull-off strength for FRP laminate systems bonded to concrete substrate. ASTM International, West Conshohocken

ASTM E1356 (2008) Standard test method for assignment of the glass transition temperatures by differential scanning calorimetry. ASTM International, West Conshohocken

Attanayake U, Aktan H (2017) Reflective cracking between precast prestressed box girders (0092):1–2

Chajes MJ, Karbhari VM, Mertz DR, Kaliakin VN, Faqiri A (1993) Rehabilitation of cracked adjacent concrete box beam bridges. In: Symposium on practical solutions for bridge strengthening and rehabilitation, pp 265–274

Chajes M, Swinheart M, Richardson D, Wenczel G (2003) Bridge Rehabilitation using advanced composites: Ashland bridge SR-82 over Red Clay Creek. In: Proceedings of the 10th international conference and exhibition-structural faults and repair conference, London

Federal Highway Administration (2018) Adjacent box beam connections: performance and optimization. FHWA Publication No.:FHWA-HRT-17–094

Finch W (1997) Investigation of bonding advanced composite materials to concrete with an application in bridge rehabilitation. PhD dissertation

Miller TC, Chajes MJ, Mertz DR, Hastings JN (2001) Strengthening of a steel bridge girder using cfrp plates. J Bridge Eng 6(6):514–522

Naaman A, Park SY, Lopez M, Stankiewicz P (1997) RC-1355 - glued-on fiber reinforced plastic (FRP) sheets for repair and rehabilitation

Saito M (1998) United States Patent-Method of reinforcing concrete slabs

# Experimental Testing of GFRP-Reinforced Concrete Beams with Mid-Span Lap Splices Utilizing Straight- and Hooked-End Bars

**Omar Nour, Osama Salem, and Ahmed Mostafa**

## 1 Introduction

The bond strength of glass fiber-reinforced polymers (GFRP) bars with concrete is a crucial topic that many researchers extensively investigated. Forces in reinforced concrete structural elements are transferred mainly by the bond developed between the reinforcing bars and concrete. In a study conducted by Tighiouart et al. (1999), it was found that the dominant failure mode of the tension lap splice of GFRP bars is splitting. Aly et al. (2006) found that the bond strength along the bar splice length was inversely proportional to the splice length and bar diameter. A study conducted by Choi et al. (2012) concluded that bond stresses were not uniformly distributed along the splice length. In the latter study, it was also concluded that increasing the splice length from thirty-times the bar diameter ($d_b$) to sixty-times the bar diameter would increase the beam failure moment by 37%, yet the increase of the splice length to sixty-times the bar diameter did not satisfy the minimum required moment-resisting capacity of a concrete beam reinforced with continuous bars. Additionally, Choi et al. (2014) found that concrete beams with splice lengths of forty-five times the bar diameter and seventy-five times the bar diameter ($d_b$) achieved 65% and 83% of the flexural strength of a similar beam but with no splice, respectively. Esfahani et al. (2013) concluded that ACI440.1R-15 (ACI 2015) overestimates the bond strength. In the studies conducted by Esfahani et al. (2013) and Rakhshanimehr et al. (2014), it

---

O. Nour · O. Salem (✉) · A. Mostafa
Department of Civil Engineering, Lakehead University, 955 Oliver Road, Thunder Bay, ON P7B 5E1, Canada
e-mail: sam.salem@lakeheadu.ca

O. Nour
e-mail: onour@lakeheadu.ca

A. Mostafa
e-mail: amostafa@lakeheadu.ca

B. Benmokrane et al. (eds.), *8th International Conference on Advanced Composite Materials in Bridges and Structures*, Lecture Notes in Civil Engineering 267,
https://doi.org/10.1007/978-3-031-09409-5_12

was found that using stirrups along the bar splice length increased the bond strength and ductility of GFRP-reinforced beams. Harajli and Abouniaj (2010) reported that the bond strength with concrete was dependent on the bar surface treatment. They also concluded that the confinement due to the use of stirrups along with the overall length of the splice had more considerable effects on the bond strength of the bars with relatively high ribs or more surface deformations.

Nevertheless, it was found that increasing the lap splice length of GFRP reinforcing bars would not be beneficial after a certain length. Thus, it is more efficient to adopt an alternative approach to enhance the bar bond strength with concrete, such as bar end anchorage. Different bar end anchorage techniques have been investigated using headed end, 90° bent bars, and 180° hooked bars. Ehsani et al. (1996) concluded that bent bars were considerably effective in pull-out tests. In another study carried out by Vint and Sheikh (2014), it was reported that all bent bar specimens that had bond strengths that meet CAN/CSA-S806-12 (CSA 2012) design standard requirements experienced 45% greater average bond strength compared to that of the straight-end bar specimens. In conclusion, it was found that bent bars would provide a greater pull-out failure load compared to that of straight-end bars and headed-end bars if bent bars have enough embedded length into the concrete.

## 2 Experimental Programme

As part of the experimental programme presented in this paper, four large-scale beams were tested to investigate the effects of bar end configuration on the ultimate flexural bending strength of concrete beams. All tested beams had mid-span GFRP reinforcement tension lap splices using straight- and hooked-end bars. The theoretical lap splice lengths using different standards were calculated and experimentally investigated in this study.

### *2.1 Test Specimens Design*

Four large-scale beam specimens were designed, fabricated, and then tested under four-point flexure bending. Beams were 2750 mm long with cross-sectional dimensions of 300 mm wide × 350 mm high. The beams had a clear span of 2200 mm and was subjected to two-point loads that were 1000 mm apart. Beams were reinforced with 20-mm diameter GFRP reinforcing bars along with 10-mm diameter steel stirrups that were distributed at 150 mm spacing along the entire length of the beam. A 60-mm thick concrete cover was used at the bottom, front, and back sides of the beam. Two of the four tested specimens had straight-end bar lap splices of 550 mm overall length, as shown in Fig. 1; while the other two specimens had 180-degree hooked-end bar lap splices of the same length, as shown in Fig. 2. Beam specimens with straight-end bar lap splices were designed as per CSA-S806-12 (CSA 2012).

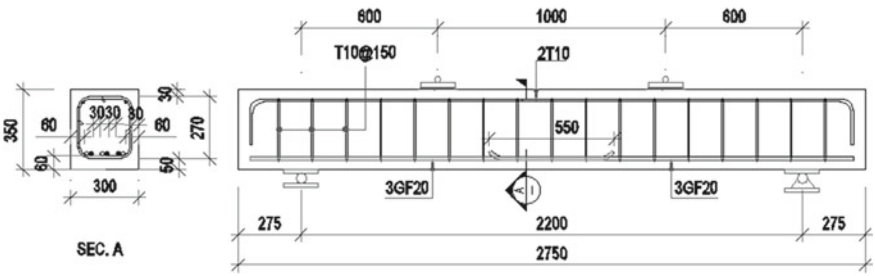

**Fig. 1** Reinforcement details of beam specimens with straight-end bar lap splices (SL-01 and SL-02)

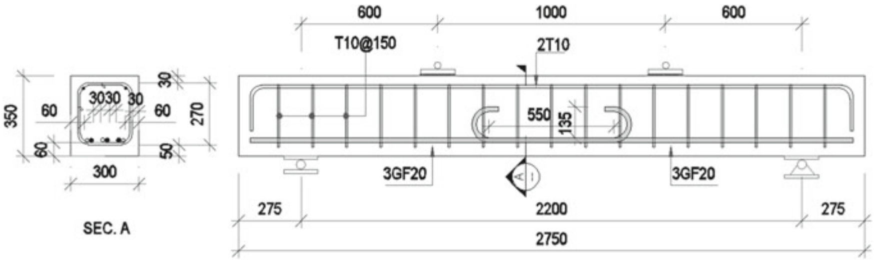

**Fig. 2** Reinforcement details of beam specimens with 180° hooked-end bar lap splices (HL-01 and HL-02)

## 2.2 Test Setup

Figure 3 shows a general test setup used for all beam specimens. The load was applied at two points, 1000 mm apart, on top of the beam specimen at a loading rate of 2 kN/min. The applied concentrated loads were then transferred to the concrete

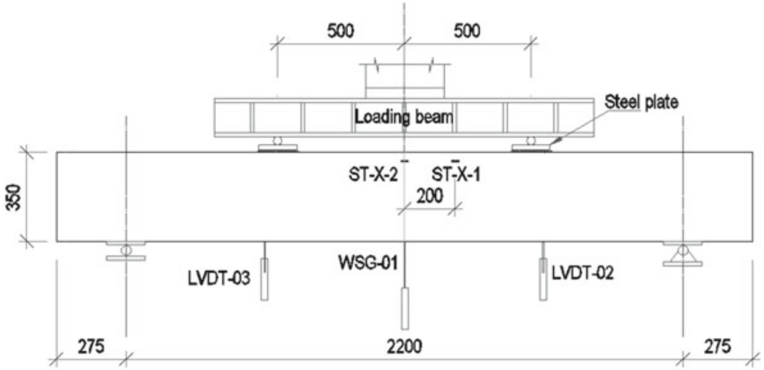

**Fig. 3** A general beam test setup with external instrumentation layout

beam's top surface over two steel plates resting on thick mortar layers to ensure smooth and leveled bearing surfaces. All beam specimens were simply supported. The beam vertical deflections were measured at three points as shown in Fig. 3.

# 3 Experimental Results

## 3.1 Cracking and Ultimate Moments of the Beams

Table 1 summarizes the experimental results of the four tested beams compared to their theoretical capacities calculated as per CSA-S806-12 (CSA 2012) and ACI440.1R-15 (ACI 2015). The calculated theoretical cracking moment for the tested beams were 20.65 and 21.39 kN.m as per CSA-S806-12 and ACI440-12, respectively, considering an average concrete compressive strength of 36.4 MPa. The cracking moment test results for all four concrete beams were greater than the theoretical cracking moment determined using CSA-S806-12 (CSA 2012) by approximately 20% on average. Also, the calculated lap splice length for the straight- and hooked-end bars as per the CSA-S806-12 requirement was 550 mm and 783 mm, respectively.

The theoretical beam resistance moment ($M_r$) was calculated at 82.5 and 121.3 kN.m as per CSA-S806-12 and ACI440.1R-15, respectively. The two beams with straight-end bar lap splices (SL-01 and SL-02) failed due to splitting at a beam mid-span moment of 89.1 and 86.7 kN.m, respectively. The experimental failure moments of the beam specimens with straight-end bar lap splices were 5% to 8% larger than the theoretical values calculated using CSA-S806-12 equations, and 26% to 28% lower than the theoretical capacity of the beam calculated as per ACI440.1R-15. The two beams with hooked-end bar lap splices failed due to concrete crushing inside the 180-degree bent hooks. Beams (HL-01 and HL-02) failed at ultimate bending moments (Mu) of 120.8 and 130.3 kN.m, respectively. The experimental moment values were 46% to 58% more than the theoretical capacity determined by CSA-S806-12 equations. The experimental results of the two beams with hooked-end bar lap splices were in good agreement with the theoretical moment estimated using ACI4401R-15 equations. It is important to notice that the ultimate moment based on the experimental test was achieved using a hooked-end bar lap splice with an overall length of 783 mm when the required lap splice length according to ACI 440.1R-15 (ACI 2015) is 1350 mm to achieve the same ultimate moment.

## 3.2 Cracking and Failure Modes

The concrete cover was removed to further investigate the failure modes of the beams and examine the reinforcing bars after failure. Figure 4a and b show the failure modes

**Table 1** Summary of experimental test results of concrete beams with straight- and hooked-end bar lap splices

| Beam ID | Test results | | CSA-S806-12 (CSA 2012) | | | | ACI440.IR-15 (ACI 2015) | | | |
|---|---|---|---|---|---|---|---|---|---|---|
| | $M_{cr}$ kN.m | $M_u$ kN.m | $M_{cr}$ kN.m | $M_{cr}$ (Exp.) /$M_{cr}$(Theo.) | $M_r$ kN.m | $M_f$ (Exp.) /$M_r$(Theo.) | $M_{cr}$ kN.m | $M_{cr}$ (Exp.) /$M_{cr}$(Theo.) | $M_r$ kN.m | $M_f$ (Exp.) /$M_r$(Theo.) |
| **SL-01** | 26.1 | 89.1 | 20.6 | 1.26 | 82.5 | 1.08 | 21.4 | 1.22 | 121.0 | 0.74 |
| **SL-02** | 25.4 | 86.7 | | 1.28 | | 1.05 | | 1.19 | | 0.72 |
| **HL-01** | 21.9 | 120.8 | | 1.06 | | 1.46 | | 1.02 | | 1.0 |
| **HL-02** | 25.8 | 130.3 | | 1.25 | | 1.58 | | 1.20 | | 1.07 |

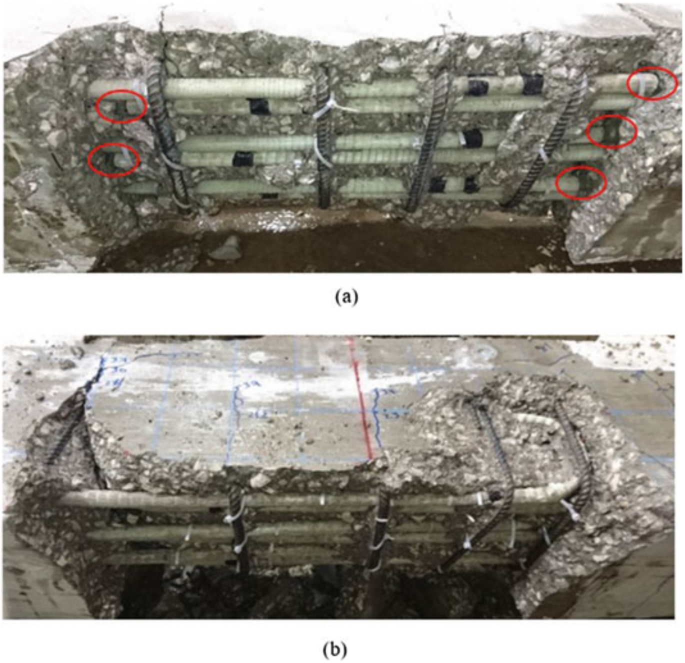

**Fig. 4** Concrete beams failure modes: **a** Beams with straight-end bar lap splices, **b** Beams with hooked-end bar lap splices

of one of the beams with each bar end configuration. For the beams with straight-end bar lap splices, there was no rapture or peeling of the surface of the spliced bars, however, the slippage of all six spliced bars was visible after the removal of the concrete cover as shown in Fig. 4a. Cracks were mainly located at the location of the stirrup that coincided with the end of the spliced bars. Whereas for the beams with hooked-end bar lap splices, large splitting cracks occurred at the external bent side of the hooks. In addition, a few other cracks developed along the beam length at the locations of the stirrups. It is noteworthy that the main failure mode of the concrete beams having hooked-end bar lap splices was found to be similar to that of the beams with hooked-end steel bar lap splices, as reported by Minor and Jirsa (1975).

## 3.3 Moment-Deflection Relationships

The moment versus mid-span deflection relationship of beam SL-02 is shown in Fig. 5. Figure 6 represents the same relationship but for beams HL-01 and HL-02 using the mid-span deflections measured by the displacement transducer labelled WSG-1 (refer to Fig. 3). From both Figs. 5 and 6, all beams experienced relatively

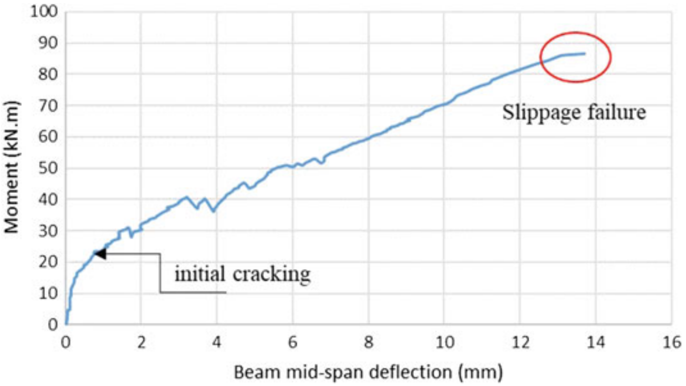

Fig. 5 Moment-deflection curve for beam (SL-02)

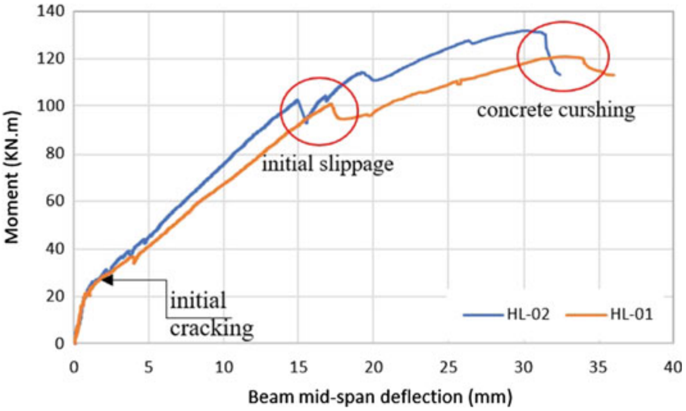

Fig. 6 Moment-deflection curves for beams (HL-01 and HL-02)

linear behavior until concrete cracking with very small mid-span deflections. As more cracks developed in the beams, slight but sudden drops in the applied loads were experienced. It should be noted that the maximum mid-span deflection for beam SL-02 was approximately 13.8 mm, while the average maximum mid-span deflection for the beams with hooked-end bars was 32.5 mm, which is more than double the deflection of the beams with straight-end bar lap splices. It is also noticed that the hooked-end bar spliced beams showed more ductile behavior compared to that of the straight-end bar spliced beams.

## 4 Conclusions

Four large-scale GFRP-reinforced concrete beams were experimentally examined until failure. Straight- and 180° hooked-end bars were utilized for the beam mid-span bar lap splices. The theoretical beam moment-resiting capacities and corresponding theoretical lap splice lengths were calculated using CSA S806-12 (CSA 2012) and ACI440.1R-15 (ACI 2015) design standards. Test results show that the use of GFRP bars with 180° hooked ends for the lap splices increases the beam's ultimate moment capacity and ductility compared to those for similar beams but with straight-end bar lap splices. It is also noticed that the bar lap splice equation included in the ACI440.1R- 15 (ACI 2015) design standard overestimates the lap splice length required if hooked-end bars were to be used for bar lap splices.

**Acknowledgements** This research project was funded using an NSERC SRC-Research Grant awarded to the second author by Lakehead University. Any opinions, findings, conclusions, or recommendations are those of the authors and do not necessarily reflect the views of the sponsoring parties. The authors would like to thank the former FRP manufacturer (TemCorp Industries Inc.) for the in-kind contribution and for providing all the GFRP bars used in fabricating all specimens tested in this study. Thanks are also extended to Harris Rebar Company (Thunder Bay branch) for its in-kind contribution and for providing the steel rebar required for all test specimens.

## References

ACI Committee 440 (2015) Guide for the design and construction of structural concrete reinforced with fiber-reinforced polymer (FRP) bars (ACI440.1R-15). Am Concr Inst 22

Aly R, Benmokrane B, Ebead U (2006) Tensile lap splicing of frp reinforcing bars in concrete. ACI Struct J 103(6)

Choi DU, Chun SC, Ha SS (2012) Bond strength of glass fibre-reinforced polymer bars in unconfined concrete. Eng Struct 34:303-313

Choi YC, Cho KH, Bae B, Choi HK (2014) Experimental study on the performance of tensile lap-spliced GFRP rebars in concrete beam. Mag Concr Res 66(24):1250-1262.

CSA (2012) Design and construction of building structures with fibre-reinforced polymers CAN/CSA S806–12. Canadian standards association, Mississauga, Ontario, Canada.

Ehsani MR, Saadatmanesh H, Tao S (1996) Design recommendations for bond of GFRP rebars to concrete. J Struct Eng 122(3):247–254

Esfahani MR, Rakhshanimehr M, Mousavi SR (2013) Bond strength of lap-spliced GFRP bars in concrete beams. J Compos Constr 17(3):314–323

Harajli M, Abouniaj M (2010) Bond performance of GFRP bars in tension: experimental evaluation and assessment of aci 440 guidelines. J Compos Constr 14(6):659–668

Minor J, Jirsa JO (1975) Behavior of bent bar anchorages. ACI J Proc 72(4):141–149

Rakhshanimehr M, Esfahani MR, Kianoush R, Mohammadzadeh BA, Mousavi SR (2014) Flexural ductility of reinforced concrete beams with lap-spliced bars. Can J Civ Eng 41(7):594–604

Tighiouart B, Benmokrane B, Mukhopadhyaya P (1999) Bond strength of glass FRP rebar splices in beams under static loading. Constr Build Mater 13(7):383–392

Vint L, Sheikh S (2014) Investigation of bond properties of alternate anchorage schemes for glass fiber-reinforced polymer bars. ACI Struct J 112(1):59–68

# Bond Behaviour of FRP Shear Reinforcement on I-Sections

**Muhammad Arslan Yaqub, Stijn Matthys, and Christoph Czaderski**

## 1 Introduction

Over the past three decades, fibre reinforced polymers (FRP) have been used for the strengthening of concrete structures in different configurations. With their main advantages of high-strength-to-weight ratio, corrosion resistance, stiffness which may be tailored to the design requirements and easy application, they have emerged as an effective and efficient repair material (fib 2019). As externally applied reinforcement (EAR), FRP strips can be used for flexural and shear strengthening of beams and slabs, confinement of columns and beam-column joints for both static as well as seismic capacity enhancement in buildings, bridges and other reinforced concrete structures.

FRP shear reinforcement is usually applied in U-shape onto the webs of the beams in the form of continuous or discrete strips. This FRP shear reinforcement when applied to the I-sections (along their shape) is comparatively less efficient when compared to their rectangular counterparts. This is due to the specific shape of the I-sections where FRP strips are susceptible to debonding around the web–flange interface. This phenomenon has been observed in various researches and different techniques such as patch anchors (Hutchinson 2000), mechanical anchors

---

M. A. Yaqub (✉) · S. Matthys
Department of Structural Engineering and Building Materials, Magnel-Vandepitte Laboratory,
Ghent University, Technologiepark-Zwijnaarde 60, 9052 Ghent, Belgium
e-mail: MuhammadArslan.Yaqub@UGent.be

S. Matthys
e-mail: Stijn.Matthys@UGent.be

C. Czaderski
Empa, Swiss Federal Laboratories for Materials Science and Technology, Überlandstrasse 129,
8600 Dübendorf, Switzerland
e-mail: Christoph.Czaderski@empa.ch

B. Benmokrane et al. (eds.), *8th International Conference on Advanced Composite Materials in Bridges and Structures*, Lecture Notes in Civil Engineering 267,
https://doi.org/10.1007/978-3-031-09409-5_13

(Murphy et al. 2012) and spike anchors (Garcia et al. 2018) were used to increase the efficiency of the FRP shear reinforcement on I-sections. These developed techniques have different limitations (as mentioned in the relevant studies) when applied to the thin webbed I-sections and the optimum solution is still needed.

This paper discusses a new test setup designed to study the early debonding of the FRP around the concave corners of the reinforced concrete I-sections. The investigation also includes the performance of continuous FRP spike anchors to delay the debonding of the FRP shear reinforcement. Finally, available standard FRP shear design or predictions models (for rectangular sections) were used to check if they can predict the strains in the FRP and ultimate shear load in case of the I-sections. Only a small part of the comprehensive test scheme is presented in this paper.

## 2 Experimental Plan

The bond tests were performed on two I-sections strengthened with externally bonded carbon fibre reinforced polymers (CFRP) shear reinforcement. The reference I-section designated as I-NA-2-R represents the strengthening configuration where two CFRP layers were applied along the I-section geometry with no anchor (Fig. 1a). The second I-section designated as I-SA-2-R represents the strengthening configuration where two CFRP layers were applied along the I-section geometry with spike anchors installed at the web–flange interface to resist the debonding (Fig. 1b). This way, a comparison can be made in order to quantify the relative increase provided by the CFRP spike anchorage system.

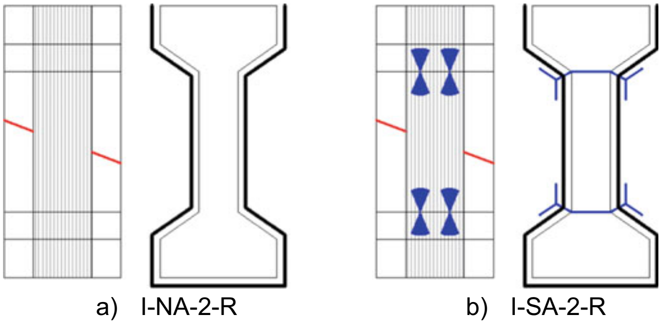

**Fig. 1** Shear strengthening configurations **a** without anchor and **b** with CFRP spike anchors

## 2.1 Specimen Preparation and Material Properties

Full-scale I-sections having a height of 700 mm were cast with a concrete strength of 62 MPa (average of the three reference cubes of 150 mm) as generally used in the construction of the prestressed concrete elements. The top and the bottom flange of the I-section were made symmetrical in order to simplify the geometry and to have an equal possibility of CFRP debonding at both the interfaces. The failure plane was made at an angle of 25° using the inclined steel plates welded to the threaded bars used to apply the load during the test. A stirrup of 6 mm rebar was also provided in the middle of the specimen. A detailed description of the specimen dimensions and test setup is given in Fig. 2. In the preceding tests, the specimens were pre-damaged across the crack plane in two pieces, that were aligned together again with the temporary steel plates on each side of the web and then EB CFRP was applied. In this way, the concrete and the stirrup contribution were already consumed and the applied load was only taken by the EB CFRP strips.

Two layers of 150 mm wide unidirectional CFRP sheets were applied consecutively. Over the first CFRP layer, thixotropic epoxy was applied in roof shaped

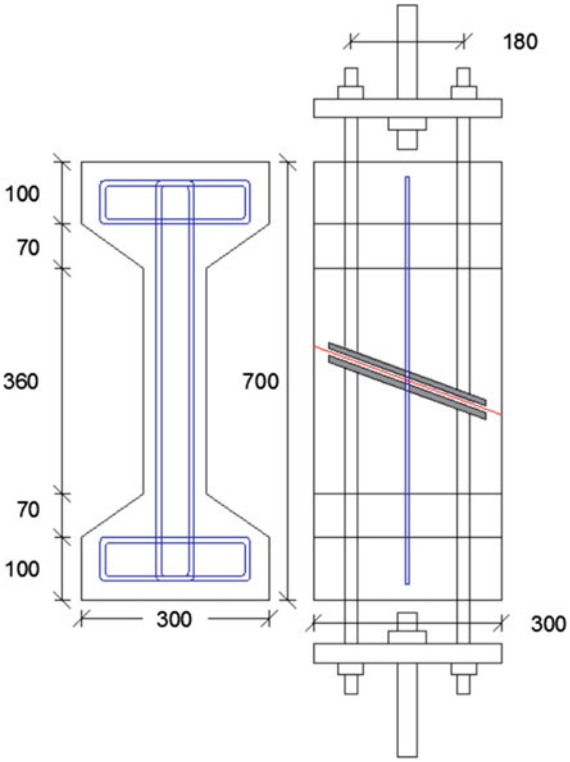

**Fig. 2** Specimen dimensions and test setup

**Table 1** Properties of CFRP sheets (defined by the manufacturer)

| Thickness (mm) | Areal weight ($g/m^2$) | Elastic modulus (GPa) | Tensile strength (MPa) | Ultimate strain (%) |
|---|---|---|---|---|
| 0.113 (1 layer) | 200 | 240 | 4400 | 1.8 |

profile along the length that was bonded onto the ground concrete substrate. Afterwards, high performance (two component) epoxy resin was used to saturate the top surface of the first layer over which the second layer was applied. Finally, the second layer was again saturated using the same epoxy resin over the top. Afterwards, resin impregnated continuous CFRP anchors as shown in Fig. 1b were installed into the predrilled holes, distributed into two equal halves and shaped into 30° fans in opposite directions were bonded to the web–flange interface. The properties (as defined by the manufacturer) of the CFRP sheets used are given in Table 1.

### 2.2 Test Setup and Instrumentation

The two threaded bars extending on top and bottom of the specimen were fixed to the 50 mm thick steel plates that were further fixed to another threaded bar through a hinge for loading as shown in Fig. 2. The specimen was fixed in the universal tensile test machine and the temporary steel plates holding the two halves of the I-section were cut. The load was applied using displacement controlled method at the rate of 0.01 mm/s. Linear variable displacement transducers (LVDTs) were mounted on both left and the right sides of the specimen to monitor the relative displacement of the two parts during the test. On the front side, 7 strain gauges were bonded on the CFRP laminate at the distance of 50, 130, 180, 350, 520, 570 and 650 mm from the top along the depth. On the rear side, a speckle pattern was applied to observe the strain variation in the CFRP laminate using Digital Image Correlation (DIC) technique. The instrumentation scheme is shown in Fig. 3.

## 3 Results and Discussion

### 3.1 Failure Mode

The specimen without the anchors (I-NA-2-R) failed by debonding of CFRP at the lower web–flange interface with a maximum load of 86 kN. The anchored specimen (I-SA-2-R) failed at a much higher load of 116 kN, with a mixed debonding and FRP fracture mode. One of the CFRP spike anchors ruptured at the corner of the drilled hole followed by the rupture and debonding of the CFRP sheet along the interface. The failure modes of both the specimens are shown in Fig. 4. Substrate cracks were

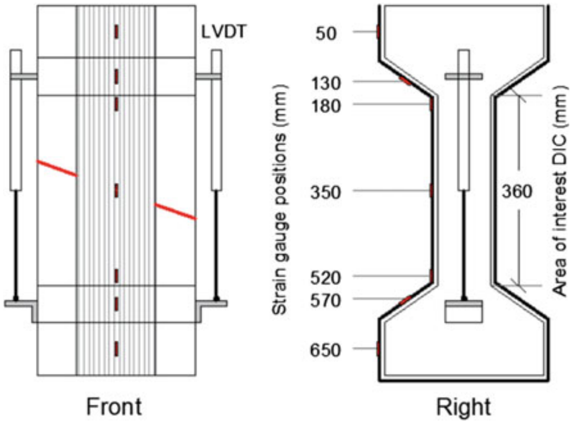

**Fig. 3** Instrumentation scheme


a) I-NA-2-R
b) I-SA-2-R

**Fig. 4** Failure mode of samples

also observed on the edges of the CFRP sheet near the failure plane which can also be seen in Fig. 6, depicting a good bond between the CFRP sheets and the concrete.

## 3.2 *Load Displacement and Strain Behaviour*

The displacement and the strain behaviour with respect to the load are shown in Fig. 5. Initially, in both the specimens, one side of the crack opens more compared to the other side, however, the magnitude of displacement is very small. Around 50 kN, the hinges balance the crack opening, and subsequently, the displacement trend

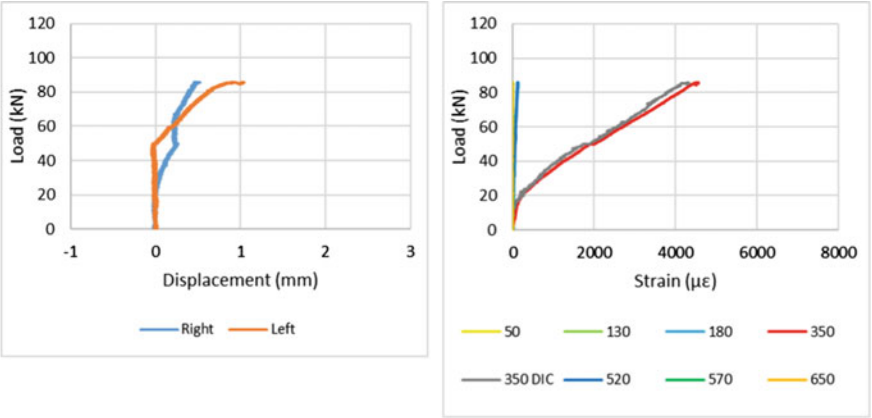

a) I-NA-2-R

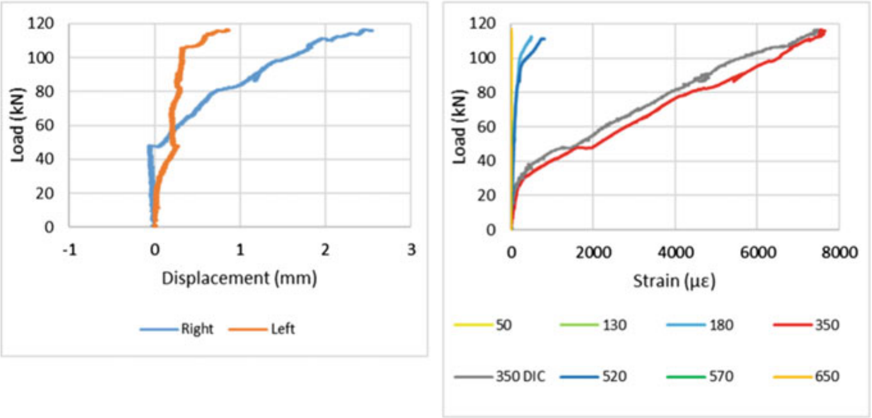

b) I-SA-2-R

**Fig. 5** Load displacement and strain behaviour

is in the same positive direction. The strains at the middle of the top (50 mm) and bottom (650 mm) flanges remained nearly zero (parallel to the vertical axis) in both the specimens. Similarly, there were no noticeable strains at the inclined halves of the top (130 mm) and the bottom (570 mm) flanges throughout the test. The strains at the web–flange interfaces (180 and 520 mm) started to develop near the failure, however, the magnitude was extremely small. The noticeable increase in strain was observed only in the vicinity of the main failure plane at the middle (350 mm). The specimen without the anchors reached 4540 με (Fig. 5a) which is 25% of the failure strain of CFRP used. Similarly, the specimen with the FRP spike anchors reached a total strain of 7477 με (Fig. 5b) which is 42% of the failure strain. This strain difference demonstrates the efficiency of CFRP spike anchors in improving the performance of CFRP shear reinforcement on I-sections.

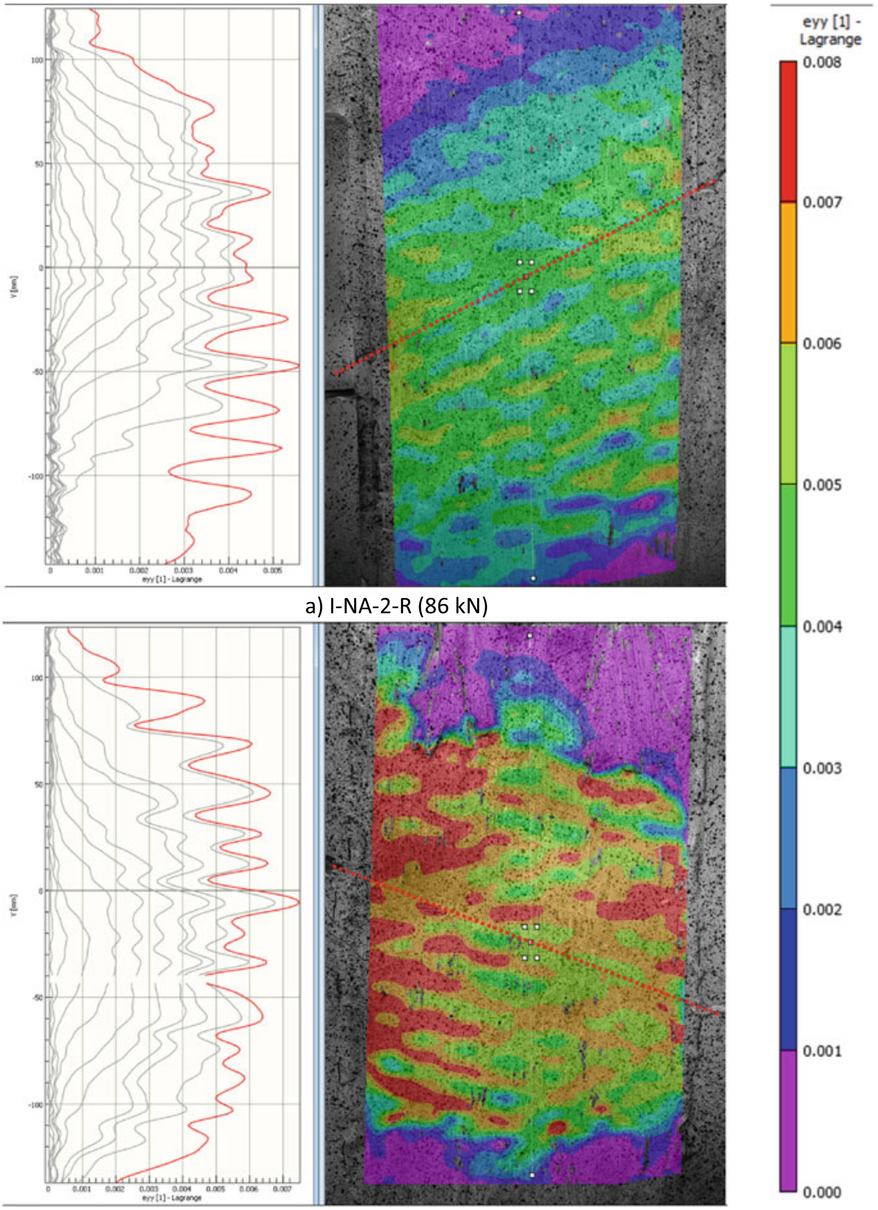

a) I-NA-2-R (86 kN)

b) I-SA-2-R (116 kN)

**Fig. 6** Strain contours from DIC

Figure 6 shows the strain contours recorded using the DIC technique with crack plane approximately in the middle near the failure load. It can be seen in case of the specimen without the anchors (Fig. 6a), that the strains are maximum over the inclined crack plane. At the higher load levels due to the bond degradation and cracks in the substrate, the strain gradually transfers from the middle to the web–flange interface, where the debonding occurred (lower side). The same phenomenon of strain transfer can be observed in the anchored specimen (Fig. 6b). However, CFRP spike anchors tightly bound the CFRP sheets over the interface with further increase in the laminate strains. The anchorage system held the CFRP strips together up to 35% additional shear load after which one of the spike anchors at the bottom interface failed due to the stress concentration at the drilled hole (not captured by the DIC).

## *3.3 Analytical Verification*

There are numerous analytical and empirical models available for the design and prediction of shear strength provided by externally bonded FRP reinforcement. However, the comparison among themselves has shown that they gave a lot of variations in prediction for the same data set. Murphy et al. (2010) concluded that these models may not be reliable for estimating the FRP shear contribution of members outside the range of the experimental tests from which they were calibrated. Most of these models have been developed for the rectangular cross sections and their application in case of complex shapes like I-sections is an open question, as they do not incorporate the efficiency reduction factors subject to the early debonding of the FRP at web–flange interfaces.

The standard models given in fib Bulletin 90 (fib 2019), fib Bulletin 14 (fib 2001) and ACI440 (ACI-440.2R 2017) have been used to check how close they predict the shear strength provided by the CFRP on I-sections. The strength reduction safety factors for CFRP were taken equal to 1 for prediction, so that the experimental values can be compared to the values from the models.

The failure of the unanchored shear strengthening configurations is mostly due to the debonding of the FRP strips. Therefore, fib B90 considers effective stress as a function of the bond stress, geometry of the strengthening configurations and the inclination of the shear crack. The empirical equations of B14 for effective strain calculation are based on the concrete strength and the stiffness of the FRP layers. Similarly, the ACI440 methodology involves a bond reduction coefficient for effective strain, that accounts for the concrete strength, FRP configuration and the stiffness of the laminate. The prediction values of strain and ultimate shear load in comparison to the experimental values are given in Table 2. It can be seen for the unanchored specimen that fib B90 and fib B14 predict the strains in the CFRP up to 90% and 95%, respectively, compared to the experimental observations. However, ACI440 overestimates the strains up to 128%. A similar trend can be seen in ultimate shear loads.

**Table 2** Prediction of strains and ultimate load in the CFRP

| Specimen | Strain ($\mu\varepsilon$) | | | | Ultimate load (kN) | | | |
|---|---|---|---|---|---|---|---|---|
| | I-NA-2-R | | I-SA-2-R | | I-NA-2-R | | I-SA-2-R | |
| Exp | 4540 | $\varepsilon_p$ / $\varepsilon_e$ | 7477 | $\varepsilon_p$ / $\varepsilon_e$ | 85.6 | $V_{f,p}$ / $V_{f,e}$ | 116.6 | $V_{f,p}$ / $V_{f,e}$ |
| fib B90 | 4100 | 0.90 | 6600 | 0.88 | 66.5 | 0.78 | 107.4 | 0.92 |
| fib B14 | 4300 | 0.95 | 8400 | 1.12 | 62.6 | 0.73 | 122.9 | 1.05 |
| ACI440 | 5800 | 1.28 | 13,500 | 1.80 | 93.6 | 1.10 | 229.7 | 1.97 |

The failure of the anchored configurations is mostly due to the rupture of the FRP or the failure of the anchorage systems. fib B90 considers the effective stress in case of anchored configurations equal to the effective stress in closed loop multiplied by the effectiveness coefficient based on the anchorage system used (maximum of 0.9). fib B14 assumes FRP rupture for the calculation in properly anchored configurations and an associated effective strain. ACI440 has no specific guidelines for the calculation of effective strains for anchored FRP shear configurations, therefore, for this study, closed loop was assumed to calculate the effective strain in the FRP. The effective strain design limits of 0.006 and 0.004 given in fib B14 and ACI440, respectively, to maintain the aggregate interlock was not considered for calculations in this study. For the anchored configurations, it can be seen in Table 2 that fib B90 estimates the effective strain equal to 88% of the experimental value. fib B14 and ACI440 overestimate the effective strains up to 112% and 180%, respectively. These values are indicative of the I-sections given the shear crack is in the middle of the web (bonded length on both sides was greater than the effective length) as in this study. However, the efficiency of the system will sufficiently decrease if the crack grows closer to the web–flange interface.

## 4 Conclusions

Shear strengthening of I-sections with FRP demands careful attention and detailing, as the FRP strips are susceptible to debonding near the web–flange interface. The choice of the anchorage system to control the FRP debonding is critical. For the present study, FRP spike anchors installed at the web–flange interface increased the ultimate shear load up to 35%. The standard models for shear strength provided by the FRP as developed and used for rectangular sections cannot be applied directly to complex shapes such as I-sections. These models do not incorporate capacity reduction factors to account for the early debonding of the FRP strips at the web–flange interface. The standard models for FRP shear design and prediction as used for I-sections, in this study, are indicative of this special situation and the performance of the FRP shear reinforcement will sufficiently decrease if the shear crack grows near the web–flange interface.

## References

ACI-440.2R (2017) Guide for the design and construction of externally bonded FRP systems for strengthening concrete structures. American Concrete Institute, Farmington Hills, MI, USA

fib (2001) Externally bonded FRP reinforcement for RC structures. In: Bulletin, vol 14. International Federation for Structural Concrete, Lausanne, Switzerland, pp 138

fib (2019) Externally applied FRP reinforcement for concrete structures. In: Bulletin, vol 90. International Federation for Structural Concrete, Lausanne, Switzerland

Garcia JE, Satrom CN, Jirsa JO, Ghannoum WM (2018) Shear strengthening of concrete girders using carbon fiber-reinforced polymer sheets and anchors. ACI Struct J 115(4):1165–1173. https://doi.org/10.14359/51702234

Hutchinson RL (2000) The use of externally bonded CFRP sheets for shear strengthening of I-shaped prestressed concrete bridge girders. PhD Thesis, University of Manitoba, Canada

Murphy M, Belarbi A, Bae SW (2012) Behavior of prestressed concrete I-girders strengthened in shear with externally bonded fiber-reinforced-polymer sheets. Pci J 63–82

Murphy M, Belarbi A, Kuchma D (2010) Shear design equations for concrete girders strengthened with FRP. In: 5th International Conference on FRP Composites in Civil Engineering; Beijing, China. p 767–771

# A Review on Properties of Carbon Nanofibre Infused Ultra-High-Performance Fibre Reinforced Concrete

**Marwa Ibrahim and Raafat El-Hacha**

## 1 Introduction

Any strengthening or new construction material shall conform to some standards and minimum requirements. These standards are concerned with durability, mechanical strength, bond properties, efficiency, execution time and cost, and lifecycle maintenance cost. Unfortunately, meeting these requirements using ordinary construction materials become more challenging when the structure features a complex design, that is irregular or subjected to harsh environmental conditions. For this reason, the industry of construction materials is continuously advancing and upgrading the available construction products to become the perfect fit for these challenging situations. This paper is concerned with a new generation of exceptional materials named Ultra-High-Performance Fibre Reinforced Concrete (UHPFRC) infused with Carbon Nanofibres (CNF). Therefore, a literature review of the relevant previous studies on CNF-UHPFRC is herein presented with emphasis on both mechanical and durability properties.

---

M. Ibrahim (✉) · R. El-Hacha
Civil Engineering Department, University of Calgary, 2500 University Dr. NW, Calgary, AB, Canada
e-mail: marwa.ibrahim@ucalgary.ca

R. El-Hacha
e-mail: relhacha@ucalgary.ca

B. Benmokrane et al. (eds.), *8th International Conference on Advanced Composite Materials in Bridges and Structures*, Lecture Notes in Civil Engineering 267,
https://doi.org/10.1007/978-3-031-09409-5_14

# 2 Definitions

## *2.1 Ultra-High-Performance Fibre Reinforced Concrete*

Ultra-High-Performance Fibre Reinforced Concrete is a special purpose cementitious material with enhanced compressive strength (>150 MPa) and a sustained post-cracking tensile strength (>5 MPa).

### 2.1.1 Compressive Strength

The material's notable high compressive strength is attributed to the removal of coarse aggregates from the mix, usage of low water-to-cement content, and incorporation of admixtures.

The interfacial link between aggregates and cement paste, termed as Transition Zone (TZ), is the weakest region in concrete. It is there where the stress is concentrated and cracking is initiated. As a result, the removal of aggregates elevates the material's strength by reducing the TZ region. Thus, UHPFRC has a more linear stress–strain relationship. Similarly, the removal of coarse aggregates improves the mix grading, which decreases the microcracks' size (Aïtcin and Flat 2015). It also densifies the particle packing in UHPFRC and lowers the matrix's permeability (Sbia et al. 2014). On the other side, using a low water-to-cement ratio increases the compressive strength by reducing the pore size and eventually increasing the binding between the hydration products and aggregates (Al-Osta 2018). Likewise, the usage of pozzolans such as fly ash increases the strength by reacting with the main hydration product in concrete, Calcium Silicate Hydrate (C-S–H) gel, to produce more of the latter. Having more binder quantities densifies the mix further and makes it stronger.

### 2.1.2 Tensile Strength:

The remarkable tensile strength increase is due to the inclusion of fibres in most mixtures, often high-strength steel fibres. They significantly increase the material's fracture toughness throughout its multiple energy-consuming mechanisms: crack bridging, fibre bending, and fibre pullout. Steel fibres absorb tensile stresses and improve the internal stress distribution in the member too. As a result, the material has an improved post-cracking ductility and possesses a steel-like high strain hardening behaviour under the uniaxial tension test. Also, reductions in pore size and microcracks size increase the material's tensile strength. This is because they are deemed as stress raisers where they concentrate stresses around their surfaces. Thus, their reduction leads to a more uniform stress distribution along the concrete matrix.

### *2.2 Carbon Nano fibre*

Carbon Nano fibres are graphite materials that enhance the crack resistance of the cementitious paste at low volume fractions while maintaining good fresh mix workability (Sbia et al. 2014). Its inclusion into the UHPFRC mix is still under study but is promising. This material has superior mechanical and electrical properties as its high tensile strength, high Young's modulus, and high conductivity. It is gaining a lot of research attention because of its good modification effect on concrete. This is attributed to its good flexibility, high specific surface area, high aspect ratio, and corrosion resistance (Wang et al. 2020). CNF's exposed edges also enhance the material's modification effect. They are carriers of high concentration active sites for the interaction with water molecules and bond formation with cement hydrates (Sbia et al. 2014). Although nanomaterials are usually of dimensions ranging from 1 to 100 nm, CNF is typically of 50–150 nm diameter and 50–100 µm length (Sharon 2021).

## 3 Mechanical and Durability Properties

Sbia et al. (2014) investigated the effect of CNF inclusion in UHPFRC. The authors utilized Polyacrylic Acid (PAA) to improve the nanomaterial's dispersion in the aqueous solution at a 0.1:1.0 polymer-to-nanomaterial weight ratio. However, they varied both CNF (60–150 nm diameter and 40–100 µm length) and steel fibre (175 µm diameter and 13 mm length) content. After performing a conical desirability analysis, they concluded that the most efficient system resulting in balanced gains comprises a moderate volume of copper-coated steel fibre and a low volume of CNF, 3.55% and 0.145% by volume of anhydrous cementitious materials, respectively.

The mixing procedure consisted of introducing the CNF, water, and PAA at the abovementioned weight ratio and continuously stirring for 12–15 h. The resultant mix is then sonicated at 40, 50, 65, and 75% of the maximum used power with a 1-min break between each cycle. The authors afterwards pulsed the mix (1 min on, 30 s off) for 10 min by subjecting it to 80% of the maximum used power. After two minutes of rest, the sonication process is repeated. Subsequently, the standardized procedure of casting UHPFRC is followed. Type 1 Portland cement used herein was of ~200 nm mean particle size, and a 0.2 water-to-binder ratio was utilized. The test specimens in this study were 150 × 50 × 12.5 $\text{mm}^3$ prismatic specimens for three-point flexure tests (ASTM C78), 150 mm × 150 mm plate with 12 mm thickness for the impact test (ASTM D7136), cylindrical specimens (12 mm long and 150 mm diameter) for the abrasion test (ASTM C944), and 50 mm cubic specimens for the compressive strength test (ASTM C109). These specimens were moist cured as per ASTM C192 at room temperature for 20 h, followed by demoulding and steam curing at 70ºC for 48 h. Seven days before testing, specimens were subjected to ambient temperature at 50% relative humidity. For the previously selected system, the authors reported improvements in the material's properties when the latter is in its fresh and hardened states. An increase in the fresh mix workability was observed, which was not expected. It is attributed to the highly hydrophilic surfaces of CNF, which benefitted the mix workability and increased the concrete's packing density. This, in turn, allowed more efficient use of the mixing water and lubricated the particulate matter more. The same system yielded 50%, 240%, 2700%, 236%, 1200%, and 5% improvements in the flexural strength, maximum deflection, energy absorption capacity, impact resistance, abrasion resistance, and compressive strength, respectively, compared to the plain (no steel fibres and CNF) concrete mix's properties. These improved characteristics correspond to the following values: 20.1 MPa for flexural strength, 29.2 mm for the maximum deflection, 3925 N.mm for the energy absorption capacity, 5.9 mm/mm for the impact resistance, 0.1 g for abrasion loss, and 159 MPa for the compressive strength. It is worth mentioning that the system that comprises high dosages of steel fibres only resulted in 34%, 54%, −4%, 18%, 400%, 18%, 400%, and 34% improvements in the same abovementioned properties.

Another investigation on incorporating CNF into UHPFRC was carried out by Meng and Khayat (2016). The authors herein used two types of surfactants: polycarboxylate-based High Range Water Reducer (HRWR) and a PAA while utilizing sonication. The surfactants are first mixed with the CNF (100 nm diameter by 50–200 μm length and 30 GPa tensile strength) and a portion of the mixing water (600 mL) with a mass ratio of 1:4:0.1 for CNF:HRWR:PAA. Sonication afterwards was performed for 7 h, taking rest every 1 min for 30 s. The suspension solution was allowed to sit for 4 h before mixing with the dry ingredients. After mixing the dry components, including sand, for 3 min at 60 rpm, the suspension solution was introduced and mixed for the same speed and duration. The remaining water and HRWR contents are added after this step, and the mixture is further mixed for 5 min at 120 rpm. Next, 0.5% by volume straight steel fibres (0.2 mm diameter, 13 mm diameter, and 1900 MPa tensile strength) are introduced into the mix within one minute while mixing at 60 rpm, and the resultant mixture is further mixed for two more minutes at 120 rpm. Meng and Khayat (2016) incorporated 0, 0.05%, 0.1%, 0.15%, 0.2%, and 0.3% CNF by binder weight. They investigated this inclusion's effect on the compressive strength, tensile strength, and flexural strength of the specimens. Curing conditions consisted of casting at 23 ºC and demoulding after 24 h, heat curing at 90 ºC for another 24 h, immersing in a lime-saturated water bath at 23 ºC for 7 days, and finally air-curing at 23 ºC until testing. A water-to-binder weight ratio of 0.2 was maintained for all specimens. However, the HRWR quantity was adjusted for each mix to give the same mini-slump reading (285 ± 5 mm) according to ASTM C230/C 230 M. The compression test (50 mm cubic specimens) was performed according to ASTM C109, flexural strength test ($76 \times 76 \times 305$ mm$^3$ specimens with 203 mm span length) according to ASTM C1609, and Direct Tension Test (DTT) on a dog-bone shaped specimen of the dimensions 25 mm thickness.

Fresh mix workability increase was only visualized upon the inclusion of up to 0.05% nanomaterials. Beyond this percentage, nanomaterials significantly adsorbed water and HRWR, decreasing the flowability. Compressive strength increased with the increase in nanomaterial content, reaching an 8 MPa increase upon the inclusion of 0.3% CNF. This is attributed to the bridging and filler effects of the nanomaterial.

Due to the same effects, nanomaterial's inclusion increased the first cracking load under DTT. This test also proved that the tensile strength increased with the increase in the CNFs' content. Thus, the energy absorption capacity in tension increased too. A 56% increase and 108% increase in tensile strength and energy absorption, herein taken as the area under the tensile load–displacement curve, were observed at 0.3% CNF inclusion compared to the reference samples. The same applies to the flexural strength test. It increased with the increase in CNF content, increasing the energy dissipation, herein taken as the area under the tensile load–deflection curve up to the span/150 deflection limit. A 46% and 174% increase in flexural strength and energy dissipation were observed in the mix containing 0.3% CNF, respectively. However, both reference samples (steel fibres without nanomaterials) and CNF-infused ones had softening behaviour.

Lim et al. (2018) investigated the inclusion of CNF into Ultra-High-Performance Concrete (UHPC) cementitious paste without steel fibres. They used two CNF products: CNF-A (40 nm diameter and 10 µm length) and CNF-B (30–300 nm diameter and 10–20 µm length). CNF-B required ultrasonication merely to become stable, homogenous, and achieve uniform nanoparticle dispersion. In contrast, CNF-A required the addition of a surfactant (Polycarboxylate ether (PCE) based Superplasticizer (SP)) prior to ultrasonication to reach the same result as CNF-B. CNF-B had a higher surface area and, most importantly, a wider range of nano-diametric tubular fibres, which significantly improves the mix's particle grading. After determining the appropriate mean of using each CNF product, the authors resumed specimen preparation. They mixed the dry constituents for three minutes, then added the CNF product and the SP. They continued mixing until satisfactory flowability is attained, which is measured according to ASTM C230. In this study, the amount of SP included by cement mass for CNF-A was 0.009 for the control plain UHPFRC mix and 0.01, 0.01, 0.011, and 0.012 by cement mass ratio for the mixes, including 0.0002, 0.0004, 0.0006, and 0.0008 CNF by cement mass, respectively. For CNF-B, the SP amount incorporated was 0.01, 0.01, 0.01, and 0.011 by cement mass for mixtures incorporating 0.002, 0.004, 0.006, and 0.008 CNF content by cement mass, respectively. The SP content is altered according to the CNF inclusion to maintain the workability of the fresh mix. However, they fixed the water-to-cement ratio to 0.2. The authors utilized the optimized particle packing approach to yield a satisfactory blend grading. Specimens were demoulded after 24 h and cured in water at room temperature.

The authors reported efficient CNF contribution to the 3rd day compressive strength gain of the 50 mm cubic specimens tested according to ASTM C109. Although CNF-A was classified as stable before its inclusion, it did not reach the compressive strength of CNF-B as the former agglomerated in the mix due to its poor dispersion. This resulted in inadequate and ineffective bridging. The mix incorporating 0.06% CNF content by cement mass resulted in the highest compressive strength gain among the CNF-A mixture (115 MPa on the 7th day and 140 MPa on the 28th day). On the contrary, 0.06% CNF-B infused UHPC specimens resulted in the highest compressive strength (140 MPa on the 7th day and 160 MPa on the 28th day) among all mixtures. Beyond this inclusion, negligible compressive strength gain resulted.

They also looked into the durability properties of the specimens of the highest compressive strength incorporating CNF-A and CNF-B products. They performed Rapid Chloride Permeability Test (RCPT) according to ASTM C1202. In this test, the current passing the cylindrical specimen (100 mm diameter and 50 mm thick) is measured in 30 min intervals for six hours. By imposing a 60 ± 0.1 V direct current voltage across the two faces of the specimen under test, the authors reported that CNF-infused specimens showed lower chloride permeability compared to the control specimen. Although, control specimens showed a very low permeability according to the test classification (less than 1000 coulombs) due to their dense pore structure. Moreover, the CNF-A infused 150 mm cubic specimen exhibited 33% less water absorption than the control specimen according to BS EN 12,390:8. Similarly, the CNF-B infused specimen exhibited 60% less water permeability. This difference is preliminary referred to the above mentioned agglomeration exhibited by CNF-A product. As a result, CNF-B had a denser microstructure with fewer macropores, which induced less water penetration. This was validated by Mercury Intrusion Porosimetry (MIP) technique. It revealed that CNF-B UHPC had less than 50 nm mesopores that are well connected by the CNF nanoparticles. On the contrary, CNF-A UHPC had pores greater than 50 nm, and the control plain specimen had pores greater than 100 nm.

## 4 Discussion

The above studies demonstrate the fact that CNF inclusion enhances UHPFRC properties. It densifies concrete's matrix further, making it less susceptible to the ingress of harmful chemicals. It also extends the size of UHPFRC's reinforcement system into the nanoscale order. As a result, it increases the pullout strength of the fibre matrix. C-S–H, the main hydration product, is of the nano order. Therefore, CNF inclusion helps in producing a better and more uniform C-S–H gel. Strength-wise, CNF increases the first tensile crack load and the material's tensile hardening ratio. Correspondingly, it increases the material's ductility, toughness, energy dissipation, and energy absorption capacity.

The type of CNF (single/multiwall) and its strength are two essential characteristics to be mentioned when reporting an experimental investigation. Similarly, the tensile strength of the steel fibres is equally important. Some of the abovementioned authors failed to report these material characteristics.

Additionally, the efficiency of the CNF is conditioned to the efficient grading of the mix and the size of the cement grains. This is because the minimum spacing of the CNF particle will be equal to the cement grain size, which might be relatively large compared to the optimal CNF spacing. Some of the abovementioned authors failed to report the cement grain size and account for the mix's grading in their investigations.

It is worth noting that CNF is highly conductive. Its inclusion into UHPFRC creates a homogenous electrically conductive network within the matrix. This allows the electrical resistivity of CNF-UHPFRC to change in response to strain, damage, or temperature change. Accordingly, testing the chloride ion penetration of CNF-UHPFRC based on electrical resistivity means, as the RCPT, yields erroneous results. Lim et al. (2018) noted that the chloride ion permeability classification ranges in the RCPT standard are very wide for a six-hour testing duration. Therefore, they were not able to adequately classify the chloride ion permeability of their material.

Differences in the observations in the above-listed studies go back to several reasons. One of which is the inclusion of steel fibres and their respective amount. Sbia et al. (2014) included a reasonable amount of steel fibres in UHPFRC. Meng and Khayat (2016), on the other hand, included only 0.5% steel fibres in their investigation. As a result, reference samples and nanomaterial-reinforced ones had tension softening behaviour under tension test. Coversely, Lim et al. had no steel fibres in their samples. Likewise, contents of the reference sample, in which the reported improvements are compared, are different. Sbia et al.,'s reference sample had no nanofibres and microfibres, while Meng et al.,'s had steel fibres with no CNF.

Another difference is the inclusion basis. Sbia et al. (2014) included CNF based on the volume of anhydrous materials while fixing the SP amounts. Meng and Khayat (2016) and Lim et al. (2018), on the other side, incorporated CNF based on cement mass and varied the SP amount accordingly.

## 5 Conclusion

The beneficial effects of reinforcing UHPFRC with a hybrid system are demonstrated in the above studies. CNF delays the inception of microcracks and steel fibres arrest larger cracks and hinder their growth. As a result, the fibres' synergic effects elevate the mechanical and durability properties of UHPFRC. CNF-UHPFRC is marketed as a green and affordable promising material with better mechanical and durability properties than traditional UHPFRC. In other words, CNF-UHPFRC meets the requirements of the most demanding applications at a competitive cost. However, as demonstrated above, these improvements are conditioned to incorporating an adequate amount of CNF into the mix and ensuring its uniform dispersion.

## References

Aïtcin, P-C, Flat R (2015) Science and technology of concrete admixtures. Elsevier Science & Technology

Al-Osta, MA (2018) Exploitation of ultrahigh-performance fibre-reinforced concrete for the strengthening of concrete structural members. In: Advances in civil engineering, vol 2018, Article ID 8678124, pp 12. https://doi.org/10.1155/2018/8678124

Lim JLG, Zain MFM, Hamid R, Lai FC, Raman SN (2018) Strength and durability performance of ultra-high-performance cementitious composite enhanced with carbon nanofibers. In: International conference on durability of concrete structures, United Kingdom, 18–20 July 2018, ICC18

Meng W, Khayat KH (2016) Mechanical properties of ultra-high-performance concrete enhanced with graphite nanoplatelets and carbon nanofibers. In: Composites part B: engineering, vol 107, pp 113–122 (Dec 2016)

Sbia LA, Peyvandi A, Soroushian P, Lu J, Balachandra AM (2014) Enhancement of ultrahigh performance concrete material properties with carbon nanofiber. In: Advances in civil engineering, vol 2014, Article ID 854729, pp 10. https://doi.org/10.1155/2014/854729

Sharon M (2021) An introduction to carbon nanofiber. Carbon Nanofibers 2021:1–20

Wang T, Xu J, Meng B, Peng G (2020) Experimental study on the effect of carbon nanofiber content on the durability of concrete. In: Construction and building materials, vol 250. ISSN 118891 0950 618. https://doi.org/10.1016/j.conbuildmat.2020.118891

# A Review on Seismic Performance of Reinforced Concrete Columns Strengthened with Smart and Composite Materials

**Adel Al Ekkawi and Raafat El-Hacha**

## 1 Introduction

Maintaining the sustainability of existing infrastructures has been the main purpose of researchers for many decades. In particular, seismic strengthening of RC columns has been a popular research study for more than three decades. This is because RC columns in bridges or building frame systems play a major role in resisting earthquakes; thus, their failure will trigger the collapse of the entire structure. Therefore, it is important to ensure that the supporting RC columns do not suffer from any type of deficiency. Another reason for the popularity of such a research field is that RC columns designed following the requirements of old codes (before 1971) suffer from poor ductility due to the inadequate design and detailing of the internal reinforcements imposed by those codes. The poor ductility arises from two main sources: (1) insufficient transverse reinforcements and (2) inadequate lap splice length in the plastic hinge zone. The insufficient transverse reinforcements will provide poor confinement to the concrete core; thus, the latter will experience crushing when subjected to seismic loading. Upon crushing the concrete core, the longitudinal reinforcements will lose their lateral support and will eventually buckle. Moreover, the insufficient transverse reinforcements will result in an inadequate shear capacity. On the other hand, the inadequate lap splice length in the plastic hinge zone will cause the splitting of the lapped flexural reinforcements; thus, absorbing the seismic energy and developing a stable inelastic deformation by yielding will be significantly reduced. As a result, the insufficient transverse reinforcements and the inadequate

---

A. Al Ekkawi (✉) · R. El-Hacha
Department of Civil Engineering, University of Calgary, 2500 University Drive NW, Alberta, Canada
e-mail: adel.alekkawi@ucalgary.ca

R. El-Hacha
e-mail: relhacha@ucalgary.ca

B. Benmokrane et al. (eds.), *8th International Conference on Advanced Composite Materials in Bridges and Structures*, Lecture Notes in Civil Engineering 267,
https://doi.org/10.1007/978-3-031-09409-5_15

lap splice lengths were the major reasons that affected the ductility of RC columns and made them vulnerable when resisting earthquakes. Therefore, strengthening systems are required to enhance the RC columns' ductility and strength and conform to the latest code requirements. In addition, the exposure of RC columns to localized damages, corrosion, higher load demands, and construction errors are other reasons for strengthening RC columns.

Developing a strengthening system for RC columns has been facing numerous challenges related to aesthetics, facility disruption time, structural requirements, and ease of strengthening application. Therefore, an adequate strengthening system is the one that balances between those four components where the shape of the column is not drastically changed, the disruption time of the facility is little, the system can be easily applied, and the structural requirements are satisfied.

The two most popular strengthening systems for RC columns are steel encasing and concrete jacketing. However, both face some disadvantages in which steel encasing is time and labour-extensive, whereas concrete jacketing changes the shape of the column and affects its aesthetics because of the jacket thickness that must be large enough to include jacket reinforcements. Moreover, concrete jacketing increases the overall weight of the structure, which leads to the increase of seismic demand on the structure as a whole and changes its global seismic performance; two undesirable effects of strengthening. As a result, engineers and researchers started decades ago to go beyond their habitual way of thinking. They have been incorporating new materials that possess very high strength and low weight. For instance, Fibre-Reinforced Polymers (FRPs) have been an attractive material for strengthening due to their very high strength-to-weight ratio. Moreover, another generation of concrete was produced, Ultra-High-Performance Fibre-Reinforced Concrete (UHPFRC) which possesses a strength that is five times stronger than conventional concrete. And finally, Shape Memory Alloys (SMAs) have been incorporated for the last 20 years in strengthening applications due to their unique and smart behaviour. SMAs can recover large deformations once unloaded or subjected to a heat source.

Correspondingly, this paper will provide a review of various strengthening and repairing systems applied to deficient RC columns by many researchers. The strengthening applications will be limited to columns that were strengthened with UHPFRC, SMAs, and FRPs. Summaries of the experimental program and results for each type of strengthening will be presented in Sects. 2, 3 and 4. After that, Sect. 5 will present the authors' general comment on the presented research studies. This is followed by Sect. 6, which will demonstrate the potential research gaps that direct the future of research in strengthening and repairing deficient RC columns.

## 2 Ultra-High-Performance Fibre-Reinforced Concrete (UHPFRC)

### *2.1 Material Overview*

The appropriate combination of cementitious materials, proper sand gradation, low water/cement ratio, fibre reinforcements, and adequate superplasticizers will result in a cementitious class called Ultra-High-Performance Concrete (UHPC) with advanced engineering properties. Such material is realized for its high mechanical strength, durability, and impermeability characteristics, achieved by refining the material's microstructure, reducing its capillary pores, and adding steel fibre reinforcements (Sbia et al. 2014). UHPC has a high compressive strength that exceeds 150 MPa, a high tensile strength that can reach 18 MPa, and reliable impact resistance. The high strength of UHPC can drastically reduce the size of structural members, thus lowering the amount of used concrete. As a result, the environmental impact of concrete industries will be mitigated.

The UHPC material suffers from brittleness due to the adopted high strength. This brings the cause of introducing short fibre reinforcements within the concrete matrix to overcome brittleness, control crack propagation, and enhance the material's ductility. Typically, UHPC included steel fibres to increase tensile strength, enhance ductility and exhibit a strain hardening behaviour when subjected to tension or flexure.

The steel fibres within the UHPC matrix exist at relatively large spacing, thus becoming ineffective in delaying the generation of microcracks in the concrete. As a result, the concrete will be exposed to the ingress of moisture and chemicals that will expedite deterioration. This brings attention to the importance of increasing the cracking resistance at the microscale level to improve durability. Nanoscale fibres were then proposed as fibre reinforcements, in addition to steel fibres, because of the dense and fine microstructure of UHPC that favours the interaction with nanomaterials (Sbia et al. 2014). The presence of nanomaterials within the concrete matrix will be at close spacing; thus, the propagation of fine microcracks can be prevented. As a result, Carbon Nano Fibres (CNF) were added to the matrix of UHPC. With that being said, the term Ultra-High-Performance-Fibre-Reinforced Concrete (UHPFRC) will be used instead of UHPC for a better indication of the existence of fibres within the concrete matrix.

### *2.2 Seismic Strengthening of RC Columns with UHPFRC*

The most frequent strengthening method is the increase of the cross-section of a concrete member, referred to as concrete jacketing. It was the first method to strengthen concrete members, where a layer of reinforced concrete is cast around. Previously, concrete jacketing was done using normal strength concrete. However, due to the relatively low strength of such concrete material, jacket reinforcements were necessary to provide additional strength. This resulted in a relatively high jacket thickness between 70 and 100 mm (Beschi et al. 2009), thus affecting the overall aesthetics of the structure and increasing its weight, which leads to a negative drawback on the seismic behaviour of the entire structure. However, since the UHPFRC possesses high tensile strength and good ductility attributed to the existence of steel fibres, jacket reinforcements became unnecessary, thus lowering the jacket thickness significantly to reach 30 mm–50 mm (Beschi et al. 2009). Moreover, the embedded steel fibres result in a strain hardening behaviour which makes it appropriate for strengthening of concrete members subjected to inelastic deformations.

Beschi et al. (2009) strengthened a square RC column with 40 mm thick High-Performance Fibre-Reinforced Concrete (HPFRC) reinforced with 1.5% by volume steel fibres. The column was subjected to a constant axial load and a lateral cyclic loading with increasing intensities. The authors reported a strength degradation at 3.5% drift due to jacket detachment and column failure at 6% drift due to rupture of the longitudinal reinforcements. Moreover, the column possessed a lateral capacity and ductility that conforms with the new Italian Code requirements.

In 2011, Massicotte and Boucher strengthened rectangular RC columns having deficient lap splice detailing, a common practice for RC columns designed before the 1970s. The purpose of strengthening was to mitigate the deficient lap splice details that contributed to the brittle failure of the structure due to their inability to develop stable inelastic behaviour when exposed to earthquakes. The strengthening process took place along the lap splice length in which a UHPFRC jacket replaced the existing concrete cover. The column was subjected to a horizontal cyclic loading to simulate seismic effects with no axial loads. The UHPFRC jacketed column recorded 365 mm displacement without any sign of strength degradation. This was attributed to the ability of the UHPFRC jacket in preventing splitting cracks and transferring loads between the bars, thus enhancing the ductility and strength of the column. A similar study was done by Dagenais et al. (2017). The UHPFRC was successful in eliminating splitting cracks and transferring the force between the column and foundation due to the ductility and high tensile strength of the UHPFRC.

In 2015, Meda et al. assessed the seismic performance of corroded square RC columns strengthened with a 40 mm thick HPFRC jacket that includes 1.2% by volume steel fibres. The longitudinal reinforcements were corroded to a level of 20% in terms of mass loss after subjecting the column to a 3% saline solution. After that, the deteriorated concrete surface was removed, the reinforcements were brushed/cleaned, the concrete surface was sandblasted for a proper bond between HPFRC and column, and finally, the HPFRC jacket was applied. The column was subjected to a constant axial load and a lateral cyclic loading after strengthening took place. The corroded strengthened column recorded a 65% increase in lateral strength and a 50% increase in energy dissipation capacity than the uncorroded unstrengthened column.

The shear behaviour of square RC columns jacketed with UHPFRC was studied by Koo and Hong (2016). The test program included several specimens with varying UHPFRC jacket thickness (30–50 mm) where the UHPFRC included 1.5% by volume steel fibres. The authors reported that a 10% and 16.7% increase in UHPFRC jacket thickness increased the shear strength by 70% and 125%, respectively. Moreover, the shear strength can be further increased by adding steel stirrups in the UHPFRC jacket.

## 3 Shape Memory Alloys (SMAs)

### *3.1 Material Overview*

Shape memory alloys (SMAs) are a unique group of alloys that can recover their undeformed shape after large deformations by either unloading or heating. Thus, they provide a perfect tool to dissipate energy with no permanent residual strains. If the shape recovery was achieved by unloading, this means that SMA adopts a *pseudoelastic behaviour*. On the other hand, if the shape recovery was achieved by heating, SMA adopts a *shape memory effect*. These outstanding properties result from temperature and stress-dependent phase transformation that controls the crystallography of the SMA's inner structure. Moreover, the properties of SMAs gave the chance to categorize such types of alloys as smart materials. The alloys can be a combination of Nickel (Ni), Titanium (Ti), Iron (Fe), Copper (Cu), Aluminium (Al), Zinc (Zn), Manganese (Mn), Gold (Au), Silver (Ag), and many others. Some types of SMAs are NiTi, NiTiFe, NiTiCu, NiTiHf, CuAlBe, FeMn, CuZn, MnCu, FePd, CuZnAlMnZr, and others. As clearly demonstrated, a wide variety of SMAs exists; however, not all can be implemented in structures due to the mechanical properties required, temperatures, and cost.

### *3.2 Seismic Strengthening of RC Columns with SMAs*

Researchers started decades ago to go beyond their habitual way of thinking where they have been incorporating new materials; one of the materials is SMAs. Prior to the evolution of SMAs, researchers demonstrated that applying external confining pressure to the concrete element, a technique referred to as active confinement, is better than the passive confinement approach. However, passive confinement refers to the engagement of the confining material after the element suffers from further damage. Active confinement faced a real challenge that was related to the technique used to apply the prestress effect. On the other hand, incorporating SMAs to actively confine RC columns resulted in reduced labour, time, and cost, thus eliminating the challenges encountered by the active confinement approach. In addition, limited researchers incorporated SMAs as flexural strengthening for RC columns.

In 2011, Shin and Adrawes assessed experimentally the seismic performance of RC columns confined with NiTi SMA wires or GFRP wraps along the plastic hinge length. The columns were designed based on the old seismic requirements of AASHTO 1969. The columns were either wrapped with pre-strained NiTi SMA wires, Glass Fibre-Reinforced Polymers (GFRP) wraps, or both SMA wires and GFRP wraps (Hybrid System); however, all three systems provided the same confining pressure. To induce active confinement by the SMA wires, the latter were heated through an electric current to activate their shape memory effect. Since SMA wires were restrained and the column concrete is incompressible, recovery stress of 460 MPa at room temperatures was induced, thus applying an active confining pressure to the column. The SMA-wrapped column recorded a significant increase in strength and ductility compared to the as-built column and the GFRP-wrapped column. Moreover, it was inferred that introducing hybrid confinement in the shape of SMA and GFRP wraps can result in improved performance even with lower costs since part of the expensive SMA is replaced by GFRP.

While Shin and Andrawes (2011) studied the effect of SMA spirals on circular RC columns with inadequate transverse reinforcements, Choi et al. (2012) implemented the same approach but on deficient lap spliced columns. The columns were wrapped with NiTiNb SMA wires of spacings 1 and 2 mm. The SMA wrapping took place along the plastic hinge length and was heated up to activate its shape memory effect. It was reported that the SMA wrapping increased the lateral strength and failure displacements of the deficient lap spliced columns.

Miralami et al. (2019) studied the lateral performance of RC columns strengthened in flexure with GFRP and SMA bars and confined with Carbon Fibre-Reinforced Polymers (CFRP) wraps. The bars were anchored in the foundation and embedded within a 50 mm secondary concrete jacket cast around the column. The GFRP flexural strengthening took place along the entire column height, whereas the SMA flexural strengthening took place along 700 mm height. It was demonstrated that GFRP strengthening bars were more effective than SMA bars in increasing the lateral load and energy dissipation capacity. However, the SMA strengthened column showed superior results in displacement recovery where this was attributed to the pseudoelastic behaviour of SMA and its ability to recover deformations upon unloading. The CFRP wrap had a significant contribution to enhancing the seismic behaviour since it confined the concrete and prevented it from early crushing.

Xing et al. (2020) conducted a similar study on the behaviour of square RC columns strengthened with Near Surface Mounted (NSM) SMA bars or CFRP bars and confined with CFRP wraps. The NSM SMA or CFRP bars were placed in a precut groove along the plastic hinge length and then anchored inside the foundation. The grooves were filled then with epoxy. It was reported that increasing the amount of SMA bars did not affect the column's behaviour. Moreover, the strain in SMA bars did not increase anymore after reaching peak load because of the slip behaviour between the epoxy and SMA bars and pull out of the latter from the foundation. Therefore, this explains why the SMA strengthened column did not record a significant increase in lateral capacity. As a result, this carried the authors to report that NSM CFRP bars yielded better enhancements in flexural capacity than NSM SMA bars due to their ribbed texture.

# 4 Fibre-Reinforced Polymers (FRPs)

## *4.1 Material Overview*

FRP is a composite material obtained by merging two or more raw materials on a macroscopic scale, creating new material with better properties than its raw components. FRP is made of high-strength fibres and a matrix in which the fibres provide the composite's strength and stiffness. In contrast, the matrix binds the fibres together and transfers the load between them. FRP became a competitive material in construction after it is widespread in large civil projects and was accompanied by a drastic reduction in manufacturing costs. Furthermore, they have had a longstanding reputation for strengthening and retrofitting deteriorated and deficit structures. FRPs exhibit a perfectly elastic behaviour up to failure and possess a high tensile capacity five times stronger than steel. FRPs are also known for their lightweight and durability against harsh environmental exposures. Fibre types used in civil engineering are Carbon, Glass, and Aramid Fibre-Reinforced Polymers, noted as CFRP, GFRP, and AFRP, respectively.

## *4.2 Seismic Strengthening of RC Columns with FRPs*

Over time, FRP material has proven its efficiency and reliability day after day to be used as a construction material for new buildings and bridges. After the extensive research and experimental work implemented on this material, it transitioned from laboratory and small-scale works to applications in real structures and as a construction material found in markets. Moreover, FRP has been used to strengthen structural elements to better resist earthquakes by enhancing the member's ductility, lateral strength, energy dissipation capacity, and ultimate drift capacity. The efficiency of strengthening with FRP against earthquakes was studied extensively and became one of the available and most selected materials for such purposes. Therefore, the following section will present a certain number of conducted research studies about the seismic strengthening of RC columns with FRP material.

In 2000, Ma et al. tested the impact of CFRP jacketing on a large-scale square RC column with improper lap splice details that were typically adopted in the pre-1971 codes. The column was wrapped with six layers of CFRP that provided a confinement pressure of 8 MPa. The CFRP wrapped column exhibited a good energy dissipation capacity that was attributed to the ability of steel reinforcements to yield in the critical lap spliced regions due to CFRP confinement. Moreover, the column did not experience severe damages at the end of testing, and CFRP debonding or rapture did not occur.

Similarly, Sause et al. (2004) investigated the effect of CFRP jacketing on non-ductile columns built per the old code seismic provisions. Different numbers of CFRP jackets were applied to the plastic hinge region. The displacement ductility and deformation capacity were significantly enhanced by the CFRP confinement but with no improvement in the lateral strength and initial stiffness of the columns. Moreover, it was found that as the jacket thickness increases, the displacement ductility increases too.

Harajli and Dagher (2008) studied the effect of CFRP confinement at the lap splice region of rectangular RC columns. The FRP confinement reduced the bond degradation of the spliced bars and allowed them to yield upon increasing drifts. Thus, the lateral strength, energy dissipation capacity, and ductility were significantly increased.

Vrettos et al. (2013) increased the flexural strength of non-seismically detailed square RC columns with externally bonded CFRP sheets placed longitudinally on the two opposite sides of the column and anchored to the foundation with carbon fibre spike anchors on each side. The CFRP confinement prevented concrete spalling, which made the specimens resist 8% drifts with no failure. The flexural strengthening significantly increased the column lateral strength and dissipation capacity. Finally, the authors concluded that fewer and bigger anchors are more effective than the high amount and light ones.

A study by Paultre et al. (2015) was conducted to explore the seismic performance of RC circular large-scale columns confined with CFRP sheets along the entire height. The parameters included the spacing of the transverse reinforcements, the intensity of the constant axial load, and the presence or absence of one layer of the CFRP sheet. In summary, it was found that the CFRP strengthening effect is more pronounced for columns with a high amount of transverse reinforcement and low axial load intensity.

## 5 Authors' Discussion

A general comment can be made on all presented works in which all researchers did not study the effect of uncertainties on the reliability of their results. Reporting the increase or decrease in any studied parameter is not enough to make general conclusions and report them publicly. The effect of different uncertainties should be taken into consideration because every measurement has uncertainty about it. For instance, reporting an increase in lateral strength and ductility is not reliable enough because there might be a difference in the concrete strength, FRP strength, SMA strength, reinforcing steel strength, and many more between the specimens. To consider such uncertainties, an analysis called "Error Propagation Analysis" should be conducted to determine the sensitivity of the reported results against several random variables. Such analysis will increase the reliability of the results and help make better and more accurate conclusions regarding the effectiveness of the strengthening systems.

## 6 Research Gaps and Conclusions

The reporting on the research works presented in this paper made it clear regarding such material's ability and its promising future in infrastructure strengthening. However, some research gaps still need to be filled when using those materials in seismic column strengthening. Those gaps are illustrated as follows:

- The CNF-UHPFRC has still not been included in the area of RC column seismic strengthening. This material's high mechanical strengths and strain hardening behaviour make it suitable for strengthening elements subjected to inelastic deformations.
- The limited research works that included SMA as flexural strengthening for RC columns faced shortcomings, mainly the debonding of the vertical SMA bars from the secondary confining concrete and the splitting of the latter from the concrete foundation. Therefore, there should be better methods for utilizing the SMA material on the surface of the RC column.

Most of the structural collapses that occurred during some major earthquake events such as Kobe Earthquake in Japan and Northridge Earthquake in United States, where both occurred in 1995, resulted from poor column performances. Closing structures such as bridges after an earthquake can severely affect the economy, traffic flows, and emergency routes. Also, the costs of repairing the bridge to reclaim its function may be substantial. Nevertheless, thousands lose their lives not because of earthquakes but due to structural collapses. Earthquakes are natural disasters that will not end. However, as engineers, we shall mitigate such a hazard by developing a proper seismic resisting system for structures and strengthening/repairing deficient structures to resist earthquakes more efficiently.

## References

Beschi C, Meda A, Riva P (2009) High performance fiber reinforced concrete jacketing in a seismic retrofitting application. In: ATC & SEI 2009 conference on improving the seismic performance of existing buildings and other structures, San Francisco, California, 9–11 Dec 2009, pp 224–233

Choi E, Choi D-H, Chung Y-S, DesRoches R 2012 Seismic protection of lap-spliced RC columns using SMA wire jackets. Mag Concr Res 64(3): 239–252. (Jan 2012)

Dagenais M-A, Massicotte B, Boucher-Proulx G (2017) Seismic retrofitting of rectangular bridge piers with deficient lap splices using ultrahigh-performance fiber-reinforced concrete. J Bridge Eng 23(2). (Nov 2017)

Harajli MH, Dagher F (2008) Seismic strengthening of bond-critical regions in rectangular reinforced concrete columns using fiber-reinforced polymer wraps. ACI Struct J 105(1): 68–77 (Feb 2008).

Koo I-Y, Hong, S-G (2016) Strengthening RC columns with ultra high performance concrete. In: The 2016 world congress on the 2016 structures congress (Structures 16), Jeju Island in Korea, Aug 28–Sept 1 2016

Ma R, Xiao Y, Li K (2000) Full-scale testing of a parking structure column retrofitted with carbon fiber reinforced composites. Constr Build Mater 14(2): 63–71. (Jan 2000)

Massicotte B, Boucher-Proulx G (2011) Seismic retrofitting of bridge piers with UHPFRC jacket. Designing and Building with UHPFRC, Chapter 35:531–540

Meda A, Mostolsi S, Rinaldi Z, Riva P (2015) Corroded RC columns repair and strengthening with high performance fiber reinforced concrete jacket. Mater Struct 49(5): 1967–1978. (May 2015)

Miralami M, Esfahani MR, Tavakkolizadeh M (2019) Strengthening of circular RC column-foundation connections with GFRP/SMA bars and CFRP wraps. Composites B Eng 172: 161–172. (May 2019)

Paultre P, Boucher-Trudeau M, Eid R, Roy N (2015) Behavior of circular reinforced-concrete columns confined with carbon fiber–reinforced polymers under cyclic flexure and constant axial load. J Composites Constr 20(3). (Oct 2015)

Sause R, Harries KA, Walkup SL, Pessiki S, Ricles JM (2004) Flexural behavior of concrete columns retrofitted with carbon fiber-reinforced polymer jackets. ACI Struct J 101(5): 708–716. (Oct 2004)

Shin M, Andrawes B (2011) Lateral cyclic behavior of reinforced concrete columns retrofitted with shape memory spirals and FRP wraps. J Struct Eng 137(11): 1282–1290. (Nov 2011)

Sbia L, Peyvandi A, Soroushian P, Lu J, Balachandra A (2014) Enhancement of ultrahigh performance concrete material properties with carbon nanofiber. Adv Civil Eng 2014. (Aug 2014)

Vrettos I, Kefala E, Triantafillou TC (2013) Innovative flexural strengthening of reinforced concrete columns using carbon-fiber anchors. ACI Struct J 110(1): 63–70. (Feb2013)

Xing G, Ozbulut OE, Al-Dhabyani MA, Chang Z, Daghash SM (2020) Enhancing flexural capacity of RC columns through near surface mounted SMA and CFRP bars. J Compos Mater 54(29):4661–4676

# Flexural Strengthening of Reinforced Concrete Structures Using Iron-Based Shape Memory Alloys: Case Studies

**Benjamin Forrest, Raafat El-Hacha, and Julien Michels**

## 1 Introduction

Human civilization depends heavily on our infrastructure. Reinforced concrete (RC) structures represent most infrastructure in the world today. When those structures become deficient either due to damage or change in use, strengthening them to restore their load carrying capacity is generally preferred over replacing them. Prestressed strengthening not only restores the load-carrying capacity but also reduces deflections and closes cracks of the deficient structure. There tends to be a trade-off between ultimate load-carrying capacity and ductility. As the level of prestress increases, the load-carrying capacity and stiffness increase as well, but ductility is sacrificed (El-Hacha and Soudki 2013). Since ductile failure is desirable for all structures, this can be considered a significant limitation of prestress strengthening. The requirement for heavy jacking equipment and sufficient anchorage to prestress the strengthening material can also be cumbersome, especially on sites with limited access. Furthermore, the efficiency of the strengthening is lowered when prestress losses occur due to friction and anchorage setting. Finally, for near-surface-mounted or externally bonded strengthening reinforcement, additional material must be removed for installing mechanical anchorage and jacking equipment to perform the prestressing.

---

B. Forrest (✉) · R. El-Hacha
Department of Civil Engineering, University of Calgary, 2500 University Dr. NW, Calgary, AB T2N 1N4, Canada
e-mail: benjamin.forrest@ucalgary.ca

R. El-Hacha
e-mail: relhacha@ucalgary.ca

J. Michels
re-fer AG, Riedmattli 9, CH-6423 Seewen, Switzerland
e-mail: jmichels@re-fer.eu

B. Benmokrane et al. (eds.), *8th International Conference on Advanced Composite Materials in Bridges and Structures*, Lecture Notes in Civil Engineering 267,
https://doi.org/10.1007/978-3-031-09409-5_16

The emergence of a novel alloy, iron-based shape memory alloy (Fe-SMA), exhibiting a unique shape recovery behavior, known as shape memory effect (SME), addresses these challenges. SME is the ability to recover relatively large deformations when heated. When the recovery is restrained, recovery stress develops instead, which can be used to transfer a prestressing force to a deficient structure. The structure can be prestressed by attaching a prestrained element to it and heating the Fe-SMA. This method of prestressing no longer requires heavy jacking equipment and sufficient anchorage; much-less original material needs to be removed for strengthening, and there are no losses to friction and anchorage setting. This kicked off an experimental campaign to investigate the feasibility of the novel technique for prestressing RC structures and validate the concept with small and medium-scale experiments (El-Hacha and Rojob 2018; Ghafoori et al. 2019; Hong et al. 2018; Michels et al. 2018a; Rojob and El-Hacha 2017a, b, 2018; Shahverdi et al. 2016; Soroushian et al. 2001). As for real applications of this novel technology, there are multiple instances of it being used in the field. However, to the best of the authors' knowledge, almost all of the projects occurred in Switzerland as it is home to a production facility, re-fer AG, which currently holds several patents for production and strengthening systems with SMA (Leinenbach et al. 2017; Motavalli et al. 2019). The motivation of this paper is to increase the awareness of using this novel material for strengthening RC by demonstrating its potential in field implementations. The article will provide a brief history of the development of Fe-SMA followed by a summary of the shape recovery mechanism and how it is being used to prestress structures. The latest examples of strengthening RC structures with Fe-SMA will be summarized, followed by a discussion of several characteristics of the technology.

## 2 Brief History of Fe-SMA

The commercial applications of the shape memory effect were first realized in the 60s in a Nickle–Titanium alloy (NiTi-SMA) (Buehler and Wang 1968). The unique phenomenon carried advantages in several fields such as medicine (Bansiddhi et al. 2008; Biesiekierski et al. 2012; Dotter et al. 1983; Kuribayashi 1989), dentistry (Pfeifer et al. 2013; Thompson 2000), robotics (Kuribayashi 1989), aerospace (Bil et al. 2013; Turner et al. 2006) and automotive (Mohd Jani et al. 2014; Stoeckel 1990; Strittmatter and Gumpel 2011). However, the temperature and stress conditions required to employ the memory effect were not suitable for civil structures. That, coupled with the high production costs of NiTi SMA, limited its use in civil structures (Janke et al. 2005). Later, the memory effect was discovered in lower cost alloys, iron-based alloys and Fe–Mn–Si alloys (Sato et al. 1982). This immediately captured the attention of civil engineer researchers, who continued to modify the processing and composition of the alloy to achieve desirable performance in civil structures. Soon, small and medium-scale experiments were conducted to investigate the prestressing and strengthening feasibility of Fe-SMA for reinforced concrete (RC) structures and the advantages and limitations of the strengthening system became apparent. The development of an innovative rolling technology in Switzerland allowed Fe-SMA strip and deformed bars to be produced at an industrial scale (Leinenbach et al. 2017). With Fe-SMA readily available, local consultants in Switzerland were able to design strengthening solutions for RC structures using Fe-SMA strips and bars.

## 3 Thermo-Mechanical Characteristics

SME is made possible by undergoing reversible phase transformations between the dominant phases of the alloy, austenite (parent or higher temperature phase) and martensite (soft or lower temperature phase).

Without mechanical loading, the phases are characterized by four distinct parameters: martensite start, $M_s$, martensite finish, $M_f$, austenite start, $A_\mathrm{s}$, and austenite finish, $A_f$, where the start and finish temperatures correspond to the beginning and end of the phase transformation. These characteristic temperatures increase with stress to a limit known as critical stress, $\sigma_{cri}$, above which, plastic, irreversible deformations occur, which inhibits SME. When austenitic SMA cools, it experiences a forward transformation to self-accommodated or twinned martensite and the macroscopic shape change is negligible. When the SMA is heated, it undergoes a reverse transformation back to austenite, again with negligible macroscopic shape deformations.

With mechanical loading, the twinned martensite becomes detwinned between the detwinning start and finish stresses ($\sigma_s$ and $\sigma_f$) and undergoes relatively large or pseudoplastic deformations. Upon removal of the load, the shape deformations remain. When the detwinned martensite is heated above $A_\mathrm{s}$, it starts the reverse transformation to austenite and begins recovering the deformations. The transformation to austenite is complete at $A_f$. When the austenite cools, it transforms back to twinned martensite and the cycle repeats. If the deformations are restrained from recovering when the Fe-SMA is heated, then recovery stress develops. For structural engineering purposes, this recovery stress is used to prestress the structure.

## 4 Case Studies

The latest projects involving Fe-SMA for prestress flexural strengthening RC structures are summarized in Table 2, which all occurred in Switzerland. This is likely attributed to the commercial availability of Fe-SMA products for strengthening by re-fer AG. The facility produces Fe-SMA in thin plates (strips of 120 mm × 1.5 mm cross-section) and ribbed bars, available in diameters of 10 and 16 mm (Michels et al. 2018b). The data reported by the manufacturer for each shape used in the latest projects is reproduced in Table 1. The manufacturer reports these products to have

**Table 1** Manufacture data for Fe-SMA strip and bar products by re-fer AG

| Product | Diameter or width x thickness (mm) | Cross-sectional area ($mm^2$) | Prestress (MPa) at 300 °C | Prestress force (kN) at t = 0 | Breaking stress (MPa) | Breaking force (kN) | Elongation at break (%) |
|---|---|---|---|---|---|---|---|
| re-bar 10 | 10 | 89.9 | 400 | 36[a] | 800 | 71.9 | 10 > 30 |
| re-bar 16 | 16 | 211 | 350 | 67.6 | 750 | 158.4 | >30 |
| re-plate | 120 × 1.5 | 180 | 380 | 68 | 1000[a] | 180 | >30 |

[a] Stress level limited to a design value of about 580 MPa due to anchorage failure and a significant stiffness reduction of Fe-SMA

very good corrosion resistance (CRC1) and experience a 15% relaxation at $t_\infty$ (re-fer AG 2019; 2020b). This section will provide an overview of how the Fe-SMA arrives on-site and is installed.

## 4.1 Processing and Shipping

The production facility processes and prestrains the bars and strips to provide the desired recovery stress required for strengthening. The bars and strips are then cut as per a provided material list, and the strips have holes for the anchors pre-punched. The bar is then shipped to the site in bundles and the strip according to the requested lengths (re-fer AG 2019, 2020b). Additional corrosion protection can be applied to the facility prior to shipping if required (re-fer AG 2020a).

## 4.2 Heating Methods

Three methods of heating Fe-SMA on-site are electrical resistivity (ER), gas torch (GT) and infrared (IR). ER passes a current from a power source through the Fe-SMA bar or strip using clamps on each end. The strip is extended beyond the anchors for the clamp attachment. The resistance of the material generates heat. The temperature can be monitored by many methods such as an infrared measuring device, thermocouple wires and liquid temperature indicators. GT requires a fuel tank and torch, and an operator passes the lit torch up and down each bar or strip until the desired temperature is reached. IR uses a custom IR heater developed by the facility. It includes a temperature sensor and is placed against the Fe-SMA and turned on until the desired temperature is reached. There are applications where a lower or more controlled temperature increase is desired such as requiring a reduced prestress or limiting the

**Table 2** Selected list of completed projects strengthening RC structures in flexure using Fe-SMA (re-fer AG 2021b)

| RC element strengthened | Year | Reason for strengthening, Fe-SMA Type | Heating method, remarks |
|---|---|---|---|
| 1. Bridge extension (Courrendlin, Switzerland) | 2021 | Carbonation of concrete, corrosion of internal reinforcement, CRM Bar and EUB strip | GT for the bar and IR for the strip |
| 2. Office girder (Rotterdam, Netherlands) | 2021 | Holes drilled through original girders during a renovation, EUB strip | IR, welded to U-shaped steel shoe anchorage and corrosion treatment of strips in factory |
| 3. Parking lot slab (Nussbaumen, Switzerland) | 2020 | Slab in parking lot, EUB strip | GT, additional protection from fire with spray mortar |
| 4. Bridge girder (Riehen, Switzerland) | 2020 | Removal of intermediate support, CRM Bar | GT, bonded using spray-mortar post-activation |
| 5. Bridge girder (Mörschwil, Switzerland) | 2020 | Girder and prestressed stands damaged from local traffic, EUB strip | IR, bridge strengthened within 2 h. Corrosion treatment of strips in factory and on site |
| 6. Precast hollow core slab (Lucerne, Switzerland) | 2020 | Relieve high-stress areas at intersection of webs, NSM Bar | GT, embedded in rebar. Controlled heating required regulated prestress |
| 7. Building slab (Zürich, Switzerland) | 2020 | Insufficient flexural and punching reinforcement in slab, CR Bar | GT, embedded in mortar |
| 8. Building slab (Freienbach, Switzerland) | 2020 | Required for a renovation, EUB strip | IR, prestress controlled with crossbow device. Fire protection with spray mortar |
| 8. Building wall (Mellingen, Switzerland) | 2019 | Consequence of large wall demolition, CR Bar | GT, welded to steel angles, embedded in mortar |
| 9. Underground vault (Jungfraujoch, Switzerland) | 2019 | Extension of station hall, CR Bar | GT, bars embedded in spray mortar |
| 10. Slab (Winterthur, Switzerland) | 2019 | Strengthen slabs in negative bending zones, NSM Bar | GT, Grooves filled with self-leveling mortar |
| 11. Balcony slab (Münchenstein, Switzerland) | 2018 | Due to a conversion in an apartment building, NSM Bar | IR, Grooves filled with mortar |
| 12. Building slab (Lake Constance, Switzerland) | 2018 | Compensate for addition of new recesses, EUB strip | IR |

*Notes* GT—gas torch; IR—infrared; ER—electrical resistivity; EUB—external-unbonded; NSM—near-surface-mounted; CRM—cover replacement method heat to not damage adjacent material. For instance, Fe-SMA installed with an additional protective layer for corrosion protection should not be heated beyond 165 °C (re-fer AG 2020b).

## *4.3 Installation and Strengthening Methods*

The strips or bars can be fastened to a deficient RC structure in either an externally-unbonded (EUB), near-surface-mounted (NSM) or cover replacement (CR) method depending on design and site requirements. Once installed, the prestrained strips are heated by a gas torch (GT), however, if there are combustibles present or for more controlled heating, the strips can be heated by IR.

EUB is a fast and relatively simple means of prestressing existing RC structures. The ends of the Fe-SMA strip are mechanically anchored to the parent structure. In instances where additional fire protection is required, a special cement-based coating can be applied to the installed strips following activation. The ends are anchored with power-actuated fasteners. Still, alternate anchoring methods can be used in cases where those fasteners are not suitable. In the case for strengthening an office girder, rendered deficient after having two large holes drilled through it during a renovation access was extremely limited. The consultant designed a custom steel U-shaped shoe for anchoring the strip to the girder (re-fer AG 2021a). EUB is also advantageous relative to other strengthening techniques in instances where a rapid intervention is desired as was the case for a girder shown in Fig. 1a of a bridge on a national road in Mörschwil, Switzerland. Traffic under the bridge needed to be diverted during repairs, and the strengthening was reported complete in only 2 hours

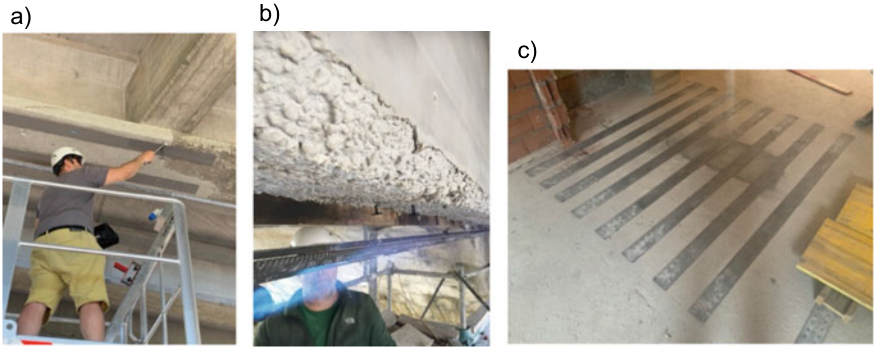

**Fig. 1** Externally unbonded Fe-SMA strips are installed for flexural strengthening of a bridge girder in Mörschwil, Switzerland (**a**), and a slab in Boncourt, Switzerland (**c**). The surface of a girder has been hydromechanically removed for strengthening in Courrendlin, Switzerland, using the cover replacement method (**b**). The reason for strengthening was corroded reinforcement and insufficient load-carrying capacity (**a**), destroyed prestressing strands and replacement of reinforcement (**b**), and insufficient internal reinforcement (**c**)

(re-fer AG 2020a). In another case, installation of EUB strips is shown in Fig. 1 for a negative moment region strengthening of a slab in Boncourt, Switzerland. The slab required strengthening due to having insufficient internal reinforcement.

The NSM method requires more surface preparation. Shallow grooves (approx. 3 cm × 3 cm) are cut on the surface to accept the strengthening material, usually deformed bars. The ends of the bars are fixed with mortar. Once the mortar is cured, the bars are heated by GT or IR and allowed to cool. Once cool, the remaining free length of the grooves is filled with mortar to allow composite action of the reinforcement. The deformed bars offer a similar bond to that of conventional rebar and therefore, the bars and mortar in the grooves act compositely with the parent structure.

The CR method requires the surface to be hydromechanically roughened to allow an effective bond between the repair mortar and the parent structure as shown in Fig. 1b for a bridge girder in Courrendlin, Switzerland. Once roughened, the ends of the bars are cast in spray mortar and then are heated and allowed to cool, prestressing the parent structure. Once cooled, the free length of the bars is covered in spray mortar.

Steel or concrete composite girders can be strengthened with externally unbonded smooth Fe-SMA rods, which in this case, are mechanically coupled and end-anchored.

### 4.4 *Finishes*

Once the prestressing is complete, cement-based grout is inserted into the grooves or free surface, additional fire protection spray plaster can be applied to the strips material. This is a requirement for EUB installations (re-fer AG 2020b).

## 5 Discussion

Looking at the latest projects reported in Table 2, it is clear, there are many applications of using Fe-SMA to prestress RC structures. It is worth noting the technology has also been used for strengthening RC concrete in shear and seismic loading (re-fer AG 2021b), however, this is outside the scope of this article. In total, re-fer AG advertises completing over 50 projects. To the best of the author's knowledge, the only other case study using Fe-SMA to prestress RC structures was in 2001 when Fe-SMA bars were used for shear strengthening a bridge girder in Michigan, USA (Soroushian et al. 2001). The variety of projects and installations shown in Table 2 demonstrate the versatility and flexibility of Fe-SMA strengthening systems.

Regarding practical heating methods in the field, ER is a widely used method for heating SMA in experiments in the literature, however, it is seldom used in practice.

The small resistivity of Fe-SMA requires a substantial amount of energy for sufficient heating. This amount is likely not practical for field application. This is evident from the case studies as the last project which used ER was in 2017. It is reported in the literature that heating two, Fe-SMA-8 mm diameter ribbed bars, (2.5 m long) required 324 kJ of energy over 22 s (Shahverdi et al. 2016). The most popular heating method seems to be GT which is not surprising as it is easily attainable and requires limited equipment. IR is the second most popular heating method but requires custom IR units provided by re-fer AG.

## 6 New Ideas

Heating by IR and GT is clearly the most popular heating methods according to the latest case studies. However, the surrounding material is also heated, resulting in wasted energy. Induction heating is an alternate heating method whichheats metal directly and the surrounding material is less affected by residual heat. Commercially available induction stove tops leave the stove top cool-to-the-touch almost immediately, after boiling a pot of water. Industrial induction heaters for cutting metal can be held by hand while it is being cut. These are examples of the potential of using this heating method for heating Fe-SMA. The energy would be focused on heating only the Fe-SMA, it would not heat the surrounding material and it would undoubtedly heat the Fe-SMA more efficiently.

It has been reported in the literature the total recovery stress generated can be reached in multiple increments (Shahverdi et al. 2018) depending on the activation temperature. Theoretically, designers could not only restore load-carrying capacity to the structure but equip them with additional reserves of prestress. These reserves could be commissioned at any point in the future simply by heating to the temperature required for the next increment. The reserves could also be used to recover prestress losses due to elastic shortening of the concrete and relaxation of the Fe-SMA. It would be interesting to see this implemented in practice.

## 7 Conclusion and Outlook

Prestressed strengthening with Fe-SMA is proving to be an outstanding strengthening technique as it addresses several challenges with active strengthening. The ability to prestress a deficient structure by installing the prestrained product and heating it on-site eliminates the need for heavy jacking equipment and proper anchorage. There is also no prestress loss due to friction, and the anchoring techniques discussed in this article have been shown to withstand the full recovery stress, with minimal anchorage setting and removal of original material to place the strengthening system. Furthermore, there is an improved economic and environmental benefit as the strengthening material is easily recycled and re-introduced into the steel casting cycle upon deconstruction The motivation of this article is to increase awareness of this novel strengthening technique and encourage additional contributions to advance the knowledge and continue to improve the technology. A brief history as and overview of the SME mechanism was discussed. The latest relevant examples of this technology being used in the field, demonstrates the real-world problems this technology resolves, and hopefully encourages a conversation of its feasibility and practicality. This way, the rest of the world could benefit from this strengthening technology just like Switzerland.

**Acknowledgements** This work was supported by Mitacs through the Mitacs Accelerate Program, Alberta Innovates, and National Science and Engineering Research Council of Canada.

## References

Bansiddhi, Sargeant, Stupp, Dunand (2008) Porous niti for bone implants: a review. Acta Biomater 4(4):773–782

Biesiekierski, Wang, Gepreel, Wen (2012) A new look at biomedical ti-based shape memory alloys. Acta Biomater 8(5):1661–1669

Bil, Massey, Abdullah (2013) Wing morphing control with shape memory alloy actuators. J Intell Mater Syst Struct 24(7):879–898

Buehler, Wang (1968) A summary of recent research on the nitinol alloys and their potential application in ocean engineering. Ocean Eng 1(1):105IN7109–7108IN10120

Dotter, Buschmann, Mckinney, Rosch (1983) Transluminal expandable nitinol coil stent grafting: preliminary report. Radiology 147(1):259–260

El-Hacha, Rojob (2018) Flexural strengthening of large-scale reinforced concrete beams using near-surface-mounted self-prestressed iron-based shape-memory alloy strips. PCI J 63(6):55–65

El-Hacha, Soudki (2013a) Prestressed near-surface mounted fibre reinforced polymer reinforcement for concrete structures—a review. Can J Civil Eng 40(11):1127–1139

Ghafoori, Neuenschwander, Shahverdi, Czaderski, Fontana (2019) Elevated temperature behavior of an iron-based shape memory alloy used for prestressed strengthening of civil structures. Constr Build Mater 211:437–452

Hong, Lee, Yeon, Jung (2018) Flexural response of reinforced concrete beams strengthened with near-surface-mounted fe-based shape-memory alloy strips. Int J Concrete Struct Mater 12(1):45

Janke, Czaderski, Motavalli, Ruth (2005) Applications of shape memory alloys in civil engineering structures—overview, limits and new ideas. Mater Struct 38(279): 578–592

Kuribayashi (1989). *Millimeter size joint actuator using shape memory alloy*. In: IEEE micro electro mechanical systems. Proceedings, 'An Investigation of Micro Structures, Sensors, Actuators, Machines and Robots'

Leinenbach, Czaderski, Michels, Graf, Kawalla (2016a) Development of rolling technology for an iron-based shape-memory-alloy. Mater Sci Forum 854:79–86

Leinenbach, Motavalli, Weber, Lee, Bronnimann and Czaderski (2017) Method for building prestressed concrete structures by means of profiles consisting of a shape-memory alloy, and structure produced using said method. United States, 9,758,968, 13

Michels, Shahverdi, Czaderski (2018a) Flexural strengthening of structural concrete with iron-based shape memory alloy strips. Struct Concrete 19(3):876–891

Michels, Shahverdi, Czaderski, El-Hacha (2018b) Mechanical performance of iron-based shape-memory alloy ribbed bars for concrete prestressing. ACI Mater J 115(6):877–886

Mohd Jani, Leary, Subic, Gibson (2014) A review of shape memory alloy research, applications and opportunities. Mater Des (1980–2015) 56:1078–1113

Motavalli, Weber, Wookijn, Rolf, Christoph C, Leinenbach C, Michels J, Shahverdi (2019) Method for producing prestressed structures and structural parts by means of sma tension elements, and structure and structural part equipped therewith, United States, 10,246,887, 11

Pfeifer, Muller, Hurschler, Kaierle, Wesling, Haferkamp (2013b) Adaptable orthopedic shape memory implants. In: First Cirp conference on biomanufacturing, vol 5, no January 1, pp 253–258

re-fer Ag (2021a) Flexural strengthening of a reinforced concrete girder in an office building, April. https://www.re-fer.eu/en/referenz/flexural-strengthening-of-a-reinforced-concrete-girder-in-an-office-building/. Accessed 30 Apr 2021a

re-fer Ag (2019) Product data sheet: Re-bar

re-fer Ag (2020a) National road, mörschwil (ch), August 31. https://www.re-fer.eu/en/referenz/national-road-moerschwil/. Accessed 30 Apr 2021

re-fer Ag (2020b). Product data sheet: Re-plate

re-fer Ag (2021b) Referenzen|referenzobjekte. https://www.re-fer.eu/referenzen/. Accessed 30 Apr 2021

Rojob, El-Hacha (2017a) Self-prestressing using fe-sma for flexural strengthening of reinforced concrete beams. ACI Struct J 114(2):523

Rojob, El-Hacha (2017b) Self-prestressing using iron-based shape memory alloy for flexural strengthening of reinforced concrete beams. Aci Struct J 114(2):523–532

Rojob, El-Hacha (2018) Performance of rc beams strengthened with self-prestressed fe-sma bars exposed to freeze-thaw cycles and sustained load. Eng Struct 169:107–118

Sato, Soma, Chishima, Mori (1982) Shape memory effect and mechanical-behavior of an fe-30mn-1si alloy single-crystal. J De Physique 43(Nc-4):797–802

Shahverdi, Czaderski, Annen, Motavalli (2016b) Strengthening of RC beams by iron-based shape memory alloy bars embedded in a shotcrete layer. Eng Struct 117:263–273

Shahverdi, Michels, Czaderski, Motavalli (2018) Iron-based shape memory alloy strips for strengthening rc members: Material behavior and characterization. Constr Build Mater 173:586–599

Soroushian, Ostowari, Nossoni, Chowdhury (2001) Repair and strengthening of concrete structures through application of corrective posttensioning forces with shape memory alloys. Des Struct 1770(1770):20–26

Stoeckel (1990) Shape memory actuators for automotive applications. Mater Des 11(6):302–307

Strittmatter, Gumpel (2011) Long-time stability of ni-ti-shape memory alloys for automotive safety systems. J Mater Eng Perform 20(4–5):506–510

Thompson (2000) An overview of nickel-titanium alloys used in dentistry. Int Endodontic J 33(4):297–310

Turner, Buehrle, Cano, Fleming (2006) Modeling, fabrication, and testing of a sma hybrid composite jet engine chevron concept. J Intell Mater Syst Struct 17(6):483–497

# GFRP Reinforced Precast Concrete Tunnel Lining Segments Under Flexural Cyclic Loading

**Basil Ibrahim, Salaheldin Mousa, Hamdy M. Mohamed, and Brahim Benmokrane**

## 1 Introduction

At the back of the tunnel-boring machine (TBM), in soft ground and weak rock tunnel constructions, precast concrete segments are used to support the tunnel bone. Combined tunnel segments, as part of a one-pass liner system, provide ground support against the tunnel-boring machine. These tunnel segments are designed to resist both the ground/groundwater permanent loads, and the production and construction temporary loads. To reduce the formwork/unit cost of the tunnel lining construction, precast concrete tunnel lining segments can be produced in reusable molds, cured, and then assembled inside the shield of the TBM to form full tunnel segmental rings.

Fiber-reinforced-polymer (FRP) composites are being seriously considered as the replacement for steel rebars in some structural concrete members to improve durability, facilitate the manufacturing process, reduce the self-weight, and provide magnetic permeability. The use of FRP reinforcement has been extensively investigated and used as reinforcement in concrete structures (Mousa et al. 2018, 2019, 2020; Humar and Razaqpur 2000; Yoo et al. 2015; Coccia et al. 2017). Current design

---

B. Ibrahim · S. Mousa · H. M. Mohamed (✉) · B. Benmokrane
Department of Civil and Building Engineering, University of Sherbrooke, Sherbrooke, QC, Canada
e-mail: Hamdy.Mohamed@Usherbrooke.ca

B. Ibrahim
e-mail: Basil.Ibrahim@usherbrooke.ca

S. Mousa
e-mail: Salaheldin.Mousa@Usherbrooke.ca

B. Benmokrane
e-mail: Brahim.Benmokrane@Usherbrooke.ca

S. Mousa
Department of Civil & Building Engineering, University of Sherbrooke, Sherbrooke, Canada

B. Benmokrane et al. (eds.), *8th International Conference on Advanced Composite Materials in Bridges and Structures*, Lecture Notes in Civil Engineering 267,
https://doi.org/10.1007/978-3-031-09409-5_17

codes and guidelines such as ACI 440.1R (2015), CSA S806 (2012), and CSA S6 (2019) allow the use of GFRP, CFRP, and AFRP as the main reinforcement in concrete structures and provide design recommendations for using these bars. However, these design provisions are not applicable to precast segmental tunnel linings reinforced with FRP bars.

To examine the possibility of replacing the traditional steel reinforced concrete precast tunnel segments with fiber bar reinforced concrete elements, Caratelli et al. (2016) experimentally investigated the behavior of GFRP reinforced precast concrete tunnel segments in terms of quality and cost reduction. The results of the study showed that the GFRP tunnel segments exhibited a better cracking control behavior compared to the traditional reinforced concrete segments, where the load related to the first crack formation was higher and the crack openings were reduced. Therefore, for this kind of structure, where the cracking limitations are the primary concern, the fiber-reinforced concrete tunnel segments can be successfully adopted. Moreover, Spagnuolo et al. (2017) performed full-scale bending tests on concrete tunnel segments reinforced with GFRP and compared their structural performance with control segments reinforced with steel bars. The experimental results showed that there is no significant difference in the flexural behavior of the GFRP reinforced segments compared to the steel reinforced ones. Substantively, the increase in the strength of the GFRP bars compensates the lack of ductility compared to the steel reinforced segments. In addition, the warning of failure in the GFRP reinforced segments is guaranteed by the extensive cracking, as the GFRP bars experience significant elongation before failure. Moreover, they have stated in their study that using the GFRP reinforcement in precast concrete tunnel segments appears to be a promising solution.

To further examine the feasibility and efficiency of using GFRP instead of steel as flexural, shear, and compression reinforcements for precast segmental tunnel linings, this study investigates the behavior of precast concrete tunnel segments reinforced with GFRP bars under cyclic flexural loading.

## *1.1 Materials*

The GFRP reinforcements employed in this study for the GFRP specimen were manufactured by the pultrusion process. GFRP bars #5 and GFRP ties #4 were used as longitudinal and transverse reinforcement, respectively. The GFRP bars and ties have a sand-coated surface, to enhance bond and force transfer between bars and concrete. Two steel bar diameters were used to reinforce the control specimen. Deformed 15 M steel bars were used as longitudinal reinforcement and deformed 10 M steel bars were used as ties. The mechanical properties of the GFRP and the steel bars used in this study are shown in Table 1, as reported by the manufacturers.

The two specimens were cast using normal-weight, ready-mixed concrete with a target compressive strength of 35 MPa. The concrete mix design is shown in Table 2.

**Table 1** Mechanical properties of the GFRP and steel reinforcement

| Reinforcement type | $d_b$ (mm) | $A_f$ (mm$^2$) | $E_f$ (GPa) | $f_{fu}$ (MPa) | $\varepsilon_{fu}$ (%) |
|---|---|---|---|---|---|
| GFRP ties #4 | 13 | 129 | 46 | 1000 | 2.17 |
| GFRP bars #5 | 15 | 198 | 46 | 1000 | 2.17 |
| Steel ties 10 M | 11 | 100 | $E_s = 200.0$ | $f_y = 480$ | $\varepsilon_y = 0.24$ |
| Steel bars 15 M | 16 | 200 | $E_s = 200.0$ | $f_y = 460$ | $\varepsilon_y = 0.23$ |

**Table 2** Concrete mix design

| Type of concrete | Cement (Kg/m$^3$) | Sand (Kg/m$^3$) | Limestone (ml/m$^3$) | Superplasticizer (ml/m$^3$) | Air entrainment (ml/m$^3$) | Water (L/m$^3$) |
|---|---|---|---|---|---|---|
| NSC | 450 | 615 | 1015 | 4500 | 140 | 170 |

**Table 3** Test matrix and details of the test specimens

| Specimen ID | Concrete strength (MPa) | Bar and Stirrup type | Flexural reinforcement | | Shear reinforcement | |
|---|---|---|---|---|---|---|
| | | | Bottom | Top | Bar size | Spacing mm |
| GFRP | 35 | GFRP | 7 No. 5 | 7 No. 5 | #4 | 200 |
| Steel | 35 | Steel | 7 bars 15 M | 7 bars 15 M | 10 M | 200 |

## 1.2 Test Specimens

A total of two full-scale precast concrete tunnel segments (one reinforced with GFRP bars and ties, and one with steel reinforcement) were constructed and tested under flexural cyclic loading. Table 3 provides the test matrix and reinforcement details of the test specimens. The length and width of the segments are 3100 mm and 1500 mm, respectively, while the thickness is 250 mm as shown in Fig. 1.

## 1.3 Test Setup

The test setup was designed and fabricated at the University of Sherbrooke's Canada Foundation for Innovation (CFI) structural laboratory. The specimens were loaded with a three-point bending load, as shown in Fig. 2, using an MTS 11,000 kN universal testing machine. The load was applied at a displacement-controlled rate of 0.8 mm/min. Quasi-static compressive loading has been applied in terms of the percentage of calculated maximum displacement. Two cycles of loading and unloading were conducted for 1.25, 2.5, 5, 10, 25, 50, and 75% of the maximum estimated displacement. Subsequently, one cycle of loading up to failure was conducted. Specimen deflection was measured using a linear potentiometer (LPOT) placed at

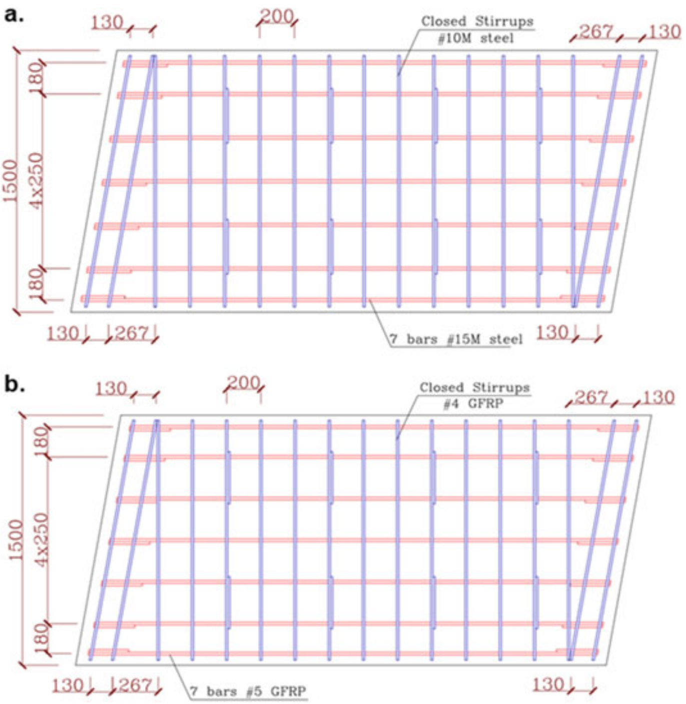

**Fig. 1** **a** GFRP specimen; **b** Steel specimen

**Fig. 2** Test setup

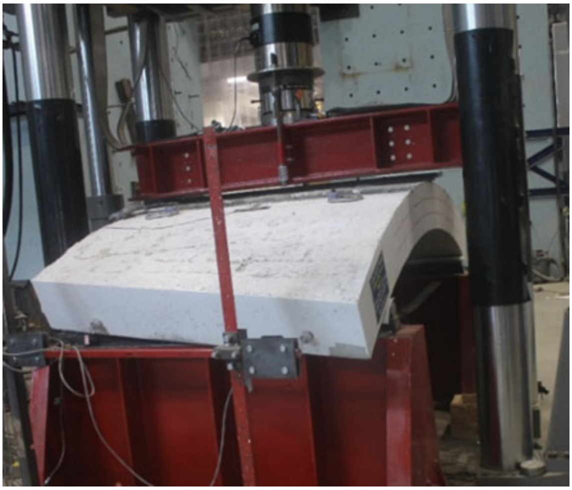

the mid-span. An automatic data-acquisition system monitored by a computer was used to record the readings of the LPOT and load cells.

## 2 Test Results and Discussion

### 2.1 General Behavior of the Test Specimens

The hysteresis behavior of both the GFRP and the steel reinforced PCTL specimens is shown in the form of load versus mid-span deflection, as shown in Fig. 3. Before cracking occurred, both GFRP and steel reinforced PCLT specimens exhibited the same linear load–deflection behavior, corresponding to the condition of the uncracked section. Similar pre-cracked behavior of the GFRP and the steel reinforced PCTL specimens is in good agreement with the experimental observations of Elgabbas et al. (2016). Beyond cracking, at 5% of the maximum displacement cycles, the stiffness of the GFRP reinforced PCTL specimen decreased with almost linear load–deflection behavior. The GFRP reinforced PCLT specimen failed due to concrete crushing at an ultimate load-carrying capacity of 271 kN. As illustrated in Fig. 3, the GFRP reinforced PCTL specimen exhibited a post-peak behavior and continued to sustain loads corresponding to the contribution of the compression reinforcement bars in enhancing the specimen's ductility and strength. On the other hand, the stiffness of the steel reinforced PCTL segment has reduced, by the yielding of the longitudinal reinforcement in the tension zone of the specimen at a load level of 140 kN, followed by a gradual decrease in the specimens' overall stiffness. Thereafter, the steel reinforced PCTL specimen continued to sustain additional loads with reduced stiffness up until the top concrete fibers crushed at a load level of 271 kN. The GFRP reinforced PCTL specimen recovered most of its deflection during the unloading of the 50%

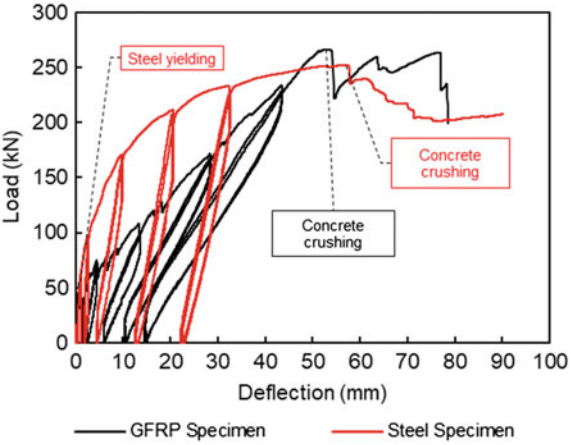

**Fig. 3** Load–deflection behavior of the tested specimens

and 75% of the maximum displacement cycles, while a permanent deflection was recorded in the unloading of the steel reinforced PCTL specimen by reaching 50% of the maximum displacement cycle, due to the yielding of the steel reinforcement bars in the tension zone.

## *2.2 Flexural Capacity and Failure Mode*

The GFRP reinforced PCTL specimen failed due to concrete crushing in the compression zone at the loading point, while the steel reinforced PCTL specimen failed due to yielding of the longitudinal steel reinforcement bars, followed by concrete crushing. The cracking pattern of both specimens (GFRP and steel) is shown in Fig. 4. The first vertical flexural crack in the GFRP reinforced PCTL specimen was initiated in the tension zone under the point of loading at a load level of 60 kN in the first 5% of the maximum displacement cycle. At 10% and 25% of the maximum displacement cycles, the flexural cracks in the GFRP reinforced PCTL specimen grew within the shear span of the specimen. Thereafter, at the first 75% of the maximum displacement cycle, the main flexural crack in the GFRP reinforced PCTL specimen widened and propagated toward the loading point. Beyond 75% of the maximum displacement cycles, the cracks along the shear span of the GFRP reinforced PCTL specimen started to incline toward the point of loading up until the failure occurred. The peak load recorded at the concrete crushing was 271 kN for the GFRP specimen. In contrast, the yielding of the tension bars in the steel specimen resulted in wider concentrated cracks at the tension zone. Yielding of the longitudinal reinforcement at the tension zone occurred at a load level of 140 kN in the first 50% of the maximum displacement cycle, followed by a reduction in the specimen's stiffness. By reaching a load level of about 252 kN, the concrete crushed in the compression zone. Overall, the flexural strength at the concrete crushing of the GFRP specimen was almost 1.8 times greater than that of the steel specimen at steel yielding with similar reinforcement.

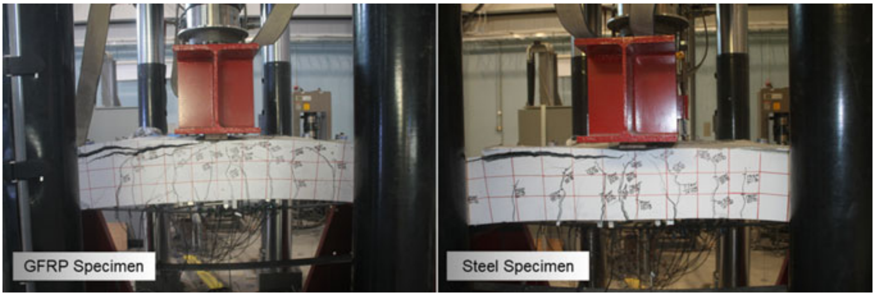

**Fig. 4** Failure modes of the test specimens

This flexural capacity ratio of the GFRP reinforced PCTL specimen to the steel reinforced PCTL specimen fits within the flexural capacity ratios of the BFRP-RC to the steel-RC members (1.74–2.19) obtained by Elgabbas et al. (2017).

## 3 Conclusions

1. The GFRP reinforced PCTL specimen failed due to concrete crushing in the compression zone at the loading point, while the steel reinforced PCTL specimen failed due to yielding of the longitudinal steel reinforcement bars, followed by concrete crushing.
2. The flexural strength at the concrete crushing of the GFRP reinforced PCTL specimen was almost 1.8 times greater than that of the steel reinforced PCTL specimen at steel yielding with similar reinforcement.
3. The GFRP reinforced specimen behaved linearly until cracking and almost linearly between cracking and concrete crushing, with reduced stiffness. Moreover, the GFRP reinforced PCTL specimen exhibited a post-peak behavior and continued to sustain loads corresponding to the contribution of the compression reinforcement bars in enhancing the specimen's ductility and strength.
4. The results of the current study show the efficiency of using GFRP bars as internal reinforcement for precast concrete segmental tunnel linings under cyclic flexural loading as an alternative to conventional steel reinforcement.

**Acknowledgements** This research was conducted with funding from the Natural Sciences and Engineering Research Council of Canada (NSERC), Mathematics of Information Technology and Complex Systems (MITACS), the Fonds de recherche du Québec en nature et technologies (FRQ-NT), Pole de Recherche et d'innovation en Materiaux Avances au quebéc (PRIMA Quebéc), and the Tier-1 Canada Research Chair in Advanced Composite Materials for Civil Structures. The authors are grateful to the precast company (Sym-Tech Béton Préfabriqué, Sainte-Hyacinthe, QC, Canada) and to the GFRP bar manufacturer (Pultrall Inc., Thetford Mines, QC, Canada) for their effective involvement in this project, and to the technical staff of the structural lab in the Department of Civil Engineering at the University of Sherbrooke.

## References

ACI (American Concrete Institute) (2015) Guide for the design and construction of structural concrete reinforced with fiber-reinforced polymer (FRP) Bars. ACI 440.1R-15, Farmington Hills, MI

Canadian Standards Association (2012) Design and construction of building structures with fibre-reinforced polymers. CAN/CSA-S806-12

Canadian Standards Association (2019) Canadian highway bridge design code. CAN/CSA-S6–19

Caratelli A, Meda A, Rinaldi Z, Spagnuolo S (2016) Precast tunnel segments with GFRP reinforcement. Tunn Undergr Space Technol 60:10–20

Coccia S, Meda A, Rinaldi Z, Spagnuolo S (2017) Influence of GFRP skin reinforcement on the crack evolution in RC ties. Compos B Eng 119:90–100

Elgabbas F, Vincent P, Ahmed EA, Benmokrane B (2016) Experimental testing of basalt-fiber-reinforced polymer bars in concrete beams. Compos B Eng 91:205–218

Elgabbas F, Ahmed EA, Benmokrane B (2017) Flexural behavior of concrete beams reinforced with ribbed basalt-FRP bars under static loads. J Compos Constr 21(3):04016098

Humar JL, Razaqpur AG (2000) Advanced Composite Materials in Bridges and Structures. 3rd International Conference Hardcover – January 1, 2000

Mousa S, Mohamed HM, Benmokrane B (2018) Flexural strength and design analysis of circular reinforced concrete members with glass fiber-reinforced polymer bars and spirals. ACI Struct J 115(5):1353–1364

Mousa S, Mohamed HM, Benmokrane B (2019) Cracking and crack control in circular concrete bridge members reinforced with fiber-reinforced-polymer bars. ASCE J. Bridge Eng. 24(1):04018108

Mousa S, Mohamed HM, Benmokrane B, Nanni A (2020) Flexural behavior of long span square reinforced concrete members with uniformly distributed fiber-reinforced polymer bars. ACI Struct J 117(4):209–222

Spagnuolo S, Meda A, Rinaldi Z, Nanni A (2017) Precast concrete tunnel segments with GFRP reinforcement. J Compos Constr 21(5):04017020

Yoo DY, Kwon KY, Park JJ, Yoon YS (2015) Local bond-slip response of GFRP rebar in ultra-high-performance fiber-reinforced concrete. Compos Struct 120:53–64

# Durability of GFRP-RC Square Columns in Severe Marine Environment

**Ahmed Elhamaymy, Hamdy M. Mohamed, and Brahim Benmokrane**

## 1 Introduction

Marine structures such as bridge piers/columns, coastal buildings, and harbor wharfs are vigorously prone to corrosion side effects on concrete due to chloride and sulfate attack. For repairing the damages that occur due to steel corrosion in RC-structures, the United States (USA) spends annually around $276 billion. Many methods have been used for eliminating steel corrosion such as epoxy coating or cathodic protection. In fact, it was found that these methods do not prevent corrosion, however, they delay it. Since the GFRP bars have proved their efficiency in the corrosive environment, GFRP reinforcing bars are widely used instead of steel in constructing many bridges in Canada and the United States. For example, in 1999, Canada constructed the first marine structure (Hall's Harbor Wharf) using GFRP bars and hybrid reinforcement (steel and GFRP bars). All codes and guidelines stipulate that columns should be contained longitudinal and transverse reinforcement, even if the concrete cross-section can withstand the applied load. Therefore, the integrity of the internal reinforcement in corrosive environments is a significant issue for studying (Mousa et al. 2019, 2020; Mohamed and Benmokrane 2014).

Although there are many valuable experimental attempts to investigate the behavior of concrete columns internally reinforced with FRP bars and spirals (Tobbi et al. 2012; Pantalides et al. 2013; Afifi et al. 2014, 2015; Mohamed et al. 2014; Hadi

---

A. Elhamaymy · H. M. Mohamed (✉) · B. Benmokrane
Department of Civil and Building Engineering, University of Sherbrooke, Sherbrooke, QC, Canada
e-mail: Hamdy.Mohamed@Usherbrooke.ca

A. Elhamaymy
e-mail: Ahmed.Elhamaymy@Usherbrooke.ca

B. Benmokrane
e-mail: Brahim.Benmokrane@Usherbrooke.ca

B. Benmokrane et al. (eds.), *8th International Conference on Advanced Composite Materials in Bridges and Structures*, Lecture Notes in Civil Engineering 267,
https://doi.org/10.1007/978-3-031-09409-5_18

et al. 2016; Hadhood et al. 2017a, b, c; Guérin et al. 2018; Abdelazim et al. 2020a, b, c, d), few studies were conducted to assess the durability of GFRP-RC columns in severe marine environments. Wei et al. (2018) evaluated the effect of using GFRP bars as longitudinal reinforcement on the ability of the concrete column to resist seawater attack. This was performed by immersing square concrete columns reinforced longitudinally with GFRP bars and transversely with steel ties in the simulated marine environment (17.5% salt concentration) at room temperature for 120 days. The results showed that after 120 days, the steel ties corroded, causing some deterioration in the concrete cover. Simultaneously, the GFRP bars were intact and can resist the applied load. Due to corrosion cracks developed in the concrete cover, the conditioned columns lost about 18% of the axial capacity of their reference counterparts. Moreover, it was found that, as the exposure period increased, the bond between bars and concrete gradually decreased. Another study was conducted by Zhou et al. (2018). This study aimed at investigating the effect of using seawater in mixing and curing on the behavior of concrete cylindrical columns fully reinforced with GFRP bars and spirals after exposure to seawater for 84 days. Three types of water with different salt concentrations (26.5, 3.5, 0% NaCl) were used for mixing, and two (3.5, 0% NaCl) for curing. The results indicated that the GFRP spirals were still intact and bonded to the concrete, providing adequate confinement for the concrete core. Moreover, the columns cast with water containing high salt concentration (26.5%) suffered a deterioration that reached 27.9% in load-carrying capacity and enhancement of 104% in the ductility. Based on this literature, the experimental research on the concentric performance of GFRP-RC columns in the marine environment is limited, which accentuates the significance of conducting more experimental work to study other parameters.

## 2 Experimental Program

### *2.1 Materials*

The GFRP bars and spirals were manufactured by a pultrusion process using continuous E-glass fibers impregnated in a thermosetting vinyl-ester resin. The GFRP bars and spirals have a sand-coated surface, as shown in Fig. 1, to enhance bond and

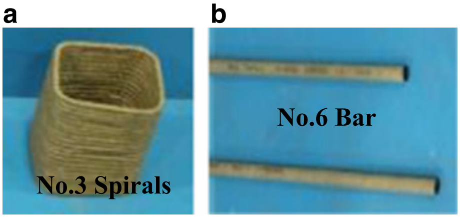

**Fig. 1** **a** GFRP spirals; **b** GFRP bars

**Table 1** Mechanical properties of the GFRP bars and spirals

| Bar size | Diameter (mm) | Area[a] ($mm^2$) | Elastic tensile modulus[b] (GPa) | Nominal tensile strength (MPa) | Tensile strain (%) |
|---|---|---|---|---|---|
| #3 (spirals) | 9.5 | 71 | 52.5 | 1328 | 2.3 |
| #6 | 19 | 285 | 52.5 | 1194 | 2.3 |

[a] Nominal area
[b] Using Nominal area

force transfer between bars and concrete. GFRP bars #6 and GFRP square spirals #3 were used as longitudinal and transverse reinforcement, respectively. Table 1 gives the mechanical proprieties of GFRP bars and spirals used in this study, as reported by the manufacturer. A single batch of ready-mixed normal-strength, normal-weight concrete with a maximum aggregate size of 20 mm was used to cast all the columns in an upright position. The w/c ratio was 0.35. The measured average concrete compressive strength after 12 months from casting were 42 MPa and 53 MPa for reference and conditioned specimens, respectively.

## 2.2 *Specimens Details and Conditioning Method*

A total of 4 laboratory-scale square concrete columns with GFRP reinforcement were constructed, conditioned, and tested under monotonic static concentrically axial loading. All of the columns had 300 mm width and 1000 mm height. All specimens had 35 mm clear concrete cover above the square spirals, which was set using a plastic wheel spacer. All columns were transversely reinforced with square spirals spaced each 125 mm at the middle and became tighter at the ends (60 mm). The four columns were listed in two groups according to longitudinal reinforcement ratio and distribution. Each group contains two specimens with the same reinforcement configuration, to assess the effect of the exposure to the simulated severe marine environment on the behavior and axial capacity of columns. The specimens in the first group (G1) were reinforced with eight (8) bars size No.6 (comprising 2.5% of cross-section area (Ag)), while those in the second group (G2) were constructed with four (4) bars size No. 6 (comprising 1.25% of cross-section area (Ag)) (G2). The size of longitudinal GFRP bars was set to comply with the least permitted size to use in columns (not less than No. 5), as specified in CSA-S6-19. Figure 2a, b illustrates the reinforcement configuration and concrete dimensions for specimens in G1 and G2. The test matrix and conditioning routine are presented in Table 2.

A wide wooden tank was fabricated and lined with a thick polyethylene sheet to accommodate two GFRP-RC square column specimens, as seen in Fig. 2c. After installing the conditioned two specimens inside the tank, the tanks were filled with a saline solution, which was prepared by mixing 35 g of dry salt (NaCl) for each

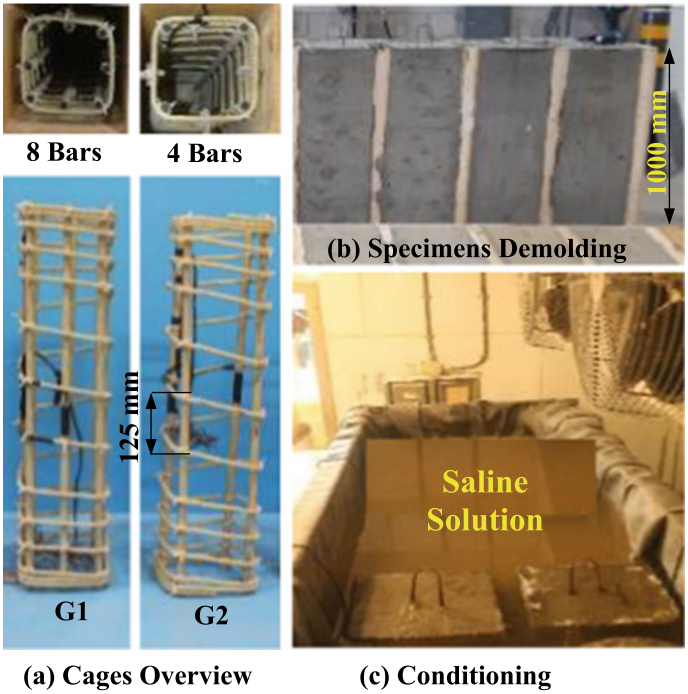

(a) Cages Overview (c) Conditioning

**Fig. 2** Specimen preparation and conditioning methods

**Table 2** Test matrix, specimen's details, conditioning routine, and test results

| Specimen ID | Conditioning regime | Longitudinal reinforcement | | Transverse reinforcement | | | $P_{peak}$ (kN) | $P_{peak}/(f_c' A_g)$ |
|---|---|---|---|---|---|---|---|---|
| | Saline solution (3.5% NaCl) | $\rho_L$ (%) | Number of bars | $\rho_T$ (%) | Bar size | Pitch (mm) | | |
| G1-8N6 | Reference | 2.5 | 8 No. 6 | 1.1 | No. 3 | 125 | 3550 | 0.93 |
| G1-8N6-60 | 60 °C | | | | | | 4350 | 0.91 |
| G2-4N6 | Reference | 1.25 | 4 No. 6 | | | | 3450 | 0.93 |
| G2-4N6-60 | 60 °C | | | | | | 4300 | 0.89 |

G1 or G2 refers to reinforcement layout; Bars number (8 or 4) and size (#6); conditioning temperature (60 °C)

kilogram of water to simulate the marine environment. The tank was stored inside a large temperature chamber to provide heat waves at 60 °C. This temperature was assigned to accelerate the degradation process as usual for GFRP bar accelerated aging tests. Eventually, the specimens were removed from the tanks and prepared for testing after 12 months.

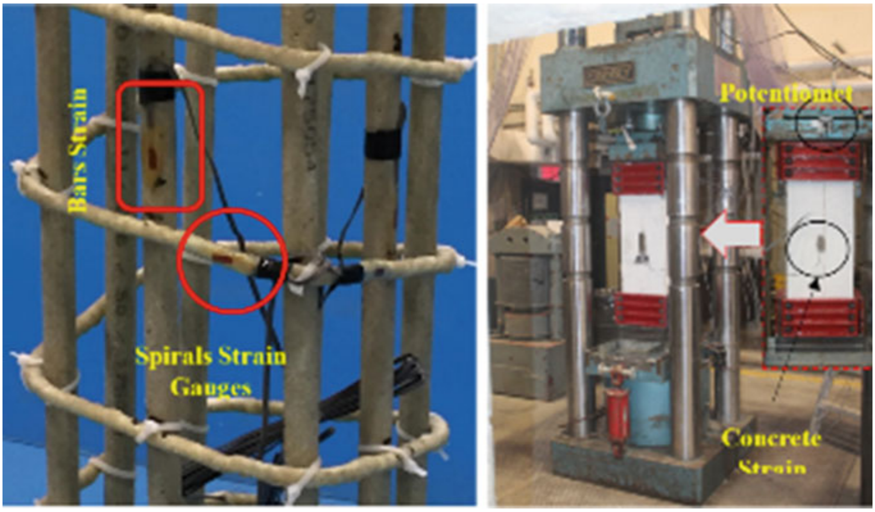

**Fig. 3** Instrumentation and test setup

### *2.3 Instrumentation and Test Setup*

All specimens were instrumented to measure the axial deformations as well as the local strains in the longitudinal bars, spirals, and concrete surface. All of the strain gauges were located at the mid-height of the columns, where the maximum strain values are expected. Two strain gauges (60 mm) were pasted on GFRP bars, and two were glued on spirals nearby the bent portion. Externally, two 100 mm strain gauges were put on the concrete surface to capture the axial compressive strain of two opposite sides. Moreover, two LPOTs were mounted between the machine wedges to capture the axial deformation during the test (see Fig. 3). The column specimens were tested with a 6000 kN MTS testing machine with a constant loading rate of 1.5 kN/s up to the failure, then the loading was manually controlled.

## 3 Test Results and Discussion

### *3.1 Failure Mode*

Figure 4 illustrates the failure modes of the reference and conditioned GFRP-RC columns after removing the load. The failure modes of all the columns could be split into two main stages. Stage one is represented by concrete rupture initiated by gradual cover spalling accompanied by a significant reduction in the load-carrying capacity of the tested column. The cracks appeared on the concrete cover when the

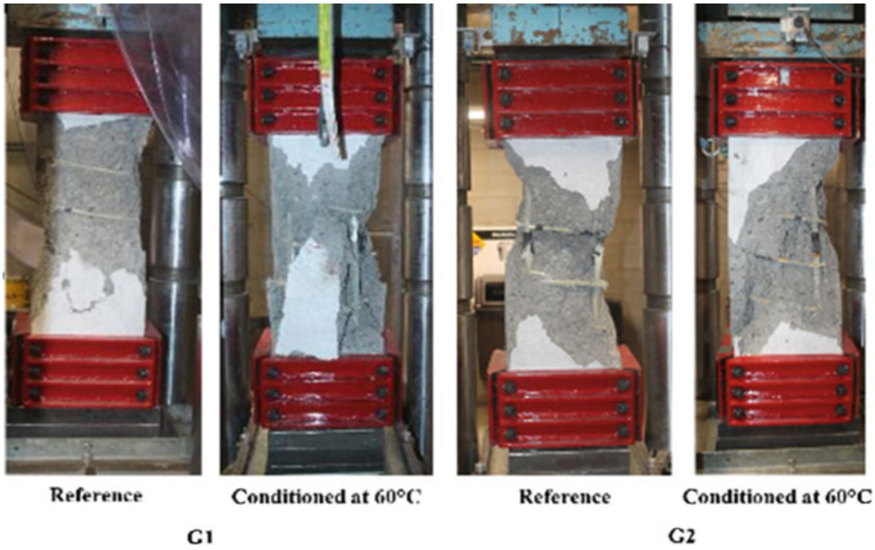

**Fig. 4** Failure mode of reference and conditioned GFRP-RC columns

load had reached approximately 90% of the peak load. These cracks rapidly widened and propagated, causing the concrete cover to spall off. The submerged GFRP-RC columns lost more load-carrying capacity after the initial spalling of the concrete cover. The second failure stage of the column corresponds to the rupture of the core components. After the peak, the core components (vertical bars and concrete) are intensively loaded to compensate the reduction in load due to cover spalling. This phenomenon led to activating the spirals to provide sufficient confinement for the concrete core and prevent the vertical bars from buckling. The failure of the core component started with the spiral's rupture at the bent portion, followed by a buckling of the longitudinal bars, and ended with concrete core crushing, as seen in Fig. 4. For specimens reinforced with four (4) vertical bars, the failure was more violent than those constructed with eight (8) bars, especially after the conditioning (see Fig. 4).

## 3.2 *Effect of Conditioning on the Load-Carrying Capacity and Axial Deformations*

Figure 5a–b depicts the comparison between the axial load–deformation relationships of the tested, unconditioned, and the submerged GFRP-RC columns for G1 and G2, respectively. The load-carrying capacity of the reference and conditioned GFRP-RC columns are summarized in Table 2. As expected, the elastic load–deformation diagram was linear during the initial loading state and up to around 85% of the

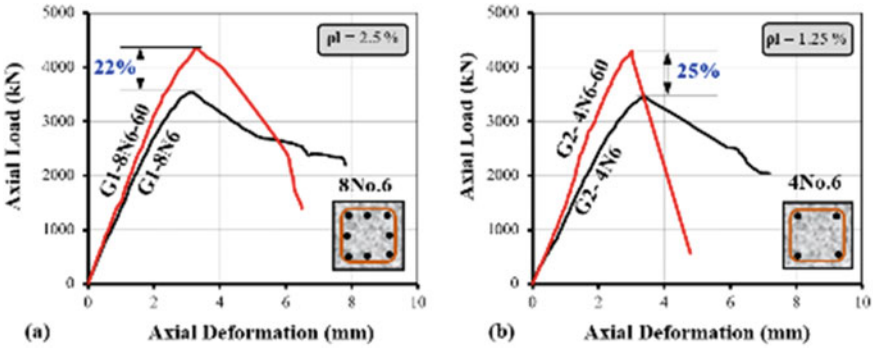

**Fig. 5** Axial load–deformation curves for conditioned and unconditioned columns

maximum peak load. The improvement ratios in the load-carrying capacity of the columns after the exposure to the simulated severe marine environment (60 °C) are illustrated in Fig. 5a–b. These improvements were 22% and 25% of the load-carrying capacity of their unconditioned counterparts in G1 and G2, respectively. The enhancement in the load-carrying capacity was due to the increase in the concrete compressive strength, as observed by testing some concrete cylinders exposed to the same conditions as the tested conditioned specimens. The enhancements in strength reflect the positive impact of moisture and temperature on the hydration process of unhydrated cement (Pantelides et al. 2013; Mukherjee and Arwikar 2005; Hamza et al. 2017). Moreover, chloride ions contributed to this improvement by reacting with the hydration products to produce salt-containing chlorine, which fills the concrete pores, leading to an increase in concrete strength (Wei et al. 2018). On the other hand, the average recorded compressive bar strain at the maximum load-carrying capacity was 3300 $\mu\varepsilon$ and 2400 $\mu\varepsilon$ (14% and 9.5% of the ultimate tensile GFRP-bar strain) for unconditioned and conditioned specimens, respectively. Despite the reduction in the measured strain in bars in conditioned specimens, the level of compressive strain in the GFRP bars in the conditioned is slightly higher than the allowable strain of 2000 με specified in CSA/S6-19 for determining the contribution of GFRP bars to the axial capacity of concrete compression members. Due to increasing the concrete strength, the contribution of the GFRP bars to load-carrying capacity decreased. Up to the peak load, the GFRP reinforcing bars did not exhibit any signs of buckling. This is indicating that GFRP spirals are intact and can provide the stability for longitudinal bars. Moreover, increasing the longitudinal reinforcement ratio does not significantly affect the axial capacity of the conditioned specimens, however, it can enhance the post-peak response.

**Fig. 6** Image taken by OM for the interface between concrete and GFRP bars for the extracted concrete covers from columns conditioned at 60 °C

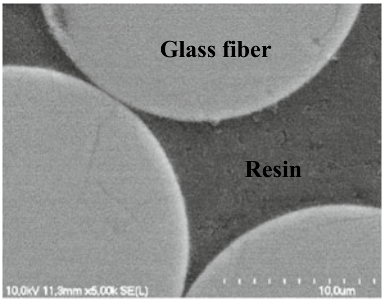

**Fig. 7** Image taken by SEM for the interface between single fibers and resin matrix of bars extracted from columns conditioned at 60 °C

## 4 Microstructural Analysis

The bond between concrete and GFRP bars is significant for providing the composite action. In addition, the integrity of the surface between concrete and GFRP bars could also be used as an index for the integrity of the glass fibers and matrix resin at the bar's edge. The interface between concrete and GFRP bars was examined by the optical microscopic (OM) technique, while the interface between single fibers and resin matrix was checked by the scanning electronic microscopy (SEM) technique. Figures 6 and 7 show the images obtained by OM and SEM, respectively. OM image indicated that there are no signs of debonding between concrete and bars after immersion in the simulated marine environment at 60 °C for 12 months as well as the SEM results showed that the fibers and resin were not affected by conditioning. This indicates that the concrete cover acted as a protective barrier for internal reinforcement.

## 5 Conclusions

1. Considering the test results, the axial capacity of the submerged columns increased as a result of an increase in concrete compressive strength. The column specimens submerged in the marine environments at 60 °C achieved, on average, 123%, respectively, of the axial load capacity of their unconditioned counterparts.

2. Increasing the GFRP reinforcement ratio and using GFRP spirals improved the post-peak response.
3. Despite the reduction in the measured strain in bars in conditioned specimens, the level of compressive strain in the GFRP bars in the conditioned is slightly higher than the allowable strain of 2000 με specified in CSA/S6-19 for determining the contribution of GFRP bars to the axial capacity of concrete compression members.
4. The optical microscopy (OM) observations indicate that the 365 days of immersion in a marine environment produced no evidence of debonding between the GFRP bars and the surrounding concrete.
5. The SEM micrographs revealed no signs of degradation of the GFRP reinforcement bars and no debonding at the fiber/resin interface.

**Acknowledgements** The authors would like to express their special thanks and gratitude to the Natural Science and Engineering Research Council of Canada (NSERC), Canada Research Chair Program, the Fonds de la recherche du Quebec–Nature et Technologie—(FRQ-NT), the University of Sherbrooke Research Centre on FRP Composite Materials for Structures (CRUSMaC) for their financial support, and Pultrall Inc. (Thetford Mines, QC, Canada) for the donation of the GFRP reinforcement. The authors thank the technical staff of the Canada Foundation for Innovation (CFI) structural laboratory in the Department of Civil Engineering at the University of Sherbrooke.

## References

Abdelazim W, Mohamed HM, Afifi MZ, Benmokrane B (2020a) Proposed slenderness limit for GFRP-RC columns based on experiments and buckling analysis. ACI Struct J 117(1), January 2020a

Abdelazim W, Mohamed HM, Benmokrane B (2020b) Inelastic second-order analysis for slender GFRP-reinforced concrete columns: experimental investigations and theoretical study. J Compos Construct, ASCE 24(3):04020016

Abdelazim W, Mohamed HM, Benmokrane B, Afifi MZ (2020c) Effect of critical test parameters on behavior of glass fiber-reinforced polymer-reinforced concrete slender columns under eccentric load. ACI Struct J 117(4), July 2020d

Abdelazim W, Mohamed HM, Benmokrane B (2020d) Strength of bridge high-strength concrete slender compression members reinforced with GFRP bars and spirals: experiments and second-order analysis. J Bridge Eng, ASCE 25(9):04020066

Afifi MZ, Mohamed HM, Benmokrane B (2014) Axial capacity of circular concrete columns reinforced with GFRP bars and spirals. J Compos Construct, ASCE 18(1):04013017

Afifi MZ, Mohamed HM, Chaallal O, Benmokrane B (2015) Confinement model for concrete columns internally confined with carbon FRP spirals and hoops. J Struct Eng 141(9):04014219. https://doi.org/10.1061/(ASCE)ST.1943-541X.0001197

Canadian Standards Association (CSA) (2012) Design and construction of building components with fiber reinforced polymers. CAN/CSAS806-12, Mississauga, Ontario, Canada, 198 pp

Guérin M, Mohamed HM, Benmokrane B, Shield CK, Nanni A (2018) Effect of glass fiber-reinforced polymer reinforcement ratio on axial-flexural strength of reinforced concrete columns. ACI Struct J 115(4):1049–1061

Hadhood A, Mohamed HM, Ghrib F, Benmokrane B (2017c) Efficiency of glass-fiber reinforced-polymer (GFRP) discrete hoops and bars in concrete columns under combined axial and flexural loads. Compos B Eng 114(6):223–236

Hadhood A, Mohamed HM, Benmokrane B (2017b) Experimental study of circular high-strength concrete columns reinforced with GFRP bars and spirals under concentric and eccentric loading. J Compos Construct, ASCE 21(2):04016078

Hadhood A, Mohamed HM, Benmokrane B (2017a) Axial load-moment interaction diagram of circular concrete columns reinforced with CFRP bars and spirals: experimental and theoretical investigations. J Compos Construct, ASCE 21(2):04016092

Hadi MN, Karim H, Sheikh MN (2016) Experimental investigations on circular concrete columns reinforced with GFRP bars and spirals under different loading conditions. J Compos Construct, ASCE 20(4):04016009. https://doi.org/10.1061/(ASCE)CC.1943-5614.0000670

Hamza A, Derogar S, Ince C (2017) The effects of silica fume and hydrated lime on the strength development and durability characteristics of concrete under hot water curing condition. In: MATEC web of conferences, vol 120. EDP Sciences, p 2004

Mohamed HM, Benmokrane B (2014) Design and performance of reinforced concrete water chlorination tank totally reinforced with GFRP bars: case study. J Compos Construct 18(1):05013001. https://doi.org/10.1061/(ASCE)CC.1943-5614.0000429

Mohamed HM, Afifi MZ, Benmokrane B (2014) Performance evaluation of concrete columns reinforced longitudinally with FRP bars and confined with FRP hoops and spirals under axial load. J Bridge Eng 19(7):04014020

Mousa S, Mohamed HM, Benmokrane B (2019) Strength and deformability aspects of circular concrete members reinforced with hybrid carbon-FRP and glass-FRP under flexure. J Compos Construct 23(2):04019005

Mousa S, Mohamed HM, Benmokrane B, Nanni A (2020) Flexural behavior of long-span square reinforced concrete members with uniformly distributed fiber-reinforced polymer bars. ACI Struct J 117(4):209–222

Mukherjee A, Arwikar SJ (2005) Performance of glass fiber-reinforced polymer reinforcing bars in tropical environments—Part I: Structural scale tests. ACI Struct J 102(5):745

Pantelides CP, Gibbons ME, Reaveley LD (2013) Axial load behavior of concrete columns confined with GFRP spirals. J Compos Construct, ASCE 17(3):305–313

Tobbi H, Farghaly AS, Benmokrane B (2012) Concrete columns reinforced longitudinally and transversally with GFRP bars. ACI Struct J 109(4):551–558

Wei M, Sun L, Zhang C, Wang Q (2018) Effect of seawater exposure on compressive behavior of concrete columns reinforced longitudinally with glass fiber reinforced polymer bars. J Compos Mater 52(17):2289–2299

Zhou A, Chow CL, Lau D (2018) Structural Behavior of GFRP reinforced concrete columns under the influence of chloride at casting and service stages. Compos B Eng 136:1–9

# Behavior of Concentrically Loaded GFRP-RC Circular Hollow Columns with Varying Transverse Reinforcement Ratios

**Mohammed Gamal Gouda, Hamdy M. Mohamed, Allan C. Manalo, and Brahim Benmokrane**

## 1 Introduction

Hollow reinforced concrete columns have been used in the past in place of their solid counterparts in the construction of bridges (columns, piles, and bridge piers). These hollow columns have several benefits over solid columns including higher structural performance than solid concrete columns in terms of stiffness-to-weight and strength-to-weight ratios (Liang et al. 2015). In addition, hollow concrete columns (HCCs) can be the solution to maximize strength–mass and stiffness–mass ratios and to reduce the mass contribution of the column to the seismic response and demand on foundations. Such members are usually reinforced with conventional steel bars and spirals or ties. Steel reinforcement has a limited-service life and entails high maintenance costs due to corrosion when used in aggressive and/or harsh marine environments. This high cost has spurred interest in alternative noncorrosive reinforcing materials such as fiber-reinforced polymer (FRP) bars. FRP bars offer many advantages over conventional steel bars, including a density of one-quarter to one-fifth that of steel,

---

M. G. Gouda · H. M. Mohamed (✉) · B. Benmokrane
Department of Civil and Building Engineering, University of Sherbrooke, Sherbrooke, QC, Canada
e-mail: Hamdy.Mohamed@Usherbrooke.ca

M. G. Gouda
e-mail: Mohammed.Gamal.Gouda.Hassaan@Usherbrooke.ca

B. Benmokrane
e-mail: Brahim.Bemokrane@Usherbrooke.ca

A. C. Manalo
School of Civil Engineering and Surveying, University of Southern Queensland, Toowoomba, Australia
e-mail: Allan.Manalo@usq.edu.au

B. Benmokrane et al. (eds.), *8th International Conference on Advanced Composite Materials in Bridges and Structures*, Lecture Notes in Civil Engineering 267,
https://doi.org/10.1007/978-3-031-09409-5_19

greater tensile strength than steel, and no corrosion even in harsh chemical environments (Chaallal and Benmokrane 1993; Maranan et al. 2016). Several studies were presented to investigate the behavior of FRP-RC columns under concentric and eccentric loading (Affi et al. 2015; Hadhood et al. 2017a, b; Salah-Eldin et al. 2019a, b). Recent studies also extended to evaluate the behavior of concrete columns reinforced with fiber-reinforced polymer (FRP) bars but were cast with the lightweight concrete (known as LWSCC: lightweight-aggregate self-consolidating concrete columns), as conducted by Bakouregui et al. (2021).

Several experimental studies were focused on investigating the behavior of FRP-RC solid columns loaded under concentric axial load (De Luca et al. 2010; Afifi 2013; Tobbi et al. 2014; Affi et al. 2014; Afifi et al. (2013) Abdelazim et al. 2020a, b, c, d). They concluded that the FRP-RC columns behaved in a similar manner to the steel RC columns counterparts, and there was no noticeable difference concerning the peak capacity. Afifi et al. (2014) revealed that the failure of the solid GFRP-RC columns reinforced with a spiral spacing of 120 mm (i.e., a volumetric ratio of 0.7%) was triggered by the buckling of the longitudinal bar. In contrast, the failure of the well-confined corresponding columns reinforced with a narrower spiral spacing of 80 or 40 mm was controlled by the crushing of the concrete core, followed by rupture of the GFRP spirals. Testing of GFRP-RC columns of the rectangular section is done to evaluate the configuration and spacing of transverse reinforcement (Tobbi et al. 2014). The test results indicated that the confinement efficiency was increased with smaller tie spacing, where the reduction in tie spacing from 120 to 80 mm (4.72–3.15 in.) yielded a strength gain of more than 20%. De Luca et al. (2010) concluded that the failure of the GFRP-RC column reinforced with tie pitched at 305 mm (12 in.) was sudden and accompanied by an explosive noise. The 76 mm (3 in.) spacing of the GFRP ties did not increase the ultimate capacity load but enhanced the confinement efficacy in the post-peak phase, where ssing GFRP ties and spirals was found to be efficient in limiting the initiation and propagation of cracks, the buckling of the longitudinal bars, and the crushing of the concrete core (Pantelides et al. 2013; Mohamed et al. 2014). Based on these studies, it has been concluded that the spacing of transverse reinforcement is the main design parameter that controls HCC performance. Tabatabaei et al. (2018) investigated the performance of lap spliced GFRP bars in RC solid circular columns. The test results indicated that the suitable splice length for GFRP bars #5 (15.90 mm, in diameter) was $8d_b$.

Limited research work has been conducted on hollow concrete columns reinforced with GFRP reinforcements. The influence of volumetric ratio on the performance of GFRP-RC hollow columns was studied by AlAjarmeh (2020a, b) and Hadi et al. (2021). The test findings revealed that increasing the volumetric ratio by decreasing the spiral spacing led to an increase in the ultimate load-carrying capacity, improving the column's ductility due to the high lateral confining efficiency. Hadi et al. (2021) concluded that the columns reinforced with a GFRP spiral with a spacing of 30 mm attained 46 and 66% higher confinement efficiency and ductility, respectively, than the column with a spiral's pitch of 90 mm. The objective of this study was to obtain experimental data and to better understand the behavior and failure mechanics of full-scale hollow concrete columns reinforced with GFRP bars and spirals tested under axial load. The effect of the transverse reinforcement ratio was investigated. The experimental data provide the evidence required to include design provisions in the forthcoming ACI 440 code for the use of GFRP bars and spirals as internal reinforcement in concentrically loaded hollow concrete compression members.

## 2 Experimental Program

### *2.1 Design of Test Specimens*

Four full-scale circular reinforced hollow concrete columns were prepared and tested to investigate the influence of the transverse reinforcement ratio $\rho_t$ (represented by the spacing of spirals) under pure axial loading. Three columns were reinforced in the transverse direction with GFRP spirals No. 3 (9.5 mm diameter) at different spiral's pitch $s$ mm ($\rho_t$ %) of 120 mm (0.75%), 80 mm (1.10%), and 40 mm (2.20%). One column was fabricated with no spirals to serve as a control specimen. All columns were reinforced with eight GFRP bars No. 5 (15.9 mm diameter) as a longitudinal reinforcement. These columns were designed with a hollow circular cross-section where the outside diameter of the columns was 305 mm, the inner diameter was 113 mm ($D_{in.}/D_{out.} = 0.37$), and the height was 1500 mm. Concrete cover for all tested columns was maintained at 27.50 mm. The GFRP-RC columns were designed based on the requirements of CSA/CAN S806-12 code. Figure 1 displays the specimen's details, GFRP-reinforcement cage, and final installation of the column specimen on the FORNEY machine. Table 1 lists the test matrix and the reinforcement details for all columns.

### *2.2 Materials*

Sand-coated GFRP bars and spirals were employed in this study No. 5 (15.90 mm, nominal diameter) as longitudinal reinforcement and No. 3 (9.50 mm, nominal diameter) as transverse reinforcement, respectively, as presented in Fig. 1. The GFRP reinforcements were manufactured by (Pultral Inc. 2012). All columns were cast with a single batch of nominal 35 MPa ready-mix normal-weight concrete with a maximum aggregate size of 10 mm. During casting, the concrete was compacted to ensure adequate consistency of the concrete paste. The average compressive strength of concrete was computed in terms of the characteristic compressive strength of ten 100 mm × 200 mm cylinders samples cured under the same conditions as the column specimens and examined after 28 days mandated by ASTM C39/C39M (2012). Table 2 reports the material properties of the GFRP, as provided by the manufacturer.

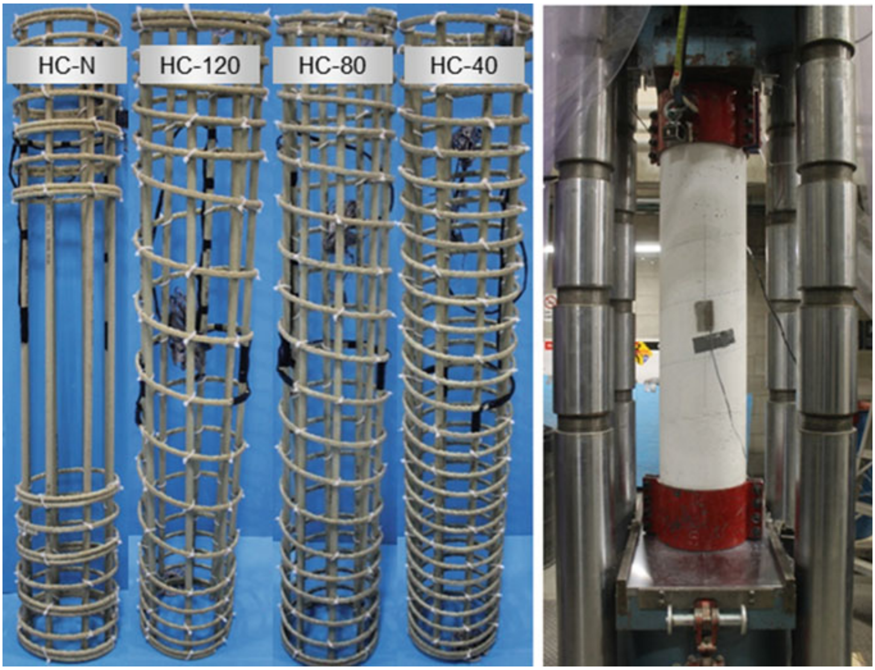

**Fig. 1** Test setup and GFRP cages

**Table 1** Test matrix and specimen details

| Column ID | Longitudinal reinforcement | Transverse reinforcement | | | |
|---|---|---|---|---|---|
| | | Type | *Bar #* | *s* mm | $\rho_t$ (%) |
| HC-N | 8 GFRP #5 | – | – | – | – |
| HC-120 | 8 GFRP #5 | GFRP spiral | 3 | 120 | 0.75 |
| HC-80 | 8 GFRP #5 | GFRP spiral | 3 | 80 | 1.10 |
| HC-40 | 8 GFRP #5 | GFRP spiral | 3 | 40 | 2.20 |

**Table 2** Mechanical properties of the GFRP reinforcement

| Type | Bar size | Diameter (mm) | Nominal area ($mm^2$) | Elastic tensile modulus (GPa) | Tensile strength (MPa) | Tensile strain (%) |
|---|---|---|---|---|---|---|
| GFRP | #3 | 9.5 | 71 | 52.5 ± 2.5 | $f_{fu}$ = 1328 | 2.30 |
| | #5 | 15.9 | 199 | 54.9 ± 2.5 | $f_{fu}$ = 1289 | 2.40 |

### 2.3 Instrumentation and Testing

During the cage's preparation stage, four strain gauges with a length of 6 mm were mounted on the bars and spirals at mid-height of the cage to monitor the column responses, (see Fig. 1). Before testing, two concrete strain gauges 60 mm in length were fixed on the exterior surface at the column and almost parallel to the bars and spirals strains, as shown in Fig. 1. Finally, the applied axial load and the axial displacement were measured, respectively, with the machine's internal load cells and linear variable differential transformers (LVDTs). All instruments were connected to a data-acquisition system for continuous recording of results.

All the columns were tested under concentric loading with a 6000 kN capacity FORNEY machine in the Construction Facilities Laboratory of the Department of Civil Engineering at the University of Sherbrooke, as displayed in Fig. 1. Prior to testing, a 20 mm self-leveling cementitious grout was utilized to level the top and bottom ends of each column. Two rigid steel collars were fastened and clamped at the ends of the column to prevent any undesired local failure at these stress-concentration zones. Lastly, the column was placed in the middle of the Forney machine and the test was conducted with a load-controlled technique at a rate of 1.50 kN/s up to failure.

## 3 Test Results and Discussion

### 3.1 Failure Modes

The GFRP-RC hollow columns exhibited a compression failure in terms of concrete cover spalling, accompanied by a drop in the column capacity. Figure 2 shows the typical failure behavior of all tested columns. The failure started by hairline cracks that propagated along the column height as the applied load increased. Spalling of the concrete cover was then observed, followed by buckling or fracture of the longitudinal bars, and/or rupturing of the GFRP spirals. Lastly, damaging of the concrete core was observed. The stages of failure are explained in detail. Column HC-N, the concrete cover, and core spalled and failed at the same time in an explosive manner. Buckling in the longitudinal GFRP bars was observed without fracturing. This was attributed to the absence of transverse reinforcement that confined the GFRP bars. Limited spalling of the concrete cover appeared at the mid-height of column HC-120. It is also observed that the perimeter of HC-120 after the concrete cover spalled off at mid-height expanded in the lateral direction, accompanied by the fracturing of the longitudinal GFRP bars. Then, rupturing of one coil of the GFRP spiral was remarked, causing extensive damage to the concrete core. This behavior was also observed by AlAjarmeh et al. (2020a). In Column, HC-80, a gradual spalling of the concrete cover was noticed. The longitudinal bars and the concrete core were perfectly confined by the transverse reinforcement. So, the inner core did not deteriorate. Failure, lastly, was due to fractures in the GFRP bars. There was no observed damage to the lateral

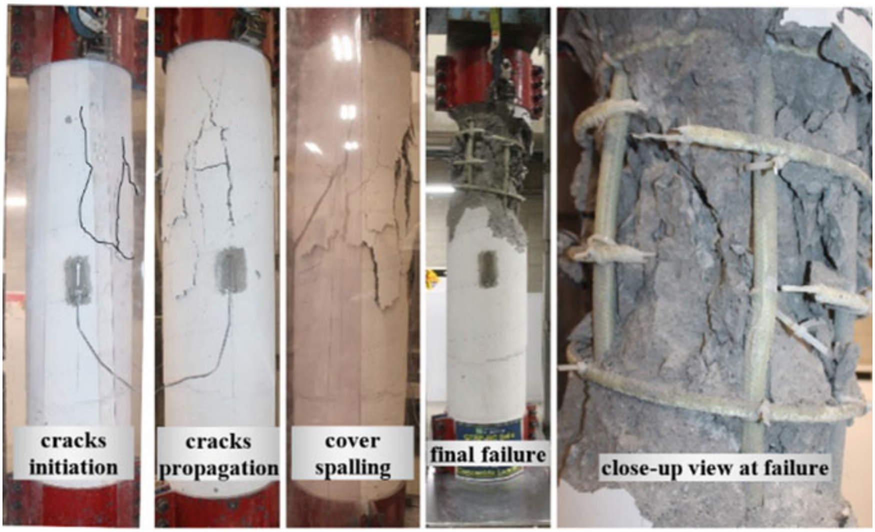

**Fig. 2** Failure mechanism of GFRP-RC hollow column

spiral. After the peak load of column HC-40, the concrete cover was completely spalled. The 40 mm GFRP spiral spacing kept the inner core well-confined, and no deterioration was noticed. Sequential fracturing of the longitudinal GFRP bars and rupturing of the lateral spiral at the top are due to the stress concentration. Figure 3 depicts close-up views of the tested columns at failure.

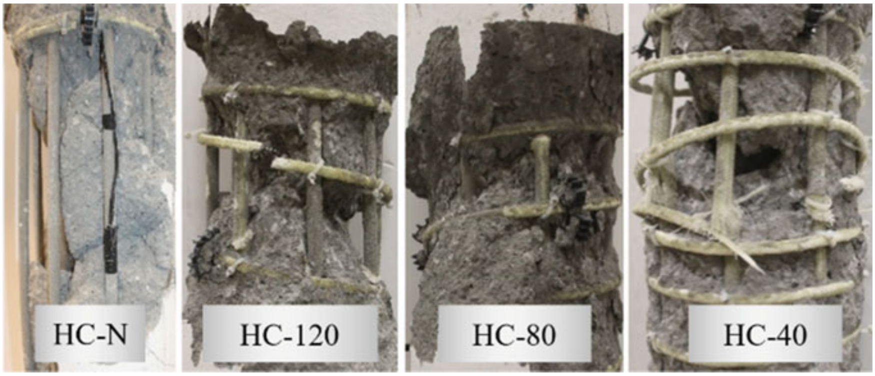

**Fig. 3** Close-up views of failure

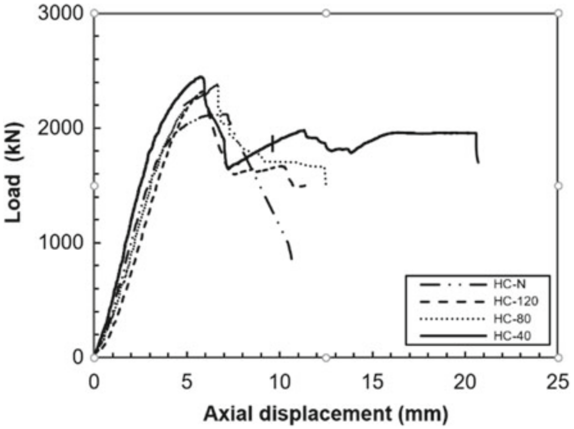

**Fig. 4** Load–displacement responses

## 3.2 Load Deformation Behavior

Figure 4 illustrates the relationship between the axial load versus the axial deformation. Before the cover spalling phase, the column specimens HC-N, HC-120, HC-80, and HC-40 behaved linearly until roughly 85% of their peak loads. A gradual loss of initial stiffness after these cracks propagated, providing a nonlinear ascending branch up to the peak loads 2150 kN, 2330 kN, 2380 kN, and 2450 kN, respectively. Afterward, a sudden load drop occurred due to the concrete cover spalling for columns HC-120, HC-80, and HC-40 by 30% of their peak loads. The applied load was transferred to the inner core, because of the GFRP spirals lateral confinement and contribution of the longitudinal bars in carrying the load, the load curve raised again until the second peak of 1670, 1700, and 2000 kN for the columns HC-120, HC-80, and HC-40. Table 3 summarizes the experimental test results.

## 3.3 Load–Strain Behavior

Figure 5 depicts the applied load to the induced strains response of the tested columns. At the peak load, the average axial compression strain monitored in the longitudinal bars was around 2900 με, which is about 12% of the ultimate tensile strain of the GFRP bars $\varepsilon_{frp,u}$, see Fig. 5a. Whereas the average bar strain at failure was about 7600 microstrains which is about 32% of $\varepsilon_{frp,u}$. These findings are consistent with the results mentioned by AlAjarmeh et al. (2020a). The average axial strains in the reinforcing bars were recorded and utilized to estimate the contributions of the compressive strength of the bars to the overall strength capacities, $P_{bars}$. $P_{bars}$ was computed based on the measured strain at the peak load, $\varepsilon_{bar}$, the cross-sectional area of the bar, $A_f$, and the bar's modulus, $E_f$. The ratios $P_{bars}/P_{exp.}$ are reported in Table 3. The average contribution of the GFRP bars in compression was around 11%

**Table 3** Experimental test results

| Column ID | Peak load | | | | | | Second peak load | | | Confinement efficiency | |
|---|---|---|---|---|---|---|---|---|---|---|---|
| | $P_{\text{Peak}}$ (kN) | $\varepsilon_c$ (microstrains) | $\varepsilon_{\text{bar}}$ (microstrains) | $\varepsilon_{\text{spiral}}$ (microstrains) | $\frac{P_{\text{bar}}}{P_{\text{Peak}}}$ (%) | $\sigma_{nor}$ (%) | $P_{\text{2nd}}$ (kN) | $\varepsilon_{nf,\text{bar}}$ (microstrains) | $\varepsilon_{nf,\text{spiral}}$ (microstrains) | $f'_{cc}$ (MPa) | $f'_{cc}/f'_{co}$ |
| HC-N | 2150 | −2400 | −2400 | – | 10 | 89 | – | – | – | – | – |
| HC-120 | 2330 | −2600 | −2450 | 250 | 9 | 97 | 1670 | −4300 | 4000 | 47 | 1.60 |
| HC-80 | 2380 | −2900 | −3500 | 500 | 13 | 95 | 1700 | −3700 | 10,000 | 48 | 1.63 |
| HC-40 | 2450 | −2700 | −3100 | 700 | 11 | 100 | 2000 | −14,800 | 14,000 | 57 | 1.90 |

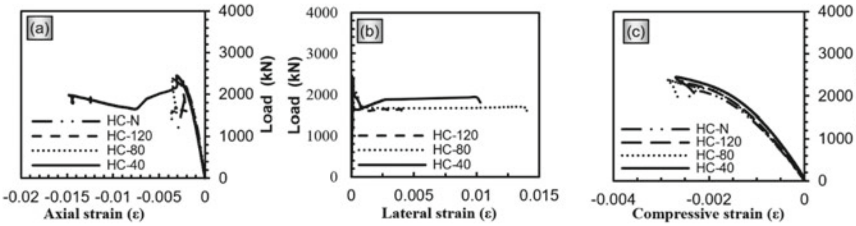

**Fig. 5** Load–strain behavior: **a** Bar axial strain, **b** spiral lateral strain, and **c** concrete compressive strain

of the experimental peak load, which contradicts with CAN/CSA S806-12, which neglects the compressive strength of the GFRP bars.

In terms of spiral strain, Table 3 and Fig. 5b. show that the lateral strain measured at the peak load ranged from 250 to 700. The lowest lateral strain at failure of 4000 με was recorded for column HC-120 because the wider spacing of the spiral caused limited concrete-core confinement. In other words, the (120 mm spacing) exhibited brittle behavior, with a faster degradation of the column's strength after the ultimate capacity accompanied by buckling of the longitudinal bars. As expected, the spiral strain of GFRP spirals was directly increased following the concrete cover spalling due to the activation of reinforcement confining pressure on the concrete core. So, the later strain for columns HC-80 and HC-40 at failure was 14,000 and 10,000 με.

Figure 5c shows that the concrete compressive strain for columns HC-N, HC-120, HC-80, and HC-40 at the peak load was 2400 με, 2600 με, 2900 με, and 2700 με, respectively. The concrete strain readings were affected and became unreliable upon the cracks widened and propagated. The failure modes of GFRP-RC columns were controlled by concrete crushing according to these measured strains, which are more than the concrete crushing strain of 2000 microstrains mandated by ACI 318 (2019).

## 4 Influence of the Transverse Reinforcement Ratio

The variation in the spacing of spirals influences the behavior of the tested GFRP-RC hollow columns. The closer spiral spacing (i.e., higher volumetric ratio) strongly affects the failure mode by delaying the longitudinal bars buckling, propagation of cracks, and concrete-core crushing. Furthermore, it increases the peak load and improves the confinement effectiveness and ductility. Three different spacings of spiral (120, 80, and 40 mm) were designed to investigate the effect of the transverse reinforcement ratio on the axial behavior of HCC. Columns HC-120, HC-80, and HC-40 have 8%, 11%, and 14%, respectively, higher peak load than HC-N.

After the peak load, the concrete core remained and uncracked until the second peak load due to the effectiveness of the spiral confinement. Equation (1) was presented to determine the confinement efficiency (C.E.).

$$C.E. = \frac{f'_{cc}}{f'_{co}} \tag{1}$$

where $f'_{cc}$ is the confined concrete compressive strength obtained from the second peak load. While $f'_{co}$ represents the unconfined concrete strength (0.85 $f'_c$). The test results indicated that the 40 mm spacing achieved its second peak load after overall concrete cover spalling, where column HC-40 attains 1.60 and 1.90 higher confinement efficacy than column HC-120 and HC-80, respectively.

## 5 Conclusions

The following conclusions can be drawn:

1. All tested GFRP-RC hollow concrete columns revealed a compression-controlled failure in terms of gradual concrete cover spalling.
2. The average contribution of the GFRP bars in compression was around 11% of the experimental peak load, which contradicts with the CSA S806-12, that neglects the compressive strength of the GFRP bars.
3. The average axial strain recorded in the GFRP longitudinal bars at the peak was about –2900 microstrains (12% of the bare-bar rupture strain).
4. The closer spiral spacing or higher volumetric ratio strongly influences the failure mode by delaying the buckling of the longitudinal bars, propagation of cracks, and crushing of the concrete core.
5. Increasing the transverse reinforcement ratio from 0.75 to 2.20% increases 8–14% in the peak and 1.60–1.90 in the confinement efficiency.
6. The ultimate capacity can be safely calculated for the GFRP-RC hollow columns by considering the contribution of the longitudinal GFRP bars of 0.002 mm/mm, as also provided by the CAN/CSA-S6-19 code.

**Acknowledgements** This research was conducted with funding from the Tier-1 Canada Research Chair in Advanced Composite Materials for Civil Structures, the Natural Sciences and Engineering Research Council of Canada (NSERC), and the Fonds de recherche du Québec en nature et technologies (FRQ-NT). The authors thank Pultrall Inc. (Thetford Mines, QC, Canada) for donating the GFRP reinforcement and the technical staff of the CFI structural laboratory in the Department of Civil Engineering at the University of Sherbrooke.

## References

ASTM (2012) Standard test method for compressive strength of cylindrical concrete specimens. ASTM C39/C39M-12, West Conshohocken, PA

Abdelazim W, Mohamed HM, Afifi MZ, Benmokrane B (2020a) Proposed slenderness limit for GFRP-RC columns based on experiments and buckling analysis. ACI Struct J 117(1), January 2020a

Abdelazim W, Mohamed HM, Benmokrane B (2020b) Inelastic second-order analysis for slender GFRP-reinforced concrete columns: experimental investigations and theoretical study. J Compos Construct, ASCE 24(3):04020016

Abdelazim W, Mohamed HM, Benmokrane B (2020c) Strength of bridge high-strength concrete slender compression members reinforced with GFRP bars and spirals: experiments and second-order analysis. J Bridge Eng, ASCE 25(9):04020066

Abdelazim W, Mohamed HM, Benmokrane B, Afifi MZ (2020d) Effect of critical test parameters on behavior of glass fiber-reinforced polymer-reinforced concrete slender columns under eccentric load. ACI Struct J 117(4), July 2020d

Afifi M, Mohamed HM, Benmokrane B (2013) Axial capacity of circular concrete columns reinforced with GFRP bars and spirals. J Compos Construct 18(1):04013017

Afifi MZ, Mohamed HM, Benmokrane B (2014) Axial capacity of circular concrete columns reinforced with GFRP bars and spirals. J Compos Construct 18(1):04013017. https://doi.org/10.1061/(asce)cc.1943-5614.0000438

Afifi MZ, Mohamed HM, Benmokrane B (2015) Theoretical stress–strain model for circular concrete columns confined by GFRP spirals and hoops. Eng Struct 102:202–213

Afifi M (2013) Behavior of circular concrete columns reinforced with FRP Bars and Stirrups (dissertation). Université de Sherbrooke

AlAjarmeh OS (2020a) Compressive behavior of hollow concrete columns reinforced with GFRP bars (dissertation). University of Southern Queensland

AlAjarmeh OS, Manalo AC, Benmokrane B, Karunasena W, Mendis P (2020b) Effect of spiral spacing and concrete strength on behavior of GFRP-reinforced hollow concrete columns. J Compos Construct 24(1):04019054

American Concrete Institute (ACI 440.1R-15) (2015) Guide for the design and construction of structural concrete reinforced with FRP bars. Farmington Hills, MI, 44 p

American Concrete Institute (ACI 318R-19) (2019) Building code requirements for structural concrete. ACI 318-14 and commentary. Farmington Hills, Mich

Bakouregui AS, Mohamed HM, Yahia A, Benmokrane B (2021) Axial load–moment interaction diagram of full-scale circular LWSCC columns reinforced with BFRP and GFRP bars and spirals: experimental and theoretical investigations. Eng Struct 242:112538

Canadian Standards Association (CAN/CSA S806-12) (2012) Design and construction of building structures with fibre-reinforced polymer. Canadian Standards Association, Toronto, Ontario, Canada, p 198

Canadian Standards Association (CAN/CSA S06-19) (2019) Canadian Highway Bridge Design Code, p 833

Chaallal O, Benmokrane B (1993) Physical and mechanical performance of an innovative glass-fiber-reinforced plastic rod for concrete and grouted anchorages. Can J Civ Eng 20(2):254–268

Hadhood A, Mohamed HM, Benmokrane B (2017a) Experimental study of circular high-strength concrete columns reinforced with GFRP bars and spirals under concentric and eccentric loading. J Compos Constr 21(2):04016078

Hadhood A, Mohamed HM, Benmokrane B (2017b) Strength of circular HSC columns reinforced internally with carbon-fiber-reinforced polymer bars under axial and eccentric loads. Construct Build Mater 141:366–378

Hadi MNS, Ahmad H, Sheikh MN (2021) Effect of using GFRP reinforcement on the behavior of hollow-core circular concrete columns. J Compos Construct 25(1):06020003. https://doi.org/10.1061/(asce)cc.1943-5614.0001103

Hadi MN, Karim H, Sheikh MN (2016) Experimental investigations on circular concrete columns reinforced with gfrp bars and helices under different loading conditions. J Compos Construct 20(4):1–12

Liang X, Beck R, Sritharan S (2015) Understanding the confined concrete behavior on the response of hollow bridge columns. Department of Civil, Construction and Environmental Engineering. Iowa State University, California Department of Transportation

De Luca A, Matta F, Nanni A (2010) Behavior of full-scale glass fiber-reinforced polymer reinforced concrete columns under axial load. ACI Struct J 107(5):589–596

Maranan G, Manalo A, Benmokrane B, Karunasena W, Mendis P (2016) Behavior of concentrically loaded geopolymer-concrete circular columns reinforced longitudinally and transversely with GFRP bars. Eng Struct 117:422–436

Mohamed HM, Afifi M, Benmokrane B (2014) Performance evaluation of concrete columns reinforced longitudinally with FRP bars and confined with FRP hoops and spirals under axial load. J Bridge Eng 19(7):04014020

Pantelides CP, Gibbons ME, Reaveley LD (2013) Axial load behavior of concrete columns confined with GFRP spirals. J Compos Construct 17(3):305–313

Pultrall Inc. (2012) Composite reinforcing rods technical data sheet. Thetford Mines, Canada, www.pultrall.com

Salah-Eldin A, Mohamed HM, Benmokrane B (2019a) Structural performance of high-strength-concrete columns reinforced with GFRP bars and ties subjected to eccentric loads. Eng Struct 185:286–300

Salah-Eldin A, Mohamed HM, Benmokrane B (2019b) Axial–flexural performance of high-strength-concrete bridge compression members reinforced with basalt-FRP bars and ties: Experimental and theoretical investigation. J Bridg Eng 24(7):04019069

Tabatabaei A, Eslami A, Mohamed HM, Benmokrane B (2018) Strength of compression lap-spliced GFRP bars in concrete columns with different splice lengths. Construct Build Mater Elsevier Ltd. 182:657–669

Tobbi H, Farghaly AS, Benmokrane B (2014) Behavior of concentrically loaded fiber-reinforced polymer reinforced concrete columns with varying reinforcement types and ratios. ACI Struct J 111:375

# Torsional Behavior of Concrete Box Girders Reinforced with Longitudinal GFRP Bars and Without Stirrups

**Ibrahim Mostafa, Salaheldin Mousa, Hamdy Mohamed, and Brahim Benmokrane**

## 1 Introduction

Numerous RC structural members in many structural applications are subjected to torsional moments that influence the design. However, spandrel beams in frame structures, curved bridge girders, eccentrically loaded box girders, a canopy or bus-stand roof beam, and helical stairway slabs are typical examples of torsional members. Generally, the torsional stresses are induced in a member when the moment acts about the longitudinal axis of this member. This moment called the torsional moment causes a rotation in the structural member and surface cracking, usually in a spiral shape. On the other hand, a concrete box girder is a significant structural element in many structural applications due to its higher torsional stiffness and low self-weight. The concrete box girders are considerably used in almost all types of bridges. Such structures are usually exposed to aggressive and/or harsh marine environments, leading to corrosion of the steel reinforcement. This type of corrosion in concrete structures is a prime cause of structural deterioration, particularly in North America, resulting in costly repairs, rehabilitation, and a considerable reduction in service life span.

---

I. Mostafa · S. Mousa · H. Mohamed (✉) · B. Benmokrane
Department of Civil and Building Engineering, University of Sherbrooke, Sherbrooke, QC, Canada
e-mail: Hamdy.mohamed@usherbrooke.ca

I. Mostafa
e-mail: Ibrahim.mostafa@usherbrooke.ca

S. Mousa
e-mail: Salaheldin.mousa@usherbrooke.ca

B. Benmokrane
e-mail: Brahim.Benmokrane@usherbrooke.ca

S. Mousa
Department of Civil & Building Engineering, University of Sherbrooke, Sherbrooke, Canada

B. Benmokrane et al. (eds.), *8th International Conference on Advanced Composite Materials in Bridges and Structures*, Lecture Notes in Civil Engineering 267,
https://doi.org/10.1007/978-3-031-09409-5_20

Fiber-reinforced polymer (FRP) reinforcing bars, on the other hand, can be used as a replacement for steel reinforcement to combat corrosion, thereby lowering maintenance costs and extending service life. There are numerous advantages to using FRP bars instead of steel bars, such as higher tensile strength, weight one-quarter to one-fifth lighter than steel, noncorroding nature, and longer service life than steel (ACI 440.1R-15). The last two decades have seen a rapid increase in the use of FRP reinforcing bars in many applications, such as bridges, piles, parking garages, marine structures, water tanks, and tunnels (Nanni and Faza 2002; Mohamed and Benmokrane 2014). Considerable research works have been conducted to investigate RC members' flexural, shear, and axial load behavior reinforced with FRP bars and stirrups (Hadhood et al. 2016; Mousa et al. 2018). However, restricted research programs have been conducted to investigate the torsional behavior of RC members reinforced with FRP reinforcement (Mohamed et al. 2014, Mohamed and Benmokrane 2015, Hadhood et al. 2020).

Mohamed et al. (2014) investigated the structural performance of large-scale RC beams reinforced with CFRP bars and stirrups subjected to pure torsional loading. Their results showed that the CFRP and steel RC beams experienced nearly the same torsional behavior in both phases pre- and post-cracking. Mohamed and Benmokrane (2015) demonstrated the torsional behavior of RC beams reinforced with and without FRP web reinforcement. Their investigation revealed that the change in the type of the longitudinal reinforcement did not affect the torsional strength and behavior. Moreover, the torsional failure of all beams without torsional reinforcement was dominated by concrete splitting irrespective of the type of reinforcement.

This study presents an experimental investigation to study the torsional behavior of RC box girders reinforced with GFRP and steel reinforcement. Two full-scale RC box girders were tested under a pure torsional moment. The girders included one box girder reinforced with longitudinal GFRP bars and one box girder reinforced with conventional longitudinal steel bars and without transverse reinforcement.

## 2 Experimental Program

### 2.1 *Specimen Details*

Two large-scale RC box girders without transverse torsional reinforcement were examined under a pure torsional moment. The test variable was the type of longitudinal reinforcement only, one girder constructed with GFRP reinforcement and the other one with steel reinforcement. All girders had the same dimensions, which were 4000 mm long, 380 mm wide, 380 mm deep, and 100 mm thick. These dimensions were selected so that there would be some similarity with the beams tested by Mitchell and Collins (1974) (PT5 and PT6). To avoid local failure before torsional failure, the test region was maintained constant at 2000 mm, and all girders had a 1000 mm extension outside the supports on each side as anchorage length. The

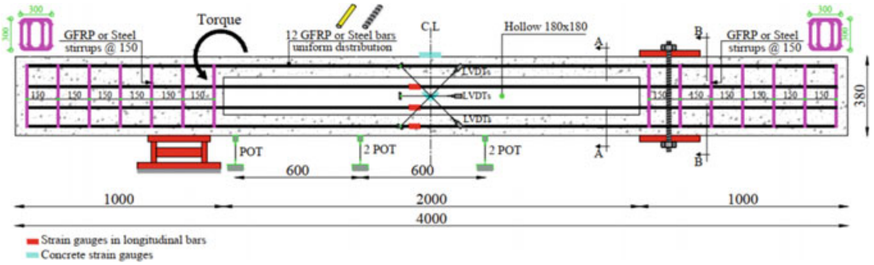

**Fig. 1** Details of the tested specimens

**Table 1** Test matrix and specimen details

| Girder ID | $f_c'$ (MPa) | Bar type | Longitudinal torsional reinforcement (uniform distribution) | $\rho_L$ (%) |
|---|---|---|---|---|
| BGW-12 | 44.5 | GFRP | 12 bars #5 | 1.66 |
| BGW-12 | 44.5 | Steel | 12 bars M15 | 1.66 |

concrete dimensions and reinforcement details are shown in Fig. 1. All girders had the same longitudinal reinforcement ratio of 1.66%. The concrete cover was maintained constant at 40 mm around all box girders. Table 1 gives the reinforcement details of the box girders. The specimens were designated with this pattern: the letter B refers to the girder specimen, the letters G and S stand for GFRP or steel as longitudinal reinforcement, and the letter W indicates specimens without transverse reinforcement. The number stands for the total number of longitudinal bars in each specimen.

## 2.2 Materials Properties

The GFRP bars employed in this study were manufactured and developed by Pultrall Inc. (Thetford Mines, QC, Canada). The GFRP bars had a sand-coated surface, as shown in Fig. 2, to improve the bond performance and force transfer between the bars

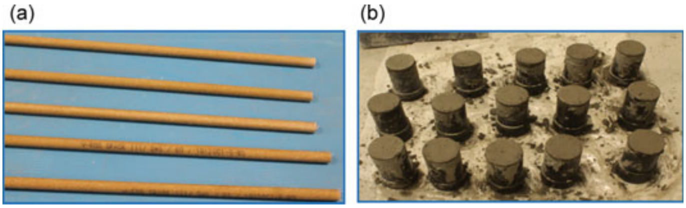

**Fig. 2** **a** GFRP bars; **b** Concrete cylinders

**Table 2** Mechanical properties of the GFRP and steel reinforcement

| Bar size | Diameter (mm) | Nominal cross-sectional area (mm$^2$) | Elastic tensile modulus (GPa) | Tensile strength (MPa) | Tensile strain (%) |
|---|---|---|---|---|---|
| *Steel bars* | | | | | |
| M15 | 16 | 200 | 200 | $f_y = 480$ | 0.24 |
| *GFRP bars* | | | | | |
| #5 | 15.9 | 198 | 62.50 | $f_{fu} = 1500$ | 2.4 |

and the surrounding concrete. Number 5 Grade III (nominal diameter of 15.90 mm) GFRP bars were used as longitudinal reinforcement in this study. The ultimate tensile strength ffu and modulus of elasticity Ef of the GFRP bars were determined according to ASTM D7205/D7205M-21, as reported by the manufacturer. The steel specimen was reinforced in the longitudinal direction with deformed M15 (nominal diameter of 16 mm) steel bars. Table 2 gives the mechanical properties of the GFRP and steel reinforcement. All RC box girders were cast using normal weight-ready mixed concrete with targeted compressive strength after 28 days of 44.5 Mpa.

## 2.3 Instrumentation and Testing Procedure

Before the testing, a torsion test setup was designed and fabricated especially to provide pure torsion for the RC box girders, as shown in Fig. 3. The torsional moment was applied to the girders through a vertical load exerted onto the rigid steel arm fastened to the girder. The box girders were supported on a hinge fixed 2000 mm apart. One 1000 kN MTS hydraulic actuator was used to apply the vertical load on the rigid steel arm near the hinge support. The fixed support is represented by a rigid steel beam resting on the girder and attached to the laboratory strong floor through two steel bars. Five electrical resistance strain gauges with a gauge length of 6 mm were mounted on the longitudinal bars at critical locations within the test regions as shown in Fig. 1. However, to measure the relative rotation of the cross-section, four potentiometers were placed at two different locations within the test region. In addition, one potentiometer was placed under the applied vertical load. An automatic data-acquisition system was observed by a computer to record the reading of the LVDTs, load cells, potentiometers, and strain gauges.

**Fig. 3** Test setup

# 3 Test Results

## 3.1 Crack Propagation and Failure Mode

The formation and propagation of a crack in all girders and the corresponding torque were signed and recorded until the end of the testing. When the applied principal tensile stresses were equivalent to the tensile strength of concrete, the first crack was initiated in all specimens in the middle of the front face of the test region. The cracking torsional strength of girders BGW-12 and BSW-12 was 37.20 and 35.70 kN·m, respectively. As applied torsional loading increased, more cracks appeared on each side and then linked with the crack on the front face, forming a spiral shape along the periphery of the specimen. The crack patterns of specimens BGW-12 and BSW-12 were almost similar in terms of failure plane angle and the number of cracks. In general, all specimens failed by concrete splitting due to a lack of transverse torsional

a-BGW12

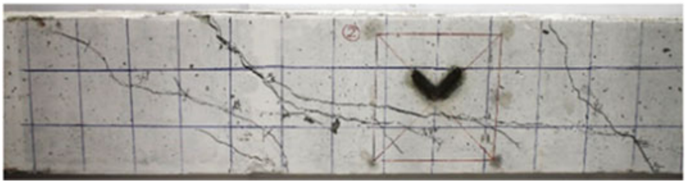

b-BSW12

**Fig. 4** Cracking propagation of the box girders

reinforcement. A major diagonal spiral crack developed within the formed crushed surface at the middle of the front face. Figure 4 shows the cracking pattern of all tested girders.

## 3.2 *Cracking Strength*

This section describes the behavior of the tested specimens up to the cracking stage. In addition, an assessment of the ACI 318-19 cracking torsional strength equation with the experimental results was accomplished. All girders experienced nearly identical linear responses from zero loading until the initiation of the first diagonal concrete crack irrespective of the type of longitudinal reinforcement, representing the uncracked condition governed by the properties of the concrete section. Therefore, it can be summed that the torsional strength is not affected by the type of longitudinal reinforcement until the cracking stage. The cracking torsional strength of the specimen BGW-12 slightly outperformed the counterpart BSW-12 by nearly 4%. It is worth mentioning that the cracking torsional strength for all specimens coincided with the ultimate torsional strength owing to the absence of the web torsional reinforcement. On the other hand, Table 3 provides the experimental cracking strength,

**Table 3** Comparison of experimental cracking torque with ACI prediction

| Girder identifier | $T_{cr(exp)}$ (kN.m) | $T_{cr(Pre)}$ (kN.m) | $T_{cr(exp)}/T_{cr(Pre)}$ |
|---|---|---|---|
| BGW-12 | 37.20 | 30.20 | 1.23 |
| BSW-12 | 35.70 | 30.20 | 1.18 |
| Average | – | – | 1.21 |

the prophesied cracking strength by ACI 318-19 as per Eq. (1), and the ratio of experimental cracking to prophesied cracking strength ($T_{cr(exp)}/T_{cr(Pre)}$). Table 3 indicates that the ACI 318-19 underestimated the cracking torsional strength by an average ratio ($T_{cr(exp)}/T_{cr(Pre)}$) of 21%.

$$T_{cr} = 0.33\sqrt{f_c'}\frac{A_{cp}^2}{P_{cp}} \tag{1}$$

## 3.3 Torque–Strain Behavior

Figure 5 plots the measured applied torsional moment on the specimens versus the strain behavior relationships for the internal GFRP and steel longitudinal bars. All the RC box girders had negligible strain readings and similar behavior from the zero loading until the initiation of the first diagonal crack, regardless of the reinforcement type. After cracking occurred, a redistribution of the internal forces from the concrete section to the longitudinal reinforcement resulted in a significant increase in the longitudinal reinforcement strains. The specimens reinforced with longitudinal GFRP bars exhibited higher bar strain after concrete cracking than the steel-reinforced specimen. This could be owing to the variation in the modulus of elasticity of the two materials. The max recorded strains in GFRP and steel bars were 2100 and 1330 microstrains, respectively. These values represent almost 9% and 55% of the ultimate tensile strain of the bars for GFRP and yielding strain of steel, respectively.

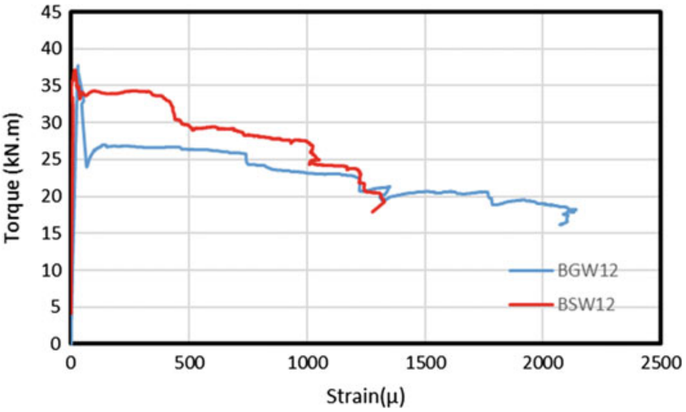

**Fig. 5** Torque versus longitudinal reinforcement strain

# 4 Conclusions

1. The test observations pointed out that the crack patterns in the steel and GFRP box girders without transverse reinforcement were nearly analogous in terms of failure plane angle and the number of cracks.
2. The test results indicated that the failure of all specimens was dominated by concrete splitting due to a lack of web reinforcement.
3. The torsional behavior of all specimens was nearly identical until the cracking stage. Moreover, the cracking torsional strength of all box girders coincided with the ultimate torsional strength.
4. ACI 318-19 design equation underestimated the cracking torque under pure torsion for the test specimens by about 21%.

**Acknowledgements** The experimental study was conducted with funding from Tier-I Canada Research Chair Advanced Composite Materials for Civil Infrastructures and Natural Sciences Engineering Research Council of Canada (NSERC-Industry Research Chair Program). The assistance of the technical staff of the structural laboratory at the Sherbrooke University's Department of Civil Engineering is also acknowledged.

# References

Hadhood A, Mohamed HM, Benmokrane B (2016) Experimental study of circular high-strength concrete columns reinforced with GFRP bars and spirals under concentric and eccentric loading. J Compos Constr 21(2):04016078

Hadhood A, Gouda MG, Agamy MH, Mohamed HM, Sherif A (2020) Torsion in concrete beams reinforced with GFRP spirals. J Eng Struct Elsevier, 201 (2019):109795

Mitchell D, Collins MP (1974) Diagonal compression field theory-a rational model for structural concrete in pure torsion. ACI Struct J 71:396–408

Mohamed HM, Benmokrane B (2014) Design and performance of reinforced concrete water chlorination tank totally reinforced with GFRP bars: a case study. J Compos Constr 18(1):05013001

Mohamed HM, Benmokrane B (2015) Torsion behavior of concrete beams reinforced with glass fiber-reinforced polymer bars and stirrups. ACI Struct J 112(5):543

Mohamed HM, Chaallal O, Benmokrane B (2014) Torsional moment capacity and failure mode mechanisms of concrete beams reinforced with carbon FRP bars and stirrups. J Compos Constr 19(2):04014049

Mousa S, Mohamed HM, Benmokrane B (2018) Cracking and crack control in circular concrete bridge members reinforced with fiber-reinforced polymer bars. J Bridge Eng 24(1):04018108

Nanni A, Faza S (2002) Designing and constructing with FRP bars: an emerging technology. Concr Int 24(11):53–58

# Application of GFRP Bars in Precast Concrete Tunnel Lining Segments

**Seyed Mohammad Hosseini, Salaheldin Mousa, Hamdy Mohamed, and Brahim Benmokrane**

## 1 Introduction

Several thousand kilometers of underground tunnels are constructed annually using tunnel boring machine (TBM) worldwide and in Canada, requiring a high demand for service life. Due to the harsh environment of tunnels, the corrosion of steel reinforcement is a major concern in precast concrete tunnel lining (PCTL) segments, especially those imposed to wastewater and aggressive soils (Caratelli et al. 2016; ACI Committee 533 2020). While rehabilitation and repair of underground structures are accompanied by such problems as high cost and serviceability interruption, using non-corroding glass fiber-reinforced polymer (GFRP) bars as a substitution for conventional steel reinforcement is a viable solution for corrosion problem in PCTL segments. GFRP bars offer such distinct advantages over conventional steel rebars as corrosion and chemical resistance, electromagnetic neutrality, high strength-to-weight ratio, high tensile strength, competitive life cycle cost, and fatigue resistance (Benmokrane et al. 2002; Robert et al. 2013). Further, reduction in concrete cover,

---

S. M. Hosseini · S. Mousa · H. Mohamed (✉) · B. Benmokrane
Department of Civil and Building Engineering, University of Sherbrooke, Sherbrooke, QC, Canada
e-mail: hamdy.mohamed@usherbrooke.ca

S. M. Hosseini
e-mail: seyed.mohammad.hosseini@usherbrooke.ca

S. Mousa
e-mail: salaheldin.mousa@usherbrooke.ca

B. Benmokrane
e-mail: brahim.benmokrane@usherbrooke.ca

S. Mousa
Department of Civil & Building Engineering, University of Sherbrooke, Sherbrooke, Canada

B. Benmokrane et al. (eds.), *8th International Conference on Advanced Composite Materials in Bridges and Structures*, Lecture Notes in Civil Engineering 267,
https://doi.org/10.1007/978-3-031-09409-5_21

suitability for parts of the tunnel that eventually should be demolished, and the possibility to create dielectric joints are among the merits of using GFRP reinforcement in tunnel segments (Spagnuolo et al. 2017).

In the previous studies conducted to evaluate the efficiency of GFRP-reinforced PCTL segments, the following parameters were investigated: (1) the type of reinforcement (steel and GFRP); (2) GFRP reinforcement configuration ("Closed Ring Reinforcement", "Lattice Reinforcement", and "Wirenet Reinforcement"); and (3) coating treatment of GFRP bars (sand-coated and smooth bars). According to the literature, the overall structural behavior of GFRP-reinforced and steel-reinforced PCTL segments did not have a significant difference. In addition, the "Closed Ring Reinforcement" configuration showed a superior behavior compared to other configurations. Besides, using sand-coated GFRP bars reduced the crack width in GFRP-reinforced PCTL segments by 70% (Caratelli et al. 2016, 2017; Spagnuolo et al. 2017). The reported failure mode for GFRP-reinforced PCTL segments in the literature was tension-controlled failure which is unfavorable according to ACI 440.1R-15 and CAN/CSA S806-12. Furthermore, the cracking behavior of GFRP-reinforced PCTL segments in the literature was unsatisfactory, especially in those reinforced with smooth GFRP bars. Therefore, it is necessary to do further studies to evaluate the structural performance of GFRP-reinforced PCTL segments before their widespread application in tunneling projects. This study is part of a great research project ongoing at the University of Sherbrooke aimed to investigate the structural performance of precast concrete tunnel lining segments reinforced with GFRP bars. Different parameters of reinforcement type, reinforcement ratio, bar size, bar spacing, concrete compressive strength, tie configuration, and concrete type were investigated in the mentioned research project. This paper presents the results obtained by testing two full-scale specimens reinforced with GFRP and steel bars to investigate the effect of bar type on the behavior of PCTL segments. In addition, the feasibility of using GFRP bars as a substitution for steel bars in PCTL segments was evaluated herein by investigating the failure mechanism, serviceability, and deflection behavior of a GFRP-reinforced PCTL segment.

## 2 Experimental Investigation

### *2.1 Material Properties*

Normal-strength concrete with a 28-day target compressive strength of 40 MPa was used to cast the specimens in this study. The tunnel segment specimens comprised of curvilinear longitudinal reinforcement in top and bottom meshes, end-anchorage U-shaped bars, and transverse ties. As GFRP bars cannot be bent after production, they should be manufactured in a curvilinear shape. An innovative manufacturing process developed by Pultrall Inc. was utilized to produce curvilinear bars in this

**Table 1** Mechanical properties of GFRP and steel reinforcement

| Reinforcement type | Bar size | $d_b$ (mm) | $A_f{}^{a}$ (mm$^2$) | $E_f$ (GPa) | $f_{fu}$ (MPa) | $\varepsilon_{fu}$ (%) |
|---|---|---|---|---|---|---|
| GFRP curvilinear bars | #5 | 15 | 199 | 53.4 ± 0.9 | 976 ± 45 | 1.8 ± 0.1 |
| GFRP U-shaped bars[b] | #5 | 15 | 199 | 53.5 ± 1.1 | 1,283 ± 42 | 2.4 ± 0.1 |
| GFRP closed ties[b] | #4 | 13 | 127 | 55.6 ± 1.6 | 1,248 ± 74 | 2.2 ± 0.1 |
| Steel | 10 M | 11.3 | 100 | 200.0 | $f_y{}^{d} = 480 \pm 10$ | $\varepsilon_y{}^{d} = 0.24$ |
|  | 15 M | 16 | 200 | 200.0 | $f_y = 480 \pm 15$ | $\varepsilon_y = 0.24$ |

[a] Nominal cross-sectional area

[b] The reported mechanical properties of GFRP closed ties and U-shaped bars were obtained by testing of straight bars manufactured with the same manufacturing process as the bent bars

[d] The reported tensile strength and ultimate tensile strain of steel bars are related to yield point

*Note* Properties calculated based on the nominal cross-sectional area

study with the predetermined radius for the top and bottom meshes. Curvilinear sand-coated bars No. 5 (15 mm) with a radius of 3305 mm and 3445 mm for the bottom and top meshes were used as longitudinal reinforcement in the GFRP-reinforced specimen, respectively. End-anchorage for longitudinal bars was provided through sand-coated #5 U-shape bars. Sand-coated GFRP closed ties No. 4 (13 mm) were used as transverse reinforcement in the GFRP-reinforced specimen. Tensile test was performed according to ASTM D7205 (2016) on the curvilinear bars with a radius of 3305 mm to determine tensile strength, modulus of elasticity, and ultimate strain of the GFRP curvilinear bars. Deformed 15 M and 10 M steel bars were used as longitudinal and transverse reinforcements in the steel-reinforced specimen. The mechanical properties of GFRP and steel reinforcement are reported in Table 1. Figure 1 shows the GFRP tunnel segment cage.

## 2.2 *Specimens Description, Instrumentation, and Testing*

To investigate the feasibility of using GFRP reinforcement in tunnel segments, two full-scale PCTL segments including one GFRP-reinforced and one steel-reinforced were constructed and tested under bending load. The original tunnel considered in this study was a metro tunnel lining with an internal diameter of 6500 mm and an external diameter of 7000 mm. A full ring of the original tunnel constitutes seven segments. A segment, parallelogram in shape, with the arc length of 3100 mm, width of 1500 mm, and thickness of 250 mm, was selected in this study (Fig. 2). A wooden formwork was designed for the casting of the specimens. The specimens were demolded and cured for seven days after casting (Table 2).

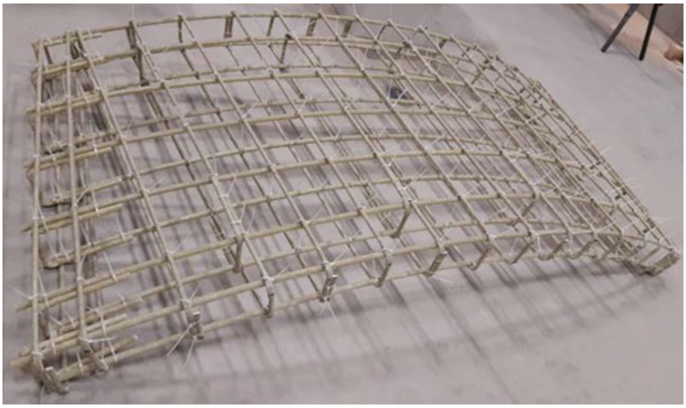

**Fig. 1** GFRP tunnel segment cage

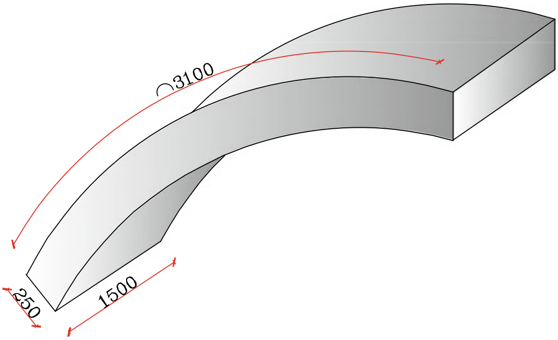

**Fig. 2** Tunnel segment dimensions

**Table 2** Test matrix and details of test specimens

| Beam ID | Bar type | Reinforcement | | |
|---|---|---|---|---|
| | | Longitudinal | $\rho_l$ (%) | Transverse |
| 7G#5 | Sand-coated GFRP bars | 7 #5 bars | 0.5 | #4 @ 200 mm |
| 7S15M | Deformed steel bars | 7 15 M bars | 0.5 | 10 M @ 200 mm |

Figure 3 shows the test setup used for testing of the tunnel segment specimens. The specimens were monotonically loaded under a three-point bending load. The supports were cylindrical in shape and covered with Teflon sheets which allowed free rotation and movement of the segment during the test with a minimized friction. The load was applied to the specimen through a 11,400 kN MTS testing machine with a displacement-control rate of 0.8 mm/min. The tests were performed at the Canada Foundation of Innovation (CFI) laboratory located at the University of Sherbrooke. To

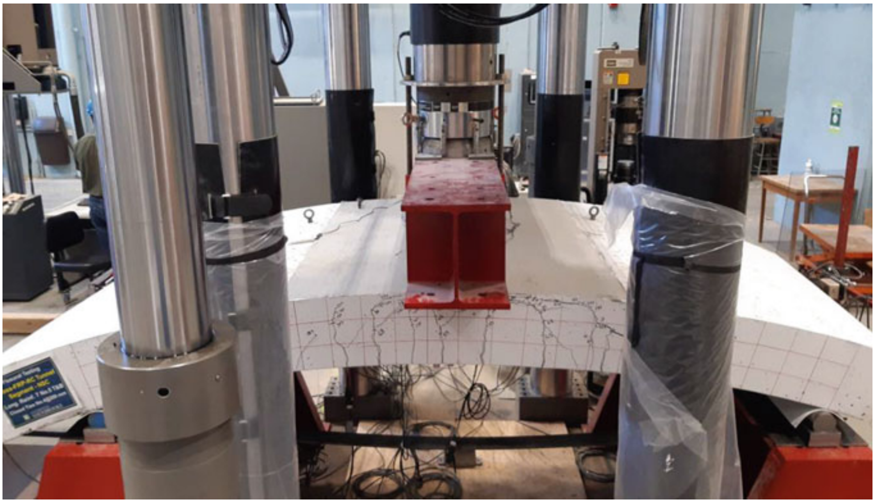

**Fig. 3** Details of the test setup

assure uniform deflection of the specimens during the test, three linear potentiometers (LPOTs) distributed along the width of the specimen recorded the deflection at mid-span.

## 3 Experimental Results

### 3.1 Crack Propagation and Failure Mode

Crack propagation in the specimens followed a typical pattern of flexural cracks in a simply supported member subjected to a three-point bending load. With the load increased, the flexural cracks increased in number and width. The specimen 7G#5 failed due to concrete crushing as expected by its higher reinforcement ratio compared to the balanced ratio. The steel-reinforced specimen failed by concrete crushing after yielding steel reinforcement which denotes tension-controlled flexural failure. By using an identical reinforcement configuration, the ultimate load-carrying capacity of 7G#5 was 33% greater than that of 7S15M. In addition, 7G#5 experienced a 50% higher deflection at peak load which shows its greater deformability. Table 3 lists cracking load, peak load, peak deflection, and mode of failure. Furthermore, Fig. 4 shows the failure modes of all the specimens.

In this study, the service load of the GFRP-reinforced specimen is calculated using the load corresponding to 2000 $\mu\varepsilon$ in the tensile reinforcement (ISIS Canada Research Network 2001). The service load for steel-reinforced specimen was considered at the longitudinal bar strain of 1200 $\mu\varepsilon$. Table 3 lists the service load crack

**Table 3** Summary of the test results

| Beam ID | $P_{cr}$ (kN) | $P_{peak}$ (kN) | Deflection at peak load (mm) | Failure mode | Crack width at service load (mm) | Deflection at service load (mm) |
|---|---|---|---|---|---|---|
| 7G#5 | 57 | 315 | 66 | Compression-controlled flexural failure | 0.35 | 2.47 |
| 7S15M | 68 | 236 | 44 | Tension-controlled flexural failure | 0.2 | 3.67 |

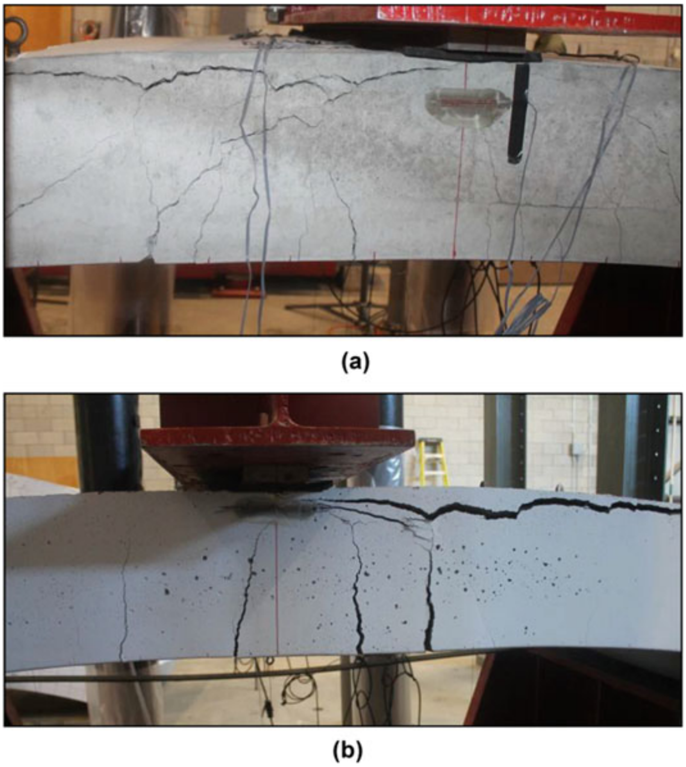

**Fig. 4** Typical failure modes of beam specimens: **a** 7G#5 and **b** 7S15M

width and deflection in the specimens. The crack width measured by the crack width ruler at service load was 0.35 mm in the GFRP-reinforced specimen. According to CAN/CSA S6-19, the maximum allowable crack width in GFRP-reinforced elements is 0.5 and 0.7 mm for the members subjected to an aggressive environment and for other members, respectively. It can be concluded that the crack width in the GFRP-reinforced specimen successfully satisfied the requirements of CAN/CSA S6-19 for the maximum crack width even in a harsh environment. The service load deflection was 33% lower than that of the steel-reinforced one. It shows that GFRP-reinforced PCTL segments can have a satisfactory service load deflection compared to their steel counterparts.

### *3.2 Load–Deflection Behavior*

The load versus mid-span deflection of the tested specimens is presented in Fig. 5. In the pre-cracking stage, all the specimens showed a linear behavior with almost the same stiffness. After the first crack occurs, the specimens experienced a temporary reduction in load. In the post-cracking stage, the flexural stiffness of the specimens decreased compared to the uncracked section due to the transition from the gross section to the effective section. The post-cracking stiffness of 7S15M specimen was 2.7 times greater than the 7G#5. While the axial stiffness of GFRP bars was 3.9 times greater than steel rebars. GFRP-reinforced specimen exhibited an almost linear behavior up to the failure which can be attributed to the linear elastic behavior of GFRP reinforcement. The steel-reinforced specimen experienced nearly linear load–deflection until the yielding point. After yielding, it followed a typical steel stress–strain plateau up to failure with a reduced stiffness. However, the ultimate load increased around 58% relative to yield load which can be attributed to strain hardening of steel rebars and increasing the bending moment arm in the section. As concrete crushing in 7S15M and 7G#5 specimens was gradual, they could carry the load to some extent after the first drop. However, as the confinement did not provide for the compression block, the concrete crushing led to a full spalling which led to a reduction in the load.

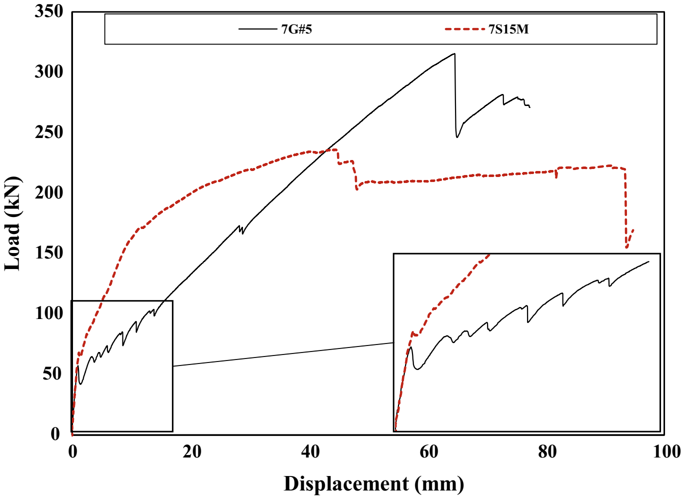

**Fig. 5** Load–deflection response for all beam specimens

## 4 Conclusions

This study evaluated the structural performance of GFRP-reinforced precast concrete tunnel lining segments reinforced with GFRP bars. Two full-scale specimens, one reinforced with GFRP and the other reinforced with steel bars with the same geometry and detail, were constructed and tested under a three-point bending load. The cracking behavior, serviceability, failure mode, and deflection behavior of the specimens were investigated. The following conclusions can be drawn:

1. GFRP-reinforced tunnel segment experienced concrete crushing failure while tension-controlled flexural failure was experienced by the steel-reinforced specimen. The recorded peak load of the GFRP-reinforced specimen was 33% greater than that of the steel-reinforced one. In addition, the replacement of steel reinforcement with GFRP one increased the peak load deflection by 50%.
2. The service load crack width in the tested GFRP-reinforced PCTL segment was 30% and 50% narrower than the allowable crack width specified by CAN/CSA S6-19 for the members subjected to the harsh environment and the members not subjected to the harsh environment, respectively. In addition, the service load deflection of the GFRP-reinforced specimen was 33% lower than that of the steel-reinforced specimen.
3. GFRP-reinforced PCTL segment showed a linear elastic behavior up to the failure including pre-cracking and post-cracking stages. Steel-reinforced specimen followed a typical load–deflection plateau of steel-reinforced flexural elements. With having an axial stiffness 3.9 times greater than the GFRP-reinforced specimen, the steel-reinforced specimen experienced 2.7 times greater axial stiffness.
4. GFRP-reinforced PCTL segment showed satisfactory structural performance in terms of failure mechanism, ultimate load and deflection, and serviceability. The application of GFRP reinforcement in PCTL segments seems to be an effective approach to mitigate the corrosion problem in such structural elements and take advantage of the unique features of GFRP bars in tunnels.

**Acknowledgements** This research was conducted with funding from the Natural Sciences and Engineering Research Council of Canada (NSERC), Mathematics of Information Technology and Complex Systems (MITACS), the Fonds de recherche du Québec en nature et technologies (FRQ-NT), The Pole de Recherche et d'innovation en Materiaux Avances au quebéc (PRIMA Quebéc), and the Tier-1 Canada Research Chair in Advanced Composite Materials for Civil Structures. The authors are grateful to the precast company (Sym-Tech Béton Préfabriqué, Sainte-Hyacinthe, QC, Canada) and to the GFRP bar manufacturer (Pultrall Inc., Thetford Mines, QC, Canada) for their effective involvement in this project, and to the technical staff of the structural lab in the Department of Civil Engineering at the University of Sherbrooke.

## References

ACI Committee 440 (2015) Guide for the design and construction of structural concrete reinforced with fiber-reinforced polymer bars (ACI 440.1R-15). American Concrete Institute, Farmington Hills, MI

ACI Committee 533 (2020) Guide for precast concrete tunnel segments (ACI 533.5R-20). American Concrete Institute, Farmington Hills, MI

ASTM D7205/D7205M-06(2016) (2016) Tandard test method for tensile properties of fiber reinforced polymer matrix composite bars. ASTM International, West Conshohocken, PA

Benmokrane B, Wang P, Ton-That TM, Rahman H, Robert J-F (2002) Durability of glass fiber-reinforced polymer reinforcing bars in concrete environment. J Compos Constr 6(3):143–153

CanadianStandardsAssociation (CSA) (2019) Canadian highway bridge design code (CAN/CSA S6-19). Mississauga, ON, Canada: CSA Group

Canadian Standards Association (CSA) (2012) Design and construction of building components with fiber reinforced polymers (CAN/CSA S806-12). Mississauga, ON, Canada: CSA Group

Caratelli A, Meda A, Rinaldi Z, Spagnuolo S (2016) Precast tunnel segments with GFRP reinforcement. Tunn Undergr Space Technol 60:10–20

Caratelli A, Meda A, Rinaldi Z, Spagnuolo S, Maddaluno G (2017) Optimization of GFRP reinforcement in precast segments for metro tunnel lining. Compos Struct 181:336–346

ISIS Canada Research Network (2001) Reinforced concrete structures with fibre reinforced polymers. ISIS Manual No. 3, University of Manitoba, Winnipeg, MB, Canada

Robert M, Benmokrane B (2013) Combined effects of saline solution and moist concrete on long-term durability of GFRP reinforcing bars. Constr Build Mater 38:274–284

Spagnuolo S, Meda A, Rinaldi Z, Nanni A (2017) Precast concrete tunnel segments with GFRP reinforcement. J Compos Constr 21(5):04017020